

8-2016

Analysis of feedback control applied with command shaping to minimize residual vibration

Nicholas L. Jacobs
Purdue University

Follow this and additional works at: https://docs.lib.purdue.edu/open_access_theses



Part of the [Mechanical Engineering Commons](#), and the [Robotics Commons](#)

Recommended Citation

Jacobs, Nicholas L., "Analysis of feedback control applied with command shaping to minimize residual vibration" (2016). *Open Access Theses*. 966.

https://docs.lib.purdue.edu/open_access_theses/966

This document has been made available through Purdue e-Pubs, a service of the Purdue University Libraries. Please contact epubs@purdue.edu for additional information.

**PURDUE UNIVERSITY
GRADUATE SCHOOL
Thesis/Dissertation Acceptance**

This is to certify that the thesis/dissertation prepared

By Nicholas L. Jacobs

Entitled

Analysis of Feedback Control Applied with Command Shaping to Minimize Residual Vibration

For the degree of Master of Science in Mechanical Engineering

Is approved by the final examining committee:

Peter H. Meckl

Chair

George T. Chiu

Raymond J. Cipra

To the best of my knowledge and as understood by the student in the Thesis/Dissertation Agreement, Publication Delay, and Certification Disclaimer (Graduate School Form 32), this thesis/dissertation adheres to the provisions of Purdue University's "Policy of Integrity in Research" and the use of copyright material.

Approved by Major Professor(s): Peter H. Meckl

Approved by: Jay P. Gore

Head of the Departmental Graduate Program

7/5/2016

Date

ANALYSIS OF FEEDBACK CONTROL APPLIED WITH COMMAND
SHAPING TO MINIMIZE RESIDUAL VIBRATION

A Thesis

Submitted to the Faculty

of

Purdue University

by

Nicholas L. Jacobs

In Partial Fulfillment of the

Requirements for the Degree

of

Master of Science

August 2016

Purdue University

West Lafayette, Indiana

Dedicated to my family

ACKNOWLEDGMENTS

I would first like to express my deep gratitude and appreciation to my major professor, Prof. Peter Meckl, for all his support, insight, and encouragement throughout my graduate research. His guidance has been invaluable throughout this entire process. I would also like to thank the other members of my advisory committee, Prof. George Chiu and Prof. Raymond Cipra, for their valuable input and the precious gift of their time. During my stay here at Purdue University I have learned a great deal from all three of my committee members, and for that I will always be extremely grateful. I would like to also extend my appreciation to my research partner Yumeng, who was a great colleague in this undertaking. The two of us would often brainstorm together, bouncing ideas off each other, and his input has always been very helpful. I would like to extend this gratitude also to the other members of the Spira Labs, as well as the staff in the E-shop for the School of Mechanical Engineering, as they have all been very helpful in providing assistance for solving the issues that arise from time to time. Last but certainly not least, I would like to thank my family and my friends, whose great support and encouragement have been unwavering and unconditional throughout this journey.

TABLE OF CONTENTS

	Page
LIST OF TABLES	vi
LIST OF FIGURES	vii
ABSTRACT	xv
CHAPTER 1. INTRODUCTION	1
1.1 Motivation	1
1.2 Literature Review	2
1.3 Overview of Thesis	6
CHAPTER 2. COMMAND SHAPING	7
2.1 Theoretical Preliminaries	7
2.2 Ramped Sinusoid	11
2.3 Versine	14
2.4 Influence of Relative Weighting Factor	16
2.5 Performance Metrics	23
CHAPTER 3. ROBOT MODEL AND SYSTEM DESCRIPTION	25
3.1 The Two-Link Flexible-Joint Robot	25
3.2 Robot Kinematics	27
3.3 Calculation of Performance Metrics for Two-Link Robot	38
3.4 Robot Dynamics	39
3.4.1 Lagrangian Model	40
3.4.2 Reduced Model	43
3.4.3 Recursive Newton-Euler Equations	44
3.5 System Parameters	50
3.6 Computed Torque Control	52
3.6.1 Computed Torque Control with Lagrangian Model	53
3.6.2 Computed Torque Control with Newton-Euler Equations	54
3.7 Configuration-Dependent Resonance	56
CHAPTER 4. MODELING, SIMULATION, AND ANALYSIS OF FEED- BACK CONTROL ON A THREE-MASS SYSTEM	60
4.1 System Description	60
4.2 Modal Analysis	64
4.3 Transfer Function Representation	68
4.4 Closed-Loop Control of the Three-Mass System	72
4.4.1 Frequency Response of the Closed-Loop System	77

	Page
4.4.2 Closed-Loop Stability and Damping	96
4.5 Calculation of Performance Metrics for the Three-Mass System . . .	104
4.6 Simulation Results of the Three-Mass System	105
4.6.1 Fast Fourier Transform	105
4.6.2 Analysis of Simulation Results	108
CHAPTER 5. APPLICATION TO THE FLEXIBLE-JOINT ROBOT . . .	132
5.1 Robot Hardware	132
5.2 Digital Implementation of Feedback Control	134
5.3 Simulation Results for the Flexible-Joint Robot	138
5.4 Experimental Results for the Flexible-Joint Robot	145
CHAPTER 6. CONCLUSIONS AND RECOMMENDATIONS	151
6.1 General Procedure for Designing a Controller to Minimize Residual Vibration	151
6.2 Unique Contributions	153
6.3 Future Work	154
LIST OF REFERENCES	157
APPENDICES	
Appendix A. Extra Simulation Results for the Three-Mass System	161
Appendix B. Extra Experimental Results for the Flexible-Joint Robot . .	182

LIST OF TABLES

Table	Page
2.1 Values of the First Ten Harmonics of Ramped Sinusoid Function. . . .	12
2.2 Nominal Natural Frequencies of Two-Link Flexible-Joint Robot.	16
3.1 Estimated values of the physical parameters of the robot, [44].	52
4.1 System parameters of the three-mass system.	63
4.2 Values of ρ needed for different levels of κ for the nominal three-mass system.	63
4.3 Maximum closed-loop damping of the three-mass system with PD control.	99
4.4 Minimum required values of controller gain K_c to ensure closed-loop stability for $\omega_{center} = 10$	102
4.5 Minimum required values of controller gain K_c to ensure closed-loop stability for $\omega_{center} = 5$	103
5.1 Simulated results on the residual vibration performance of the two-link flexible-joint robot for the versine profile.	143
5.2 Simulated results on the residual vibration performance of the two-link flexible-joint robot for the ramped sinusoid profile.	143
5.3 Experimental results on the residual vibration performance of the two-link flexible-joint robot for the versine profile.	150
5.4 Experimental results on the residual vibration performance of the two-link flexible-joint robot for the ramped sinusoid profile.	150

LIST OF FIGURES

Figure	Page
2.1 First Three Harmonics of the Normalized Ramped Sinusoid Function, [37]	13
2.2 First Three Harmonics of the Normalized Versine Function, [37]	15
2.3 Influence of ρ on κ for Ramped Sinusoid	18
2.4 Influence of ρ on κ for Acceleration Segment of Versine	18
2.5 Influence of ρ on κ for Deceleration Segment of Versine	19
2.6 Influence of ρ on Average Magnitude of Fourier Transform for First Natural Frequency of the Ramped Sinusoid Function	20
2.7 Influence of ρ on Average Magnitude of Fourier Transform for Second Natural Frequency of the Ramped Sinusoid Function	20
2.8 Influence of ρ on average magnitude of Fourier Transform for first natural frequency in the acceleration segment of the versine function	21
2.9 Influence of ρ on average magnitude of Fourier Transform for second natural frequency in the acceleration segment of the versine function . . .	21
2.10 Influence of ρ on average magnitude of Fourier Transform for first natural frequency in the deceleration segment of the versine function	22
2.11 Influence of ρ on average magnitude of Fourier Transform for second natural frequency in the deceleration segment of the versine function . . .	22
3.1 The two-link flexible-joint robot	26
3.2 Schematic of the two-link flexible-joint robot, [40]	27
3.3 Schematic of two-link flexible-joint robot with the XYZ and UVW coordinate frames	29
3.4 Idealized model of joint flexibility, [2]	49
3.5 Block diagram of computed torque controller using Lagrangian model, [44]	53
3.6 Variations in ω_1 and ω_2 as functions of link angle θ_2	58
4.1 The three-mass system	61
4.2 Pole-Zero map of the undamped open-loop system	72

Figure	Page
4.3 Pole-Zero map of the lightly-damped open-loop system	73
4.4 Bode plot of the transfer function relating the input to the first mass .	74
4.5 Block diagram of feedforward and feedback control of the three-mass system	74
4.6 Block diagram of computed torque control of the three-mass system . .	75
4.7 Example Bode plot of a PD controller	78
4.8 Bode plot of the open-loop transfer function for the PD controlled three-mass system	79
4.9 Bode plot of a Lead compensator	80
4.10 Bode plot of a Lag compensator	81
4.11 Bode plot of a Lead-Lag compensator	82
4.12 Magnitude plot of a Lead-Lag compensator	82
4.13 Example Bode plot of an unstable closed-loop three-mass system when using a Lead-Lag compensator with $K_c = 1$, $\omega_{center} = 5$, $\omega_{width} = 1$, and $a = 10$	83
4.14 Example Bode plot of a stable closed-loop three-mass system when using a Lead-Lag compensator with $K_c = 250$, $\omega_{center} = 5$, $\omega_{width} = 1$, and $a = 10$	84
4.15 Rearranged block diagram of the feedback control loop	84
4.16 Bode plot of frequency response relating input to controller output with different values of K_c and $z_{pd} = -30$	85
4.17 Bode plot of frequency response relating input to controller output with different values of z_{pd} when $K_c = 20$	86
4.18 Bode plot of frequency response relating input to controller output with different values of z_{pd} when $K_c = 100$	87
4.19 Bode plot of frequency response relating input to controller output for Lead-Lag controller with different frequencies	87
4.20 Bode plot of frequency response relating input to controller output for Lead-Lag controller with control gains of $K_c = 50, 100, 150$, with $\omega_{center} = 5 \frac{\text{rad}}{\text{s}}$, $\omega_{width} = 1 \frac{\text{rad}}{\text{s}}$, and $a = 2$	88
4.21 Bode plot of frequency response relating input to controller output for Lead-Lag controller with control gains of $K_c = 500, 1000, 1500$, with $\omega_{center} = 5 \frac{\text{rad}}{\text{s}}$, $\omega_{width} = 1 \frac{\text{rad}}{\text{s}}$, and $a = 2$	89

Figure	Page
4.22 Bode plot of frequency response relating input to controller output for Lead-Lag controller with different Pole-Zero ratios when $\omega_{center} = 5 \frac{\text{rad}}{\text{s}}$, $\omega_{width} = 1 \frac{\text{rad}}{\text{s}}$, and $K_c = 250$	89
4.23 Bode plot of the feedforward controller	90
4.24 Rearranged block diagram of the feedback control loop for the computed torque configuration	90
4.25 Bode plot of the computed torque frequency response with different values of K_c when $z_{pd} = -30$	92
4.26 Bode plot of the computed torque frequency response with different values of z_{pd} when $K_c = 20$	93
4.27 Bode plot of the computed torque frequency response for Lead-Lag controllers with control gains of $K_c = 50, 100, 150$, with $\omega_{center} = 5 \frac{\text{rad}}{\text{s}}$, $\omega_{width} = 1 \frac{\text{rad}}{\text{s}}$, and $a = 2$	94
4.28 Bode plot of the computed torque frequency response for Lead-Lag controllers with control gains of $K_c = 500, 1000, 1500$, with $\omega_{center} = 5 \frac{\text{rad}}{\text{s}}$, $\omega_{width} = 1 \frac{\text{rad}}{\text{s}}$, and $a = 2$	95
4.29 Root Locus of the closed-loop for the three-mass system with PD control where $z_{pd} = -30$ on the real axis	97
4.30 Root Locus of the closed-loop for the three-mass system with PD control where $z_{pd} = -10$ on the real axis	98
4.31 Root Locus of the closed-loop for the three-mass system with PD control where $z_{pd} = -5$ on the real axis	99
4.32 Root Locus of the closed-loop for the three-mass system with PD control where $z_{pd} = -1$ on the real axis	100
4.33 Root Locus of the three-mass system with a Lead-Lag compensator where $\omega_{center} = 5 \frac{\text{rad}}{\text{s}}$, $\omega_{width} = 1 \frac{\text{rad}}{\text{s}}$, and ratio $a = 10$	101
4.34 Root Locus of the three-mass system with a Lead-Lag compensator where $\omega_{center} = 10 \frac{\text{rad}}{\text{s}}$, $\omega_{width} = 2 \frac{\text{rad}}{\text{s}}$, and ratio $a = 10$	102
4.35 Example FFT of the feedforward controller output for a ramped sinusoid profile with $\kappa = 3$, a PD controller of $K_c = 20$ and $z_{pd} = -30$, and a -5% error in the natural frequencies	107
4.36 Example FFT of the feedback controller output for a ramped sinusoid profile with $\kappa = 3$, a PD controller of $K_c = 20$ and $z_{pd} = -30$, and a -5% error in the natural frequencies	108

Figure	Page
4.37 Example FFT of the total controller output for a ramped sinusoid profile with $\kappa = 3$, a PD controller of $K_c = 20$ and $z_{pd} = -30$, and a -5% error in the natural frequencies	109
4.38 Simulated response of the three-mass system using the feedforward configuration for a PD controller with $K_c = 20$, $z_{pd} = -30$, -5% error, and a versine profile with $\kappa = 3$	110
4.39 Simulated response of the three-mass system using the feedforward configuration for a PD controller with $K_c = 20$, $z_{pd} = -30$, -5% error, and a ramped sinusoid profile with $\kappa = 3$	111
4.40 Simulated response of the three-mass system using the feedforward configuration for a PD controller with $K_c = 20$, $z_{pd} = -30$, -5% error, and a ramped sinusoid profile with $\kappa = 15$	112
4.41 Response of the three-mass system for a ramped sinusoid profile with $\kappa = 3$ using feedforward controller and no error in the natural frequencies . .	113
4.42 Response of the three-mass system for a versine profile with $\kappa = 3$ using feedforward controller and no error in natural frequencies	114
4.43 Response of the three-mass system for a ramped sinusoid profile with $\kappa = 3$ using feedforward controller and -5% error in the natural frequencies .	115
4.44 Response of the three-mass system for a versine profile with $\kappa = 3$ using feedforward controller and -5% error in the natural frequencies	116
4.45 Response of the three-mass system for a ramped sinusoid profile with $\kappa = 3$ using feedforward controller and $+5\%$ error in the natural frequencies .	117
4.46 Response of the three-mass system for a versine profile with $\kappa = 3$ using feedforward controller and $+5\%$ error in the natural frequencies	118
4.47 Response of the three-mass system for a ramped sinusoid profile with $\kappa = 9$ using feedforward controller and $+5\%$ error in the natural frequencies .	119
4.48 Response of the three-mass system for a ramped sinusoid profile with $\kappa = 15$ using feedforward controller and $+5\%$ error in the natural frequencies	120
4.49 Response of the three-mass system for a ramped sinusoid profile with $\kappa = 3$ using computed torque controller and -5% error in the natural frequencies	121
4.50 Response of the three-mass system for a ramped sinusoid profile with $\kappa = 3$ using computed torque controller and $+5\%$ error in the natural frequencies	122
4.51 Response of the three-mass system for a versine profile with $\kappa = 3$ using computed torque controller and -5% error in the natural frequencies .	123

Figure	Page
4.52 Response of the three-mass system for a versine profile with $\kappa = 3$ using computed torque controller and +5% error in the natural frequencies	124
4.53 Response of the three-mass system for a ramped sinusoid profile with $\kappa = 15$ using computed torque controller and +5% error in the natural frequencies	125
4.54 Response of the three-mass system for a versine profile with $\kappa = 3$ when using feedforward control with a Lead-Lag compensator with $\omega_{center} = 10\frac{rad}{s}, \omega_{width} = 1\frac{rad}{s}$ and a -5% error in the natural frequencies	126
4.55 Response of the three-mass system for a versine profile with $\kappa = 3$ when using feedforward control with a Lead-Lag compensator with $\omega_{center} = 10\frac{rad}{s}, \omega_{width} = 1\frac{rad}{s}$ and a +5% error in the natural frequencies	127
4.56 Response of the three-mass system for a versine profile with $\kappa = 3$ when using feedforward control with a Lead-Lag compensator with $\omega_{center} = 5\frac{rad}{s}, \omega_{width} = 1\frac{rad}{s}$ and a -5% error in the natural frequencies	128
4.57 Response of the three-mass system for a versine profile with $\kappa = 3$ when using feedforward control with a Lead-Lag compensator with $\omega_{center} = 5\frac{rad}{s}, \omega_{width} = 1\frac{rad}{s}$ and a +5% error in the natural frequencies	129
4.58 Response of the three-mass system for a versine profile with $\kappa = 3$ when using computed torque control with a Lead-Lag compensator with $\omega_{center} = 5\frac{rad}{s}, \omega_{width} = 1\frac{rad}{s}$ and a -5% error in the natural frequencies	130
4.59 Response of the three-mass system for a versine profile with $\kappa = 3$ when using computed torque control with a Lead-Lag compensator with $\omega_{center} = 5\frac{rad}{s}, \omega_{width} = 1\frac{rad}{s}$ and a +5% error in the natural frequencies	131
5.1 Simulated response of Original PD controller with $K_{p,1} = 6400, K_{v,1} = 160, K_{p,2} = 400$, and $K_{v,2} = 40$ when applying a versine input with $\kappa = 6$	140
5.2 Simulated response of Alternative PD controller with $K_{p,1} = 3200, K_{v,1} = 160, K_{p,2} = 400$, and $K_{v,2} = 40$ when applying a versine input with $\kappa = 6$	141
5.3 Simulated response of Lead-Lag controller when applying a versine input with $\kappa = 6$	142
5.4 Simulated response of Hybrid controller when applying a versine input with $\kappa = 6$	145
5.5 Experimental response of Original PD controller with $K_{p,1} = 6400, K_{v,1} = 160, K_{p,2} = 400$, and $K_{v,2} = 40$ when applying a versine input with $\kappa = 6$	146
5.6 Experimental response of Alternative PD controller with $K_{p,1} = 3200, K_{v,1} = 160, K_{p,2} = 400$, and $K_{v,2} = 40$ when applying a versine input with $\kappa = 6$	147

Figure	Page
5.7 Experimental response of Lead-Lag controller with $K_{c,1} = 3200$, $K_{c,2} = 400$, $\omega_{center,1} = \omega_{center,2} = 3.75 \frac{\text{rad}}{\text{s}}$, $\omega_{width,1} = \omega_{width,2} = 0.5 \frac{\text{rad}}{\text{s}}$, and $a_1 = a_2 = 4$ when applying a versine input with $\kappa = 6$	148
5.8 Experimental response of Hybrid controller when applying a versine input with $\kappa = 6$	149
A.1 Response of the three-mass system for a ramped sinusoid profile with $\kappa = 9$ when using feedforward control with a PD controller and no error in the natural frequencies	161
A.2 Response of the three-mass system for a ramped sinusoid profile with $\kappa = 15$ when using feedforward control with a PD controller and no error in the natural frequencies	162
A.3 Response of the three-mass system for a versine profile with $\kappa = 9$ when using feedforward control with a PD controller and no error in the natural frequencies	163
A.4 Response of the three-mass system for a versine profile with $\kappa = 15$ when using feedforward control with a PD controller and no error in the natural frequencies	164
A.5 Response of the three-mass system for a ramped sinusoid profile with $\kappa = 9$ when using feedforward control with a PD controller and -5% error in the natural frequencies	165
A.6 Response of the three-mass system for a ramped sinusoid profile with $\kappa = 15$ when using feedforward control with a PD controller and -5% error in the natural frequencies	166
A.7 Response of the three-mass system for a versine profile with $\kappa = 9$ when using feedforward control with a PD controller and -5% error in the natural frequencies	167
A.8 Response of the three-mass system for a versine profile with $\kappa = 15$ when using feedforward control with a PD controller and -5% error in the natural frequencies	168
A.9 Response of the three-mass system for a versine profile with $\kappa = 9$ when using feedforward control with a PD controller and $+5\%$ error in the natural frequencies	169
A.10 Response of the three-mass system for a versine profile with $\kappa = 15$ when using feedforward control with a PD controller and $+5\%$ error in the natural frequencies	170

Figure	Page
A.11 Response of the three-mass system for a ramped sinusoid profile with $\kappa = 9$ when using computed torque control with a PD controller and no error in the natural frequencies	171
A.12 Response of the three-mass system for a ramped sinusoid profile with $\kappa = 15$ when using computed torque control with a PD controller and no error in the natural frequencies	172
A.13 Response of the three-mass system for a ramped sinusoid profile with $\kappa = 9$ when using computed torque control with a PD controller and -5% error in the natural frequencies	173
A.14 Response of the three-mass system for a ramped sinusoid profile with $\kappa = 15$ when using computed torque control with a PD controller and -5% error in the natural frequencies	174
A.15 Response of the three-mass system for a ramped sinusoid profile with $\kappa = 9$ when using computed torque control with a PD controller and $+5\%$ error in the natural frequencies	175
A.16 Response of the three-mass system for a versine profile with $\kappa = 9$ when using computed torque control with a PD controller and no error in the natural frequencies	176
A.17 Response of the three-mass system for a versine profile with $\kappa = 15$ when using computed torque control with a PD controller and no error in the natural frequencies	177
A.18 Response of the three-mass system for a versine profile with $\kappa = 9$ when using computed torque control with a PD controller and -5% error in the natural frequencies	178
A.19 Response of the three-mass system for a versine profile with $\kappa = 15$ when using computed torque control with a PD controller and -5% error in the natural frequencies	179
A.20 Response of the three-mass system for a versine profile with $\kappa = 9$ when using computed torque control with a PD controller and $+5\%$ error in the natural frequencies	180
A.21 Response of the three-mass system for a versine profile with $\kappa = 15$ when using computed torque control with a PD controller and $+5\%$ error in the natural frequencies	181
B.1 Experimental response of Original PD controller when applying a versine input with $\kappa = 9$	182

Figure	Page
B.2 Experimental response of Original PD controller when applying a ramped sinusoid input with $\kappa = 6$	183
B.3 Experimental response of Original PD controller when applying a ramped sinusoid input with $\kappa = 9$	184
B.4 Experimental response of Alternative PD controller when applying a versine input with $\kappa = 9$	185
B.5 Experimental response of Alternative PD controller when applying a ramped sinusoid input with $\kappa = 6$	186
B.6 Experimental response of Alternative PD controller when applying a ramped sinusoid input with $\kappa = 9$	187
B.7 Experimental response of Lead-Lag controller with $K_{c,1} = 3200$, $K_{c,2} = 400$, $\omega_{center,1} = \omega_{center,2} = 3.75 \frac{\text{rad}}{\text{s}}$, $\omega_{width,1} = \omega_{width,2} = 0.5 \frac{\text{rad}}{\text{s}}$, and $a_1 = a_2 = 4$ when applying a versine input with $\kappa = 9$	188
B.8 Experimental response of Lead-Lag controller with $K_{c,1} = 3200$, $K_{c,2} = 400$, $\omega_{center,1} = \omega_{center,2} = 3.75 \frac{\text{rad}}{\text{s}}$, $\omega_{width,1} = \omega_{width,2} = 0.5 \frac{\text{rad}}{\text{s}}$, and $a_1 = a_2 = 4$ when applying a ramped sinusoid input with $\kappa = 6$	189
B.9 Experimental response of Lead-Lag controller with $K_{c,1} = 3200$, $K_{c,2} = 400$, $\omega_{center,1} = \omega_{center,2} = 3.75 \frac{\text{rad}}{\text{s}}$, $\omega_{width,1} = \omega_{width,2} = 0.5 \frac{\text{rad}}{\text{s}}$, and $a_1 = a_2 = 4$ when applying a ramped sinusoid input with $\kappa = 9$	190
B.10 Experimental response of Hybrid controller when applying a versine input with $\kappa = 9$	191
B.11 Experimental response of Hybrid controller when applying a ramped sinusoid input with $\kappa = 6$	192
B.12 Experimental response of Hybrid controller when applying a ramped sinusoid input with $\kappa = 9$	193

ABSTRACT

Jacobs, Nicholas L. MS, Purdue University, August 2016. Analysis of Feedback Control Applied with Command Shaping to Minimize Residual Vibration. Major Professor: Peter H. Meckl, School of Mechanical Engineering.

Joint flexibility is a physical trait that affects all robotic systems to some degree. This characteristic has been shown to be very detrimental to the performance of these robotic systems when implementing fast point-to-point motion. During such motion, the robot will induce vibrations in its structure that will extend past the completion of the move. Many techniques have been applied over the years in order to minimize these residual vibrations. One such method is known as command shaping, which will construct the input profile so as to avoid exciting the natural frequencies of the system. This work seeks to extend this by analyzing how the feedback controller interacts with the input signal. Since a robotic manipulator is inherently nonlinear, this investigation is begun using a linear three-mass system that mimics the important dynamics of a two-link flexible-joint robot. A model of this three-mass system is derived and simulated in order to provide a new testbed for analyzing the problem of reducing residual vibration. It is shown that by appropriately designing the feedback controller so as to minimize the level of energy at the natural frequencies, lower residual vibration amplitudes are achieved. However, in some instances, these vibrations may take longer to settle out, which is directly correlated to the closed-loop damping of the system. This provides guidelines on how to appropriately construct a feedback controller so as to minimize residual vibration. Using this better understanding of the influence of the feedback, several different controllers are then tested on a two-link flexible-joint robot. The results of these experiments show correlation with the results obtained from the linear system analysis completed, and the trends are now better understood by applying the knowledge gained from the three-mass system.

With the influence of the feedback controller on the level of residual vibration that ensues from fast point-to-point motion identified, the separate problems of command shaping and feedback control are tied together so as to achieve even lower levels of residual vibration.

CHAPTER 1. INTRODUCTION

1.1 Motivation

As technology has advanced over the years, robots have become more and more prevalent throughout industry. This is due not only to decreasing costs and faster processors that permit much lighter and more efficient systems, but also to advances in the understanding of how to successfully control these systems. One of the great advantages of robotic manipulators is that they are exceptional at performing tasks that are repeated time and time again, and can do so quickly with great precision. However, as is the case for any physical system, there are significant mechanical constraints that inhibit the performance of a robot during fast point-to-point motion. One such factor is joint flexibility.

Joint flexibility is a natural property inherent in all robotic systems to some degree. It is important to observe that in many cases some compliance in the joint is beneficial, such as to protect from collisions or to allow for better interaction with the environment. In certain instances it may not be a desired characteristic, but may be included due to other constraints as, for example, in space structures where there are weight limits for the overall system. It is known that joint flexibility can severely degrade performance when implementing fast point-to-point motion, as this movement will excite vibrations in the structure of the robot that will continue past the end of the move. This is due to resonance from the flexible modes that are present. Also, while a system may not have high levels of joint compliance, the same issues will arise when there is any physical characteristic that exhibits resonance. Because of this, there is a wide array of systems where the problem of residual vibration is important. Since these vibrations often prevent the robot from accomplishing its task, typically these oscillations will be allowed to settle out after motion has ended.

This is accomplished by having the robot wait for some time between successive movements until the residual vibrations have sufficiently settled. Another method to reduce the level of residual vibration is by limiting the acceleration forces that are utilized. However, this also limits how fast the robot can complete a given task and lowers productivity. Both of these approaches, while effective in reducing structural vibration, actually hinder the goal of fast and precise motion.

Solutions have been proposed and applied to improve performance by appropriately designing the input trajectory so as to minimize the effects of resonance. In the case of open-loop control, this would be sufficient in ensuring that residual vibration is minimized. However, feedback is required in order to provide robust and reliable motion. Because of this, analysis is also needed on the performance of the system during closed-loop control. This research aims to study the influence of the closed-loop controller on the performance of the robot and also seeks to develop a procedure for designing controllers that will minimize residual vibration. This is combined with the benefits obtained from appropriately shaping the input trajectory in order to greatly improve performance.

1.2 Literature Review

There is an extensive body of work concerning the dynamics of robotic systems and the issues related to their control. Good overviews of the analysis of robotic systems, including the topics of dynamics and control, can be found in [1–3].

Many of the studies performed for industrial robots utilize models that incorporate only the rigid-body dynamics of the system, thus neglecting any elasticity present in the links or the joints. This greatly simplifies the resulting equations. However, it has been shown that the unmodeled dynamics present in an elastic joint greatly affect the performance of the system. Analytical models for compliant drive systems are derived by Sweet and Good, who also give several important results concerning how this affects controller design [4].

Simple Proportional-Derivative (PD) control using motor feedback is sufficient to obtain global asymptotic stability [5]. This is proven using the fact that a flexible joint does not add energy to the system, so Lyapunov stability is preserved. However, while a PD controller is sufficient to obtain a stable system, its performance can be greatly improved using more advanced techniques. One such technique that can be applied to nonlinear systems is feedback linearization [6]. This class of nonlinear controllers is widely used in controlling robotic manipulators and includes inverse dynamics control and computed torque control [3]. Note that while rigid manipulators are always feedback-linearizable, this may not be the case in general when flexibility is included in the model [5]. However, dynamic feedback linearization has been applied successfully by De Luca to both linearize and decouple the nonlinear dynamics [7]. Simplifications to the model can also allow the use of static feedback linearization, as done by Spong [8]. Readman [9] and Spong [8] have both separately modeled the fast dynamics of the elastic joint using singular perturbation theory. Spong goes on to develop several different controllers that utilize feedback linearization and integral manifolds [8, 10].

Variable structure control, which is a branch of nonlinear control that includes sliding mode control, is applied in [11]. Here the controller switches between several available controllers so as to move along a sliding manifold. Iterative learning control can also be utilized so as to have the robot controller update itself iteratively so as to learn how to better compensate for residual vibration. This is done through batch trials where the controller improves as more experiments are completed. This can be performed using techniques from the frequency-domain, as done by De Luca [12], or in the time-domain using the tracking error [13]. These techniques can quickly become fairly complicated, so van de Wijdeven breaks the problem into two time segments, consisting of an actuation time window and an observation time window [14, 15]. This partitioning allows for the problems of stability and vibration attenuation to be dealt with separately, which helps to make the procedure more robust. This work has also been extended to Multiple-Input Multiple-Output (MIMO) systems [16].

Another way to minimize residual vibration is to carefully construct the input signal so as to avoid resonant behavior. This is the basis of the field of work known as command shaping, which can be performed in multiple ways. An overview of the field, which concentrates on the development of input shaping filters, is provided by Singhose [17].

It has been shown mathematically that the energy levels in the frequency spectra that occur at the natural frequencies are directly correlated to the level of residual vibration seen at the end of motion [18]. Thus, by reducing the energy at these frequencies it is possible to reduce residual vibration. In fact, Bhat and Miu show that in a system with no damping, a necessary and sufficient condition for zero residual vibration is for the Laplace Transform of the time-bounded input to have zeros at the system poles. In the frequency domain, this corresponds to having zero energy at the natural frequencies of the system. However, if there is damping in the system then this result does not guarantee zero residual vibration [19].

One of the earliest forms of command shaping is known as Posicast control, which was developed by Smith in the late 1950s [20]. Posicast control removes vibrations in underdamped systems by incorporating a time delay that breaks the move into multiple pieces. If the vibrations from these successive input signals are sufficiently out of phase, then the oscillations from the motion cancel out. Inspired by this work, an input shaper known as the zero-vibration (ZV) shaper was created by Singer and Seering [21]. This input filter convolves a sequence of impulses with a given signal in order to achieve a desired level of residual vibration. However, one of the challenges seen at this time was in the implementation of these concepts, as these early versions of input shaping were very sensitive to modeling error [17]. In the 1980s, several advances were made to generate more robust methods, including the use of acausal input filters [21]. These input filters were initially designed so as to attenuate a single mode of vibration, but can be convolved together in order to suppress multiple modes. Alternatively, a solution to directly solve for a multi-mode input shaper is presented by Hyde, which achieves better performance than the equivalent impulse sequence

obtained by convolving single-mode filters [22]. Rappole extended the technique to account for time-varying natural frequencies. This is done by dynamically modifying the filter parameters using lookup tables [23]. Iterative Learning can be applied to produce similar results without needing dynamic estimation of the time-varying natural frequencies, but at the cost of running many trials in order to achieve good performance [24]. Note that input shaping filters are always better at suppressing residual vibration than both notch filters and low-pass filters, as shown by Singhose [25].

These ideas have also been incorporated into controllers for industrial cranes in order to assist the human operator in limiting payload swing [25, 26]. This has been shown to greatly improve performance, even for untrained users. These results have also been examined on ship-based boom cranes [27].

Work has been done to incorporate Posicast control into the feedback loop, as seen in [28]. This helps to greatly reduce the sensitivity of the system, as the compensator is designed to stabilize the system with Posicast already built into the feedback loop.

It is also possible to generate a command-shaped profile using series expansions. Aspinwall did this in 1980 by using a finite Fourier Series expansion that minimized energy content over certain frequency ranges [29]. However, this resulted in profiles that were much longer than the time-optimal bang-bang input. Meckl proposed a different methodology that would construct the input using the harmonics of appropriate basis functions [18]. In this way, it is possible to directly optimize the input in relation to a predefined cost function by choosing the influence of each of the harmonics for the basis function used in the shaped profile. The ramped sinusoid basis function was presented in [30, 31] while the versed sine, or versine, was presented in [18, 32]. Meckl also derived mathematical relationships between the frequency spectra and the residual vibration for both of these inputs [18]. De Roover and Sperling discuss the different forms of command shaping and their effects on feedback and feedforward control in [33]. These results have been extended in more recent years to include

systems with parameter mismatch [34], configuration-dependent resonance [35, 36], and different kinds of cost functions [37].

1.3 Overview of Thesis

This research studies the effects of feedback control on the level of residual vibration seen at the end of point-to-point motion. While command shaping is used to generate input trajectories that minimize the energy at the natural frequencies of the system, there is no guarantee that the feedback controller will not inject energy back into those frequencies. This problem is first analyzed using a three-mass system, which is linear and time-invariant, so as to apply classical control theory to study the properties of different feedback controllers. This system was chosen because it is linear yet also contains multiple modes of vibration. A simulation of this three-mass system is used to show the levels of residual vibration that occur when performing point-to-point motion. The knowledge learned from this linear system is then applied to a two-link flexible-joint robot in both simulation and experiment.

The theoretical background for command shaping is presented in Chapter 2, along with several important considerations such as configuration-dependent resonance and the performance metrics used throughout this work. The two-link flexible-joint robot is described and modeled mathematically in Chapter 3. Chapter 4 derives the model for a three-mass system, and then simulates and analyzes the results of applying different kinds of feedback. Chapter 5 then applies the knowledge gained from the three-mass system to the robot itself, both in simulation and experiment. Lastly, Chapter 6 summarizes these results, providing important design factors that need to be considered during the design of a feedback controller for a flexible-joint manipulator. It also provides several suggestions for potential areas of future work.

CHAPTER 2. COMMAND SHAPING

In order to minimize residual vibration, the input trajectory can be constructed so as to remove energy at the natural frequencies. This technique is referred to as command shaping. Section 2.1 will describe the theoretical background needed to construct these signals, while sections 2.2 and 2.3 will go into more detail concerning the two basis functions that will be used throughout this work. These are the ramped sinusoid and the versine functions, respectively. Section 2.4 will then examine the influence of the relative weighting factor used in the optimization fitness function and how this affects both the levels of peak input acceleration and the energy in the frequency spectra at the natural frequencies. Section 2.5 will then define several different measures of the residual vibration that are used to quantify the performance of the system.

2.1 Theoretical Preliminaries

In [18], Meckl derives an analytical relationship between residual vibration and the magnitude of the frequency spectra at the natural frequencies using Fourier Transforms. This is constructed using a two-mass system with a single mode of vibration,

$$A^* = \omega_n T_f |F^*(\omega_n T_f)|, \quad (2.1)$$

where A^* is the dimensionless amplitude of the residual vibration, ω_n is the natural frequency, and T_f is the move time. The dimensionless magnitude of the Fourier Transform of the forcing function, $|F^*(\omega_n T_f)|$, is calculated at the natural frequency and is defined as

$$|F^*(\omega_n T_f)| = \frac{|F(\omega_n T_f)|}{F_{max} T_f}, \quad (2.2)$$

with F_{max} being the peak amplitude of the forcing function. Note that the Fourier Transform for any function $f(t)$ which starts at time $t = 0$ and ends at time $t = T_f$ will be

$$F(\omega) = \int_0^{T_f} f(t)e^{-j\omega t} dt = [F_R(\omega) + jF_I(\omega)]e^{-j\frac{\omega T_f}{2}}, \quad (2.3)$$

where $F_R(\omega)$ and $F_I(\omega)$ are the real and imaginary parts, respectively. A command-shaped profile can be written in the general form

$$\ddot{\theta} = \ddot{\theta}_{d,max} f^*(t) = \ddot{\theta}_{d,max} \sum_{l=1}^L B_l^* \Phi_l^*(t), \quad (2.4)$$

where $\Phi_l^*(t)$ is the l^{th} harmonic of the appropriate basis function, B_l^* is the normalized coefficient of the l^{th} harmonic, L is the number of harmonics, and $f^*(t)$ is the command-shaped profile normalized so that it falls in the range

$$-1 \leq f^*(t) \leq 1. \quad (2.5)$$

Once the normalized function is generated, it can be multiplied by the desired peak input acceleration to obtain the finished profile. The desired peak acceleration can be given using a dimensionless parameter κ that is defined as

$$\kappa = \frac{\ddot{\theta}_{d,max}}{\ddot{\theta}_{BB}}, \quad (2.6)$$

where $\ddot{\theta}_{d,max}$ is the desired peak acceleration and $\ddot{\theta}_{BB}$ is the acceleration of a bang-bang profile. This is included here because the optimization procedure will attempt to mimic a bang-bang profile, which has been shown mathematically to be the time-optimal solution [38,39]. Because of this, when moving between two points in space, it is impossible to be faster than the bang-bang profile for a given input amplitude. This can be seen by more closely examining the bang-bang profile, which utilizes constant values for both the acceleration and deceleration phases. When there is a constraint on the peak input, the bang-bang has the maximum area under the

curve for the acceleration and deceleration segments. Any change from the bang-bang input reduces this area, assuming the peak input and final time remain the same. However, the final position is predetermined for any given motion. In order to meet this requirement, a penalty is induced for any input that is not the bang-bang profile. This cost in efficiency requires that either the peak input acceleration or the move time must be increased in order to reach the same final position. This results in a competing set of objectives, namely, the implementation of fast point-to-point motion while also minimizing residual vibration. To accomplish both of these goals concurrently, a weighted multi-objective cost function is created. This is written as

$$J = \frac{1}{T_f} \left[\int_0^{T_f/2} [1 - f(t)]^2 dt + \int_{T_f/2}^{T_f} [-1 - f(t)]^2 dt \right] + \rho \sum_{i=1}^{11} (\omega_i T_f)^2 |F^*(\omega_i T_f)|^2, \quad (2.7)$$

where the first two terms penalize the difference of the input profile from the time-optimal bang-bang profile and the last term adds a penalty to the spectral magnitude of the input profile at the natural frequency of the system. The non-dimensional parameter ρ is used to define the relative importance of the two competing objectives in relation to each other. Observe that an increase in ρ will result in a profile that more heavily penalizes the energy at the natural frequencies. Further observations on the influence of ρ can be found in section 2.4.

It has been arbitrarily chosen to use eleven frequencies around resonance in order to provide an attenuation window around the nominal natural frequency. This adds robustness in case of modeling error or time-varying systems, such as when the natural frequency shifts during motion. An instance where this occurs is configuration-dependent resonance, which is a physical phenomenon that appears in flexible-joint robots.

The eleven frequencies where the magnitude of the Fourier Transform is minimized are chosen so that they are equally distributed throughout a certain tolerance range. This range is set as $\pm X\%$ of the nominal natural frequency as follows:

$$\left(1 - \frac{X\%}{100}\right)\omega_n \leq \omega_n \leq \left(1 + \frac{X\%}{100}\right)\omega_n. \quad (2.8)$$

This window can be adjusted to give whatever tolerance band is desired. It is important to remember that there are trade-offs associated with how wide the attenuation window is made. While the robustness of the method is improved by increasing the width of the window, it also becomes less efficient in its attempts to attenuate the natural frequencies. This is due to the profile diminishing energy at frequencies further away from resonance and so a more shallow trough will be created in the frequency spectra for a given value of ρ . There is a design choice here on whether to use a wide but shallow window for each frequency or one that is narrow but deep. In fact, the different basis functions may end up using dissimilar-size windows based on how they are utilized. A further discussion on this topic can be found for the ramped sinusoid and the versine in sections 2.2 and 2.3, respectively.

The procedure given here can be extended for a multiple-mode system by using an updated objective function instead of Equation (2.7), written as

$$J = \frac{1}{T_f} \left[\int_0^{T_f/2} [1 - f(t)]^2 dt + \int_{T_f/2}^{T_f} [-1 - f(t)]^2 dt \right] + \rho \sum_{i=1}^{11M} (\omega_i T_f)^2 |F^*(\omega_i T_f)|^2, \quad (2.9)$$

where M is the number of modes that will be attenuated. Note that ρ is the relative weighting factor between the contrasting objectives found in Equation (2.9) and is a very important parameter whose influence will be studied in section 2.4.

Equation (2.9) can be used to solve for the optimal solution in terms of the input parameters that have been specified. This is done by partially differentiating Equation

(2.9) with respect to its coefficients B_l and setting these derivatives to zero, expressed as

$$\frac{\partial J}{\partial B_r} = 0, \quad (2.10)$$

where $r = 1, 2, \dots, L$ refers to a specific harmonic l . This generates a set of L equations that can be used to solve for the L number of coefficients. In order to achieve adequate approximation of a square wave, the shaped profiles will utilize $L = 20$ harmonics. In order to ensure that Equation (2.5) holds, it is necessary to normalize the forcing function. This is done by computing a scaling factor SF such that

$$SF = \max|f(t)|. \quad (2.11)$$

The coefficients B_l are then normalized:

$$B_l^* = \frac{B_l}{SF}, \quad (2.12)$$

which allows construction of the normalized profile. With the normalized forcing function in hand, Equation (2.4) can be used to compute the final input trajectory.

2.2 Ramped Sinusoid

The ramped sinusoid basis function was introduced by Meckl in [30] and is given by

$$\Phi_l^*(t) = \frac{1}{\alpha_l} \left(\frac{1}{2} - \tau \right) + \frac{1}{\alpha_l^2} \sin(\alpha_l \tau) - \frac{1}{2\alpha_l} \cos(\alpha_l \tau), \quad (2.13)$$

where τ is the dimensionless time

$$\tau = \frac{t}{T_f}, \quad (2.14)$$

and T_f is the actuation time. This is the time it takes to complete a certain motion. The characteristic number associated with each of the harmonics is α_l . A function is desired that has zero magnitude and slope at the beginning and the end of motion,

which gives four boundary conditions on the solution. This results in the following constraint on the harmonics of the ramped sinusoid

$$\alpha_l \sin(\alpha_l) + 2 \cos(\alpha_l) - 2 = 0, \quad (2.15)$$

with $\alpha_l \neq n\pi$, where n is an even integer. The first ten harmonics are given in Table 2.1 and Figure 2.1 shows the first three harmonics superimposed over each other.

Table 2.1. Values of the First Ten Harmonics of Ramped Sinusoid Function.

$l^{th} Harmonic$	Value
α_1	8.9688
α_2	15.4505
α_3	21.8082
α_4	28.1324
α_5	34.4415
α_6	40.7426
α_7	47.0389
α_8	53.3321
α_9	59.6232
α_{10}	65.9128

The Fourier Transform of the Ramped Sinusoid is given as

$$F(\omega) = jF_I(\omega)e^{-j\frac{\omega T_f}{2}}, \quad (2.16)$$

which is a simplified form of Equation (2.3). $F_I(\omega)$ can be calculated using

$$F_I(\omega) = \frac{FT_f}{SF} \left| \left(\frac{2 \sin(\frac{\omega T_f}{2}) - \omega T_f \cos(\frac{\omega T_f}{2})}{(\omega T_f)^2} \right) \sum_{l=1}^L \frac{B_l \alpha_l}{\alpha_l^2 - (\omega T_f)^2} \right|, \quad (2.17)$$

which was derived by Meckl in [30].

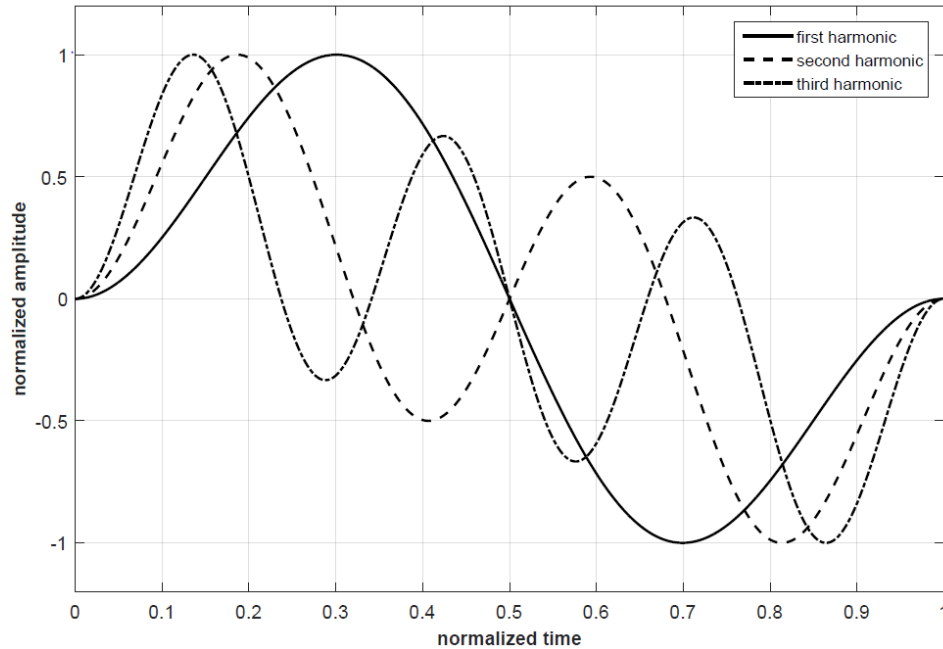


Figure 2.1. First Three Harmonics of the Normalized Ramped Sinusoid Function, [37].

The ramped sinusoid basis function is able to approximate the full cycle of a bang-bang profile. This is useful since the entire profile can be solved for in a single step. However, there are several concerns that need to be taken into consideration, such as when using this basis function for velocity-limited systems. One example of a limit to the peak velocity of a system is the saturation of the supply voltage. When this occurs, the motor has accelerated to a point where the supply voltage is just balanced by voltage loss due to resistance in the motor windings and by back-EMF voltage, which is a function of the motor velocity. For this reason, a span of time where the motor travels at peak velocity may be desired. However, a profile with a stage at constant velocity cannot be constructed using the ramped sinusoid.

Another issue that must be taken into account is if the system is time-varying. One situation where this occurs is with configuration-dependent resonance, as would be the case in a flexible-joint robot. In this instance, the natural frequencies are changing over time due to the moment of inertia for the robot changing as a function of the configuration of its links. This affects how well a command-shaped profile can

attenuate those frequencies. This is an example where having an attenuation window with sufficient width is necessary, as it will allow for the designer to specify an input profile that attenuates a range of frequencies. This range must be wide enough to cover the natural frequencies through which a system shifts during motion. For this work, the attenuation window for the ramped sinusoid is always set to $\pm 10\%$ in order to adequately cover the natural frequencies.

2.3 Versine

The versed sine, or versine, basis function was introduced in [18] and is given by

$$\Phi_l^*(t) = 1 - \cos(2\pi l\tau), \quad (2.18)$$

where l denotes the harmonic and is a positive integer value. τ is the dimensionless time

$$\tau = \frac{t}{T_p}, \quad (2.19)$$

where T_p is the profile time. This is the time it takes to complete a single segment of the versine.

Figure 2.2 shows the first three harmonics of a single cycle of the versine function.

The Fourier Transform of the versine function can be written as

$$F(\omega) = F_R(\omega)e^{-j\frac{\omega T_p}{2}}, \quad (2.20)$$

which is a simplified form of Equation (2.3). $F_R(\omega)$ can be calculated using

$$F_R(\omega) = 2\frac{FT_p}{SF} \left| \sum_{l=1}^L \frac{B_l(2\pi l)^2 \sin(\frac{\omega T_p}{2})}{\omega T_p[(2\pi l)^2 - (\omega T_p)^2]} \right|, \quad (2.21)$$

which was derived by Meckl in [18].

One benefit of using the versine is that it allows segmentation of the profile into multiple pieces, as introduced by Beazel in [35, 36]. This proposal allows for the

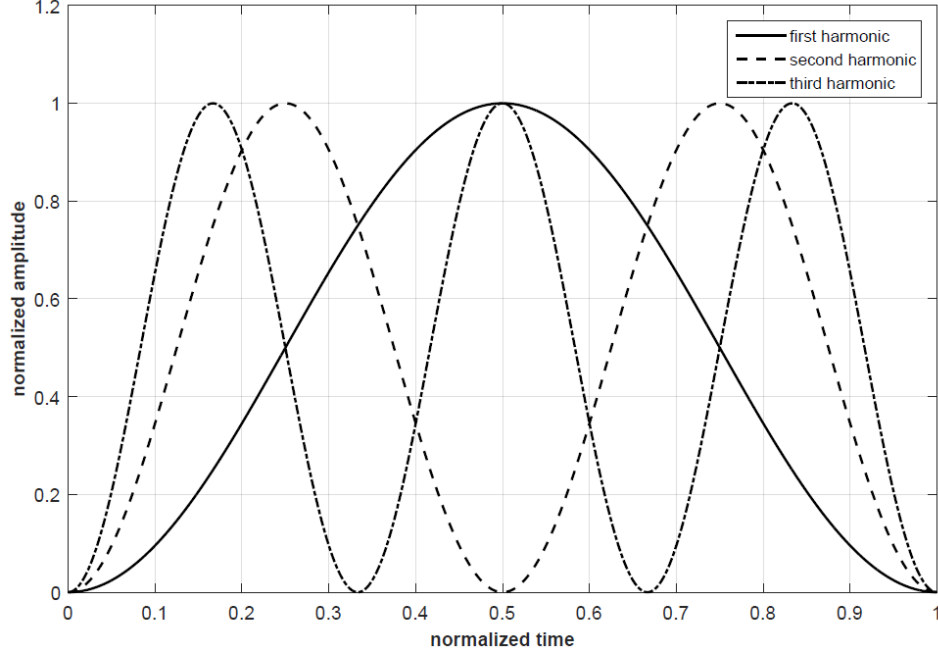


Figure 2.2. First Three Harmonics of the Normalized Versine Function, [37].

input trajectory to be designed around multiple operating points. By designing these points around the natural frequencies of a time-varying system, this allows for more precise attenuation of the energy at those frequencies. It also permits the use of an intermediate segment with zero acceleration where the system will move at constant velocity, which is a useful feature for velocity-limited systems.

Since the versine only generates a single segment of the profile at a time, the objective function of Equation (2.9) needs to be slightly modified. This is given as

$$J = \frac{1}{T_p} \int_0^{T_p} [1 - f(t)]^2 dt + \rho \sum_{i=1}^{11M} (\omega_i T_p)^2 |F^*(\omega_i T_p)|^2, \quad (2.22)$$

where the term associated with the deceleration segment of the bang-bang profile has been removed.

While there are several advantages to using a versine function, there are disadvantages as well. One of these is that every segment will need its own solution. This means more work will be required as the optimal solution to Equation (2.22) will need

to be calculated for every segment individually. Another disadvantage is that there will be inflection points where the acceleration is zero both at the beginning and the end of every segment. If an excessive number of segments is included then this will degrade performance, as noted by Beazel in [35].

Only two segments will be used here, one for acceleration and one for deceleration. This allows for more precise attenuation of configuration-dependent resonance than the ramped sinusoid can achieve, so the versine function will use a $\pm 5\%$ attenuation window for each segment.

2.4 Influence of Relative Weighting Factor

In order to solve Equations (2.9) or (2.22), it is necessary to define certain input parameters. Some of these, such as the natural frequencies, are defined by the system itself. Others depend on the motion that is desired, such as the move time. The final parameter that is required is the relative weighting factor ρ .

In order to complete this examination, the natural frequencies of the flexible-joint robot are utilized. Since the robot is a time-varying system with configuration-dependent resonance, the mean is taken of the natural frequencies that appear during motion. This average will correspond to the nominal natural frequencies that are utilized in the command shaping procedure. These values can be found in Table 2.2. The natural frequencies of the flexible-joint robot can be found in Figure 3.6 as a

Table 2.2. Nominal Natural Frequencies of Two-Link Flexible-Joint Robot.

	ω_1	ω_2
Ramped Sinusoid	3.7090 $[\frac{\text{rad}}{\text{s}}]$	15.7338 $[\frac{\text{rad}}{\text{s}}]$
Versine (Acceleration)	3.6473 $[\frac{\text{rad}}{\text{s}}]$	16.4378 $[\frac{\text{rad}}{\text{s}}]$
Versine (Deceleration)	3.8118 $[\frac{\text{rad}}{\text{s}}]$	14.8203 $[\frac{\text{rad}}{\text{s}}]$

function of θ_2 . More discussion on the topic of configuration-dependent resonance, as well as the calculation of these natural frequencies, can be found in section 3.7.

Note that Equations (2.9) and (2.22) have multiple competing objectives that they seek to optimize. The first objective tries to approximate a bang-bang profile in order to move a certain distance as quickly as possible. The second objective adds in a penalty related to the energy in the frequency spectra at eleven points surrounding each of the natural frequencies of the system. To weight the relative importance of these two competing objectives, the non-dimensional factor ρ is utilized. Because of this, as ρ changes so will the optimal solution that minimizes the cost of Equations (2.9) and (2.22).

Since a bang-bang input profile is known to be the time-optimal solution for point-to-point motion, anything other than a bang-bang function will require either a higher peak input acceleration or a longer move time. In this work, the move time is fixed at 2 seconds. This means any differences in the output will appear as changes in the peak input acceleration. This can be measured by κ as defined in Equation (2.6).

The influence of ρ on κ can be seen for the ramped sinusoid in Figure 2.3 and the versine in Figures 2.4 and 2.5. Since the versine has acceleration and deceleration segments that use different natural frequencies, the same value of ρ will give a different value of κ depending on which segment is being examined. Note that as ρ increases, κ will increase monotonically for both the ramped sinusoid and the versine. This is due to the profile trying harder to attenuate the natural frequencies at the cost of reducing how effectively it can approximate a bang-bang input. In order to ensure the profile still reaches the same final position, the peak acceleration of the profile is increased, resulting in higher values of κ . Another value that is useful to examine is the magnitude of the Fourier Transform at the eleven frequencies used in the optimization procedure. Since ρ is directly related to how much these frequencies are attenuated, an increase in ρ should result in a corresponding decrease in the energy within the tolerance window defined in Equation (2.8). Note that this quantity is calculated as

$$|\text{Mean}(F(\omega_M))| = \frac{1}{11} \sum_{l=1}^{11} |(F(\omega_M))|, \quad (2.23)$$

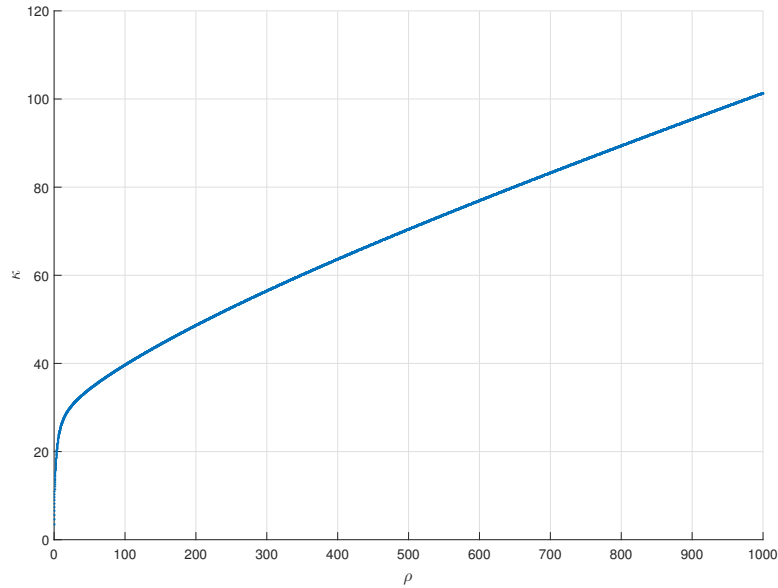


Figure 2.3. Influence of ρ on κ for ramped sinusoid.

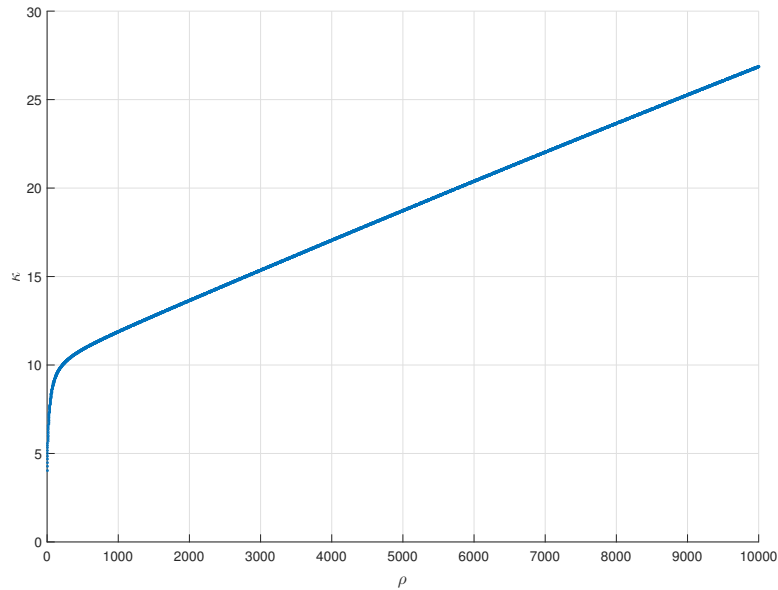


Figure 2.4. Influence of ρ on κ for acceleration segment of versine.

for the M^{th} mode, and the output is converted to decibels. This averages the spectral magnitude at the eleven frequencies used in the tolerance window and uses this as a measure of the total attenuation across the window. The differences seen in the

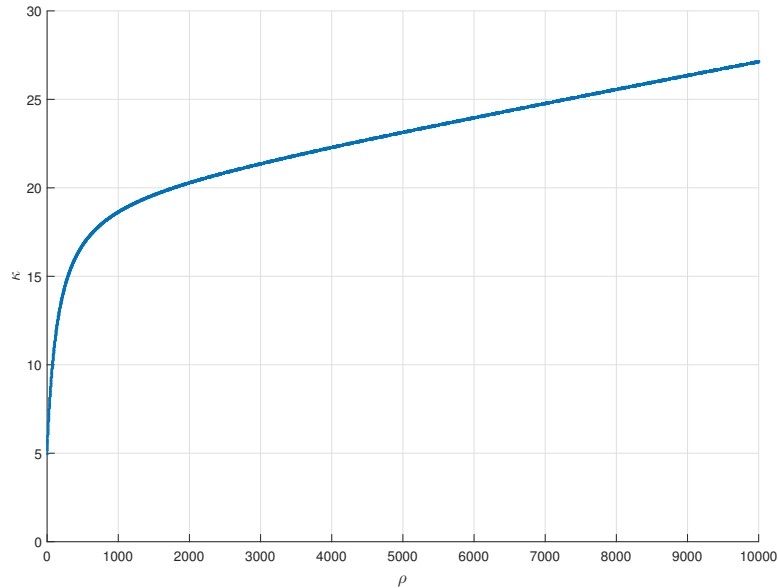


Figure 2.5. Influence of ρ on κ for deceleration segment of versine.

average energy level for each of the natural frequencies that result from changing ρ are shown in Figures 2.6 through 2.11.

Note that while the magnitude of the Fourier Transform does tend to decrease as ρ increases, it is not monotonic. This is unlike the trend seen with κ . One potential reason for this is that ρ diminishes the energy at multiple modes and so it attempts to minimize the overall energy for all modes considered. In other words, if one natural frequency has a decrease in energy that is more than the increase in energy at the other natural frequency, this still corresponds to an overall lower level of energy for both modes.

Note that this does not change the global trend that appears and there should still be an overall decrease in energy as ρ increases. It can be quickly seen that, in general, this is indeed the case and that as ρ increases a corresponding decrease in the magnitude of the Fourier Transform does occur. In order to have a consistent basis for comparison that can be used for both the ramped sinusoid and the versine, the non-dimensional parameter κ will be utilized. This allows the examination of both types of profiles on an equal footing. However, κ is a measure of the command-shaped

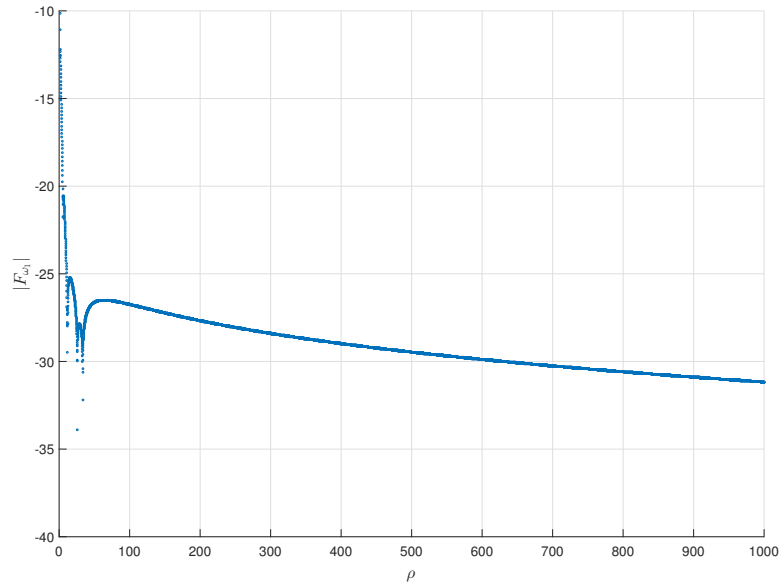


Figure 2.6. Influence of ρ on average magnitude of Fourier Transform for first natural frequency of the ramped sinusoid function.

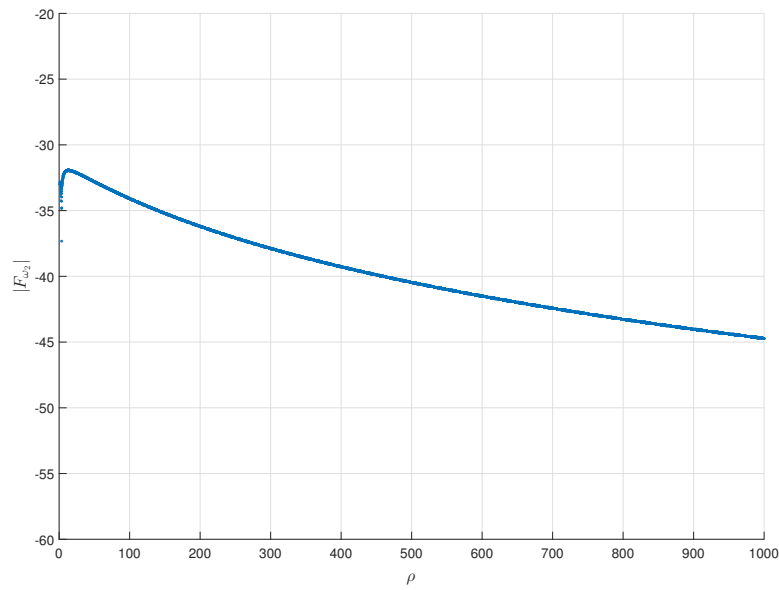


Figure 2.7. Influence of ρ on average magnitude of Fourier Transform for second natural frequency of the ramped sinusoid function.

profile that is only known after the profile has been generated and does not show up in Equation (2.9) or (2.22). Because of this, a procedure is needed in order to find

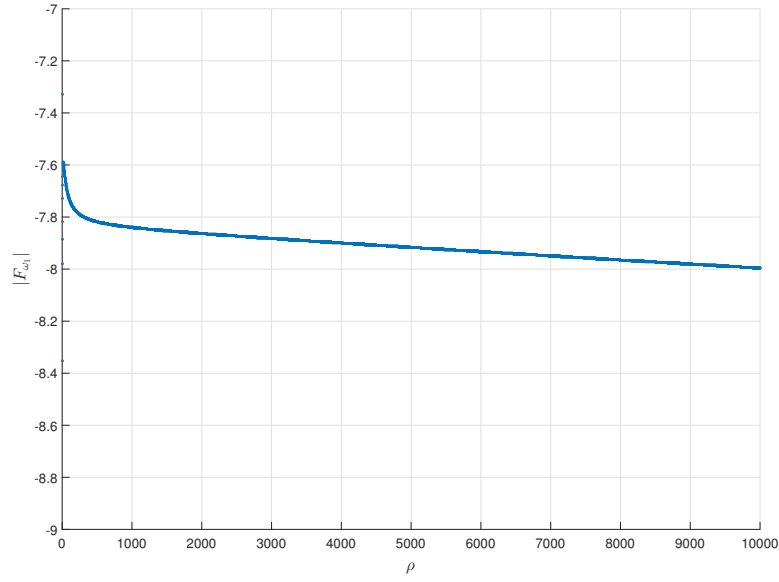


Figure 2.8. Influence of ρ on average magnitude of Fourier Transform for first natural frequency in the acceleration segment of the versine function.

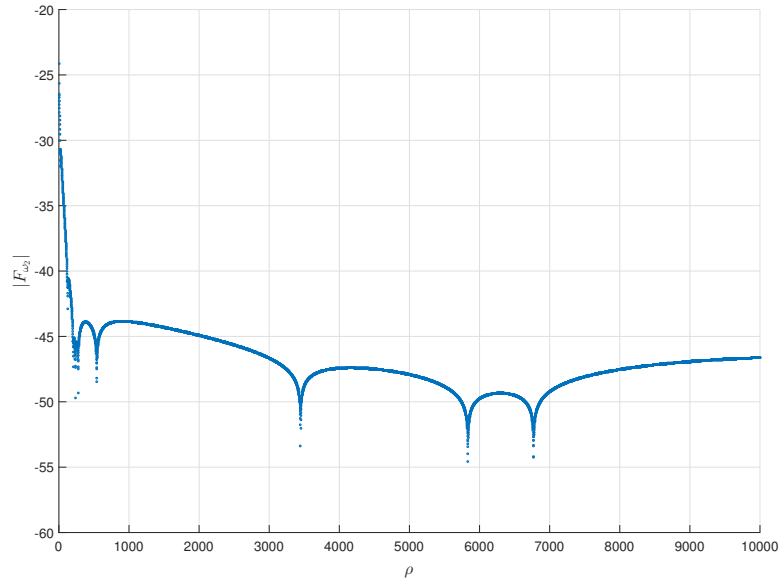


Figure 2.9. Influence of ρ on average magnitude of Fourier Transform for second natural frequency in the acceleration segment of the versine function.

the appropriate ρ that generates a profile with a specific κ . To accomplish this task, ρ is updated in an iterative procedure until the desired κ is reached.

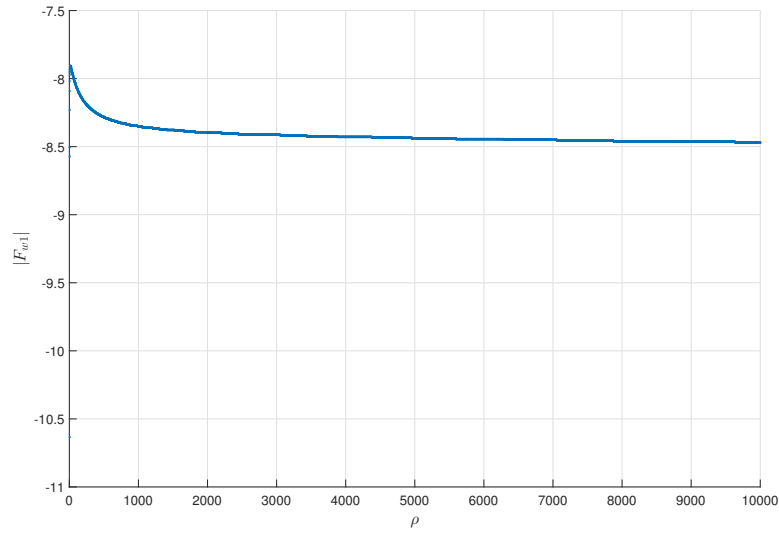


Figure 2.10. Influence of ρ on average magnitude of Fourier Transform for first natural frequency in the deceleration segment of the versine function.

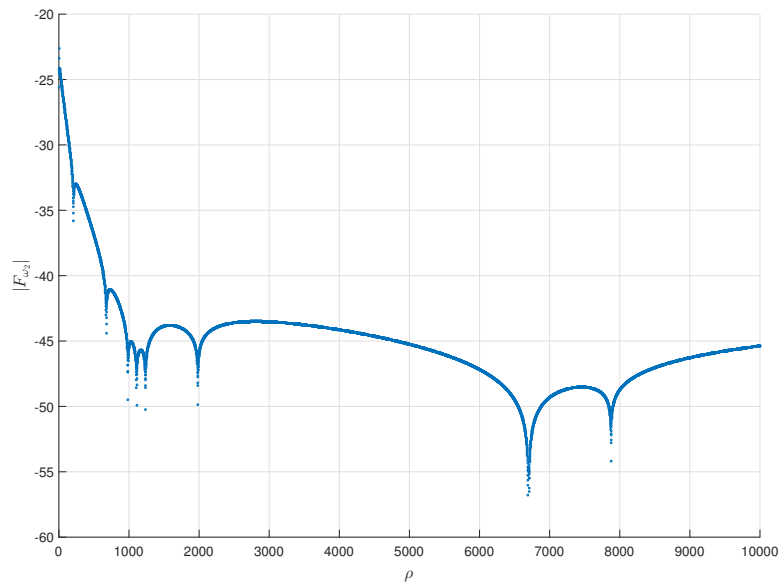


Figure 2.11. Influence of ρ on average magnitude of Fourier Transform for second natural frequency in the deceleration segment of the versine function.

To perform these iterations, an initial guess on the value of ρ is made. This starting value of ρ can be estimated by referring to Figures 2.3, 2.4, or 2.5. Then κ is calculated by computing the maximum input acceleration of the resultant profile.

This is compared to a desired κ to find the error in the peak acceleration of the input profile

$$error = \kappa_{desired} - \kappa_{actual}. \quad (2.24)$$

This error is then used to update ρ using

$$\rho_{new} = \rho_{old} + rate * error, \quad (2.25)$$

where *rate* refers to a learning rate that can be specified *a priori*. This continues until the error in κ falls within a predetermined tolerance window.

2.5 Performance Metrics

In order to examine the performance of different input profiles, measures of the residual vibration are needed. Two characteristics that are useful to study are the amplitude of the residual vibrations and the time these oscillations take to settle out. Another added measure of the performance is the peak deflection from the end position.

The peak amplitude of the residual vibration is given by the maximum magnitude of the acceleration signal after completion of movement. Likewise, the peak deflection can be written in terms of the maximum displacement from the final steady-state position after motion has ended.

The classical definition for settling time is how long it takes for a system to reach and stay within a certain error band around the final steady-state position. This description will not be used in this work as the interest here is not on the position signal but rather the performance of the acceleration signal. Because of this, settling time is redefined as the time it takes for the acceleration signal to fall and remain within a certain vibration threshold, measured from the end of motion. This gives a direct measure of how well the system dissipates vibration. Note that this threshold needs to be predefined so as to allow this measure of performance to fall within the

range of time when experiment or simulation data is recorded. If the threshold is set too high then the resulting signal will always be within the vibration threshold and a settling time of zero is calculated. However, if the threshold is set too low then the signal does not settle out during the experiment and any sensor noise may lead to inconsistent calculations of the settling time. In order to have this metric fall within the appropriate time range and also be sufficiently robust to sensor noise, this threshold is predefined beforehand so that it is at a consistent value when comparing different input profiles and controller designs.

Equations to calculate each of these metrics are included in sections 3.3 and 4.5 for the two-link flexible-joint robot and three-mass system, respectively.

CHAPTER 3. ROBOT MODEL AND SYSTEM DESCRIPTION

A two-link flexible-joint robot is used to provide an experimental testbed where the performance of different controllers and input commands can be studied. Section 3.1 gives a description of this robot and its hardware while section 3.2 derives the forward kinematic analysis of the system. Section 3.3 then determines the equations required to quantify the measures of performance for the robot. Section 3.4 gives several models of the dynamics, including a full Lagrangian model, a reduced Lagrangian model, and a set of recursive Newton-Euler equations. Note that the Newton-Euler equations are derived here with the intent of using them in the feedforward portion of a computed torque controller, but the actual application of these equations is left for future work. The system parameters are given in section 3.5, while section 3.6 discusses the computed torque controller that is used to control the robot. Lastly, the issue of configuration-dependent resonance is discussed in section 3.7.

3.1 The Two-Link Flexible-Joint Robot

A two-link flexible-joint robot has been constructed in the Ruth and Joel Spira Laboratory for Electromechanical Systems at Purdue University. This robot is shown in Figure 3.1. A top-down schematic, which was generated by Nho in [40], is shown in Figure 3.2. Note that the robot is mounted on a table with its workspace in the horizontal plane.

This system was originally constructed by Yegerlehner [41] as a rigid-joint two-link manipulator in order to provide a testbed for studying the use of artificial neural networks for controlling a nonlinear time-varying system. Springs were added to the joints by Kinceler [42] when he modified the robot to add joint flexibility.

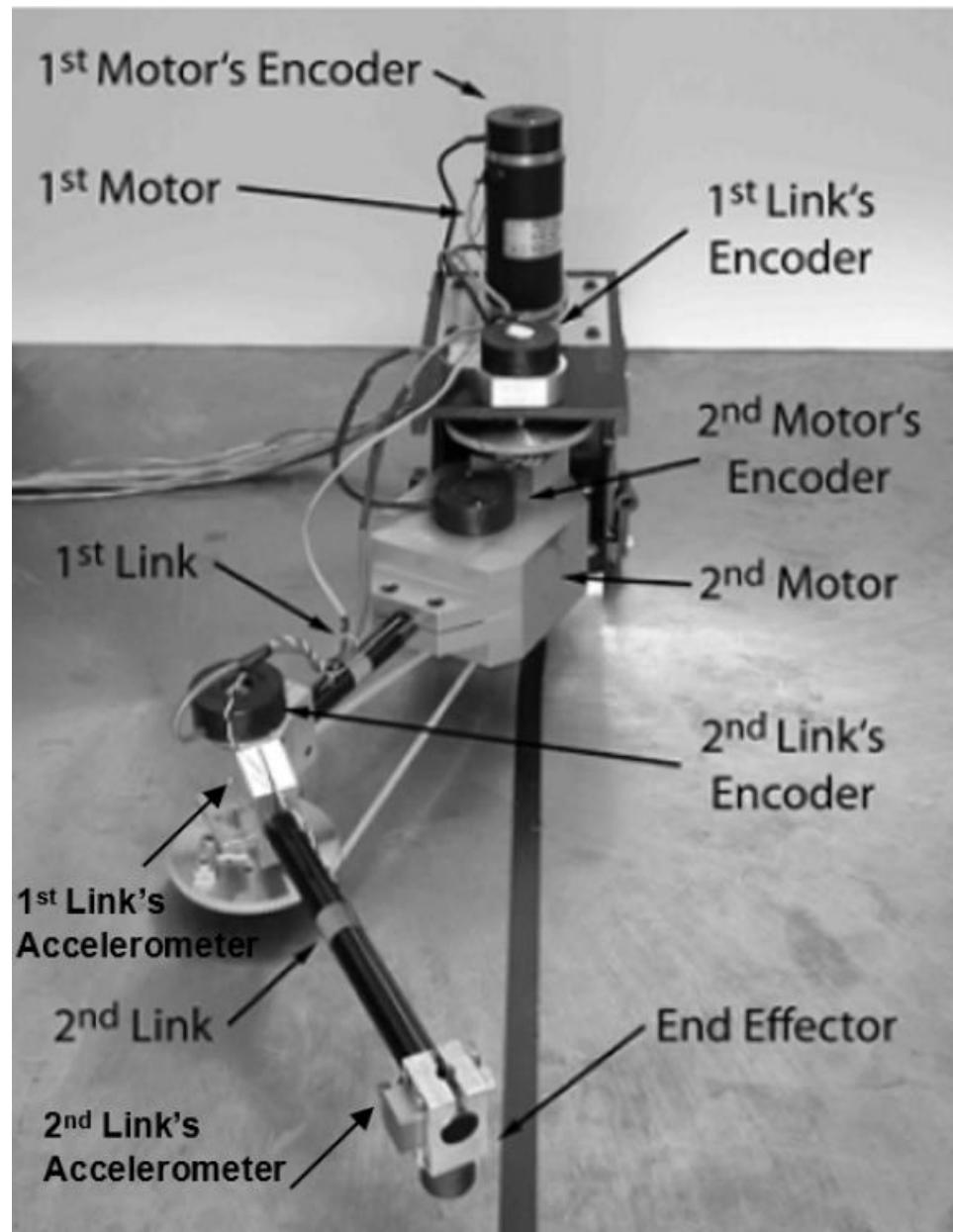


Figure 3.1. The two-link flexible-joint robot.

The robot base houses the first motor, which is connected to a sprocket through a chain drive. This sprocket is then connected to link 1 through a spring in the joint. The second motor resides on link 1, so it is in a non-inertial reference frame. Link 2 is driven using the same method as link 1, through a chain drive connected to a sprocket and a spring. Both chain drives have gear ratios of 5. Note that the motors

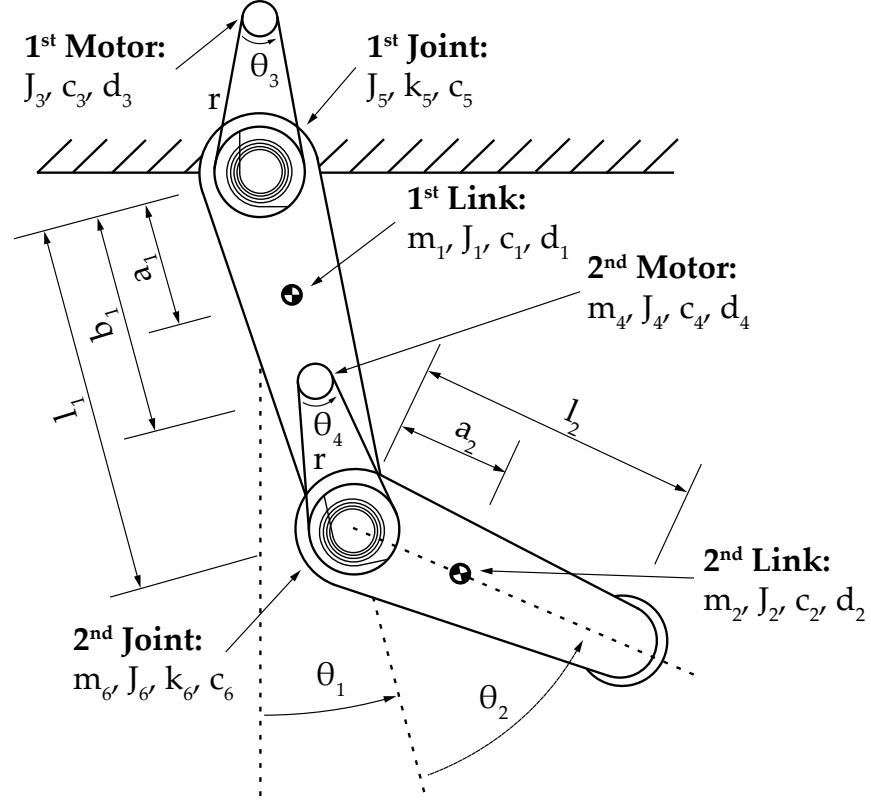


Figure 3.2. Schematic of the two-link flexible-joint robot, [40].

do not act on the links directly, but only through the torsional springs installed in the joints. Since these springs have spring coefficients that are designed to be low in comparison to industrial robots, this provides a challenging testbed that exhibits high levels of residual vibration with relatively slow motion.

3.2 Robot Kinematics

Before modeling the dynamics of the robot it is useful to study the kinematics of this serial manipulator in order to obtain a good understanding of its motion. Since this is only a kinematic analysis of the links of the robot, the issue of joint compliance does not come into play throughout this section. This means that only θ_1 and θ_2 are found here, while the motion of the motors, given by θ_3 and θ_4 , will be included when modeling the dynamics of the flexible joints in section 3.4.

The procedure used in this work is common for modeling the kinematics of a robotic manipulator and can be found in robotics textbooks, such as [1], [2], and [3], although the notation may differ depending on the source. The approach presented here follows the same format as seen in ME 572, which is a graduate robotics course taught in the School of Mechanical Engineering at Purdue University [43].

In order to model the motion of the links, coordinate frames are placed on the robot at the beginning and end of each joint and link. The geometry of the robot is thus completely defined by the location and orientation of these coordinate frames. By deriving the transformations from one frame to the next, the equations that describe the position, velocity, and acceleration for each joint and link are derived. These can be given with respect to either the fixed world reference frame or a moving body frame. This allows for easy conversions between joint space and cartesian space so that the values of θ_1 and θ_2 may be transformed to values of the linear motion of the end of each link, and vice versa. Note that moving from joint space to cartesian space is known as the forward kinematics solution, while going from cartesian space to joint space is the inverse kinematics solution. Only the forward kinematics solution is derived here. This means that given certain values of the joint angles, the locations of the links can be calculated and given using cartesian coordinates in three-dimensional space.

The coordinate frames of the robot are defined as follows:

1. The fixed world reference frame is the XYZ_0 Frame
2. The UVW_i frame is the coordinate frame after joint i
3. The XYZ_i frame is the coordinate frame at the end of link i
4. This is repeated for n links so that the end effector of the robot is in the XYZ_n frame. This is commonly called the end effector coordinate system, or the *EECS*

The Z_i and W_i axes are always co-aligned with the axis of a joint. For the two-link flexible-joint robot, this means that they are always pointing up, or out of the page.

Figure 3.3 shows a schematic of the two-link manipulator with all the reference frames included.

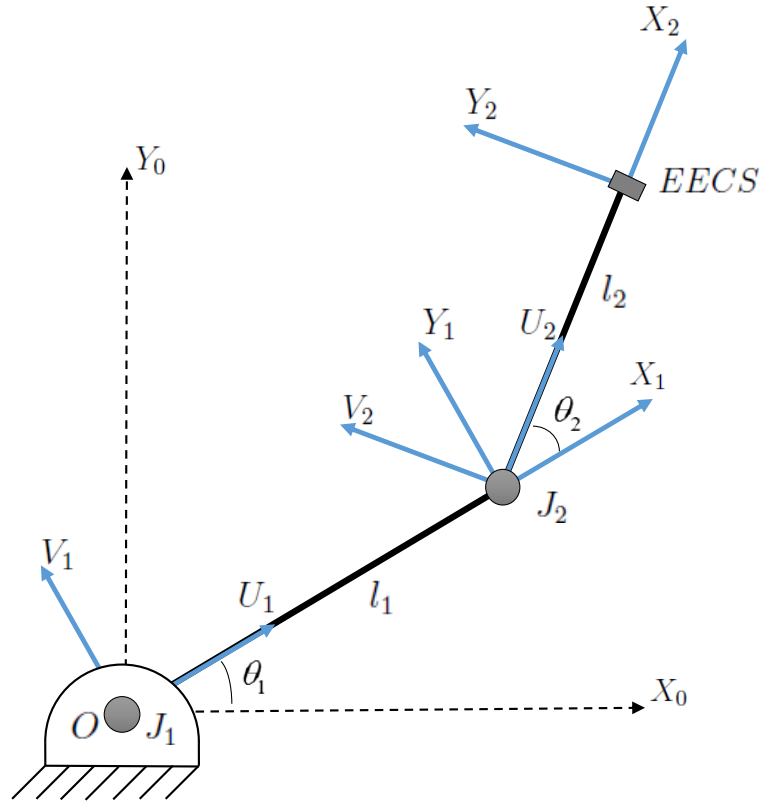


Figure 3.3. Schematic of two-link flexible-joint robot with the XYZ and UVW coordinate frames.

Now that each reference frame has been placed on the robot, it is possible to mathematically define the transformations from one frame to the next. Before this is done there are two things that are useful to consider:

1. Any conversion from the XYZ_{i-1} frame to the UVW_i frame is simply a rotation. This is done through a homogeneous transform and will be referred to as ϕ_i for joint i

2. Any conversion from the UVW_i frame to the XYZ_i frame is simply a translation. This is done through a homogeneous transform and will be referred to as T_i for link i

With these rules in mind it is now relatively easy to define these transformations, as they are pure rotations or pure translations. The homogeneous transforms for the two joints and the two links can be written as

$$\phi_1 = \begin{bmatrix} \cos(\theta_1) & -\sin(\theta_1) & 0 & 0 \\ \sin(\theta_1) & \cos(\theta_1) & 0 & 0 \\ 0 & 0 & 1 & 0 \\ 0 & 0 & 0 & 1 \end{bmatrix}, \quad (3.1)$$

$$T_1 = \begin{bmatrix} 1 & 0 & 0 & l_1 \\ 0 & 1 & 0 & 0 \\ 0 & 0 & 1 & 0 \\ 0 & 0 & 0 & 1 \end{bmatrix}, \quad (3.2)$$

$$\phi_2 = \begin{bmatrix} \cos(\theta_2) & -\sin(\theta_2) & 0 & 0 \\ \sin(\theta_2) & \cos(\theta_2) & 0 & 0 \\ 0 & 0 & 1 & 0 \\ 0 & 0 & 0 & 1 \end{bmatrix}, \quad (3.3)$$

$$T_2 = \begin{bmatrix} 1 & 0 & 0 & l_2 \\ 0 & 1 & 0 & 0 \\ 0 & 0 & 1 & 0 \\ 0 & 0 & 0 & 1 \end{bmatrix}. \quad (3.4)$$

These four matrices are multiplied together as

$$T_m = \phi_1 T_1 \phi_2 T_2 = A_{01} A_{12}, \quad (3.5)$$

which gives the manipulator transform. This describes the location and orientation of the *EECS* in the fixed world reference frame.

The transformations from the XYZ_{i-1} frame to the XYZ_i frame are defined as $A_{(i-1)(i)}$ and are calculated to be

$$A_{01} = \phi_1 T_1 = \begin{bmatrix} \cos(\theta_1) & -\sin(\theta_1) & 0 & l_1 \cos(\theta_1) \\ \sin(\theta_1) & \cos(\theta_1) & 0 & l_1 \sin(\theta_1) \\ 0 & 0 & 1 & 0 \\ 0 & 0 & 0 & 1 \end{bmatrix}, \quad (3.6)$$

$$A_{12} = \phi_2 T_2 = \begin{bmatrix} \cos(\theta_2) & -\sin(\theta_2) & 0 & l_2 \cos(\theta_2) \\ \sin(\theta_2) & \cos(\theta_2) & 0 & l_2 \sin(\theta_2) \\ 0 & 0 & 1 & 0 \\ 0 & 0 & 0 & 1 \end{bmatrix}, \quad (3.7)$$

while the manipulator transform is

$$T_m = \begin{bmatrix} C(\theta_1)C(\theta_2) - S(\theta_1)S(\theta_2) & -S(\theta_1)C(\theta_2) - C(\theta_1)S(\theta_2) & 0 & P_x \\ S(\theta_1)C(\theta_2) + C(\theta_1)S(\theta_2) & C(\theta_1)C(\theta_2) - S(\theta_1)S(\theta_2) & 0 & P_y \\ 0 & 0 & 1 & 0 \\ 0 & 0 & 0 & 1 \end{bmatrix}, \quad (3.8)$$

where

$$C(\theta) = \cos(\theta), \quad (3.9)$$

$$S(\theta) = \sin(\theta), \quad (3.10)$$

and the location of the end effector is given by

$$P_x = l_1 C(\theta_1) + l_2 C(\theta_1)C(\theta_2) - l_2 S(\theta_1)S(\theta_2), \quad (3.11)$$

$$P_y = l_1 S(\theta_1) + l_2 S(\theta_1)C(\theta_2) + l_2 C(\theta_1)S(\theta_2). \quad (3.12)$$

Equation (3.8) can be simplified using the sum-difference formulas of trigonometry, written as

$$\cos(\theta_1 \pm \theta_2) = \cos(\theta_1) \cos(\theta_2) \mp \sin(\theta_1) \sin(\theta_2), \quad (3.13)$$

$$\sin(\theta_1 \pm \theta_2) = \sin(\theta_1) \cos(\theta_2) \pm \cos(\theta_1) \sin(\theta_2), \quad (3.14)$$

which results in the following manipulator transform

$$T_m = \begin{bmatrix} \cos(\theta_1 + \theta_2) & -\sin(\theta_1 + \theta_2) & 0 & P_x \\ \sin(\theta_1 + \theta_2) & \cos(\theta_1 + \theta_2) & 0 & P_y \\ 0 & 0 & 1 & 0 \\ 0 & 0 & 0 & 1 \end{bmatrix}, \quad (3.15)$$

where

$$P_x = l_1 \cos(\theta_1) + l_2 \cos(\theta_1 + \theta_2), \quad (3.16)$$

$$P_y = l_1 \sin(\theta_1) + l_2 \sin(\theta_1 + \theta_2). \quad (3.17)$$

This gives the final position of the end effector in three-dimensional space. Note that there is no translation or rotation in the $\pm Z$ direction. Because of this, the third row and column could be removed from the manipulator transform. This is not done here so as to preserve generality.

Since the interest of this work is on the residual vibration of the end effector, the velocity and acceleration signals are also required. Luckily, these signals can be easily derived by differentiating Equation (3.5) using the product rule and the following observations:

1. The shape of each link is constant, so $\frac{\partial T}{\partial t} = 0$ for all links
2. The motion of ϕ_i is a pure rotation for the i^{th} joint

Observe that if the robot has flexible links, then the first point made here does not hold true. In that instance, the shape of the link would change during motion.

However, the two-link flexible-joint robot used here has rigid links, so the assumption that the shape of the links is constant is valid.

The second point here is useful, as it permits a matrix to be defined that when multiplied with ϕ_i will always give the derivative of ϕ_i with respect to time. For a revolute joint, this derivative operator matrix is

$$Q_R = \begin{bmatrix} 0 & -1 & 0 & 0 \\ 1 & 0 & 0 & 0 \\ 0 & 0 & 0 & 0 \\ 0 & 0 & 0 & 0 \end{bmatrix}, \quad (3.18)$$

which can be used to find the derivative of Equation (3.5). This is given as

$$\frac{\partial T_m}{\partial t} = \frac{\partial \phi_1}{\partial t} T_1 \phi_2 T_2 + \phi_1 T_1 \frac{\partial \phi_2}{\partial t} T_2 = \dot{\theta}_1 Q_R \phi_1 T_1 \phi_2 T_2 + \dot{\theta}_2 \phi_1 T_1 Q_R \phi_2 T_2, \quad (3.19)$$

where the scalar values $\dot{\theta}_1$ and $\dot{\theta}_2$ have been pulled to the front of their respective terms. Since Equation (3.19) is just a set of matrix multiplications, it can be easily calculated either by hand or symbolically using MATLAB, Mathematica, or another tool capable of multiplying matrices. The resulting translational velocity of the end effector in the world reference frame is

$$\dot{P}_x = -l_1 \dot{\theta}_1 \sin(\theta_1) - l_2 (\dot{\theta}_1 + \dot{\theta}_2) \sin(\theta_1 + \theta_2), \quad (3.20)$$

$$\dot{P}_y = l_1 \dot{\theta}_1 \cos(\theta_1) + l_2 (\dot{\theta}_1 + \dot{\theta}_2) \cos(\theta_1 + \theta_2). \quad (3.21)$$

This process can be repeated to calculate the acceleration of the end effector. Differentiating Equation (3.19) gives

$$\begin{aligned} \frac{\partial^2 T_m}{\partial t^2} = & \ddot{\theta}_1 Q_R \phi_1 T_1 \phi_2 T_2 + \dot{\theta}_1^2 Q_R^2 \phi_1 T_1 \phi_2 T_2 + 2\dot{\theta}_1 \dot{\theta}_2 Q_R \phi_1 T_1 Q_R \phi_2 T_2 \\ & + \dot{\theta}_2^2 \phi_1 T_1 Q_R^2 \phi_2 T_2 + \ddot{\theta}_2 \phi_1 T_1 Q_R \phi_2 T_2, \end{aligned} \quad (3.22)$$

where the first and last terms are tangential accelerations, the second and fourth terms are normal accelerations, and the third term is a Coriolis acceleration. Completing these multiplications results in

$$\begin{aligned}\ddot{P}_x = & -l_1\ddot{\theta}_1 \sin(\theta_1) - l_1\dot{\theta}_1^2 \cos(\theta_1) - l_2(\dot{\theta}_1^2 + 2\dot{\theta}_1\dot{\theta}_2 + \dot{\theta}_2^2) \cos(\theta_1 + \theta_2) \\ & - l_2(\ddot{\theta}_1 + \ddot{\theta}_2) \sin(\theta_1 + \theta_2),\end{aligned}\tag{3.23}$$

$$\begin{aligned}\ddot{P}_y = & l_1\ddot{\theta}_1 \cos(\theta_1) - l_1\dot{\theta}_1^2 \sin(\theta_1) - l_2(\dot{\theta}_1^2 + 2\dot{\theta}_1\dot{\theta}_2 + \dot{\theta}_2^2) \sin(\theta_1 + \theta_2) \\ & + l_2(\ddot{\theta}_1 + \ddot{\theta}_2) \cos(\theta_1 + \theta_2),\end{aligned}\tag{3.24}$$

which gives the linear acceleration of the end effector with respect to the world reference frame. Observe that Equations (3.19) and (3.22) are not necessarily required if only the linear acceleration is desired, as Equations (3.16) and (3.17) can be differentiated directly. However, Equation (3.22) also calculates how fast the end effector is rotating in comparison to the world reference frame, thus giving a more complete result. Also note that Equations (3.23) and (3.24) can be transformed so as to be located in the body frames of link 1 or 2, as needed.

Instead of first calculating the kinematics in the world reference frame and only later converting the result to a link reference frame, another approach is possible. That is, the derivation can be completed directly in the link frame. This allows a recursive procedure to be performed, where the kinematics are solved by moving from link-to-link. This is the method applied here, as it is also part of the recursive Newton-Euler equations that are found in section 3.4.3. Note that some of the intermediate equations derived here in the kinematics will be needed to complete the Newton-Euler model.

This derivation uses the following steps:

$${}^i\vec{P}_i^* = {}^i\vec{L}_i,\tag{3.25}$$

$${}^i\vec{\omega}_i = {}^i\hat{R}_{i-1}\{{}^{i-1}\vec{\omega}_{i-1} + \dot{q}_i({}^{i-1}\vec{e}_i)\},\tag{3.26}$$

$${}^i\vec{\alpha}_i = {}^i\hat{R}_{i-1}\{{}^{i-1}\vec{\alpha}_{i-1} + [\ddot{q}_i({}^{i-1}\vec{e}_i) + \dot{q}_i({}^{i-1}\vec{\omega}_{i-1}) \times ({}^{i-1}\vec{e}_i)], \quad (3.27)$$

$${}^i\vec{a}_{B_i} = {}^i\hat{R}_{i-1}\{{}^{i-1}\vec{a}_{B_{i-1}}\} + ({}^i\vec{\alpha}_i) \times ({}^i\vec{P}_i^*) + ({}^i\vec{\omega}_i) \times [({}^i\vec{\omega}_i) \times ({}^i\vec{P}_i^*)], \quad (3.28)$$

where ${}^i\vec{P}_i^*$ is the distance from the origin of the i^{th} frame to the end of link i , ${}^i\vec{\omega}_i$ is the angular velocity of joint i , ${}^i\vec{\alpha}_i$ is the angular acceleration of joint i , and ${}^i\vec{a}_{B_i}$ is the acceleration of the end of link i . The notation here signifies that everything is being calculated in the XYZ_i reference frame. The generalized coordinate q_i refers to the variable of joint i . In this instance these will be θ_1 and θ_2 , respectively.

For the two-link robot, Equation (3.25) is given as

$${}^1\vec{P}_1^* = \begin{bmatrix} l_1 \\ 0 \\ 0 \end{bmatrix}, \quad (3.29)$$

$${}^2\vec{P}_2^* = \begin{bmatrix} l_2 \\ 0 \\ 0 \end{bmatrix}, \quad (3.30)$$

while the rotation matrices are

$${}^0\hat{R}_1 = \begin{bmatrix} \cos(\theta_1) & -\sin(\theta_1) & 0 \\ \sin(\theta_1) & \cos(\theta_1) & 0 \\ 0 & 0 & 1 \end{bmatrix}, \quad (3.31)$$

$${}^1\hat{R}_2 = \begin{bmatrix} \cos(\theta_2) & -\sin(\theta_2) & 0 \\ \sin(\theta_2) & \cos(\theta_2) & 0 \\ 0 & 0 & 1 \end{bmatrix}, \quad (3.32)$$

which are purely rotations about the Z_i axis. Since all rotations are done about the Z_i axis, the following equation is always true:

$${}^{i-1}\vec{e}_i = \begin{bmatrix} 0 \\ 0 \\ 1 \end{bmatrix}, \quad (3.33)$$

which simplifies the derivations of Equations (3.26) and (3.27).

These rotations are defined from the $i - 1$ frame to the i frame, so it is necessary to take their inverse in order to apply them to Equations (3.26), (3.27), and (3.28). Since the inverse of a rotation matrix is also its transpose, given as

$${}^i\hat{R}_{i-1} = {}^{i-1}\hat{R}_i^{-1} = {}^{i-1}\hat{R}_i^T, \quad (3.34)$$

the derivation for the two-link robot can be completed as follows:

$${}^1\vec{\omega}_1 = {}^0\hat{R}_1^T \{ {}^0\vec{\omega}_0 + \dot{\theta}_1 ({}^0\vec{e}_1) \} = \begin{bmatrix} 0 \\ 0 \\ \dot{\theta}_1 \end{bmatrix}, \quad (3.35)$$

since

$${}^0\vec{\omega}_0 = \begin{bmatrix} 0 \\ 0 \\ 0 \end{bmatrix}, \quad (3.36)$$

$${}^2\vec{\omega}_2 = {}^1\hat{R}_2^T \{ {}^1\vec{\omega}_1 + \dot{\theta}_2 ({}^1\vec{e}_2) \} = \begin{bmatrix} 0 \\ 0 \\ \dot{\theta}_1 + \dot{\theta}_2 \end{bmatrix}, \quad (3.37)$$

$${}^1\vec{\alpha}_1 = {}^0\hat{R}_1^T \{ {}^0\vec{\alpha}_0 + [\ddot{\theta}_1 ({}^0\vec{e}_1) + \dot{\theta}_1 ({}^0\vec{\omega}_0) \times ({}^0\vec{e}_1)] \} = \begin{bmatrix} 0 \\ 0 \\ \ddot{\theta}_1 \end{bmatrix}, \quad (3.38)$$

since

$${}^0\vec{\alpha}_0 = \begin{bmatrix} 0 \\ 0 \\ 0 \end{bmatrix}, \quad (3.39)$$

$${}^2\vec{\alpha}_2 = {}^1\hat{R}_2^T \{ {}^1\vec{\alpha}_1 + [\ddot{\theta}_2({}^1\vec{e}_2) + \dot{\theta}_2({}^1\vec{\omega}_1) \times ({}^1\vec{e}_2)] \} = \begin{bmatrix} 0 \\ 0 \\ \ddot{\theta}_1 + \ddot{\theta}_2 \end{bmatrix}. \quad (3.40)$$

In order to simulate the effect of gravity, the base frame is given a pseudo acceleration as

$${}^0\vec{a}_{B_0} = \begin{bmatrix} 0 \\ 0 \\ g \end{bmatrix}, \quad (3.41)$$

which will affect the dynamic equations of motion by accounting for the weight of the robot. The accelerations of the ends of links 1 and 2 are given as

$${}^1\vec{a}_{B_1} = {}^0\hat{R}_1^T \{ {}^0\vec{a}_{B_0} \} + ({}^1\vec{\alpha}_1) \times ({}^1\vec{P}_1^*) + ({}^1\vec{\omega}_1) \times [({}^1\vec{\omega}_1) \times ({}^1\vec{P}_1^*)] = \begin{bmatrix} -l_1\dot{\theta}_1^2 \\ l_1\ddot{\theta}_1 \\ g \end{bmatrix}, \quad (3.42)$$

$$\begin{aligned} {}^2\vec{a}_{B_2} &= {}^1\hat{R}_2^T \{ {}^1\vec{a}_{B_1} \} + ({}^2\vec{\alpha}_2) \times ({}^2\vec{P}_2^*) + ({}^2\vec{\omega}_2) \times [({}^2\vec{\omega}_2) \times ({}^2\vec{P}_2^*)] \\ &= \begin{bmatrix} l_1\ddot{\theta}_1 \sin(\theta_2) - l_1\dot{\theta}_1^2 \cos(\theta_2) - l_2(\dot{\theta}_1 + \dot{\theta}_2)^2 \\ l_1\ddot{\theta}_1 \cos(\theta_2) + l_1\dot{\theta}_1^2 \sin(\theta_2) + l_2(\ddot{\theta}_1 + \ddot{\theta}_2) \\ g \end{bmatrix}. \end{aligned} \quad (3.43)$$

Equation (3.43) gives the acceleration of the endpoint in the link 2 reference frame. This matches the results found using a vector approach, which is the method applied by Agrawal in [37].

3.3 Calculation of Performance Metrics for Two-Link Robot

In order to quantify the residual vibration of the system, the three measures of performance that are defined in section 2.5 are used.

The magnitude of the linear acceleration of the end effector can be calculated as

$$a = \sqrt{\ddot{P}_x^2 + \ddot{P}_y^2}, \quad \left[\frac{\text{m}}{\text{s}^2}\right] \quad (3.44)$$

with \ddot{P}_x and \ddot{P}_y found from Equations (3.23) and (3.24), respectively, or by the \hat{i}_2 and \hat{j}_2 elements of Equation (3.43). In general, the choice of what equations to use will depend on the measurements available. This decision will also hinge on the coordinate system the resulting acceleration signal should be located in. Observe that the measure of residual acceleration used here is scalar, and only gives the magnitude of the acceleration. Since the only interest in this work is on the overall magnitude of the residual vibration, the direction of the acceleration vector is not important here. Because of this, it does not matter which of these equations, or which reference frame, is utilized. In fact, both these equations are easy to implement in practice using the measurements obtained from the encoders and accelerometers installed on the robot.

The peak residual acceleration can be described as

$$a_{rv} = \max(a(t)), \quad \left[\frac{\text{m}}{\text{s}^2}\right] \quad (3.45)$$

where time t is in the range $T_f \leq t \leq T_{end}$, T_f is the time at the end of motion and T_{end} is the time at the end of the experiment.

The peak deflection can be calculated using Equations (3.16) and (3.17), which give the position of the endpoint. This calculation can be written as

$$\Delta_x = P_x - P_{x,SS}, \quad [\text{m}] \quad (3.46)$$

$$\Delta_y = P_y - P_{y,SS}, \quad [\text{m}] \quad (3.47)$$

$$\Delta_P = \sqrt{\Delta_x^2 + \Delta_y^2}, \quad [\text{m}] \quad (3.48)$$

where P_x and P_y give the location of the endpoint and $P_{x,SS}$ and $P_{y,SS}$ are the steady-state values of the final position of the endpoint. The peak deflection is given as

$$\Delta_{P,max} = \max(\Delta_P(t)), \quad [\text{m}] \quad (3.49)$$

for time in the range $T_f \leq t \leq T_{end}$. Observe that, as for the peak acceleration, this derivation also accounts for only the magnitude of the peak deflection, and not the direction it occurs in.

The settling time is found by taking the signal of the acceleration magnitude, as was derived in Equation (3.44), and finding the final time it is above a certain tolerance threshold, which is set at $0.075 \frac{\text{m}}{\text{s}^2}$ when studying the flexible-joint robot. This is measured from the end of the input profile, meaning it falls in the range $T_f \leq t \leq T_{end}$. There are several aspects that need to be considered when establishing this threshold. This is done through experience with some trial and error. If the window is set too low, noise entering into the sensors may become a concern as it may lead to inconsistent calculations of the settling time. Also, there is the possibility that the signal will not even settle out before the experiment ends. Conversely, if the threshold is set too high then the acceleration magnitude will always be inside the window, thus resulting in a settling time of zero seconds. Neither of these cases is useful as a measure of residual vibration, so the threshold needs to be set so as to allow differences in performance to be observed.

3.4 Robot Dynamics

While kinematic analysis is useful when examining the motion of the system with respect to its geometry, it does not derive any results that describe the behavior of the robot due to the forces that act on it. In order to study this behavior, mathematical models of the dynamics are required. Several models are derived to accomplish this

task. In section 3.4.1, a full Lagrangian model is presented, which was derived by Nho [40]. Section 3.4.2 will show a reduced model given by Spong [8], while a set of Newton-Euler equations will be derived in section 3.4.3.

The angles θ_1 and θ_2 measure the positions of links 1 and 2 while the angles θ_3 and θ_4 measure the positions of motors 1 and 2, respectively. Note that θ_1 and θ_3 are absolute angles measured with respect to ground, while θ_2 and θ_4 are relative angles measured from the angle of the first link.

For this work, the effect of any payload is ignored and it is assumed that there are no forces from the environment acting on the end effector.

3.4.1 Lagrangian Model

In [40], Nho derived a Lagrangian model for the robot that included a payload mass at the end effector. This payload has now been omitted.

The general form of a Lagrangian model can be written as

$$\mathbf{M}(\theta)\ddot{\theta} + \mathbf{V}(\theta, \dot{\theta}) + \mathbf{C}\dot{\theta} + \mathbf{K}\theta + \mathbf{D}(\dot{\theta}) = \mathbf{T}, \quad (3.50)$$

where θ is the vector of generalized coordinates θ_i , $\mathbf{M}(\theta)$ is the inertia matrix, $\mathbf{V}(\theta, \dot{\theta})$ is the vector containing the forces associated with the Coriolis and Centrifugal terms, \mathbf{C} is the viscous damping matrix, \mathbf{K} is the stiffness matrix, $\mathbf{D}(\dot{\theta})$ is the Coulomb friction vector, and \mathbf{T} is the driving torque vector. Note that any fast dynamics associated with the electrical subsystems, including the servo amplifiers, are neglected and the motors are modeled as ideal torque sources.

Each of the terms in Equation (3.50) can be written in terms of the parameters of the robot. The inertia matrix $\mathbf{M}(\theta)$ is written as

$$\mathbf{M}(\theta) = \begin{bmatrix} \mathbf{M}_1(\theta_2) & \mathbf{M}_2 \\ \mathbf{M}_2^T & \mathbf{M}_3 \end{bmatrix}, \quad (3.51)$$

with

$$\mathbf{M}_1(\theta_2) = \begin{bmatrix} m_{11} & m_{12} \\ m_{21} & m_{22} \end{bmatrix}, \quad (3.52)$$

$$\mathbf{M}_2 = \begin{bmatrix} 0 & m_{14} \\ 0 & 0 \end{bmatrix}, \quad (3.53)$$

$$\mathbf{M}_3 = \begin{bmatrix} m_{33} & 0 \\ 0 & m_{44} \end{bmatrix}, \quad (3.54)$$

and the matrix elements are

$$\begin{aligned} m_{11} = & m_1 a_1^2 + m_2 (l_1^2 + a_2^2) + m_4 b_1^2 + m_6 l_1^2 \\ & + J_1 + J_2 + J_4 + J_6 + 2l_1 m_2 a_2 \cos(\theta_2), \end{aligned} \quad (3.55)$$

$$m_{12} = m_{21} = m_2 a_2^2 + J_2 + l_1 m_2 a_2 \cos(\theta_2), \quad (3.56)$$

$$m_{14} = J_4 + \frac{J_6}{r}, \quad (3.57)$$

$$m_{22} = m_2 a_2^2 + J_2, \quad (3.58)$$

$$m_{33} = J_3 + \frac{J_5}{r^2}, \quad (3.59)$$

$$m_{44} = J_4 + \frac{J_6}{r^2}, \quad (3.60)$$

with m_i as the lumped masses, J_i as the moments of inertia, l_i as the link lengths, and a_i as the distance from joint i to the center of gravity for link i . The distance from the second motor to the center of the first joint is b_1 and the gear ratio of the chain drive is r .

The Coriolis and Centrifugal terms are given as

$$\mathbf{V}(\theta, \dot{\theta}) = \begin{bmatrix} \mathbf{V}_L \\ 0 \end{bmatrix} = \begin{bmatrix} -l_1 m_2 a_2 (2\dot{\theta}_1 \dot{\theta}_2 + \dot{\theta}_2^2) \sin(\theta_2) \\ l_1 m_2 a_2 \dot{\theta}_1^2 \sin(\theta_2) \\ 0 \\ 0 \end{bmatrix}, \quad (3.61)$$

while the viscous damping matrix is

$$\mathbf{C} = \begin{bmatrix} c_1 + c_5 & 0 & -\frac{c_5}{r} & 0 \\ 0 & c_2 + c_6 & 0 & -\frac{c_6}{r} \\ -\frac{c_5}{r} & 0 & c_3 + \frac{c_5}{r^2} & 0 \\ 0 & -\frac{c_6}{r} & 0 & c_4 + \frac{c_6}{r^2} \end{bmatrix}, \quad (3.62)$$

the stiffness matrix is

$$\mathbf{K} = \begin{bmatrix} k_5 & 0 & -\frac{k_5}{r} & 0 \\ 0 & k_6 & 0 & -\frac{k_6}{r} \\ -\frac{k_5}{r} & 0 & \frac{k_5}{r^2} & 0 \\ 0 & -\frac{k_6}{r} & 0 & \frac{k_6}{r^2} \end{bmatrix}, \quad (3.63)$$

the vector of Coulomb friction is

$$\mathbf{D}(\dot{\theta}) = \begin{bmatrix} \mathbf{D}_L \\ \mathbf{D}_M \end{bmatrix} = \begin{bmatrix} d_1 \text{sign}(\dot{\theta}_1) \\ d_2 \text{sign}(\dot{\theta}_2) \\ d_3 \text{sign}(\dot{\theta}_3) \\ d_4 \text{sign}(\dot{\theta}_4) \end{bmatrix}, \quad (3.64)$$

and the motor driving torque vector is

$$\mathbf{T} = \begin{bmatrix} 0 \\ \mathbf{T}_m \end{bmatrix} = \begin{bmatrix} 0 \\ 0 \\ T_1 \\ T_2 \end{bmatrix}, \quad (3.65)$$

where T_1 and T_2 are the torques for the first and second motors, respectively.

3.4.2 Reduced Model

In [8], Spong derived a simplified model of the Lagrangian equations for a flexible-joint robot. This is useful since it retains most of the dynamic properties of the full Lagrangian model, yet greatly reduces the complexity of the resulting equations.

Several assumptions are key to these results. First, the damping of the torsional springs, c_5 and c_6 , is neglected. This reduces the viscous damping matrix shown in Equation (3.62) to a diagonal matrix, written as

$$\mathbf{C}_{\text{red}} = \begin{bmatrix} \mathbf{C}_{\mathbf{L}} & 0 \\ 0 & \mathbf{C}_{\mathbf{M}} \end{bmatrix} = \begin{bmatrix} c_1 & 0 & 0 & 0 \\ 0 & c_2 & 0 & 0 \\ 0 & 0 & c_3 & 0 \\ 0 & 0 & 0 & c_4 \end{bmatrix}, \quad (3.66)$$

where $\mathbf{C}_{\mathbf{L}}$ and $\mathbf{C}_{\mathbf{M}}$ are the damping matrices for the links and the motors, respectively. This assumption is valid, as the damping from the torsional springs is typically much smaller in magnitude when compared to the other sources of viscous damping present in this system.

The second assumption made by Spong is that the kinetic energy of the motors is primarily due to their own rotation. This is an assumption that is often made when there is a large gear ratio between the links and the motors, that is when $r \gg 1$. This results in the motor having an angular velocity that is much larger than the angular velocity of the links, which in turn means that while the motor may be moving in space, the kinetic energy associated with this movement is much smaller than the kinetic energy that comes from the angular velocity of the motor itself. This assumption creates a reduced inertia matrix

$$\mathbf{M}_{\text{red}}(\theta) = \begin{bmatrix} \mathbf{M}_1(\theta_2) & 0 \\ 0 & \mathbf{M}_3 \end{bmatrix}, \quad (3.67)$$

which differs from Equation (3.51) by neglecting the non-diagonal term \mathbf{M}_2 .

With these two simplifications, the reduced model is

$$\mathbf{M}_{\text{red}}(\theta)\ddot{\theta} + \mathbf{V}(\theta, \dot{\theta}) + \mathbf{C}_{\text{red}}\dot{\theta} + \mathbf{K}\theta + \mathbf{D}(\dot{\theta}) = \mathbf{T}, \quad (3.68)$$

where the cross-coupling terms between the links and the motors have been neglected.

Since the cross-coupling terms have dropped out of the Lagrangian model, Equation (3.68) can be split up into separate equations for the motors and the links. These are written as

$$\mathbf{M}_1(\theta_L)\ddot{\theta}_L + \mathbf{V}_L(\theta_L, \dot{\theta}_L) + \mathbf{C}_L\dot{\theta}_L + \mathbf{K}_S(\theta_L - \frac{\theta_M}{r}) + \mathbf{D}_L(\dot{\theta}_L) = 0, \quad (3.69)$$

for the links and

$$\mathbf{M}_3\ddot{\theta}_M + \mathbf{C}_M\dot{\theta}_M + \mathbf{K}_S(\frac{\theta_M}{r^2} - \frac{\theta_L}{r}) + \mathbf{D}_M(\dot{\theta}_M) = \mathbf{T}_M, \quad (3.70)$$

for the motors. Observe that the only term that appears in both Equations (3.69) and (3.70) is \mathbf{K}_S , which is a diagonal matrix containing the spring coefficients, written as

$$\mathbf{K}_S = \begin{bmatrix} k_5 & 0 \\ 0 & k_6 \end{bmatrix}, \quad (3.71)$$

which shows that the only connections between the links and the motors are the torsional springs in the joints.

3.4.3 Recursive Newton-Euler Equations

The dynamic equations of motion for a robotic manipulator can also be derived using the Newton-Euler approach. This is done using the kinematic equations of section 3.2 with respect to the body frame of each link. This allows a procedure to be defined that works for n links, where the equations of motion are derived for each link of the serial chain recursively. This is done in two steps.

1. Calculate the forward kinematics of each link in the link reference frame. This is done starting from link 1 and continuing forward sequentially through the links until the end effector is reached
2. Calculate the inverse dynamics of each link in the link reference frame. This is done starting from the end effector located on link n and going backwards through the links until the base of the robot is reached

The first step was mostly completed in section 3.2, where the kinematic equations for the ends of the links were derived. However, one piece is missing. That is, the Newton-Euler equations require the acceleration of the center of gravity for each link. This requires one more equation, given as

$${}^i\vec{a}_{G_i} = {}^i\vec{a}_{B_i} + ({}^i\vec{\alpha}_i) \times ({}^i\vec{G}_i) + ({}^i\vec{\omega}_i) \times [({}^i\vec{\omega}_i) \times ({}^i\vec{G}_i)]. \quad (3.72)$$

The assumption is made that the center of gravity will always be located at the center of the link. This is given as

$${}^1\vec{G}_1 = \begin{bmatrix} -\frac{1}{2}l_1 \\ 0 \\ 0 \end{bmatrix}, \quad (3.73)$$

$${}^2\vec{G}_2 = \begin{bmatrix} -\frac{1}{2}l_2 \\ 0 \\ 0 \end{bmatrix}, \quad (3.74)$$

which can be used in Equation (3.72) as follows:

$${}^1\vec{a}_{G_1} = {}^1\vec{a}_{B_1} + ({}^1\vec{\alpha}_1) \times ({}^1\vec{G}_1) + ({}^1\vec{\omega}_1) \times [({}^1\vec{\omega}_1) \times ({}^1\vec{G}_1)] = \begin{bmatrix} -\frac{1}{2}l_1\dot{\theta}_1^2 \\ \frac{1}{2}l_1\ddot{\theta}_1 \\ g \end{bmatrix}, \quad (3.75)$$

$$\begin{aligned}
{}^2\vec{a}_{G_2} &= {}^2\vec{a}_{B_2} + ({}^2\vec{\alpha}_2) \times ({}^2\vec{G}_2) + ({}^2\vec{\omega}_2) \times [({}^2\vec{\omega}_2) \times ({}^2\vec{G}_2)] \\
&= \begin{bmatrix} l_1\ddot{\theta}_1 \sin(\theta_2) - l_1\dot{\theta}_1^2 \cos(\theta_2) - \frac{1}{2}l_2(\dot{\theta}_1 + \dot{\theta}_2)^2 \\ l_1\ddot{\theta}_1 \cos(\theta_2) + l_1\dot{\theta}_1^2 \sin(\theta_2) + \frac{1}{2}l_2(\ddot{\theta}_1 + \ddot{\theta}_2) \\ g \end{bmatrix}. \tag{3.76}
\end{aligned}$$

As noted at the beginning of this section, all calculations of the forces and torques are done using the acceleration of the center of gravity for each link. This is an application of Newton's second law

$$\vec{F} = m\vec{a}. \tag{3.77}$$

The procedure for using this first principle, along with the Euler equations of motion for rotating bodies, can be written as

$${}^i\vec{F}_i = {}^i\hat{R}_{i+1}({}^{i+1}\vec{F}_{i+1}) + m_i({}^i\vec{a}_{G_i}), \tag{3.78}$$

$${}^i\vec{M}_i = {}^i\hat{I}_i({}^i\vec{\alpha}_i) + {}^i\vec{\omega}_i \times ({}^i\hat{I}_i {}^i\vec{\omega}_i), \tag{3.79}$$

$${}^i\vec{T}_i = {}^i\hat{R}_{i+1}({}^{i+1}\vec{T}_{i+1}) + ({}^i\vec{P}_i^*) \times ({}^i\hat{R}_{i+1} {}^{i+1}\vec{F}_{i+1}) + m_i({}^i\vec{P}_i^* + {}^i\vec{G}_i) \times ({}^i\vec{a}_{G_i}) + {}^i\vec{M}_i, \tag{3.80}$$

$$D_i = {}^{i-1}\hat{R}_i({}^i\vec{T}_i) \cdot ({}^{i-1}\vec{e}_i) + c_i\dot{q}_i, \tag{3.81}$$

where, in order to calculate the forces, it is necessary to work backwards from the end effector. This process is started by defining the force of the environment acting on the end effector, which in this instance is assumed to be zero. This means that

$${}^3\vec{F}_3 = \begin{bmatrix} 0 \\ 0 \\ 0 \end{bmatrix}, \tag{3.82}$$

$${}^3\vec{T}_3 = \begin{bmatrix} 0 \\ 0 \\ 0 \end{bmatrix}, \quad (3.83)$$

so that the derivation follows as

$${}^2\vec{F}_2 = {}^2\hat{R}_3({}^3\vec{F}_3) + m_2({}^2\vec{a}_{G_2}) = \begin{bmatrix} m_2 l_1 \ddot{\theta}_1 \sin(\theta_2) - m_2 l_1 \dot{\theta}_1^2 \cos(\theta_2) - \frac{1}{2} m_2 l_2 (\dot{\theta}_1 + \dot{\theta}_2)^2 \\ m_2 l_1 \ddot{\theta}_1 \cos(\theta_2) + m_2 l_1 \dot{\theta}_1^2 \sin(\theta_2) + \frac{1}{2} m_2 l_2 (\ddot{\theta}_1 + \ddot{\theta}_2) \\ m_2 g \end{bmatrix}, \quad (3.84)$$

$${}^1\vec{F}_1 = {}^1\hat{R}_2({}^2\vec{F}_2) + m_1({}^1\vec{a}_{G_1}) = \begin{bmatrix} -\frac{1}{2} m_2 l_2 ((\dot{\theta}_1 + \dot{\theta}_2)^2 \cos(\theta_2) + (\ddot{\theta}_1 + \ddot{\theta}_2) \sin(\theta_2)) - (m_2 l_1 + \frac{1}{2} m_1 l_1) \dot{\theta}_1^2 \\ -\frac{1}{2} m_2 l_2 ((\dot{\theta}_1 + \dot{\theta}_2)^2 \sin(\theta_2) - (\ddot{\theta}_1 + \ddot{\theta}_2) \cos(\theta_2)) + (m_2 l_1 + \frac{1}{2} m_1 l_1) \ddot{\theta}_1 \\ (m_1 + m_2) g \end{bmatrix}. \quad (3.85)$$

The links are assumed to be rigid rods, which means the mass moment of inertia for each link can be modeled as

$${}^1\hat{I}_1 = \begin{bmatrix} 0 & 0 & 0 \\ 0 & \frac{m_1 l_1^2}{12} & 0 \\ 0 & 0 & \frac{m_1 l_1^2}{12} \end{bmatrix}, \quad (3.86)$$

$${}^2\hat{I}_2 = \begin{bmatrix} 0 & 0 & 0 \\ 0 & \frac{m_2 l_2^2}{12} & 0 \\ 0 & 0 & \frac{m_2 l_2^2}{12} \end{bmatrix}, \quad (3.87)$$

$${}^1\vec{M}_1 = {}^1\hat{I}_1({}^1\vec{\alpha}_1) + {}^1\vec{\omega}_1 \times ({}^1\hat{I}_1 {}^1\vec{\omega}_1) = \begin{bmatrix} 0 \\ 0 \\ \frac{m_1 l_1^2 \ddot{\theta}_1}{12} \end{bmatrix}, \quad (3.88)$$

$${}^2\vec{M}_2 = {}^2\hat{I}_2({}^2\vec{\alpha}_2) + {}^2\vec{\omega}_2 \times ({}^2\hat{I}_2 {}^2\vec{\omega}_2) = \begin{bmatrix} 0 \\ 0 \\ \frac{m_2 l_2^2 (\ddot{\theta}_1 + \ddot{\theta}_2)}{12} \end{bmatrix}, \quad (3.89)$$

The torque needed for the second link is given as

$${}^2\vec{T}_2 = {}^2\hat{R}_3({}^3\vec{T}_3) + ({}^2\vec{P}_2^*) \times ({}^2\hat{R}_3 {}^3\vec{F}_3) + m_2({}^2\vec{P}_2^* + {}^2\vec{G}_2) \times ({}^2\vec{a}_{G_2}) + {}^2\vec{M}_2 = \begin{bmatrix} 0 \\ -\frac{1}{2}m_2 l_2 g \\ \frac{1}{2}m_2 l_1 l_2 (\ddot{\theta}_1 \cos(\theta_2) + \dot{\theta}_1^2 \sin(\theta_2)) + \frac{1}{3}m_2 l_2^2 (\ddot{\theta}_1 + \ddot{\theta}_2) \end{bmatrix}, \quad (3.90)$$

where the \hat{j} component is the holding torque needed to resist gravity and hold the link parallel to the horizontal plane.

The torque needed for the first link is

$${}^1\vec{T}_1 = {}^1\hat{R}_2({}^2\vec{T}_2) + ({}^1\vec{P}_1^*) \times ({}^1\hat{R}_2 {}^2\vec{F}_2) + m_1({}^1\vec{P}_1^* + {}^1\vec{G}_1) \times ({}^1\vec{a}_{G_1}) + {}^1\vec{M}_1 = \begin{bmatrix} \frac{1}{2}m_2 l_2 g \sin(\theta_2) \\ -\frac{1}{2}m_2 l_2 g \cos(\theta_2) - (m_2 + \frac{1}{2}m_1)l_1 g \\ \frac{1}{2}m_2 l_1 l_2 ((2\ddot{\theta}_1 + \ddot{\theta}_2) \cos(\theta_2) + (\dot{\theta}_1^2 - (\dot{\theta}_1 + \dot{\theta}_2)^2) \sin(\theta_2)) + \\ \frac{1}{3}m_2 l_2^2 (\ddot{\theta}_1 + \ddot{\theta}_2) + (m_2 l_1^2 + \frac{1}{3}m_1 l_1^2) \ddot{\theta}_1 \end{bmatrix}, \quad (3.91)$$

which also gives the holding torque required to resist gravity.

The drive efforts needed to move the robot links are

$$D_{l,1} = {}^0\hat{R}_1({}^1\vec{T}_1) \cdot ({}^0\vec{e}_1) + c_1 \dot{\theta}_1 = \frac{1}{2}m_2 l_1 l_2 ((2\ddot{\theta}_1 + \ddot{\theta}_2) \cos(\theta_2) + (\dot{\theta}_1^2 - (\dot{\theta}_1 + \dot{\theta}_2)^2) \sin(\theta_2)) + \frac{1}{3}m_2 l_2^2 (\ddot{\theta}_1 + \ddot{\theta}_2) + (m_2 l_1^2 + \frac{1}{3}m_1 l_1^2) \ddot{\theta}_1 + c_1 \dot{\theta}_1, \quad (3.92)$$

$$D_{l,2} = {}^1\hat{R}_2({}^2\vec{T}_2) \cdot ({}^1\vec{e}_2) + c_2 \dot{\theta}_2 = \frac{1}{2}m_2 l_1 l_2 (\ddot{\theta}_1 \cos(\theta_2) + \dot{\theta}_1^2 \sin(\theta_2)) + \frac{1}{3}m_2 l_2^2 (\ddot{\theta}_1 + \ddot{\theta}_2) + c_2 \dot{\theta}_2, \quad (3.93)$$

where c_1 and c_2 correspond to the viscous damping of the joints. Upon closer inspection of Equations (3.92) and (3.93), similarities may be observed with the elements of the matrices that make up the full Lagrangian model of Equation (3.50). This is unsurprising, as both methods should produce analogous results.

However, note that these equations only model the dynamics of the links and the compliance of the joints has not yet been incorporated. The joint elasticity is added using an idealized model of the joints, which was given by Spong [2]. This joint model is shown in Figure 3.4.

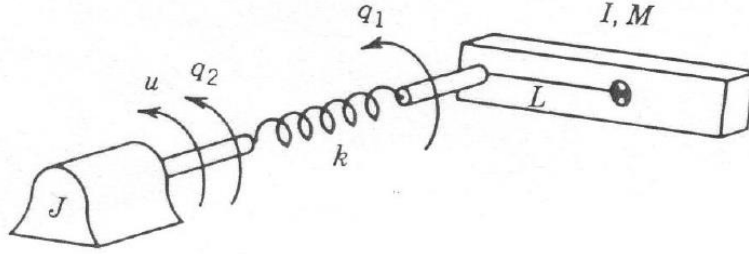


Figure 3.4. Idealized model of joint flexibility, [2].

There are two equations of motion for the joint, one for the link side of the spring and one for the motor side of the spring. These are given as

$$J_{l,i}\ddot{\theta}_{l,i} + c_{l,i}\dot{\theta}_{l,i} + k_i(\theta_{l,i} - \theta_{m,i}) = 0, \quad (3.94)$$

$$J_{m,i}\ddot{\theta}_{m,i} + c_{m,i}\dot{\theta}_{m,i} - k_i(\theta_{l,i} - \theta_{m,i}) = u_i, \quad (3.95)$$

for the i^{th} joint, where u_i is the drive effort of the i^{th} motor, $J_{l,i}$ is the inertia of the i^{th} link, and $J_{m,i}$ is the inertia of the i^{th} motor. The damping and stiffness coefficients of the i^{th} joint are given by $c_{l,i}$, $c_{m,i}$, $k_{l,i}$, and $k_{m,i}$, for the link and motor

side, respectively. By inserting Equation (3.94) into Equation (3.95) the following is obtained:

$$J_{m,i}\ddot{\theta}_{m,i} + c_{m,i}\dot{\theta}_{m,i} + J_{l,i}\ddot{\theta}_{l,i} + c_{l,i}\dot{\theta}_{l,i} = J_{m,i}\ddot{\theta}_{m,i} + c_{m,i}\dot{\theta}_{m,i} + D_{l,i} = u_i, \quad (3.96)$$

where $D_{l,i}$ is the drive effort needed to move each link, given by Equations (3.92) and (3.93).

However, this does not take into account the gear ratio between the motors and the links. Notice the similarity between Equations (3.94) and (3.95) and Equations (3.69) and (3.70). Taking into account the gear ratio results in the following adjusted equations:

$$J_{l,i}\ddot{\theta}_{l,i} + c_{l,i}\dot{\theta}_{l,i} + k_i(\theta_{l,i} - \frac{\theta_{m,i}}{r}) = 0, \quad (3.97)$$

$$J_{m,i}\ddot{\theta}_{m,i} + c_{m,i}\dot{\theta}_{m,i} - k_i(\frac{\theta_{l,i}}{r} - \frac{\theta_{m,i}}{r^2}) = u_i, \quad (3.98)$$

$$J_{m,i}\ddot{\theta}_{m,i} + c_{m,i}\dot{\theta}_{m,i} + \frac{1}{r}(J_{l,i}\ddot{\theta}_{l,i} + c_{l,i}\dot{\theta}_{l,i}) = J_{m,i}\ddot{\theta}_{m,i} + c_{m,i}\dot{\theta}_{m,i} + \frac{D_{l,i}}{r} = u_i. \quad (3.99)$$

3.5 System Parameters

In order for any of these models to correlate well with dynamics of the robot itself, it is crucial to get accurate values of the physical parameters of the system. This is important not only to design adequate controllers and to generate command inputs, but also to build good simulations of the robot behavior. For this purpose, some system identification is required. Multiple techniques have been applied to the two-link flexible-joint robot over the years in order to obtain parameter estimates using methods that best match the different research problems that have been studied.

Nho [40] used a least squares approach to perform system identification. In order to accomplish this task, certain nonlinear parameter groups were defined. This permits the model to be represented in a manner that is linear with respect to the parameters. Linear least squares regression can then be applied directly to the nonlinear

parameter groups in order to determine their values simultaneously using open-loop experimental data.

In [34], Lee used a nonlinear autoregressive moving average with exogenous inputs, or NARMAX, model to find accurate parameter estimates using a prediction error approach. This was then combined with a roughness penalty obtained through Fourier regularization to obtain a more accurate long-term prediction model, while avoiding issues such as overfitting.

Scheel [44] proposed a new technique that decomposes the system into its constituent parts. System identification is then performed on each of these subsystems. While this means that all the parameters cannot be calculated in a single experiment, it does help to ensure that the experimental data has enough information to achieve reliable parameter estimates. It also allows the response data for the system to be acquired using less complex experiments, so long as they are designed specifically for the subsystem being identified. Scheel splits the procedure into smaller subproblems of identifying the motors, the second link, and the first link, done in that order. Breaking up the procedure for system identification in this manner resulted in parameter values that closely matched the observed dynamic behavior of the robot. Because of this, these estimates will be used in this work. Table 3.1 lists the values of these physical parameters. Note that the grouped parameters of the system are given as

$$p_1 = m_1 a_1^2 + m_2 l_1^2 + m_4 b_1^2 + m_6 l_1^2 + J_1 + J_4 + J_6, \quad \left[\frac{\text{kgm}^2}{\text{rad}} \right] \quad (3.100)$$

$$p_2 = m_2 a_2^2 + J_2, \quad \left[\frac{\text{kgm}^2}{\text{rad}} \right] \quad (3.101)$$

$$p_3 = l_1 m_2 a_2. \quad \left[\frac{\text{kgm}^2}{\text{rad}} \right] \quad (3.102)$$

Table 3.1. Estimated values of the physical parameters of the robot, [44].

<i>Parameter</i>	Value		<i>Parameter</i>	Value	
p_1	0.1402	$[\frac{\text{kgm}^2}{\text{rad}}]$	c_4	1.4975×10^{-3}	$[\frac{\text{Nms}}{\text{rad}}]$
p_2	0.01962	$[\frac{\text{kgm}^2}{\text{rad}}]$	c_5	0.005	$[\frac{\text{Nms}}{\text{rad}}]$
p_3	0.02338	$[\frac{\text{kgm}^2}{\text{rad}}]$	c_6	8.128×10^{-5}	$[\frac{\text{Nms}}{\text{rad}}]$
J_3	4.1571×10^{-5}	$[\frac{\text{kgm}^2}{\text{rad}}]$	k_5	2.848	$[\frac{\text{Nm}}{\text{rad}}]$
J_4	7.5429×10^{-4}	$[\frac{\text{kgm}^2}{\text{rad}}]$	k_6	2.848	$[\frac{\text{Nm}}{\text{rad}}]$
J_5	0.025	$[\frac{\text{kgm}^2}{\text{rad}}]$	d_1	0.01987	[Nm]
J_6	0.025	$[\frac{\text{kgm}^2}{\text{rad}}]$	d_2	0.0323	[Nm]
c_1	0.04	$[\frac{\text{Nms}}{\text{rad}}]$	d_3	0.0053	[Nm]
c_2	0.02143	$[\frac{\text{Nms}}{\text{rad}}]$	d_4	0.0271	[Nm]
c_3	1.8937×10^{-4}	$[\frac{\text{Nms}}{\text{rad}}]$			

3.6 Computed Torque Control

Many different approaches to controlling a nonlinear system, such as a robotic manipulator, have been proposed. One such architecture is computed torque control, which is a special case of the branch of nonlinear control known as feedback linearization.

Computed torque applies both feedforward and feedback components together to achieve adequate control of the robot. This is done by dividing the controller into two parts, which are called the model-based and servo-based components. The model-based portion utilizes a model of the system dynamics as a feedforward element, which provides the feedback linearization. This allows a feedback loop to be incorporated in the servo-based portion that requires only a linear controller, such as PD or Lead-Lag compensators.

Note that the model-based portion can be derived using either the Lagrangian model or the Newton-Euler equations, which is an observation made in [1].

corrections to the desired acceleration reference. This corrected reference signal is then fed into the dynamic model of the system.

The model-based portion can now be given separately as

$$\mathbf{T}_{\text{mb}} = \mathbf{C}_{\mathbf{M}}\dot{\theta}_M + \mathbf{D}_{\mathbf{M}} + \mathbf{K}_{\mathbf{S}}\left(\frac{\theta_M}{r^2} - \frac{\theta_L}{r}\right), \quad (3.104)$$

since the inertia of the links has been neglected. This is a direct application of Equation (3.70).

The total torque sent to the robot is

$$\mathbf{T}_{\text{CT}} = \mathbf{T}_{\text{mb}} + \mathbf{T}_{\text{sb}}. \quad (3.105)$$

This can be equated to the motor equations from the Spong Model, Equation (3.70), in order to obtain the closed-loop motor dynamics, written as

$$\ddot{\theta}_M + \mathbf{K}_{\mathbf{v}}\dot{\theta}_M + \mathbf{K}_{\mathbf{p}}\theta_M = \ddot{\theta}_{M,d} + \mathbf{K}_{\mathbf{v}}\dot{\theta}_{M,d} + \mathbf{K}_{\mathbf{p}}\theta_{M,d}, \quad (3.106)$$

which can be rearranged to give the motor tracking error $e_M = \theta_{M,d} - \theta_M$ as

$$\ddot{e}_M + \mathbf{K}_{\mathbf{v}}\dot{e}_M + \mathbf{K}_{\mathbf{p}}e_M = 0. \quad (3.107)$$

The control gains are chosen so that Equation (3.107) is Hurwitz, which ensures asymptotic tracking and closed-loop stability of the internal dynamics. This ensures closed-loop stability of the robot, as the joints do not add energy to the system and thus the entire system is Lyapunov stable.

3.6.2 Computed Torque Control with Newton-Euler Equations

It is possible to derive an analogous control scheme using the Newton-Euler equations, as shown in Fu, Gonzalez and Lee [1]. This derivation is completed here for the two-link flexible-joint robot with the intent of testing several different models in the

feedforward portion of the computed torque controller. In this manner, the performance of the feedforward portion of the computed torque controller may be examined in greater detail. However, the actual application of the Newton-Euler equations is left to be completed in future work.

This control scheme is derived by redefining the servo-based and model-based components of the computed torque controller. The motor acceleration is pulled out of Equation (3.99) and used to define a new servo-based control law, given as

$$T_{sb,i} = J_{m,i} \ddot{\theta}_{m,new,i}, \quad (3.108)$$

for the i^{th} motor, with $\ddot{\theta}_{m,new,i}$ written as

$$\ddot{\theta}_{m,new,i} = \ddot{\theta}_{m,d,i} + k_{p,i}(\theta_{m,d,i} - \theta_{m,i}) + k_{v,i}(\dot{\theta}_{m,d,i} - \dot{\theta}_{m,i}). \quad (3.109)$$

The model-based portion can be written as

$$T_{mb,i} = c_{m,i} \dot{\theta}_{m,d,i} + \frac{1}{r} D_{l,i}, \quad (3.110)$$

where $D_{l,i}$ is found using Equations (3.92) and (3.93) for the i^{th} link. Combining these components results in the complete computed torque control law for each motor, as given by Equation (3.105).

The same arguments for the closed-loop dynamics and stability that were used in section 3.6.1 apply here as well. As long as the control gains are chosen so that the closed-loop system is Hurwitz, then asymptotic tracking and stability are ensured.

Note that measurements of the link angles are needed in order to implement computed torque control. This requirement is not an issue for the two-link robot used in this work, as both the link and motor angles are measured using encoders. However, in industrial robots only the motor angle is typically known. This means the link angle would need to be estimated or new sensors would need to be added in order to obtain these measurements. On the other hand, these measurements may

be available if the robot is aware of the elasticity present in its joints. These robots tend to possess a more extensive set of sensors, so the necessary measurements may be available [46].

3.7 Configuration-Dependent Resonance

When applying command shaping to a robotic manipulator, there is a very important nonlinear and time-varying piece of the dynamics that must be considered. This is configuration-dependent resonance.

As a robotic manipulator changes its configuration, it also alters its moment of inertia. This causes the natural frequencies of the robot to shift based on the configuration of the links. In fact, by examining Equations (3.51) and (3.67) it becomes apparent that the inertia is a function of the angle θ_2 . Consideration of this phenomenon is crucial when applying command shaping, as the input is designed based on the natural frequencies of the system.

In order to determine the natural frequencies of this nonlinear time-varying system, the equations of motion need to be linearized around an equilibrium point. This is done for the closed-loop system by substituting Equation (3.105) into the full Lagrangian model in Equation (3.50). Then a Taylor series expansion is taken to linearize around an equilibrium point that has zero velocity and zero acceleration as a function of θ_2 . This is done up to the first-order terms and all higher-order terms are neglected. The derivatives of the terms of the Coulomb friction vector are assumed to be zero with respect to the angle velocities. This causes the Coulomb friction to drop out of the linearized equations. The closed-loop linear equations are then written as

$$\mathbf{M}_{\text{lin}}\ddot{\theta} + \mathbf{C}_{\text{lin}}\dot{\theta} + \mathbf{K}_{\text{lin}}\theta = 0, \quad (3.111)$$

where the linearized inertia matrix is given as

$$\mathbf{M}_{\text{lin}} = \begin{bmatrix} m_{11,\text{lin}} & m_{12,\text{lin}} & 0 & m_{14} \\ m_{21,\text{lin}} & m_{22} & 0 & 0 \\ 0 & 0 & m_{33} & 0 \\ m_{14} & 0 & 0 & m_{44} \end{bmatrix}, \quad (3.112)$$

with the inertia terms $m_{11,\text{lin}}$, $m_{12,\text{lin}}$, and $m_{21,\text{lin}}$ written as

$$m_{11,\text{lin}} = m_1 a_1^2 + m_2 (l_1^2 + a_2^2) + m_4 b_1^2 + m_6 l_1^2 + J_1 + J_2 + J_4 + J_6 + 2l_1 m_2 a_2 \cos(\theta_{2,\text{eq}}), \quad (3.113)$$

$$m_{12,\text{lin}} = m_{21,\text{lin}} = m_2 a_2^2 + J_2 + l_1 m_2 a_2 \cos(\theta_{2,\text{eq}}), \quad (3.114)$$

the closed-loop damping matrix is

$$\mathbf{C}_{\text{lin}} = \begin{bmatrix} c_1 + c_5 & 0 & -\frac{c_5}{r} & 0 \\ 0 & c_2 + c_6 & 0 & -\frac{c_6}{r} \\ 0 & 0 & m_{33}K_{v,3} & 0 \\ 0 & 0 & 0 & m_{33}K_{v,4} \end{bmatrix}, \quad (3.115)$$

and the closed-loop stiffness matrix is

$$\mathbf{K}_{\text{lin}} = \begin{bmatrix} k_5 & 0 & -\frac{k_5}{r} & 0 \\ 0 & k_6 & 0 & -\frac{k_6}{r} \\ 0 & 0 & m_{33}K_{p,3} & 0 \\ 0 & 0 & 0 & m_{33}K_{p,4} \end{bmatrix}. \quad (3.116)$$

The control gains $K_{p,i}$ and $K_{v,i}$ correspond to the proportional and derivative control gains when using PD controllers for the motor feedback.

The linearized system matrix \mathbf{A} is given by

$$\mathbf{A} = \begin{bmatrix} 0 & \mathbf{I} \\ -\mathbf{M}_{\text{lin}}^{-1}\mathbf{K}_{\text{lin}} & -\mathbf{M}_{\text{lin}}^{-1}\mathbf{C}_{\text{lin}} \end{bmatrix}, \quad (3.117)$$

where \mathbf{I} is the identity matrix. The natural frequencies of this system can be calculated by finding the imaginary part of the eigenvalues of Equation (3.117). This gives the dependence of the natural frequencies ω_1 and ω_2 on the angle of the second link as shown in Figure 3.6.

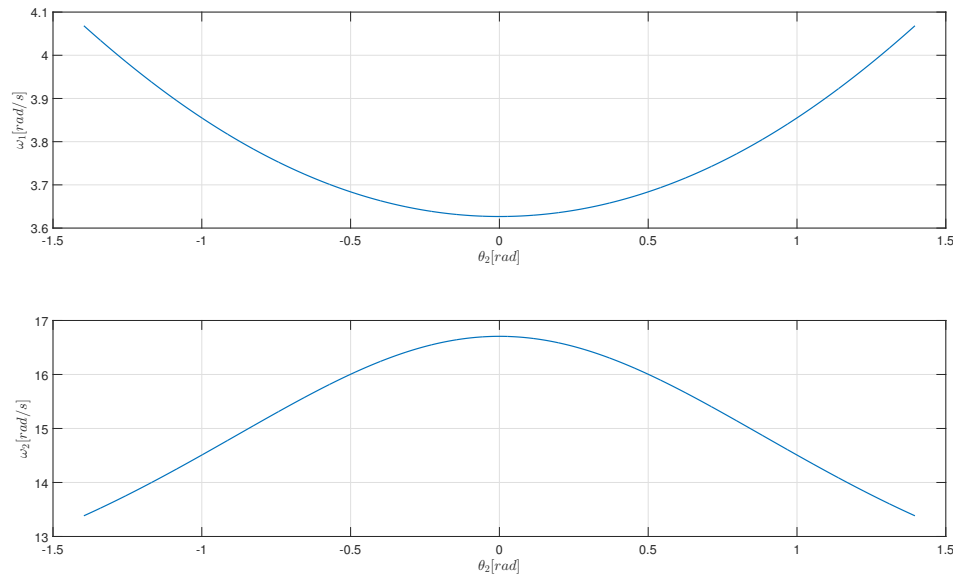


Figure 3.6. Variations in ω_1 and ω_2 as functions of link angle θ_2 .

As the closed-loop damping increases, it is known that the peaks due to resonance will flatten out. The damped natural frequency will also shift as the closed-loop damping increases. Meckl studied the effects of damping on the command shaping procedure in [18], and concluded that the response of the system degrades with more damping present when such damping is not considered when constructing the input profile. However, while the command shaping procedure is made for undamped systems, it does still work well when used with lightly-damped systems ($\zeta < 0.3$). This

is because the damped natural frequency will still be approximately equal to the undamped natural frequency if the closed-loop damping is low. Since the two-link robot is a lightly-damped system and there are limits to how much damping the feedback controller can add, the effects of damping can be safely neglected while constructing inputs through command shaping. This is shown during the analysis of feedback control for a linear three-mass system in section 4.4.1.

CHAPTER 4. MODELING, SIMULATION, AND ANALYSIS OF FEEDBACK CONTROL ON A THREE-MASS SYSTEM

Since a robotic manipulator is inherently nonlinear, it is useful to begin the study of feedback control using a linear system instead. This allows for linear design and analysis methods to be utilized. With these tools available, the interplay between the input profile, the feedforward controller, and the feedback controller may be studied in great detail. Once the understanding of these connections is improved, this knowledge may then be applied to the nonlinear system of the flexible-joint robot, as done in chapter 5.

In order to preserve the important dynamics present in the two-link robot, a three-mass system is modeled, simulated, and analyzed. The three-mass system is chosen because it also possesses two modes of vibration, just like the robot. Section 4.1 will provide a description of this system, while section 4.2 uses modal analysis in order to compute the undamped natural frequencies. Then the transfer functions representing the input-to-output behavior of the three masses are derived in section 4.3. Section 4.4 analyzes the closed-loop behavior of the feedback portion of the three-mass system, and section 4.5 defines the performance metrics for the three-mass system. Lastly, section 4.6 simulates and analyzes the results of applying different kinds of feedback to the three-mass system in order to track different kinds of input profiles.

4.1 System Description

A translational three-mass system with springs and dampers provides a useful testbed to begin analysis on the performance of feedback control when attempting to minimize residual vibration. This system is shown in Figure 4.1.

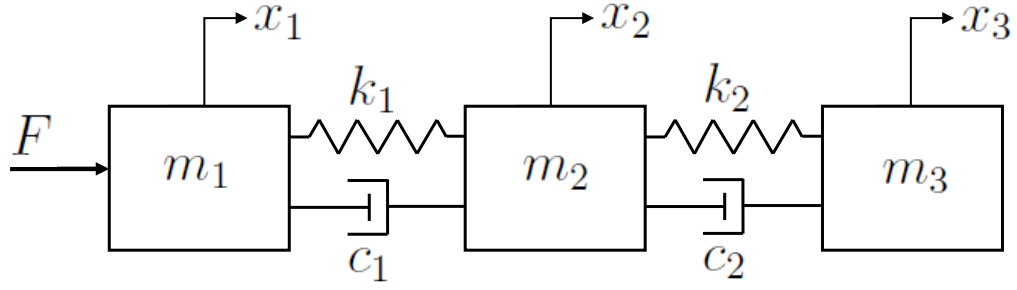


Figure 4.1. The three-mass system.

The input force F is applied to the first mass and all interactions with the environment are neglected. The spring stiffnesses are k_1 and k_2 while the viscous damping coefficients are c_1 and c_2 . The masses are m_1 , m_2 , and m_3 , while x_1 , x_2 , and x_3 are the variables that describe the translational motion of each mass, respectively.

The entire system is unattached to ground, so the input force will result in all three masses moving from one point in space to another point in space. This movement can be described by a set of differential equations of motion, which are given as

$$m_1 \ddot{x}_1 = F + k_1(x_2 - x_1) + c_1(\dot{x}_2 - \dot{x}_1), \quad (4.1)$$

$$m_2 \ddot{x}_2 = -k_1(x_2 - x_1) - c_1(\dot{x}_2 - \dot{x}_1) + k_2(x_3 - x_2) + c_2(\dot{x}_3 - \dot{x}_2), \quad (4.2)$$

$$m_3 \ddot{x}_3 = -k_2(x_3 - x_2) - c_2(\dot{x}_3 - \dot{x}_2), \quad (4.3)$$

These can be written in matrix form as

$$\mathbf{M}\ddot{\mathbf{X}} + \mathbf{C}\dot{\mathbf{X}} + \mathbf{K}\mathbf{X} = \mathbf{U}, \quad (4.4)$$

where

$$\mathbf{M} = \begin{bmatrix} m_1 & 0 & 0 \\ 0 & m_2 & 0 \\ 0 & 0 & m_3 \end{bmatrix}, \quad (4.5)$$

$$\mathbf{C} = \begin{bmatrix} c_1 & -c_1 & 0 \\ -c_1 & c_1 + c_2 & -c_2 \\ 0 & -c_2 & c_2 \end{bmatrix}, \quad (4.6)$$

$$\mathbf{K} = \begin{bmatrix} k_1 & -k_1 & 0 \\ -k_1 & k_1 + k_2 & -k_2 \\ 0 & -k_2 & k_2 \end{bmatrix}. \quad (4.7)$$

Observe that \mathbf{C} and \mathbf{K} are nonsingular matrices, which is a result that occurs when the entire system is unattached to ground. The input is

$$\mathbf{U} = \begin{bmatrix} F \\ 0 \\ 0 \end{bmatrix}, \quad (4.8)$$

and the position vector is

$$\mathbf{X} = \begin{bmatrix} x_1 \\ x_2 \\ x_3 \end{bmatrix}. \quad (4.9)$$

The system parameters used are shown in Table 4.1. These values have been chosen so that the modes of vibration roughly mimic the modes seen on the two-link flexible-joint robot. Also, the second and third masses are both designed to have lower magnitudes than the first mass. This simulates the effect of having a gear ratio between the motor and the link, as is typically the case in a robotic manipulator. Note that in this instance the first mass is analogous to the mass of a motor for the robot, while the other two masses together would represent the mass for one of the links. In order to provide a consistent basis for comparison when applying the different types of command-shaped profiles, the non-dimensional parameter κ is utilized, as defined in chapter 2. Remember that κ is the ratio between the peak input acceleration of the command-shaped profile and the peak input acceleration of the time-optimal bang-bang profile. Table 4.2 shows the values of ρ needed for both

Table 4.1. System parameters of the three-mass system.

<i>Parameter</i>	Value		<i>Parameter</i>	Value	
m_1	1	[kg]	$\omega_{1,nominal}$	4.7528	$[\frac{\text{rad}}{\text{s}}]$
m_2	0.75	[kg]	$\omega_{2,nominal}$	15.2450	$[\frac{\text{rad}}{\text{s}}]$
m_3	0.25	[kg]	$\zeta_{1,2}$	0.1	

the ramped sinusoid and the versine in order to obtain three different values of κ for the three-mass system. Observe that only one value of ρ is required for the entire versine profile. This is due to the fact that this system is time-invariant and does not possess configuration-dependent resonance. In other words, the natural frequencies of the acceleration and deceleration segments of the versine are the same, which results in the following relationship for ρ_V , given as

$$\rho_{V,acc} = \rho_{V,dec} = \rho_V, \quad (4.10)$$

where $\rho_{V,acc}$ and $\rho_{V,dec}$ are the values of ρ for the acceleration and deceleration segments of the versine, respectively.

Table 4.2. Values of ρ needed for different levels of κ for the nominal three-mass system.

κ	ρ_V	ρ_{RS}
3	1.5444066	0.257624
9	142.504965	19.850186
15	1212.061225	56.552180

4.2 Modal Analysis

Modal analysis is a powerful tool that provides a general method for analyzing fairly complex systems in a straightforward manner. Background on this technique can be found in [47], or any other textbook concerning mechanical vibrations.

For the undamped system, all the elements of the matrix \mathbf{C} equal zero. In the case of free vibration the forcing term is also zero. This results in

$$\begin{bmatrix} m_1 & 0 & 0 \\ 0 & m_2 & 0 \\ 0 & 0 & m_3 \end{bmatrix} \begin{bmatrix} \ddot{x}_1 \\ \ddot{x}_2 \\ \ddot{x}_3 \end{bmatrix} + \begin{bmatrix} k_1 & -k_1 & 0 \\ -k_1 & k_1 + k_2 & -k_2 \\ 0 & -k_2 & k_2 \end{bmatrix} \begin{bmatrix} x_1 \\ x_2 \\ x_3 \end{bmatrix} = \vec{0}, \quad (4.11)$$

for the undamped system of equations with free vibration. This is the system that will be examined here, as the interest is on deriving the undamped modes of vibration.

The assumption is made that the solution to the set of differential equations of motion given by Equation (4.11) is harmonic. That is, the solution will be sinusoidal, and is given by

$$x_i(t) = X_i \cos(\omega t + \phi), \quad (4.12)$$

where $x_i(t)$ is the position of mass i as a function of t . The amplitude of the resultant sinusoidal response is X_i , while the frequency and phase angle are ω and ϕ , respectively. Differentiating Equation (4.12) twice gives the velocity and acceleration signals, which are written as

$$\dot{x}_i(t) = -\omega X_i \sin(\omega t + \phi), \quad (4.13)$$

$$\ddot{x}_i(t) = -\omega^2 X_i \cos(\omega t + \phi). \quad (4.14)$$

Inserting Equations (4.12) and (4.14) into Equation (4.11) gives

$$\begin{bmatrix} k_1 - m_1\omega^2 & -k_1 & 0 \\ -k_1 & (k_1 + k_2) - m_2\omega^2 & -k_2 \\ 0 & -k_2 & k_2 - m_3\omega^2 \end{bmatrix} \mathbf{X} = \vec{0}, \quad (4.15)$$

which is an eigenvalue problem, as it can be written in the form

$$\mathbf{A}\mathbf{X} = \mathbf{B}, \quad (4.16)$$

where the eigenvalues are the squared natural frequencies ω^2 and the eigenvectors are the modal vectors. These modal vectors describe how each mode affects the response of each individual mass.

The eigenvalues can be found by taking the determinant of the system matrix \mathbf{A} of Equation (4.15) and setting it equal to zero. This gives

$$\begin{aligned} \omega^2[m_1m_2m_3\omega^4 - (m_1m_2k_2 + m_1m_3(k_1 + k_2) + m_2m_3k_1)\omega^2 \\ + (m_1 + m_2 + m_3)k_1k_2] = 0, \end{aligned} \quad (4.17)$$

which can be factored in terms of ω^2 to find the modes of vibration. These modes are given as

$$\omega_0^2 = 0, \quad \left[\frac{\text{rad}^2}{\text{s}^2}\right] \quad (4.18)$$

$$\begin{aligned} \omega_1^2 = \frac{(m_1m_2k_2 + m_1m_3(k_1 + k_2) + m_2m_3k_1)}{2m_1m_2m_3} \\ - \frac{\sqrt{(m_1m_2k_2 + m_1m_3(k_1 + k_2) + m_2m_3k_1)^2 - 4(m_1m_2m_3)((m_1 + m_2 + m_3)k_1k_2)}}{2m_1m_2m_3}, \end{aligned} \quad \left[\frac{\text{rad}^2}{\text{s}^2}\right] \quad (4.19)$$

$$\omega_2^2 = \frac{(m_1 m_2 k_2 + m_1 m_3 (k_1 + k_2) + m_2 m_3 k_1)}{2 m_1 m_2 m_3} + \frac{\sqrt{(m_1 m_2 k_2 + m_1 m_3 (k_1 + k_2) + m_2 m_3 k_1)^2 - 4(m_1 m_2 m_3)((m_1 + m_2 + m_3)k_1 k_2)}}{2 m_1 m_2 m_3}, \quad \left[\frac{\text{rad}^2}{\text{s}^2}\right] \quad (4.20)$$

where ω_0 is the rigid body mode of the system and ω_1 and ω_2 are the flexible modes of the system. A rigid body mode occurs when the system moves without the masses translating with respect to each other. Because of this, the vibration of this mode has a frequency of $\omega_0 = 0 \frac{\text{rad}}{\text{s}}$. This is what would occur if there were rigid connections between the three masses instead of springs. However, with flexibility added to the three-mass system because of the springs, there are also two flexible modes where the masses do move in relation to each other. These flexible modes occur at the frequencies ω_1 and ω_2 .

Upon closer inspection of Equation (4.17) it may be observed that these equations can be simplified. Dividing both sides of Equation (4.17) by $m_1 m_2 m_3$ results in

$$\omega^2[\omega^4 - (\frac{k_2}{m_3} + \frac{(k_1 + k_2)}{m_2} + \frac{k_1}{m_1})\omega^2 + (\frac{k_1 k_2}{m_2 m_3} + \frac{k_1 k_2}{m_1 m_3} + \frac{k_1 k_2}{m_1 m_2})] = 0, \quad (4.21)$$

where certain groups of parameters appear. These parameter groupings are defined as

$$a_1 = \frac{k_1}{m_1}, \quad (4.22)$$

$$a_2 = \frac{k_1}{m_2}, \quad (4.23)$$

$$a_3 = \frac{k_2}{m_2}, \quad (4.24)$$

$$a_4 = \frac{k_2}{m_3}, \quad (4.25)$$

which means that Equation (4.21) can be rewritten as

$$\omega^2[\omega^4 - (a_1 + a_2 + a_3 + a_4)\omega^2 + (a_2 a_4 + a_1 a_4 + a_1 a_3)] = 0. \quad (4.26)$$

Two non-dimensional parameters can also be defined to relate the masses to each other, which are given as

$$\alpha = \frac{m_1}{m_2}, \quad (4.27)$$

$$\beta = \frac{m_2}{m_3}, \quad (4.28)$$

which allows the following equalities to be defined:

$$a_2 = a_1\alpha, \quad (4.29)$$

$$a_4 = a_3\beta. \quad (4.30)$$

These non-dimensional parameters are useful as they will also apply to the viscous damping coefficients. Once damping is reintroduced to the system, utilizing α and β will lower the number of parameters needed to specify the damped transfer functions of the system. This is seen in section 4.3.

The determinant can now be rewritten as

$$\omega^2[\omega^4 - ((1 + \alpha)a_1 + (1 + \beta)a_3)\omega^2 + ((1 + \beta + \alpha\beta)a_1a_3)] = 0, \quad (4.31)$$

where the undamped natural frequencies are

$$\omega_0^2 = 0, \quad \left[\frac{\text{rad}^2}{\text{s}^2}\right] \quad (4.32)$$

$$\omega_1^2 = \frac{((1 + \alpha)a_1 + (1 + \beta)a_3)}{2} - \frac{\sqrt{((1 + \alpha)a_1 + (1 + \beta)a_3)^2 - 4((1 + \beta + \alpha\beta)a_1a_3)}}{2}, \left[\frac{\text{rad}^2}{\text{s}^2}\right] \quad (4.33)$$

$$\omega_2^2 = \frac{((1 + \alpha)a_1 + (1 + \beta)a_3)}{2} + \frac{\sqrt{((1 + \alpha)a_1 + (1 + \beta)a_3)^2 - 4((1 + \beta + \alpha\beta)a_1a_3)}}{2}, \left[\frac{\text{rad}^2}{\text{s}^2}\right] \quad (4.34)$$

Any motion of the three-mass system can be written as a linear combination of the three modes. That is

$$\vec{X}(t) = \vec{X}_0 x(\omega_0 t) + \vec{X}_1 x(\omega_1 t) + \vec{X}_2 x(\omega_2 t), \quad (4.35)$$

where $\vec{X}(t)$ is the vector describing the total motion of the three masses. Observe that \vec{X}_j is the eigenvector associated with the j^{th} mode.

These modes correspond to the undamped natural frequencies. Since this work is interested in examining cases that are lightly-damped, the assumption is made that the damping ratio ζ is small and falls in the range

$$0 \leq \zeta \leq 0.3, \quad (4.36)$$

which allows the approximation

$$\omega_d \approx \omega_n, \quad (4.37)$$

where ω_d is the damped natural frequency. This observation is necessary, as system damping will shift the natural frequency. However, for very-lightly-damped systems this change is negligible. For this work, the system damping ratios ζ_1 and ζ_2 are defined to be equal to 0.1, which in turn sets the values of the viscous damping coefficients c_1 and c_2 . Note that this is the damping ratio for the modes of the system and is not the closed-loop damping ratio, which will be studied in section 4.4.

4.3 Transfer Function Representation

The dynamics of the three-mass system can also be represented using transfer functions. This is done by taking the Laplace transforms of Equations (4.1) through (4.3), given as

$$m_1 s^2 X_1 = F + k_1(X_2 - X_1) + c_1(sX_2 - sX_1), \quad (4.38)$$

$$m_2 s^2 X_2 = -k_1(X_2 - X_1) - c_1(sX_2 - sX_1) + k_2(X_3 - X_2) + c_2(sX_3 - sX_2), \quad (4.39)$$

$$m_3 s^2 X_3 = -k_2(X_3 - X_2) - c_2(sX_3 - sX_2), \quad (4.40)$$

where it is assumed that the initial conditions for all three masses are zero.

Rearranging Equations (4.38) through (4.40) in terms of the signals X_i gives

$$(m_1 s^2 + c_1 s + k_1)X_1 = F + (c_1 s + k_1)X_2, \quad (4.41)$$

$$(m_2 s^2 + (c_1 + c_2)s + (k_1 + k_2))X_2 = (c_1 s + k_1)X_1 + (c_2 s + k_2)X_3, \quad (4.42)$$

$$(m_3 s^2 + c_2 s + k_2)X_3 = (c_2 s + k_2)X_2, \quad (4.43)$$

which can be solved backwards from the third mass to find the transfer functions that describe the motion of each mass in relation to each other.

The transfer function from the second mass to the third mass is

$$\frac{X_3}{X_2} = \frac{(c_2 s + k_2)}{(m_3 s^2 + c_2 s + k_2)}, \quad (4.44)$$

which can be substituted into Equation (4.42). This places Equation (4.42) only in terms of the first mass and the second mass. Rearranging the result gives the corresponding transfer function, written as

$$\frac{X_2}{X_1} = \frac{(c_1 s + k_1)(m_3 s^2 + c_2 s + k_2)}{m_2 m_3 s^4 + (m_2 c_2 + m_3(c_1 + c_2))s^3 + (m_2 k_2 + m_3(k_1 + k_2) + c_1 c_2)s^2 + (k_1 c_2 + k_2 c_1)s + k_1 k_2}, \quad (4.45)$$

and repeating this procedure gives the transfer function from the input to the first mass

$$\frac{X_1}{F} = \frac{m_2 m_3 s^4 + (m_2 c_2 + m_3(c_1 + c_2))s^3 + (m_2 k_2 + m_3(k_1 + k_2) + c_1 c_2)s^2 + (k_1 c_2 + k_2 c_1)s + k_1 k_2}{s^2(m_1 m_2 m_3 s^4 + (m_1 m_2 c_2 + m_1 m_3(c_1 + c_2) + m_2 m_3 c_1)s^3 + (m_1 m_2 k_2 + m_1 m_3(k_1 + k_2) + (m_1 + m_2 + m_3)c_1 c_2 + m_2 m_3 k_1)s^2 + ((m_1 + m_2 + m_3)(k_1 c_2 + k_2 c_1))s + (m_1 + m_2 + m_3)k_1 k_2)}. \quad (4.46)$$

Observe that the denominator of Equation (4.46) is similar to the determinant found in Equation (4.17). This is not surprising as it is known that the eigenvalues of

the system correspond to the locations of the system poles. In fact, the characteristic equation can be rewritten as

$$s^2(s^2 + 2\zeta_1\omega_1 + \omega_1^2)(s^2 + 2\zeta_2\omega_2 + \omega_2^2) = 0, \quad (4.47)$$

where the natural frequencies ω_1 and ω_2 are found from Equations (4.19) and (4.20). Equation (4.47) is the general form of the characteristic equation for a three-mass system that possesses a rigid body mode and two flexible modes. By matching the coefficients of Equation (4.47) with the denominator of Equation (4.46), the values of c_1 and c_2 can be calculated so as to obtain the desired damping ratios ζ_1 and ζ_2 .

Alternatively, the equations of motion can be written in a simplified form. This is done using the non-dimensional parameters α and β that were defined in Equations (4.27) and (4.28). Since this system is damped, the following parameter groups are defined

$$b_1 = \frac{c_1}{m_1}, \quad (4.48)$$

$$b_3 = \frac{c_2}{m_2}, \quad (4.49)$$

where the parameter groups b_2 and b_4 are

$$b_2 = b_1\alpha, \quad (4.50)$$

$$b_4 = b_3\beta. \quad (4.51)$$

Note that by using α and β in describing this system the number of required parameter groups has dropped to six, thus simplifying the resultant equations. If these two non-dimensional parameters were not used then the equations would require eight different parameter groups. The damped equations of motion can now be given as

$$\ddot{x}_1 = \frac{F}{m_1} + a_1(x_2 - x_1) + b_1(\dot{x}_2 - \dot{x}_1), \quad (4.52)$$

$$\ddot{x}_2 = -\alpha a_1(x_2 - x_1) - \alpha b_1(\dot{x}_2 - \dot{x}_1) + a_3(x_3 - x_2) + b_3(\dot{x}_3 - \dot{x}_2), \quad (4.53)$$

$$\ddot{x}_3 = -\beta a_3(x_3 - x_2) - \beta b_3(\dot{x}_3 - \dot{x}_2), \quad (4.54)$$

with the damped transfer functions

$$\frac{X_3}{X_2} = \frac{\beta b_3 s + \beta a_3}{s^2 + \beta b_3 s + \beta a_3}, \quad (4.55)$$

$$\frac{X_2}{X_1} = \frac{(\alpha b_1 s + \alpha a_1)(s^2 + \beta b_3 s + \beta a_3)}{s^4 + (\alpha b_1 + (1 + \beta)b_3)s^3 + (\alpha a_1 + (1 + \beta)a_3 + \alpha\beta b_1 b_3)s^2 + \alpha\beta(a_1 b_3 + a_3 b_1)s + \alpha\beta a_1 a_3}, \quad (4.56)$$

$$\frac{X_1}{F} = \frac{(\frac{1}{m_1})(s^4 + (\alpha b_1 + (1 + \beta)b_3)s^3 + (\alpha a_1 + (1 + \beta)a_3 + \alpha\beta b_1 b_3)s^2 + \alpha\beta(a_1 b_3 + a_3 b_1)s + \alpha\beta a_1 a_3)}{s^2(s^4 + ((1 + \alpha)b_1 + (1 + \beta)b_3)s^3 + ((1 + \alpha)a_1 + (1 + \beta)a_3 + (1 + \beta + \alpha\beta)b_1 b_3)s^2 + (1 + \beta + \alpha\beta)(a_1 b_3 + a_3 b_1)s + (1 + \beta + \alpha\beta)a_1 a_3)}, \quad (4.57)$$

where the characteristic equation can still be represented by Equation (4.47).

The transfer function of Equation (4.57) describes the relationship between the input force and the motion of the first mass. Observe that this transfer function has six open-loop poles and four open-loop zeros, whose locations can be plotted in the complex plane. This generates a pole-zero map, as seen in Figure 4.2 for the undamped case, and in Figure 4.3 for the lightly-damped case.

Note that the undamped system will have all its poles and zeros directly on the imaginary axis, while any damping added to the system will bend the poles and zeros into the Left Half Plane (LHP). Because of this, the system is both stable and minimum-phase. However, it is still crucial to be very careful when incorporating feedback control for this system, as it is possible to induce instability.

The frequency response of Equation (4.57) can also be shown by using a Bode plot. This is done in Figure 4.4. Observe that this system possesses two resonant peaks, as well as two anti-resonances. These correspond to the poles and zeros of Equation (4.57). Note that the location of the anti-resonances is a function of not only the modes of the system, but also its masses. If the ratio between the masses changes, so will the location of the system zeros. This will affect the dynamics of the system.

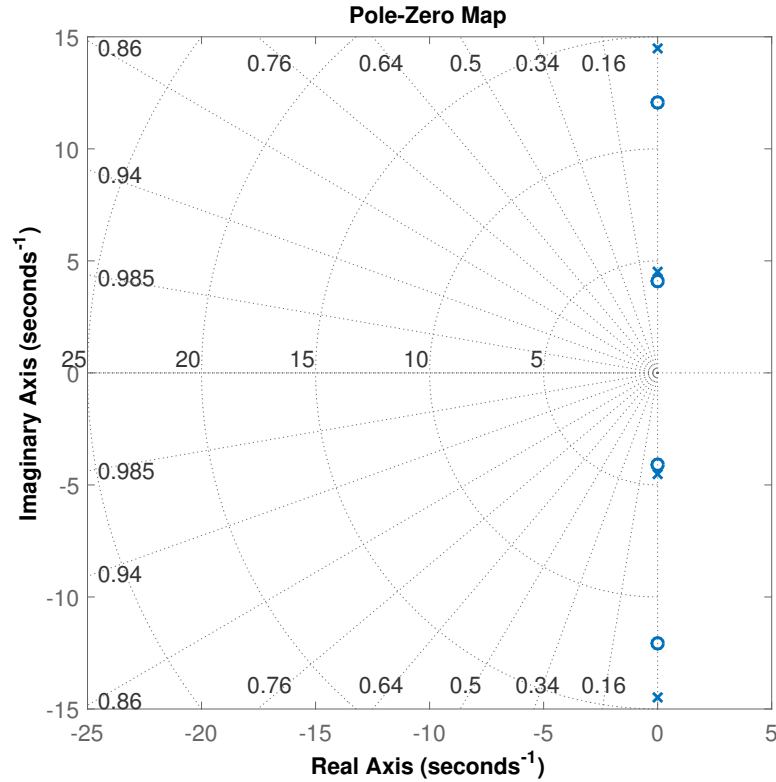


Figure 4.2. Pole-Zero map of the undamped open-loop system.

4.4 Closed-Loop Control of the Three-Mass System

In order to provide reliable and robust motion of the three-mass system, closed-loop control is required. This task requires that the response of the first mass be fed back into a feedback controller so as to create a closed-loop system. Note that the second and third masses are not used in the feedback controller for this application. This decision is made in order to avoid the more complicated problem of non-collocated control.

A feedforward controller is also applied to the three-mass system. This is designed to be the inverse of the plant transfer function, given as

$$C_{FF} = s^2 G_{p1}^{-1}, \quad (4.58)$$

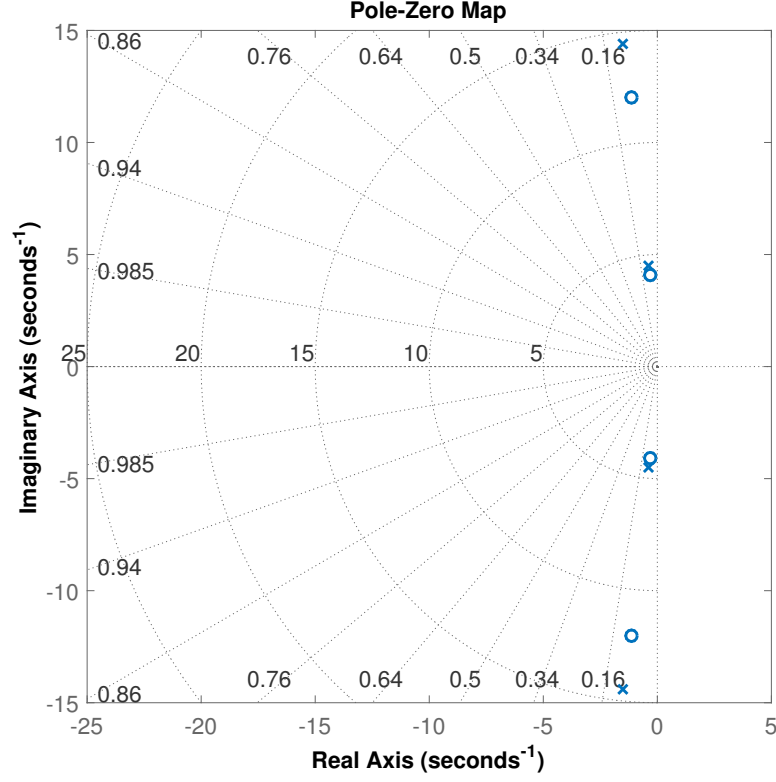


Figure 4.3. Pole-Zero map of the lightly-damped open-loop system.

where G_{p1} is the transfer function of Equation (4.57). Observe that the two poles of the rigid body mode have been removed from the feedforward controller. This is a crucial step that is required in order to make Equation (4.57) bi-proper, which then allows it to be inverted. However, this also means that the reference signal that is fed forward will need to be the acceleration reference and not the position reference.

The closed-loop system of Figure 4.5 may be analyzed by deriving the closed-loop transfer function. This is done as follows:

$$X_1 = G_{p1}(C_{FF}R_{acc} + C_{FB}E) = G_{p1}C_{FF}R_{acc} + G_{p1}C_{FB}R_{pos} - G_{p1}C_{FB}X_1, \quad (4.59)$$

$$X_1 = \frac{G_{p1}C_{FF}}{1 + G_{p1}C_{FB}}R_{acc} + \frac{G_{p1}C_{FB}}{1 + G_{p1}C_{FB}}R_{pos}, \quad (4.60)$$

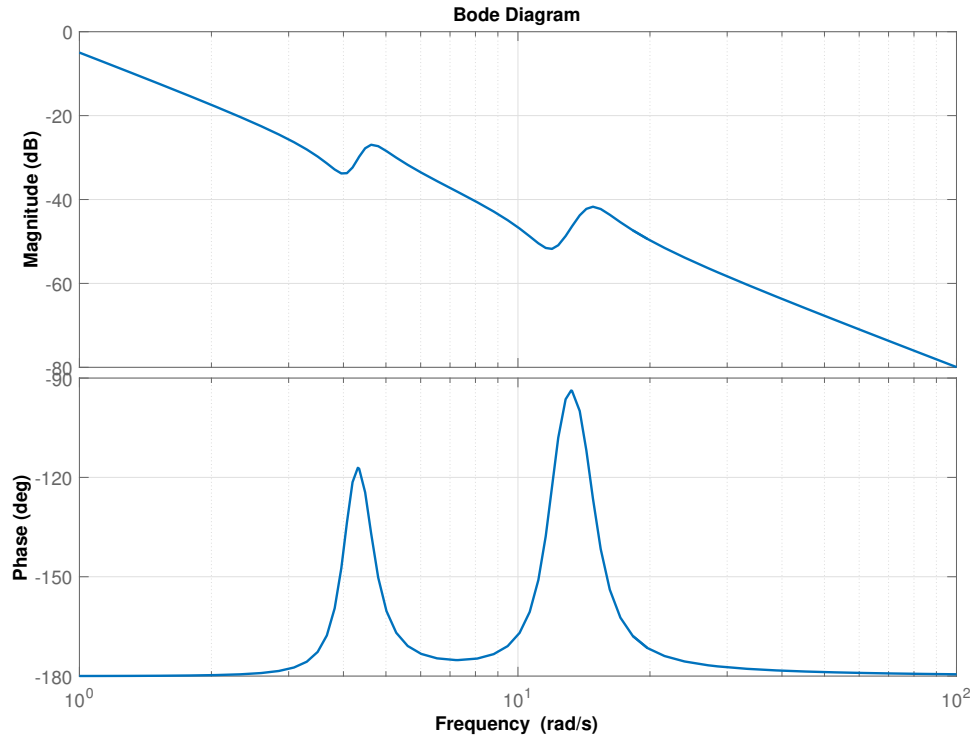


Figure 4.4. Bode plot of the transfer function relating the input to the first mass.

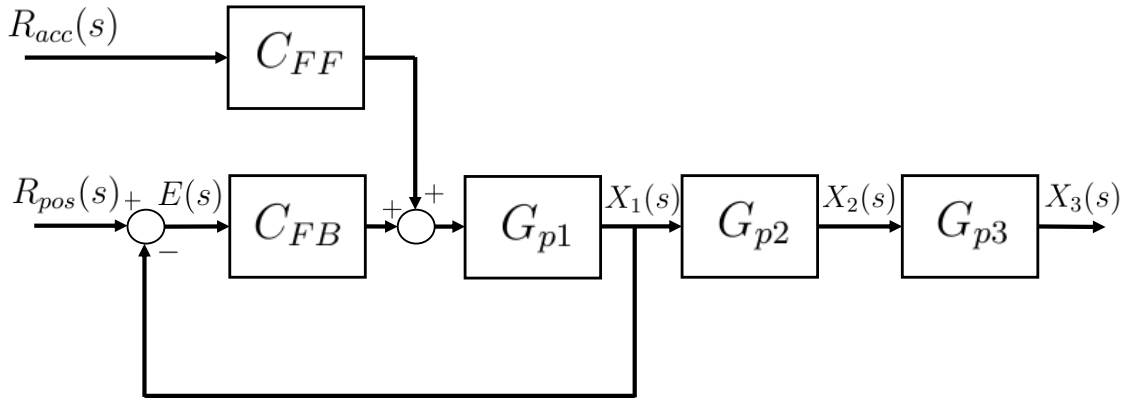


Figure 4.5. Block diagram of feedforward and feedback control of the three-mass system.

$$X_2 = \left(\frac{G_{p1}C_{FF}}{1 + G_{p1}C_{FB}} R_{acc} + \frac{G_{p1}C_{FB}}{1 + G_{p1}C_{FB}} R_{pos} \right) G_{p2}, \quad (4.61)$$

$$X_3 = \left(\frac{G_{p1}C_{FF}}{1 + G_{p1}C_{FB}} R_{acc} + \frac{G_{p1}C_{FB}}{1 + G_{p1}C_{FB}} R_{pos} \right) G_{p2}G_{p3}, \quad (4.62)$$

where the Laplace arguments have been neglected so as to simplify the presentation. Note that the relationship between the acceleration reference and the position reference is given as

$$R_{pos} = \frac{R_{acc}}{s^2}. \quad (4.63)$$

The stability of the entire system is ensured by finding a feedback controller that stabilizes the closed-loop of the first mass, as both Equations (4.56) and (4.55) are stable. Observe that setting up the controller in this manner is analogous to using motor feedback on the two-link robotic manipulator.

A second controller architecture is also applied to the three-mass system. This configuration is shown in Figure 4.6, where the controller is designed so as to emulate the computed torque controller of the robot. However, there is an important distinction here. This controller is not truly a computed torque controller, as it is not linearizing the system. The feedforward element in this configuration is merely attempting to cancel out the dynamics of the first mass. However, this chapter will refer to the closed-loop system of Figure 4.6 as a computed torque controller as a matter of convenience, not because they are equivalent.

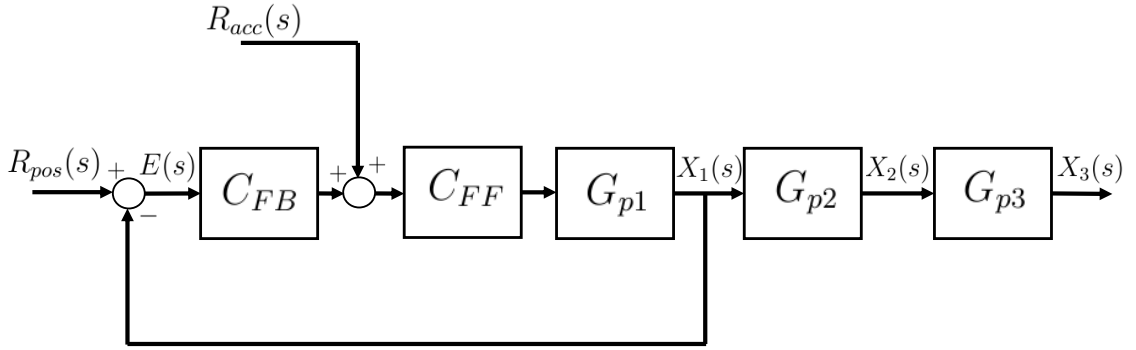


Figure 4.6. Block diagram of computed torque control of the three-mass system.

The position error transfer function may be written as

$$E = R_{pos} - X_1 = \frac{1}{1 + G_{p1}C_{FB}}R_{pos} - \frac{G_{p1}C_{FF}}{1 + G_{p1}C_{FB}}R_{acc}, \quad (4.64)$$

where the terms of the numerator can be split up to show the sensitivity of both the feedback and feedforward controllers. Several things can be seen from this result. First, if the feedforward controller perfectly models the dynamics of the system plant, then the numerator of Equation (4.64) will drop to zero. That is, if a perfect model is used then the closed-loop system for the first mass will exhibit perfect tracking. However, this motion may still induce residual vibrations in the motion of the second and third masses. Another observation that can be made is that the first mass will track the reference better if the feedback controller uses higher control gains, thus increasing the magnitude of the denominator in Equation (4.64). As will be seen later in this section, this might not result in improvements in performance for the other masses.

The computed torque architecture can be similarly analyzed. This is done by finding the transfer function for the closed-loop system as follows:

$$\begin{aligned} X_1 = G_{p1}C_{FF}(R_{acc} + C_{FB}E) = G_{p1}C_{FF}R_{acc} \\ + G_{p1}C_{FF}C_{FB}R_{pos} - G_{p1}C_{FF}C_{FB}X_1, \end{aligned} \quad (4.65)$$

$$X_1 = \frac{G_{p1}C_{FF}}{1 + G_{p1}C_{FF}C_{FB}}R_{acc} + \frac{G_{p1}C_{FF}C_{FB}}{1 + G_{p1}C_{FF}C_{FB}}R_{pos}, \quad (4.66)$$

$$X_2 = \left(\frac{G_{p1}C_{FF}}{1 + G_{p1}C_{FF}C_{FB}}R_{acc} + \frac{G_{p1}C_{FF}C_{FB}}{1 + G_{p1}C_{FF}C_{FB}}R_{pos} \right) G_{p2}, \quad (4.67)$$

$$X_3 = \left(\frac{G_{p1}C_{FF}}{1 + G_{p1}C_{FF}C_{FB}}R_{acc} + \frac{G_{p1}C_{FF}C_{FB}}{1 + G_{p1}C_{FF}C_{FB}}R_{pos} \right) G_{p2}G_{p3}, \quad (4.68)$$

As before, the position error can be derived as

$$E = R_{pos} - X_1 = \frac{1}{1 + G_{p1}C_{FF}C_{FB}}R_{pos} - \frac{G_{p1}C_{FF}}{1 + G_{p1}C_{FF}C_{FB}}R_{acc}, \quad (4.69)$$

where, as before, if the feedforward model is perfect then the position error will be zero. Also, an increase in the feedback gains will still lower the tracking error. The important difference between these two controller architectures is the inclusion of

the feedforward controller into the feedback loop, which will affect the characteristic equation of the closed-loop system.

4.4.1 Frequency Response of the Closed-Loop System

The main interest of this work concerns how to bring together all the different pieces of this vibration problem. That is, what is the interplay between the input shaping, the feedforward control, and the feedback control? To begin this study, it is most natural to start in the frequency domain, as this is where the command-shaped profiles are constructed and where this work originally began.

There are two different kinds of feedback controllers that are applied to the three-mass system: Proportional-Derivative (PD) Control and Lead-Lag Control. PD controllers are very common in practice, as they are relatively simple and easy to implement, yet very effective. The general form for a PD controller can be represented in the Laplace domain as

$$C_{pd} = K_p + K_d s = K_c \left(\frac{1}{z_{pd}} s + 1 \right), \quad (4.70)$$

where K_c is the overall control gain and z_{pd} is a controller zero located on the real axis. The frequency response of a PD controller can be seen by plotting the Bode plot, as seen in Figure 4.7.

Since this is a minimum-phase system it is possible to study some of the system characteristics using the open-loop Bode plot that consists of the PD controller multiplied by the system plant. An example of this can be seen in Figure 4.8, where the control gain $K_c = 20$ and the controller zero $z_{pd} = -30$.

The stability margins of the system can be examined using Figure 4.8. This shows that the gain margin is infinite, as there is no phase crossover frequency. This means that the controller gain K_c may be any positive value from zero to infinity. On the other hand, the phase margin is finite, but is always positive for any gain crossover frequency. This shows that regardless of the location of the controller zero z_{pd} or the

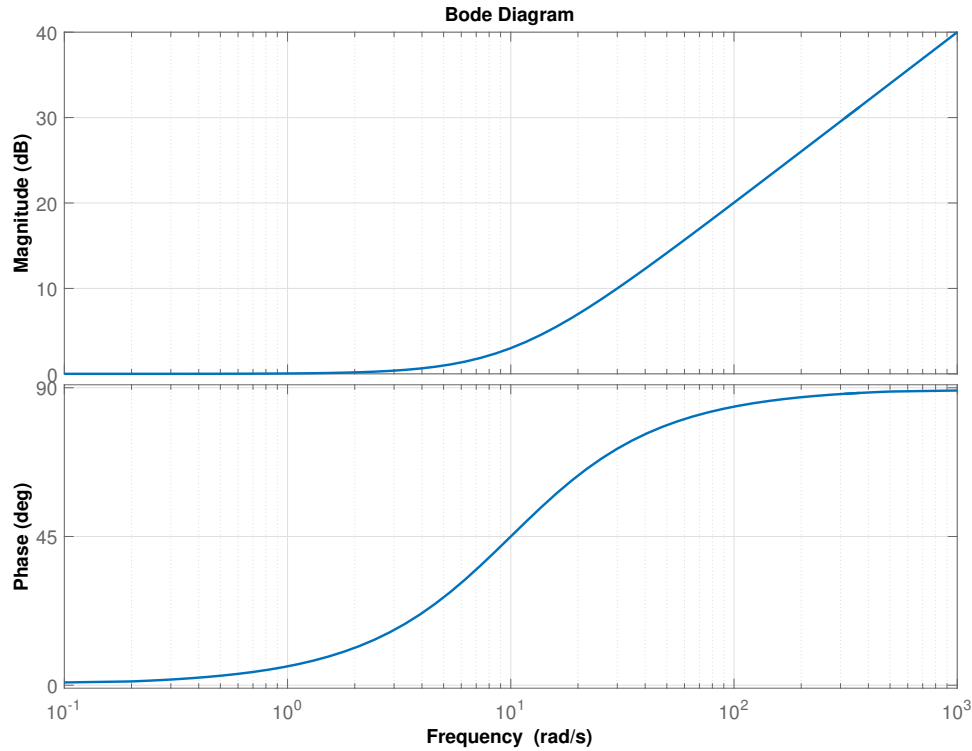


Figure 4.7. Example Bode plot of a PD controller.

controller gain K_c , the PD-controlled system is always stable. This result is consistent for any PD controller whose control gain K_c is strictly positive and whose controller zero is in the LHP.

As can be seen in Figure 4.7, the PD controller amplifies the high-frequencies of a signal. This means that if there are any high-frequency components present, such as some types of noise, then those frequencies will be magnified. In order to help alleviate this issue, the Lead compensator was developed. This controller adds an extra pole to its transfer function in order to flatten out the magnitude spectra at high frequencies. An example of the Bode plot for a Lead compensator can be seen in Figure 4.9. Note that the name of this controller comes from the fact that it adds phase lead to the system, which appears as a bump in the phase.

A similar controller is known as the Lag compensator, which adds phase lag to the system. An example can be seen in Figure 4.10. Here the controller will magnify

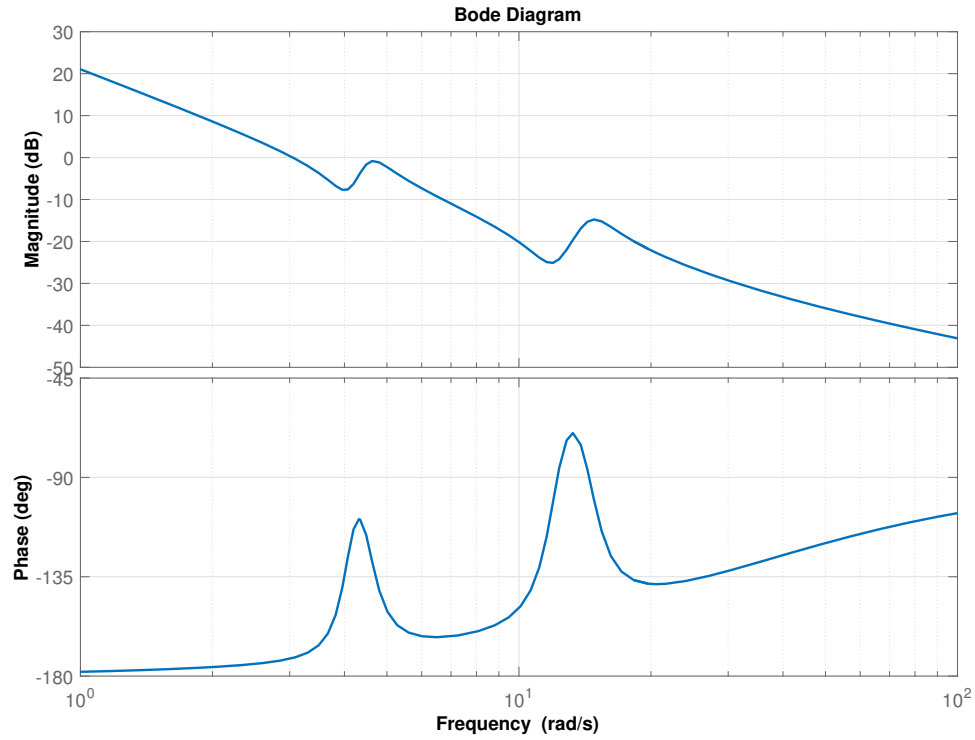


Figure 4.8. Bode plot of the open-loop transfer function for the PD controlled three-mass system.

the low frequencies and will decrease the phase. By combining both Lead and Lag compensators in series, the Lead-Lag compensator is created. Figure 4.11 shows an example of this controller.

The Lead-Lag compensator is of interest here as it will create a trough in the magnitude. This can be designed so that it is located at the natural frequencies of the system. Theoretically, this drop should help to attenuate these modes in the feedback loop and thus improve performance with respect to the level of residual vibration seen at the endpoint. This controller is designed as shown in Figure 4.12.

The Lead-Lag compensator takes the form

$$C_{lead-lag} = K_c \left(\frac{\left(\frac{1}{\omega_{z,lead}} \right) s + 1}{\left(\frac{1}{\omega_{p,lead}} \right) s + 1} \right) \left(\frac{\left(\frac{1}{\omega_{z,lag}} \right) s + 1}{\left(\frac{1}{\omega_{p,lag}} \right) s + 1} \right), \quad (4.71)$$

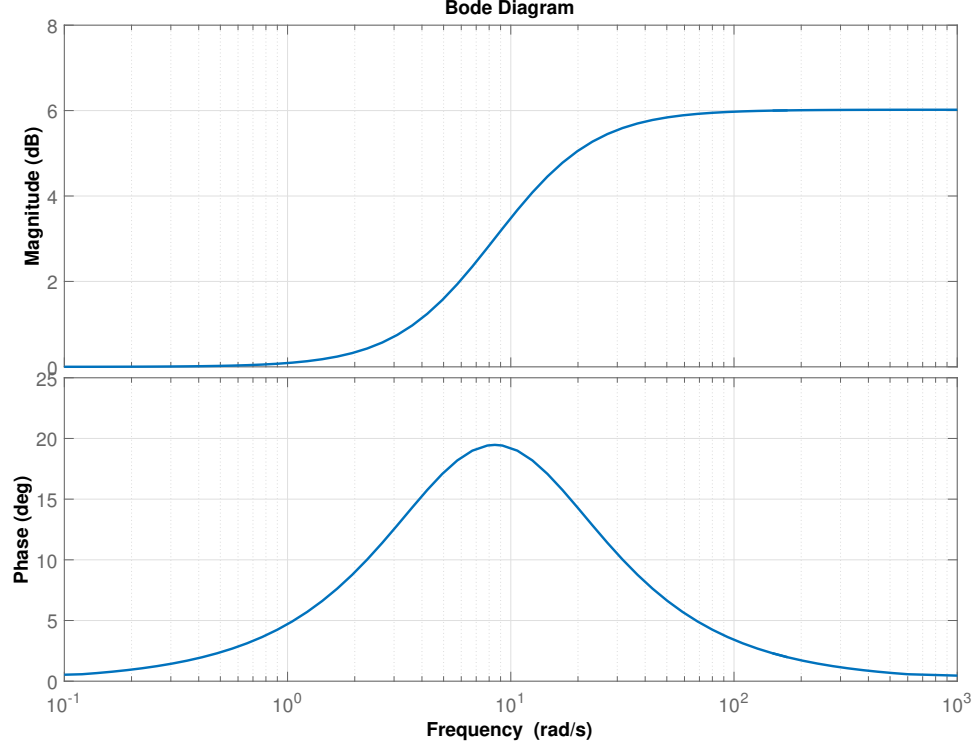


Figure 4.9. Bode plot of a Lead compensator.

where $\omega_{z,lead}$ and $\omega_{z,lag}$ are defined as

$$\omega_{z,lead} = \omega_{center} + \omega_{width}, \quad (4.72)$$

$$\omega_{z,lag} = \omega_{center} - \omega_{width}, \quad (4.73)$$

with ω_{center} as the center of the trough that is created in the magnitude, ω_{width} is the distance from the center frequency to the frequencies of the zeros in $\frac{\text{rad}}{\text{s}}$, and a is the ratio between the poles and zeros for both the Lead and Lag compensators. The ratio a is constrained to be equal for both a_{lead} and a_{lag} , given as

$$a_{lead} = \frac{1}{a_{lag}} = a, \quad (4.74)$$

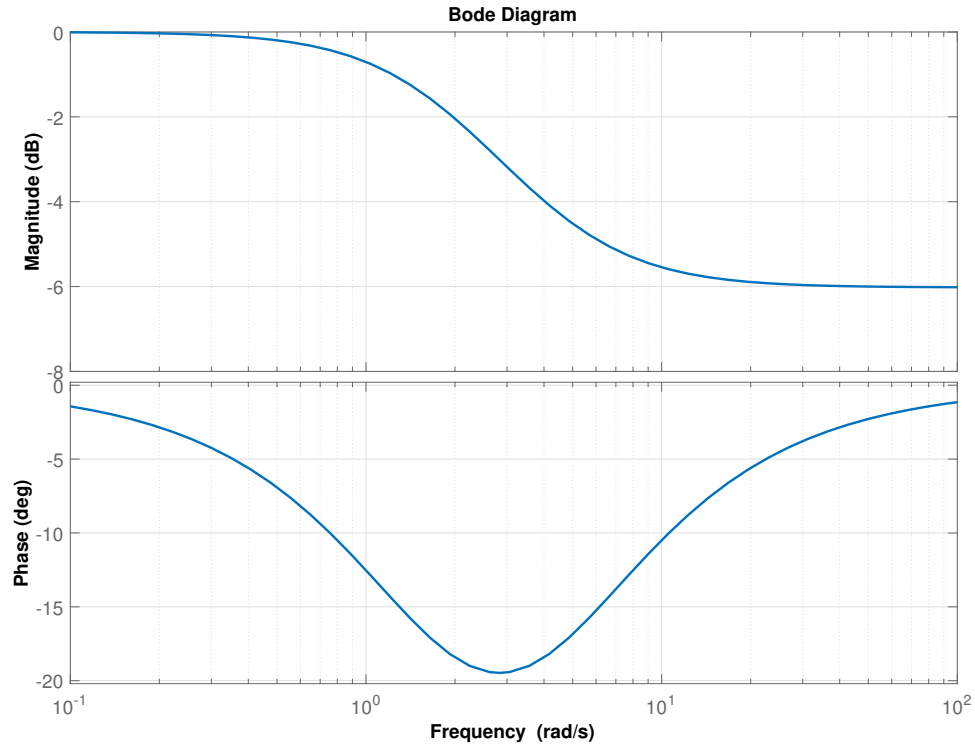


Figure 4.10. Bode plot of a Lag compensator.

where a must be greater than 1, by definition. This defines the relationships between the frequencies of the poles and zeros, which may be given as

$$\omega_{p,lead} = a_{lead}\omega_{z,lead} = a\omega_{z,lead}, \quad (4.75)$$

$$\omega_{p,lag} = a_{lag}\omega_{z,lag} = \frac{1}{a}\omega_{z,lag}, \quad (4.76)$$

While there are benefits in applying a Lead-Lag compensator, it comes at a trade-off. Observe that the phase lag of the Lag compensator will decrease the phase margin of the closed-loop system. This phase lag can be calculated mathematically by first deriving the phase lead of the Lead compensator, which is given as

$$\sin(\phi_{lead}) = \frac{a_{lead} - 1}{a_{lead} + 1}, \quad (4.77)$$

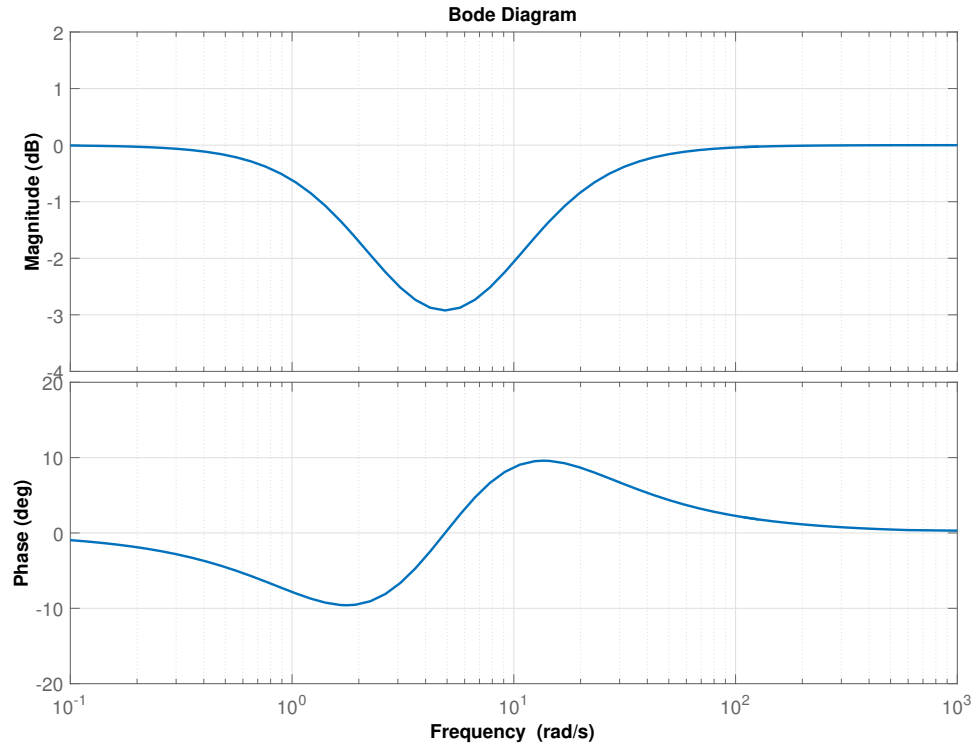


Figure 4.11. Bode plot of a Lead-Lag compensator.

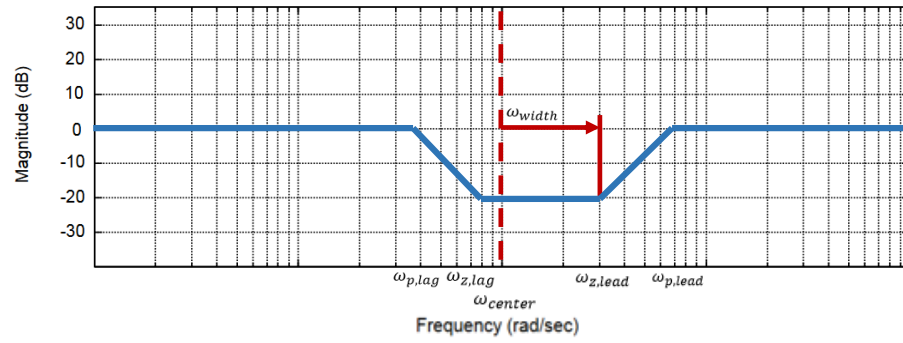


Figure 4.12. Magnitude plot of a Lead-Lag compensator.

where ϕ_{lead} is the phase added, while a_{lead} is the ratio of the pole and the zero of the Lead compensator. Due to the symmetry imposed on the Lead-Lag controller, the phase lag contributed by the Lag compensator can be given as

$$\phi_{lag} = -\phi_{lead}, \quad (4.78)$$

which is true only because the two compensators are symmetric, so the phase lead of the Lead compensator is equal to the phase lag of the Lag compensator.

While the PD controller is always stable when using positive controller gains K_c , this is not the case for a Lead-Lag controller. This is because the decrease in phase may destabilize the system, as seen in Figure 4.13. However, this issue can be easily remedied. Increasing the controller gain K_c will shift the gain crossover frequency, and the system bandwidth, to higher frequencies. This is accomplished by increasing the magnitude, as shown in Figure 4.14. At some point this will result in the phase margin becoming positive once again, thus regaining stability. The corresponding minimum values of the controller gains can be found using the root locus plot, as will be done in section 4.4.2.

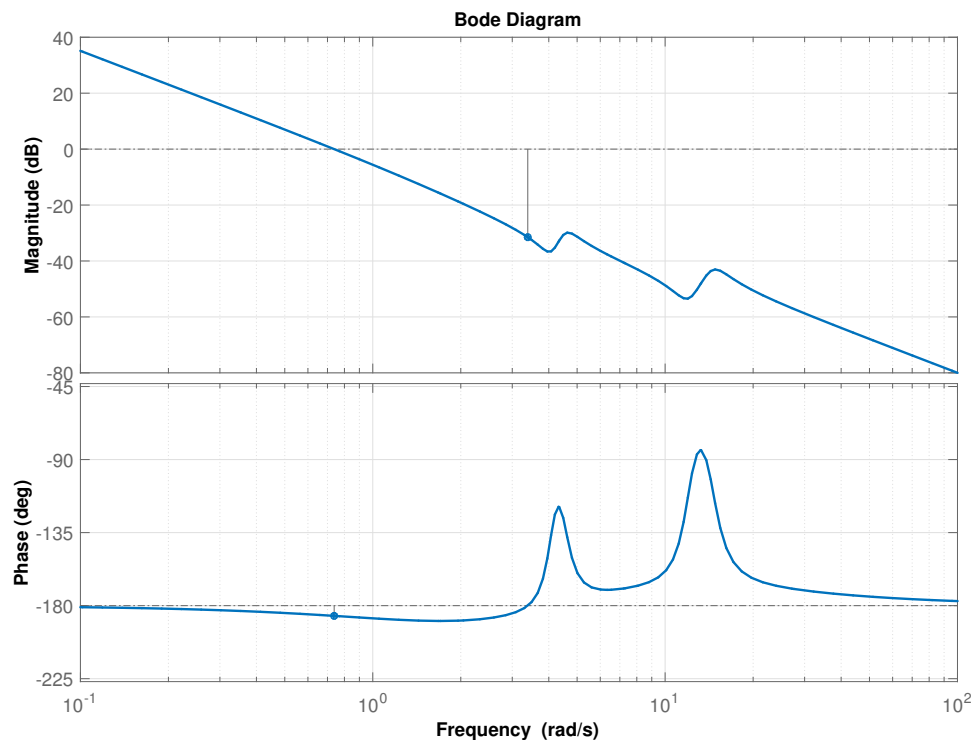


Figure 4.13. Example Bode plot of an unstable closed-loop three-mass system when using a Lead-Lag compensator with $K_c = 1$, $\omega_{center} = 5$, $\omega_{width} = 1$, and $a = 10$.

This is not the only way to study the frequency response of the system. In fact, by deriving the equivalent closed-loop system, more complete results may be obtained.

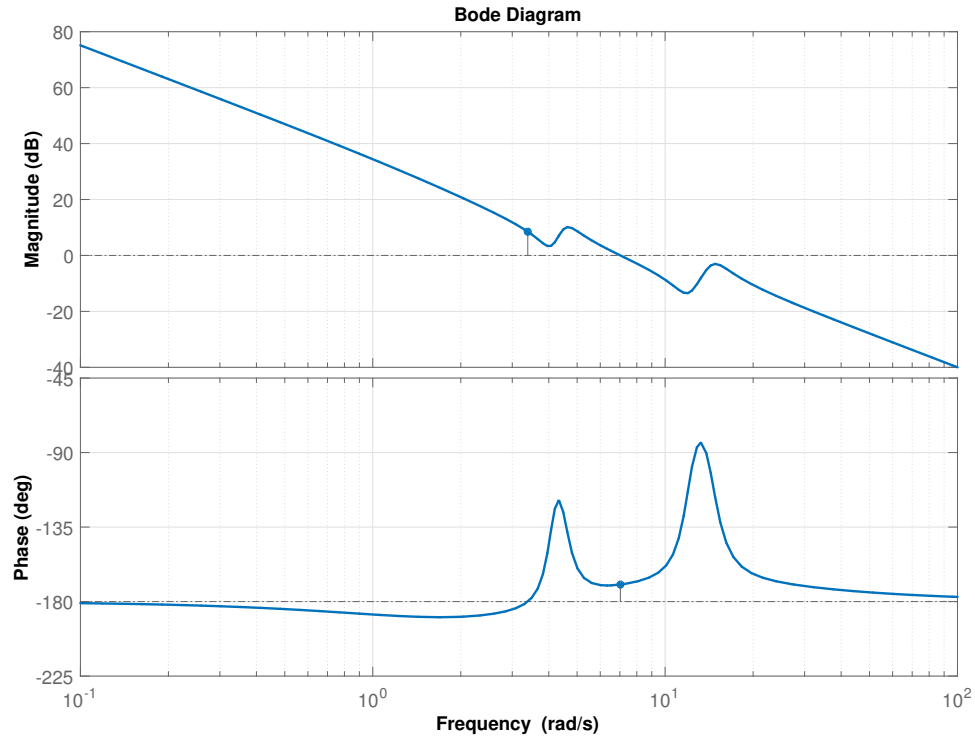


Figure 4.14. Example Bode plot of a stable closed-loop three-mass system when using a Lead-Lag compensator with $K_c = 250$, $\omega_{center} = 5$, $\omega_{width} = 1$, and $a = 10$.

The interest here is on the controller output, so the block diagram is rearranged as shown in Figure 4.15 and the closed-loop transfer function for this system is analyzed. Observe that the Feedforward controller is neglected here, as its frequency response will not change when the feedback controller is varied.

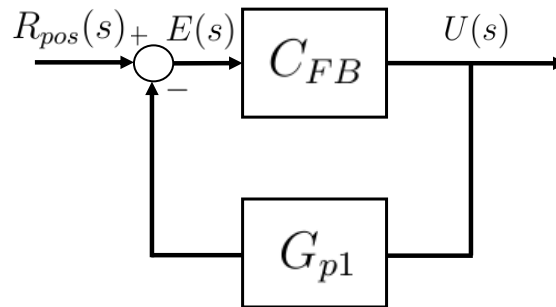


Figure 4.15. Rearranged block diagram of the feedback control loop.

The closed-loop transfer function that represents the block diagram shown in Figure 4.15 is

$$G_{FB,FF} = \frac{C_{FB}}{1 + C_{FB}G_{p1}}, \quad (4.79)$$

which can be used to find how the feedback controller behaves in the frequency domain. This is shown for several PD controllers in Figure 4.16, which has a controller zero at $z_{pd} = -30$ and several different values of controller gain K_c .

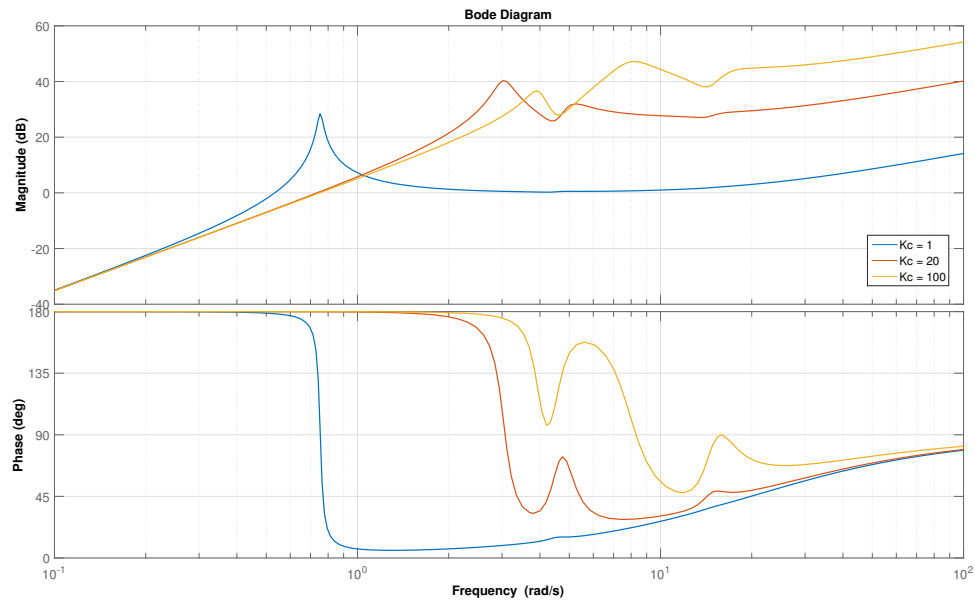


Figure 4.16. Bode plot of frequency response relating input to controller output with different values of K_c and $z_{pd} = -30$.

Figure 4.16 clearly shows that, as the controller gain is increased, the frequency response of the closed-loop system will change. In fact, with high values of the control gains, the feedback may inject energy back into the natural modes of the system. For some instances this may lead to higher levels of residual vibration.

In the same manner, the frequency response can be shown when the controller zero is varied. Here the control gain is set to be $K_c = 20$ and the zero z_{pd} is adjusted. Figure 4.17 shows the results. Here the changes in z_{pd} do not affect the shape of the frequency response nearly as much as changing the control gain does. However, there are a couple things to take note of in this result. First, the high frequencies are

amplified more if the zero is closer to the imaginary axis. This is not surprising, as the frequency where the PD controllers start to magnify the signal is a function of the zero location. Secondly, there is more variation in the magnitude at the resonant peaks of the closed-loop system for zeros that are further into the LHP. This is repeated in Figure 4.18 for a control gain $K_c = 100$, and the trends remain the same as a function of the zero location.

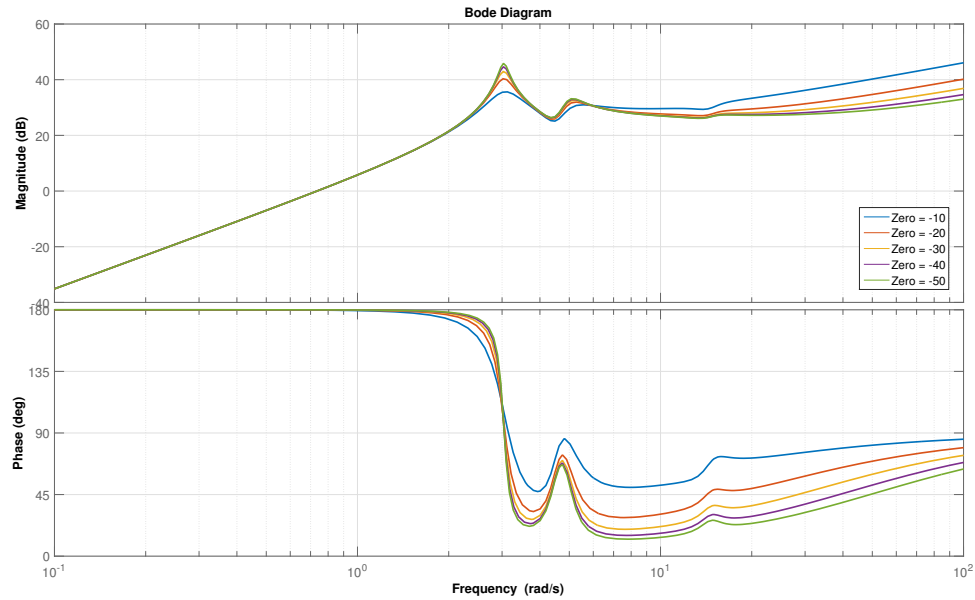


Figure 4.17. Bode plot of frequency response relating input to controller output with different values of z_{pd} when $K_c = 20$.

The same analysis can be performed for the Lead-Lag controller. Figure 4.19 shows the frequency response of a system with varied frequencies ω_{center} and ω_{width} . Note that both K_c and a are held constant. Observe how the Lead-Lag compensator does in fact prevent the excessive magnification of higher frequencies that is seen with PD control. Figure 4.19 also shows that there is more variation in the magnitude at the resonant peaks for the Lead-Lag controllers that attempt to attenuate both of the natural frequencies when compared to the Lead-Lag controllers that concentrate on the first mode only.

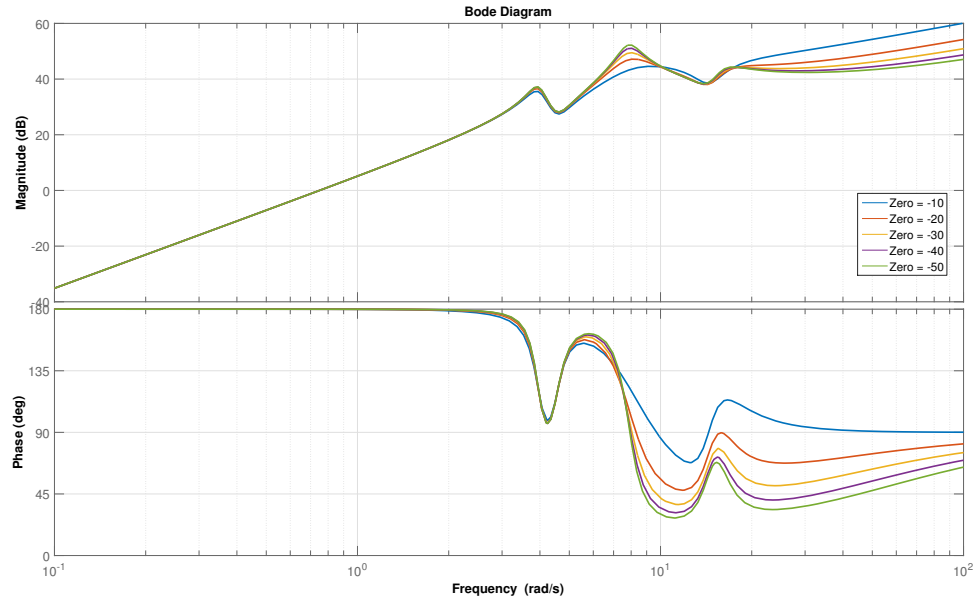


Figure 4.18. Bode plot of frequency response relating input to controller output with different values of z_{pd} when $K_c = 100$.

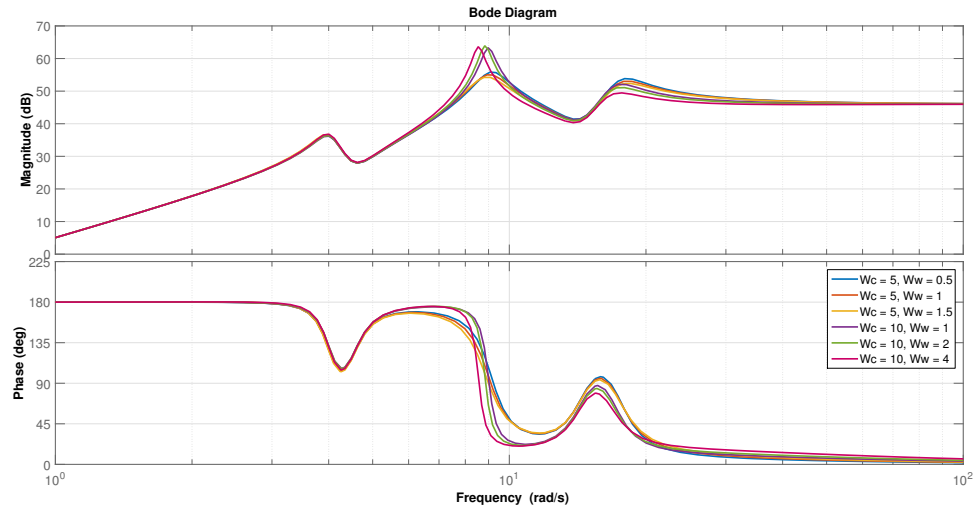


Figure 4.19. Bode plot of frequency response relating input to controller output for Lead-Lag controller with different frequencies.

In order to see how the Lead-Lag compensated system changes due to variations of the control gain, the specific case where $\omega_{center} = 5 \frac{\text{rad}}{\text{s}}$, $\omega_{width} = 1 \frac{\text{rad}}{\text{s}}$, and $a = 2$ is examined in greater detail. Figures 4.20 and 4.21 show these variations to different levels of the control gain K_c . Notice that the response does shift into higher

frequencies as K_c increases, and the overall energy of the signal is larger. However, there may be frequency bands where the magnitude of the controller output is lower even if the gain K_c is increased.

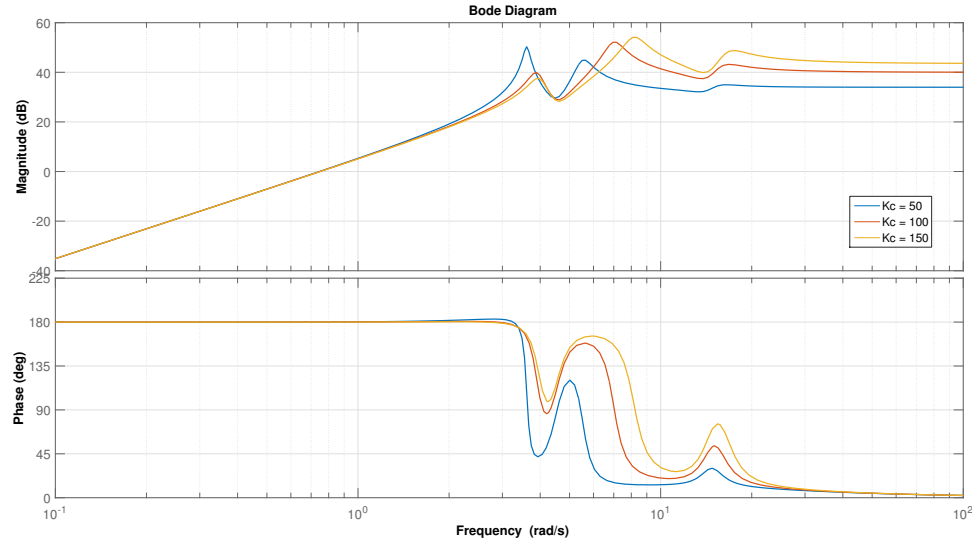


Figure 4.20. Bode plot of frequency response relating input to controller output for Lead-Lag controller with control gains of $K_c = 50, 100, 150$, with $\omega_{center} = 5 \frac{\text{rad}}{\text{s}}$, $\omega_{width} = 1 \frac{\text{rad}}{\text{s}}$, and $a = 2$.

The frequency response can also be examined for different values of the ratio a . Note that a defines the depth of the trough seen in the magnitude of the Lead-Lag Compensator. As in Figures 4.20 and 4.21, the other parameters of the Lead-Lag Compensator are set at $\omega_{center} = 5 \frac{\text{rad}}{\text{s}}$ and $\omega_{width} = 1 \frac{\text{rad}}{\text{s}}$, and in this case $K_c = 250$. Here it can be seen that the lower values of a have more variation in the magnitude spectra of their frequency response.

The frequency response of the feedforward controller can also be examined, as is shown in Figure 4.23. This is useful as it shows how the feedforward controller affects the frequency spectra of the input. Observe that the resonant and anti-resonant peaks of the system have been inverted. This means that the feedforward controller will amplify the frequencies just below resonance. Because of this, if there is parameter error that affects the location of the natural frequencies, the feedforward controller will perform worse if the actual natural frequency is less than the nominal natural

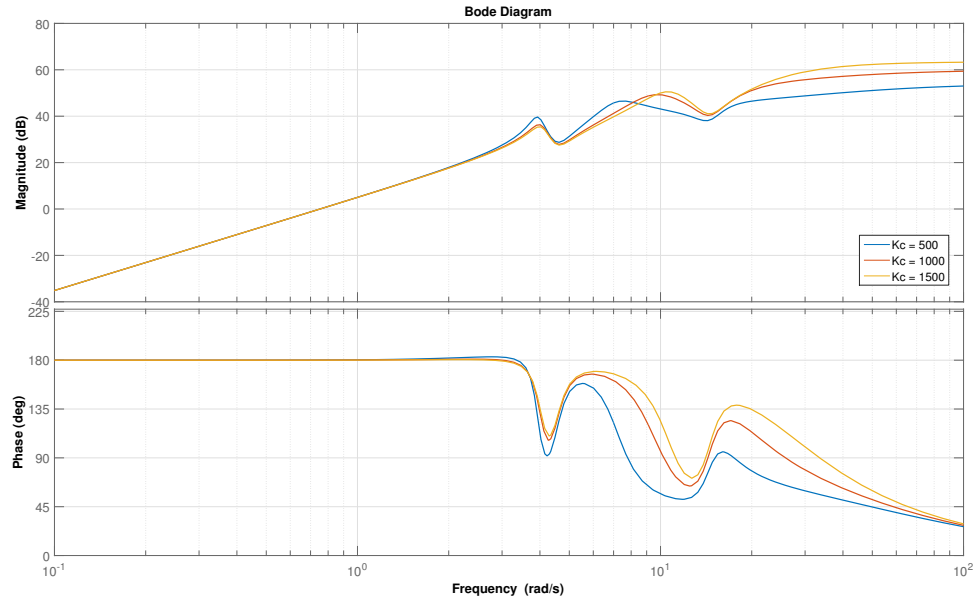


Figure 4.21. Bode plot of frequency response relating input to controller output for Lead-Lag controller with control gains of $K_c = 500, 1000, 1500$, with $\omega_{center} = 5 \frac{\text{rad}}{\text{s}}$, $\omega_{width} = 1 \frac{\text{rad}}{\text{s}}$, and $a = 2$.

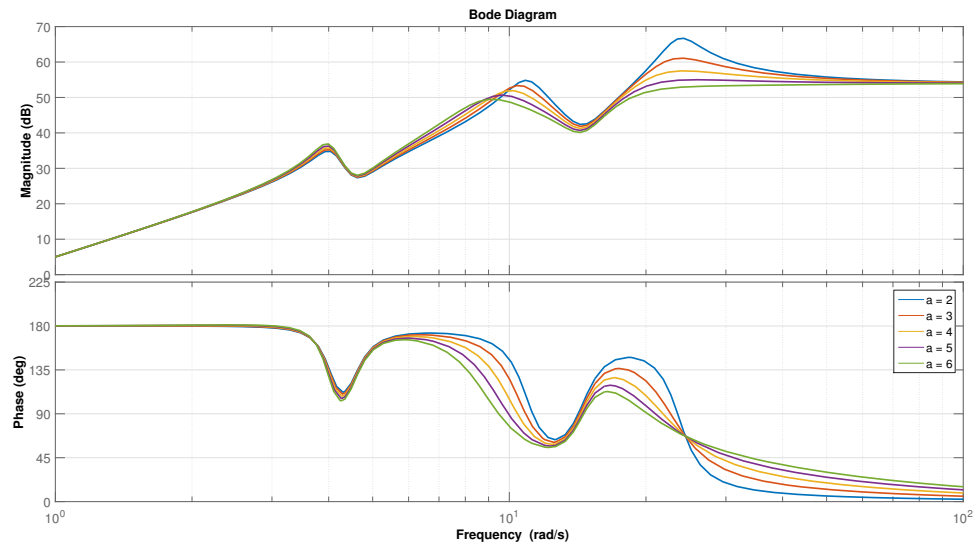


Figure 4.22. Bode plot of frequency response relating input to controller output for Lead-Lag controller with different Pole-Zero ratios when $\omega_{center} = 5 \frac{\text{rad}}{\text{s}}$, $\omega_{width} = 1 \frac{\text{rad}}{\text{s}}$, and $K_c = 250$.

frequency. This is apparent since it will inject more energy into the system modes

in this instance. This can be verified through the simulation results shown in section 4.6.

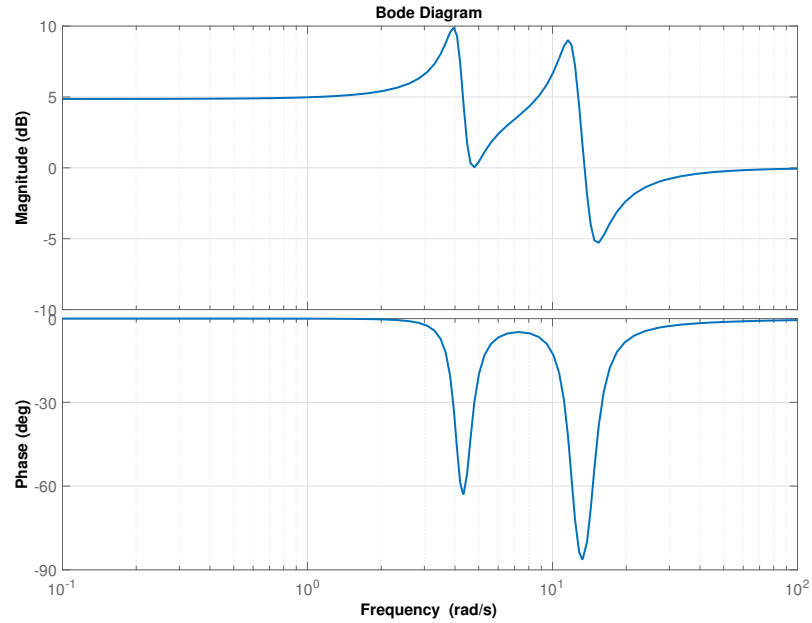


Figure 4.23. Bode plot of the feedforward controller.

In the case of the closed-loop system of Figure 4.6, the same kind of procedure can be applied. This will allow examination of the influence of the feedback controller on the energy present at the natural frequencies of the system when the feedforward controller is incorporated into the feedback loop. This is done by rearranging the closed-loop system into the form seen in Figure 4.24.

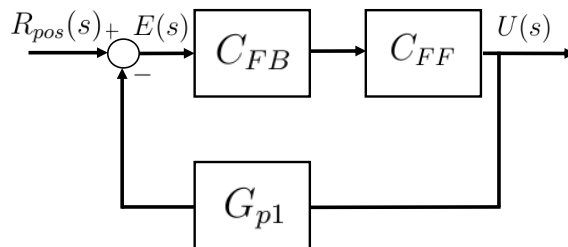


Figure 4.24. Rearranged block diagram of the feedback control loop for the computed torque configuration.

The closed-loop transfer function from the input signal to the controller output may be given as

$$G_{FB,CT} = \frac{C_{FB}C_{FF}}{1 + C_{FB}C_{FF}G_{p1}}, \quad (4.80)$$

which can be examined with different feedback controllers in order to study how it influences the energy at the natural frequencies. Note that this equation is very similar to Equation (4.79), but it is also significantly different. Here the feedforward controller has been incorporated into the feedback loop, which changes the response. Also, an observation may be made that Equations (4.79) and (4.80) look very similar to the sensitivity functions of the closed-loop system. In fact, this analysis could continue further by examining the sensitivity and complementary sensitivity transfer functions, as is common when undertaking control design in the frequency domain. Pursuing this further may allow the designer to directly construct a controller so as to minimize its contribution to the system at resonance. This is not performed here, as the interest of this work is on examining the influence of the feedback controller and not on finding the optimal controller for this closed-loop system.

Using Equation (4.80), the Bode plot representing the frequency response of the input to the controller output may be constructed. This will follow the same methodology as done on the closed-loop system that had the feedforward controller outside the feedback loop, starting with the PD controller and then continuing to the Lead-Lag controller.

Figure 4.25 is very similar to Figure 4.16. An observation may be made from this Bode plot that increasing the controller gains will bring up the magnitude of the controller output at high frequencies. However, the contribution of the feedforward controller may be seen in these responses, as the anti-resonant troughs and resonant peaks of the feedforward frequency response show up in this Bode plot. Notice also that as K_c increases from 20 to 100, the magnitude at the first mode actually decreases. This is significant as this does not appear in Figure 4.16 for the case with the feedforward controller outside of the feedback loop.

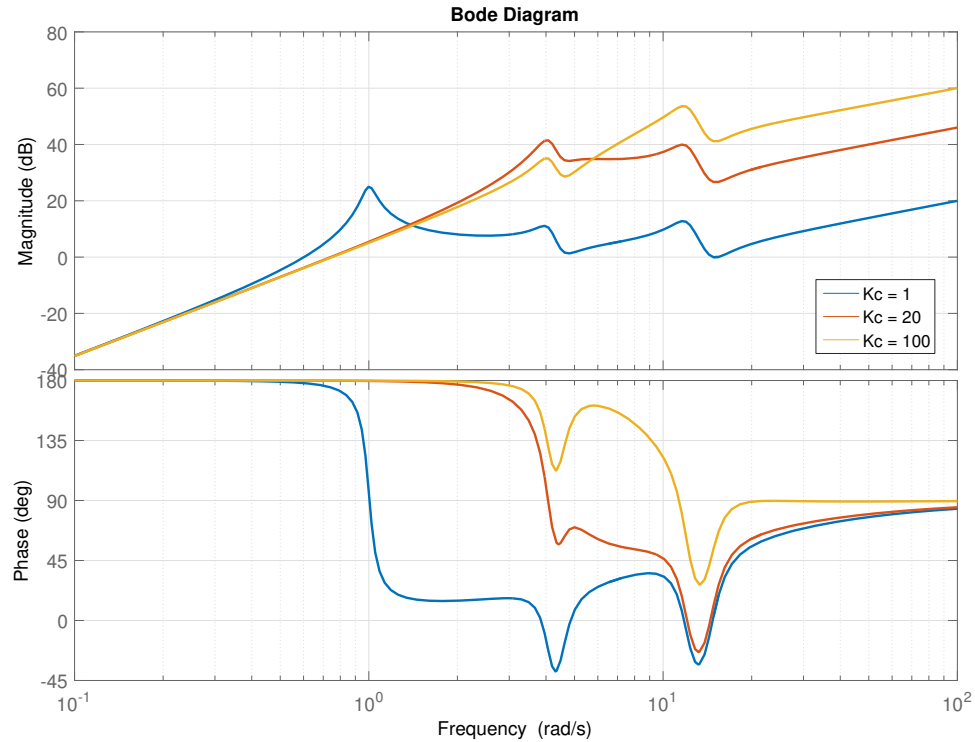


Figure 4.25. Bode plot of the computed torque frequency response with different values of K_c when $z_{pd} = -30$.

The same analysis may be completed for the case of Lead-Lag compensation, as shown in Figures 4.27 and 4.28. Here the discrepancies between the feedforward and computed torque architectures are even more obvious. In Figure 4.27 there is a significant increase in the energy added to the second mode as K_c increases, but the first mode actually has less energy added to it. As the gains are increased even further, the bandwidth of the system increases and a point is reached where the energy contributed to the second mode begins to decrease once more. This trend may also be observed when the feedforward controller is outside the feedback loop, but in that instance the differences between the different feedback controllers are much less significant. However, notice that even in this case there is a wide range of controller gains where the energy at resonance will have only small variations.

These results imply that as the settings of the controller are altered, the performance of the system will have significant variations as well.

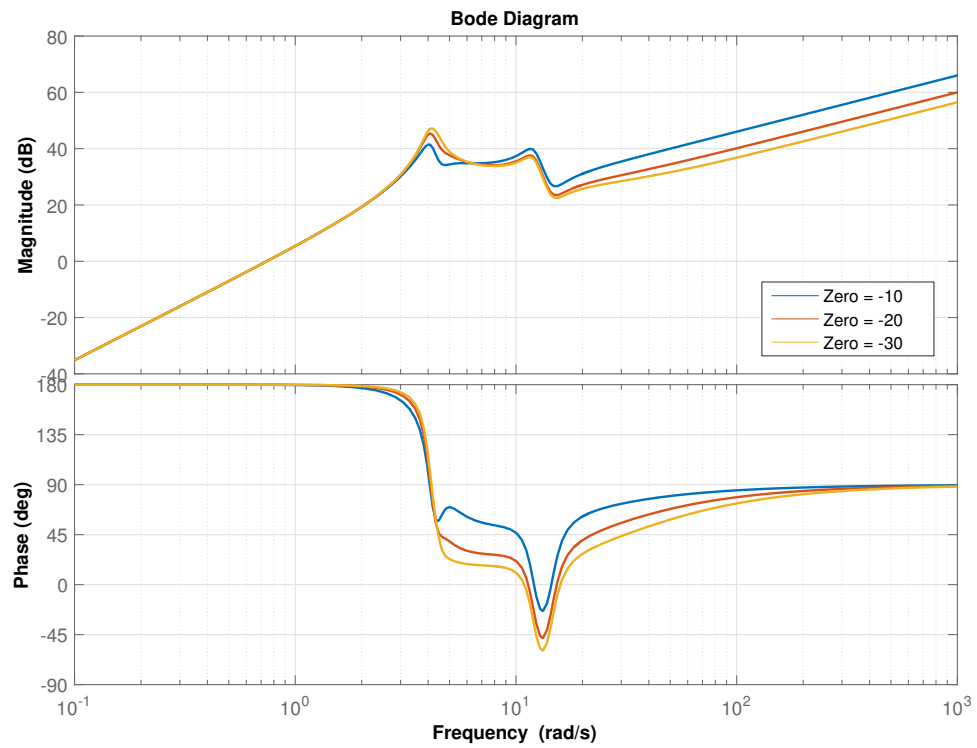


Figure 4.26. Bode plot of the computed torque frequency response with different values of z_{pd} when $K_c = 20$.

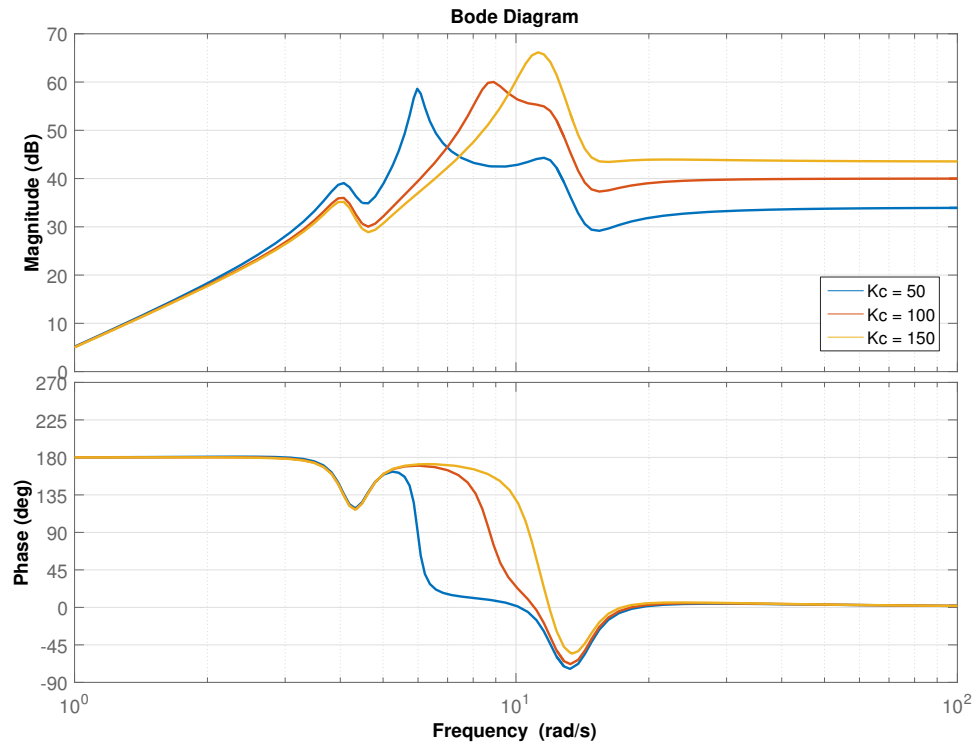


Figure 4.27. Bode plot of the computed torque frequency response for Lead-Lag controllers with control gains of $K_c = 50, 100, 150$, with $\omega_{center} = 5 \frac{\text{rad}}{\text{s}}$, $\omega_{width} = 1 \frac{\text{rad}}{\text{s}}$, and $a = 2$.

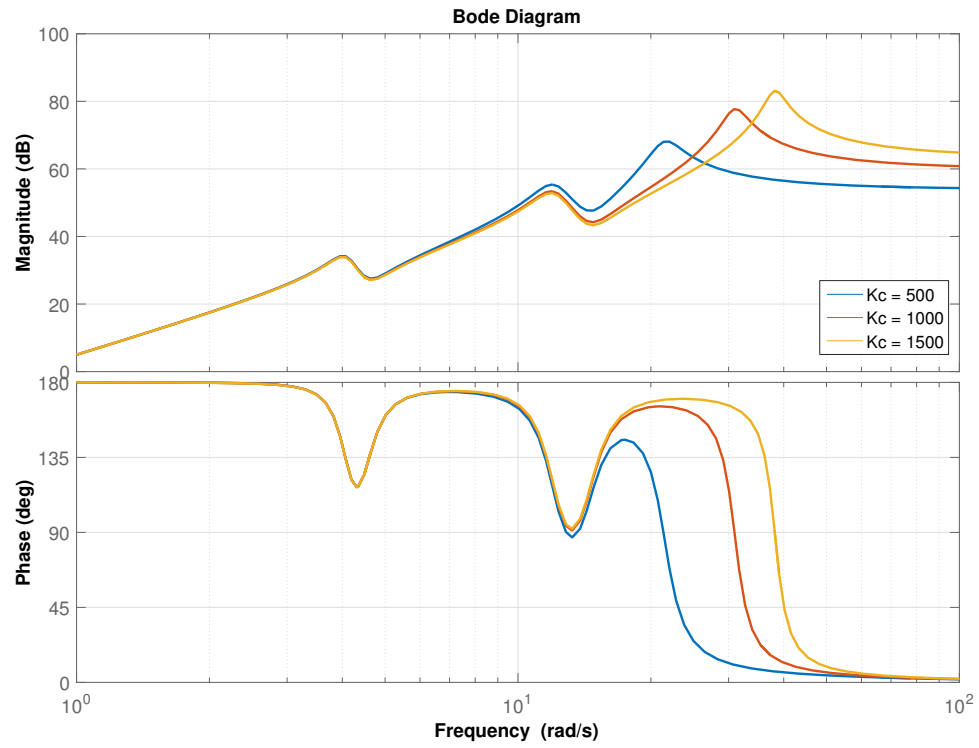


Figure 4.28. Bode plot of the computed torque frequency response for Lead-Lag controllers with control gains of $K_c = 500, 1000, 1500$, with $\omega_{center} = 5 \frac{\text{rad}}{\text{s}}$, $\omega_{width} = 1 \frac{\text{rad}}{\text{s}}$, and $a = 2$.

4.4.2 Closed-Loop Stability and Damping

In order to ensure the closed-loop stability of the system, Equations (4.60) and (4.68) must be Hurwitz. This is always true for the feedforward controller because the open-loop zeros of the system are located in the LHP, so when the system plant is inverted, the denominator of the feedforward controller is Hurwitz. Thus, the stability of the entire system is dependent only on the stability of the closed-loop system. That is, the feedback controller must ensure closed-loop stability.

The dominant poles of the open-loop system are the two poles that are located at the origin of the complex plane. These correspond to the rigid body mode of the system. However, it is important to observe that the other sets of poles are only slightly further into the LHP, so they will still significantly affect the response of the system. This can be seen for the closed-loop system by plotting the root locus plot of the loop transfer function.

As the control gain K_c is increased, the closed-loop poles will move along the paths of the root locus. These will start at the open-loop poles of the system and will move towards either the open-loop zeros or towards an asymptote. When using PD control with this system, the root locus plot may take several different shapes. This is shown in Figures 4.29 through 4.32, where the shape of the root locus depends on the location of the controller zero. This is important to show in order to examine both closed-loop stability and closed-loop damping.

When the controller zero is far away from the imaginary axis, the root locus plot will look similar to Figure 4.29 or 4.30, although the break-in point on the real axis and the maximum closed-loop damping will change depending on the location of the zero. Note that in these two instances the paths of the root locus that break into the real axis will begin at the open-loop poles corresponding to the second mode.

As the controller zero is moved closer to the real axis, the break-in point will also shift. After moving far enough, the paths starting from the open-loop poles of the first mode will break-in to the real axis, which drastically changes the shape of the

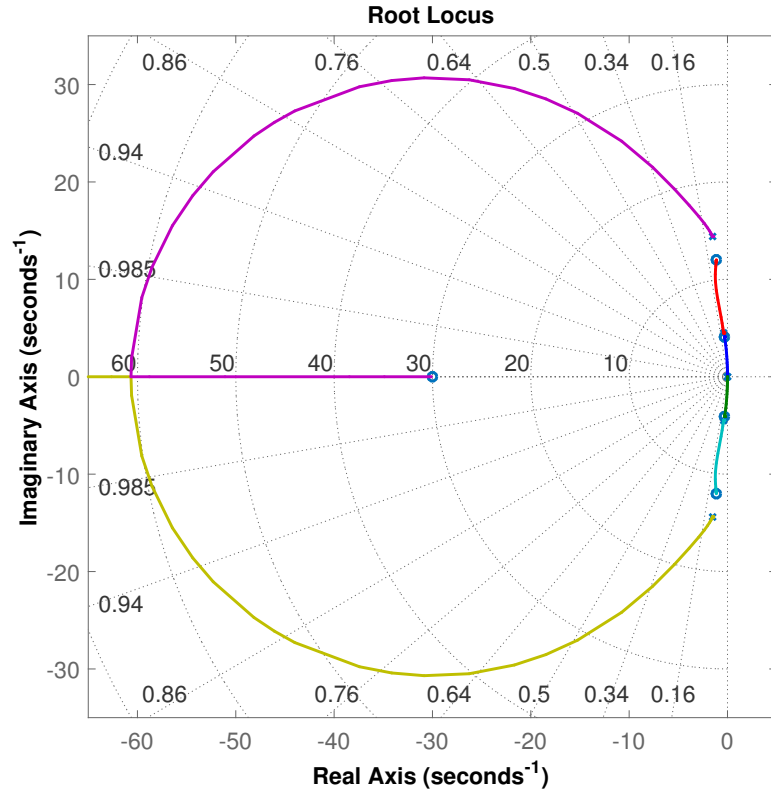


Figure 4.29. Root Locus of the closed-loop for the three-mass system with PD control where $z_{pd} = -30$ on the real axis.

root locus plot. This can be seen when $z_{pd} = -5$, as shown in Figure 4.31. This change will affect the behavior of the closed-loop damping of the system.

Moving the controller zero z_{pd} even closer to the imaginary axis results in still another form of the root locus plot. Here paths of the root locus starting at the poles of the rigid body mode will break-in to the real axis, as shown in Figure 4.32. Note that this case is not ideal. This is because having z_{pd} this close to the imaginary axis will result in the controller output having large transients, which may cause saturation of the output signal, among other complications.

The maximum level of closed-loop damping depends both on the location of the controller zero z_{pd} and on the magnitude of the control gain K_c . The maximum levels of the damping ratio for different controller zeros z_{pd} are shown in Table 4.3, along with the corresponding K_c for each case. Observe that $\zeta_{CL,max}$ is consistently in the

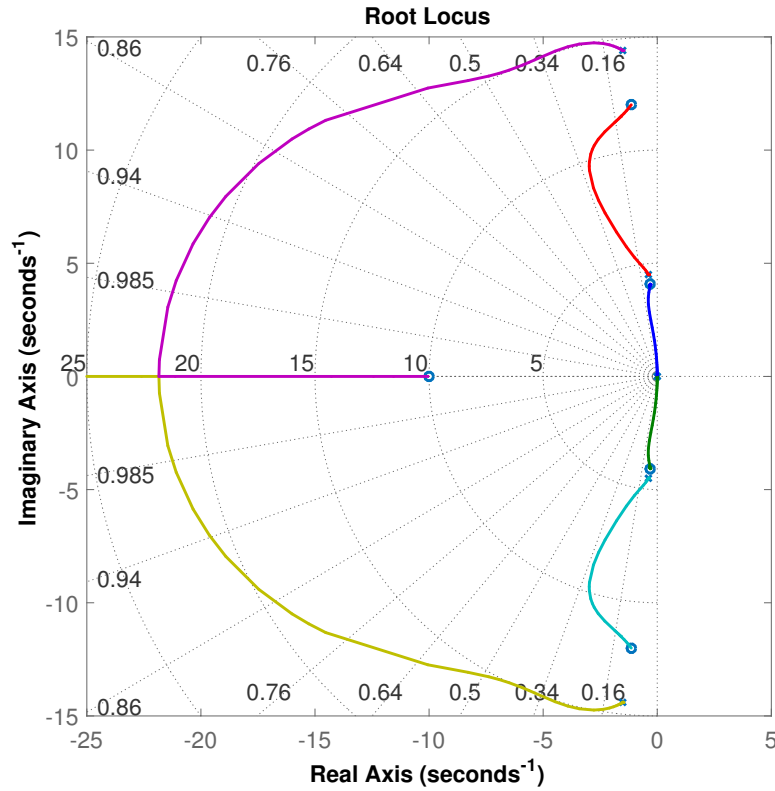


Figure 4.30. Root Locus of the closed-loop for the three-mass system with PD control where $z_{pd} = -10$ on the real axis.

range $0 \leq \zeta \leq 0.3$, which shows that the assumption made that this is a lightly-damped system remains valid. The only instance this is not the case is when z_{pd} is close to the origin. However, as mentioned earlier in this section, these cases tend not to perform well due to the increase in overshoot that appears when having a zero close to the origin. In all instances where PD control is used, the root locus plots show that the system is always stable. This is true since the closed-loop poles never cross into the RHP. This analysis assumes that the controller zero z_{pd} will always be placed in the LHP, which keeps the closed-loop system minimum-phase, and that the control gain K_c will always be positive.

The root locus can also be used for the cases that apply Lead-Lag control. Several examples of how the root locus will appear in these instances are shown in Figures 4.33 and 4.34.

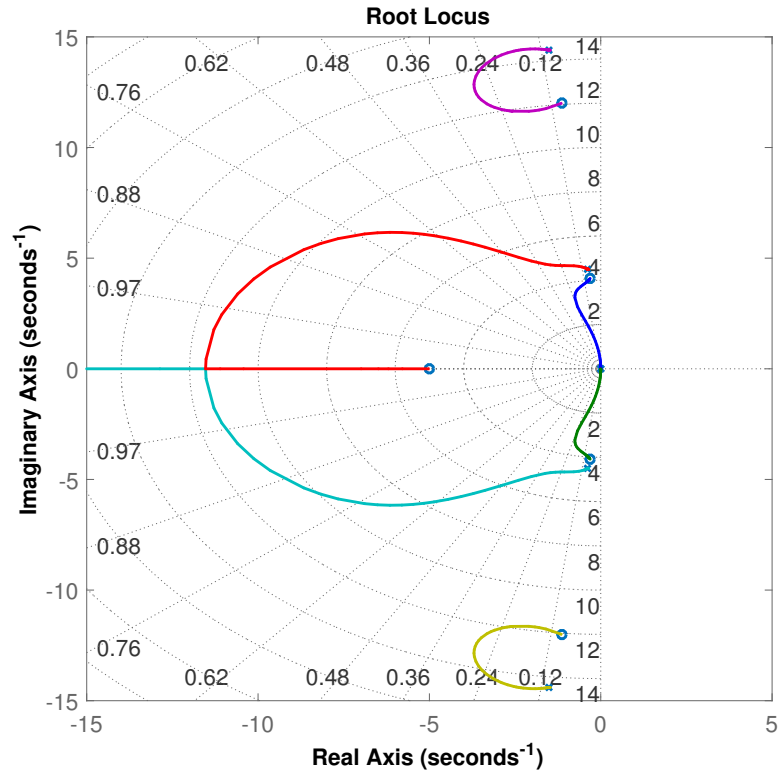


Figure 4.31. Root Locus of the closed-loop for the three-mass system with PD control where $z_{pd} = -5$ on the real axis.

Table 4.3. Maximum closed-loop damping of the three-mass system with PD control.

z_{pd}	$\zeta_{CL,max}$	K_c
2	0.341	3.5
4	0.300	18.2
6	0.195	15.7
8	0.149	17.1
10	0.121	23.1
15	0.087	28.5
20	0.0755	∞
25	0.0755	∞

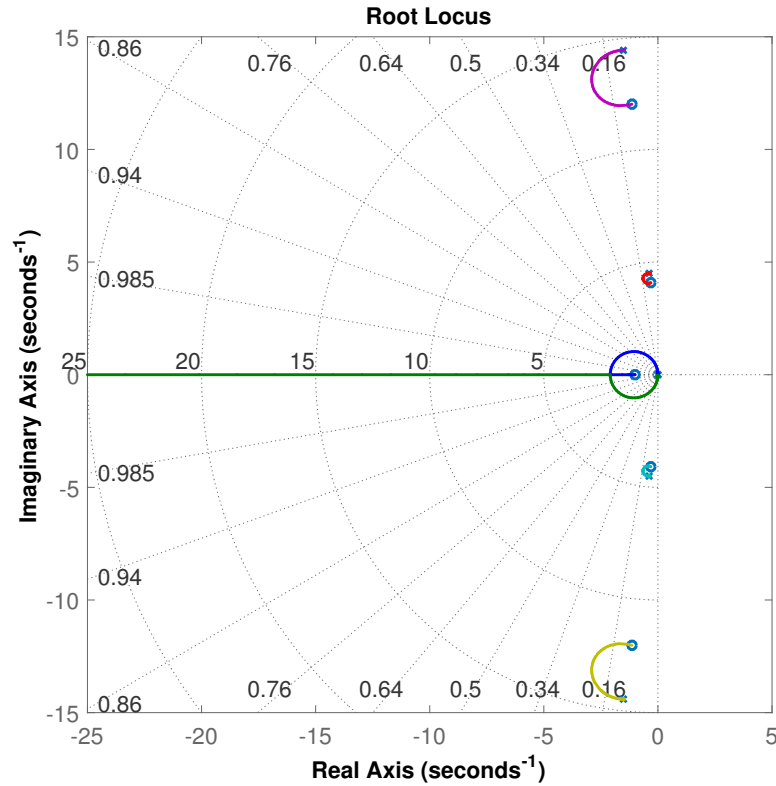


Figure 4.32. Root Locus of the closed-loop for the three-mass system with PD control where $z_{pd} = -1$ on the real axis.

In the case of PD control, closed-loop stability is attained by placing the controller zero in the LHP and choosing a positive controller gain K_c . However, this is not the case for Lead-Lag control. Figures 4.33 and 4.34 show that the paths of the root locus do in fact cross over into the RHP. This issue means that there is a set of minimum control gains that will be required to ensure stability. Tables 4.4 and 4.5 show the approximate requirements on these minimum values for different values of ω_{center} , ω_{width} , and a . Note that these are approximate values that have been found using the root locus, and they have been rounded up to integer values in intervals of 5. This both gives cleaner results and adds some buffer to the stability margins of the system.

Examples of the closed-loop damping for the system when using Lead-Lag control can be seen using the root locus plots of Figures 4.33 and 4.34. There is much less

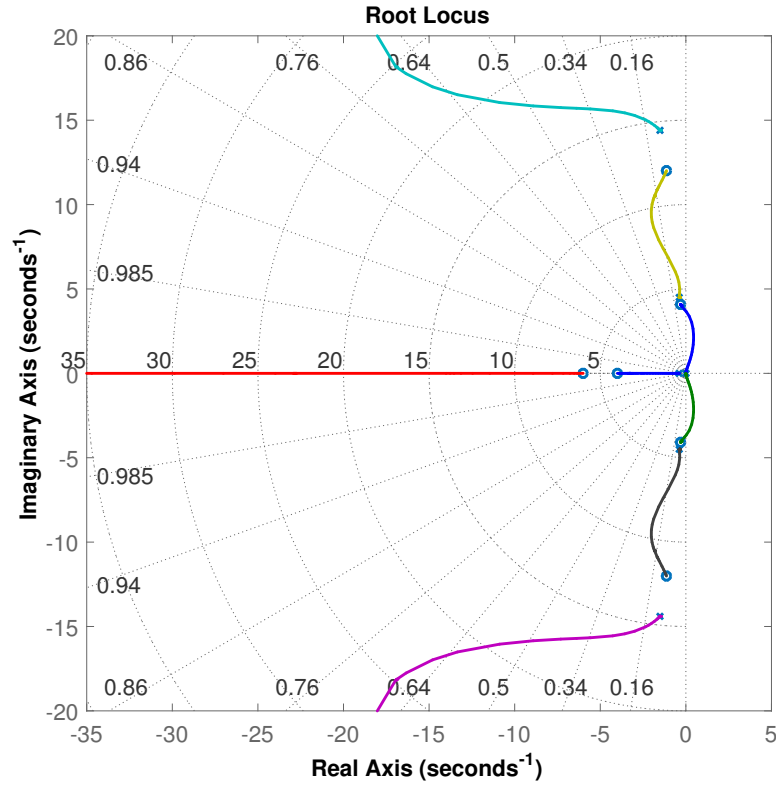


Figure 4.33. Root Locus of the three-mass system with a Lead-Lag compensator where $\omega_{center} = 5 \frac{\text{rad}}{\text{s}}$, $\omega_{width} = 1 \frac{\text{rad}}{\text{s}}$, and ratio $a = 10$.

variation here in the maximum closed-loop damping than for the instances that use PD control, although there are still some differences as K_c is increased. Also, the assumption that this is a lightly-damped system does still apply here when using a Lead-Lag controller.

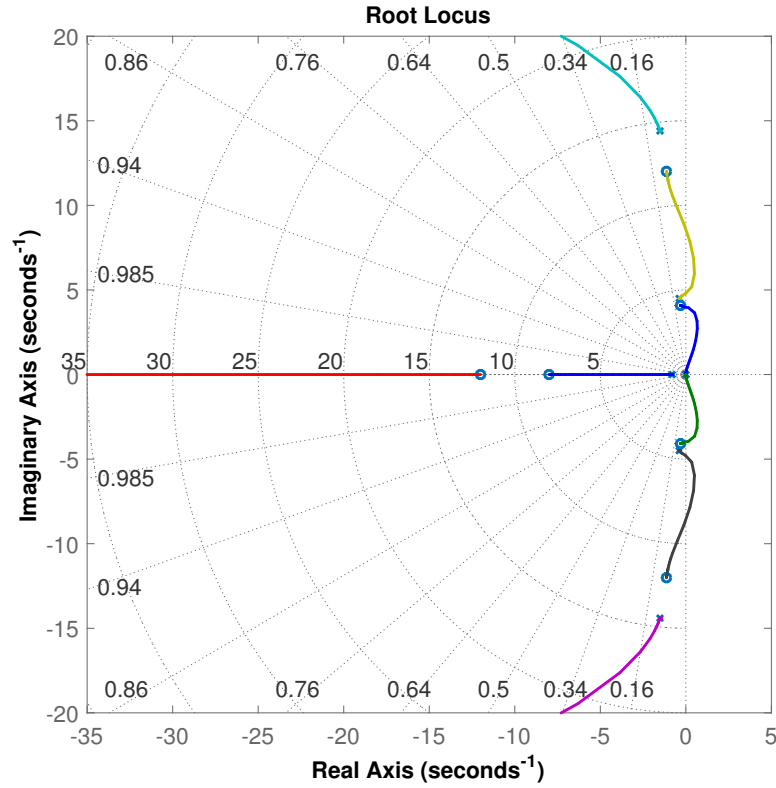


Figure 4.34. Root Locus of the three-mass system with a Lead-Lag compensator where $\omega_{center} = 10 \frac{\text{rad}}{\text{s}}$, $\omega_{width} = 2 \frac{\text{rad}}{\text{s}}$, and ratio $a = 10$.

Table 4.4. Minimum required values of controller gain K_c to ensure closed-loop stability for $\omega_{center} = 10$.

$\omega_{width} = 1$		$\omega_{width} = 2$		$\omega_{width} = 4$	
a	K_c	a	K_c	a	K_c
1.5	25	1.5	30	1.5	35
2	40	2	45	2	55
2.5	125	2.5	145	2.5	140
3	175	3	200	3	190
3.5	225	3.5	240	3.5	230
4	260	4	275	4	270
4.5	300	4.5	325	4.5	310
5	335	5	360	5	350

Table 4.5. Minimum required values of controller gain K_c to ensure closed-loop stability for $\omega_{center} = 5$.

$\omega_{width} = 0.5$		$\omega_{width} = 1$		$\omega_{width} = 1.5$	
a	K_c	a	K_c	a	K_c
1.5	25	1.5	30	1.5	30
2	40	2	40	2	45
2.5	50	2.5	50	2.5	55
3	60	3	60	3	70
3.5	70	3.5	75	3.5	80
4	80	4	85	4	90
4.5	90	4.5	100	4.5	110
5	100	5	110	5	120

4.5 Calculation of Performance Metrics for the Three-Mass System

The three measures of performance that were defined in section 2.5 will be utilized to compute the quantitative performance of the three-mass system. For this simulation, there are two locations of interest, the first mass and the third mass.

The first mass is the location where the input is added to the system, while The third mass corresponds to the motion of the end effector. Since both of these locations are of interest to this work, the performance calculations for the three-mass system will include results for both the first mass and the third mass.

The peak residual acceleration is found as

$$a_{rv} = \max(a(t)) - \min(a(t)), \quad \left[\frac{\text{m}}{\text{s}^2}\right] \quad (4.81)$$

where the time t is in the range $T_f \leq t \leq T_{end}$, T_f is the time at the end of motion and T_{end} is the end time of the simulation. Note that the acceleration signal is not always positive here, unlike for the performance metrics of the two-link flexible-joint robot. This is because no calculation is needed to compute the overall magnitude, as the motion only occurs in the $\pm X$ direction, and the signal is measured directly in simulation.

The peak deflection can be found by examining the position signal instead of the acceleration. This calculation can be written as

$$\Delta_{p,max} = \max(|p(t) - p_{ss}|), \quad [\text{m}] \quad (4.82)$$

where $\Delta_{p,max}$ is the max deflection and p_{ss} is the steady-state position. This calculation is done for time in the range $T_f \leq t \leq T_{end}$.

The settling time is found by taking the acceleration signal and finding the final time it is outside a certain tolerance threshold, which is set at $\pm 0.3 \frac{\text{m}}{\text{s}^2}$. This is measured from the end of the input profile, meaning it falls in the range $T_f \leq t \leq T_{end}$.

4.6 Simulation Results of the Three-Mass System

In order to examine the behavior of this three-mass system, a model was created in MATLAB to simulate the response. This utilizes the transfer functions of Equations (4.55) through (4.57), with the different types of controllers presented in section 4.4.

Because any mathematical model of the real world is never perfect, errors in the natural frequencies of the system are incorporated into this simulation. This allows the examination of the three-mass system when the feedforward controller does not perfectly match the system itself. For the simulations included in this work, three cases are examined. The first case utilizes a perfect model in the feedforward controller, while the second and third cases apply $\pm 5\%$ error to the natural frequencies. These errors are defined as

$$\omega_{error} = \frac{\omega_{actual} - \omega_{nominal}}{\omega_{nominal}}, \quad \left[\frac{\text{rad}}{\text{s}^2} \right] \quad (4.83)$$

which is multiplied by 100 to obtain the percent error.

The performance of the feedback controllers is also studied using different types of input profiles, namely, both the ramped sinusoid and the versine will be applied. The output is normalized so that the position of the three-mass system will always move from a location of zero to a location of one, with units of length.

4.6.1 Fast Fourier Transform

When analyzing the energy of a signal at certain frequencies it is best to represent that signal in the frequency domain. This is done through a Fourier Transform.

In the case of an arbitrary set of discrete data values, this transformation can be calculated using the Discrete Fourier Transform (DFT). Given N uniformly sampled discrete data points of the function $f(t)$, this can be given as

$$F(n) = \frac{1}{N} \sum_{n=0}^{N-1} f(t) e^{-i \frac{2\pi n t}{N}}. \quad (4.84)$$

Implementing the DFT directly is quite inefficient, as it requires $O(N^2)$ operations. Luckily, there exists an efficient algorithm for computing the DFT, which is known as the Fast Fourier Transform (FFT). The FFT only requires $O(N \log(N))$ computations, which is a very significant increase in efficiency. Cooley and Tukey presented their algorithm that accomplished this in 1965 [48], although it is believed that Carl Friedrich Gauss may have known a similar algorithm 150 years prior [49]. A comprehensive view of the different algorithms that can be used to implement the FFT is given by Van Loan in his seminal work on the topic [50].

In this application, the FFT is used to transform the outputs of the system controllers into the frequency domain. This allows examination of the level of energy at the natural frequencies after the feedforward and feedback controllers have acted on those signals. Note that the data set has been zero padded to include 2^{22} samples, which greatly improves the resolution of the frequency spectra. The cost of this addition to the data set is that it requires the function to be zero outside the interval measured, due to the periodicity of the DFT. While this assumption may not necessarily be true, the interest here is only on the controller output during motion. This is the portion of the signal that has been shaped to reduce energy at the natural frequencies. Because of this, it is reasonable to neglect the effects of the controller after motion has been completed. Examples of the magnitude spectra for the controller outputs are shown in Figures 4.35 and 4.36. Note that these cases utilize the ramped sinusoid input profile with $\kappa = 3$, as well as a PD controller in the Feedforward configuration with $K_c = 20$ and $z_{pd} = -30$.

When comparing Figures 4.35 and 4.36, several things become apparent. First, the feedforward controller has a significantly higher magnitude spectrum than the feedback does. This is because the feedforward is doing most of the work and the feedback is only correcting for the errors seen in the response. In fact, as the feedforward model gets better, the feedback controller should be able to contribute even less. Note that this will lead to different trends in the simulation results when there is -5% error versus when there is $+5\%$ error. This is because the feedforward ele-

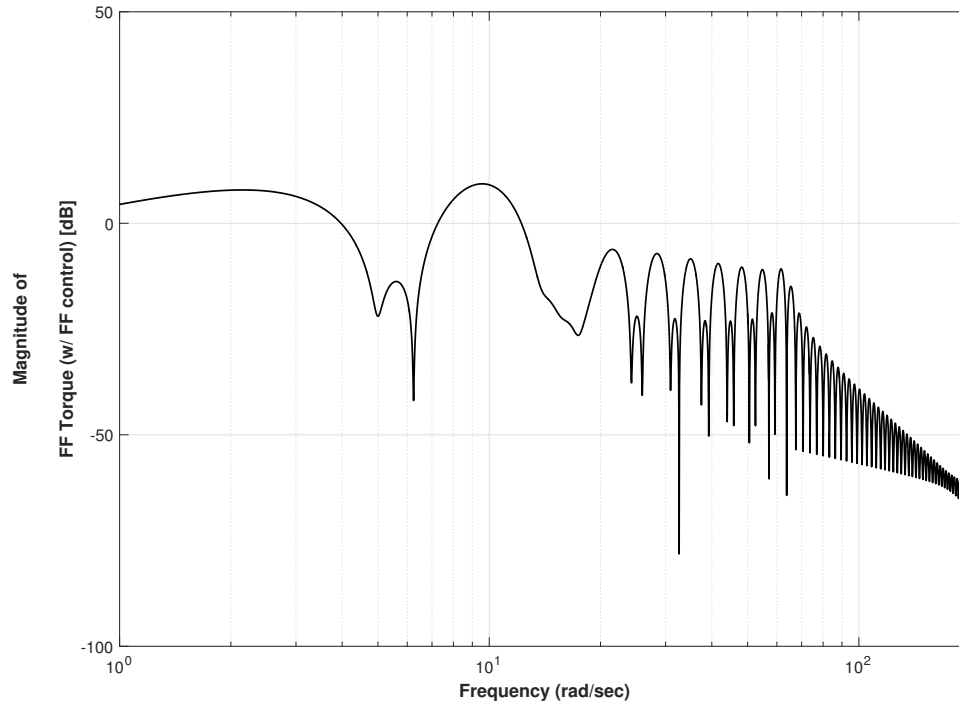


Figure 4.35. Example FFT of the feedforward controller output for a ramped sinusoid profile with $\kappa = 3$, a PD controller of $K_c = 20$ and $z_{pd} = -30$, and a -5% error in the natural frequencies.

ment performs better with the instances that have $+5\%$ error, so the changes in the feedback controller are less significant.

When in the feedforward controller configuration of Figure 4.5, these two signals are added together. This combined response can also be recorded and transformed to the frequency domain. This is also done using an FFT, and the result is shown in Figure 4.37.

This result can be used to quantify the level of energy in the frequency spectra. To accomplish this, the average is taken of the frequencies of the FFT that are inside a $\pm 5\%$ window around the nominal natural frequencies. This produces a scalar value of the energy for each mode. With the energy of the frequency spectra calculated, it can now be compared with the values of the performance metrics found in section 4.5.

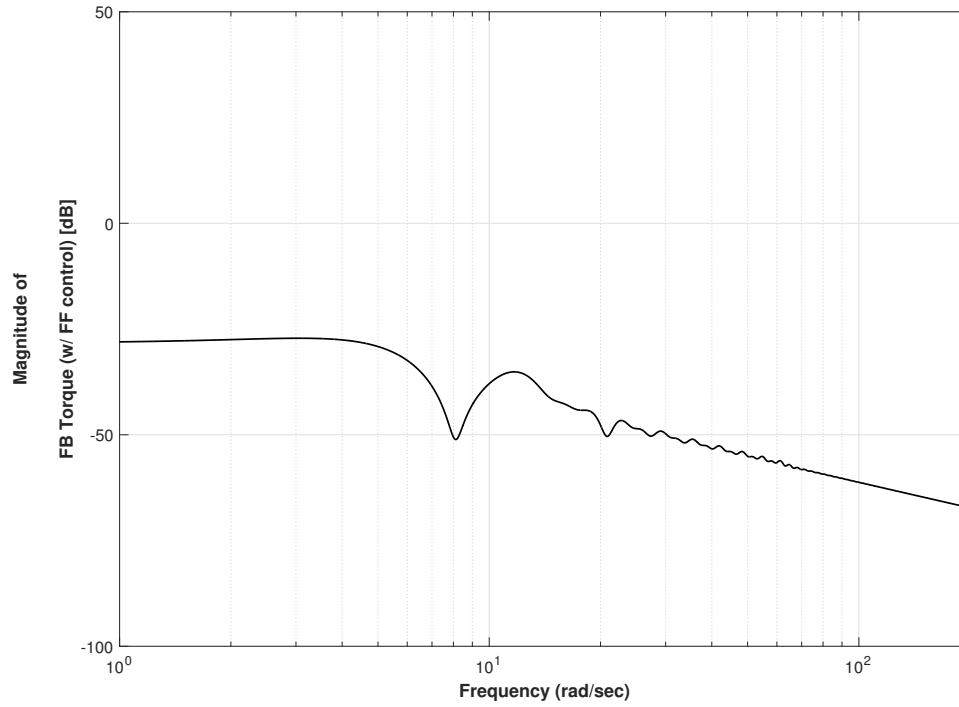


Figure 4.36. Example FFT of the feedback controller output for a ramped sinusoid profile with $\kappa = 3$, a PD controller of $K_c = 20$ and $z_{pd} = -30$, and a -5% error in the natural frequencies.

4.6.2 Analysis of Simulation Results

Several examples of the output of the three-mass simulation are shown in Figures 4.38 through 4.40. The top four plots in these figures show the frequency spectra for the input profile, the feedback controller, the feedforward controller, and the total controller output, starting from the top left and moving towards the right from top to bottom. The bottom six plots show the position, velocity, and acceleration signals of the first mass on the left and the third mass on the right. Note that these three examples all use the same feedback controller, which is a PD controller with $K_c = 20$ and $z_{pd} = -30$. There is also a -5% error in the system natural frequency.

Figure 4.38 shows the response when a versine profile is used with $\kappa = 3$. This is still a fairly small value for κ , so there is a fair amount of residual vibration seen in the motion of the third mass.

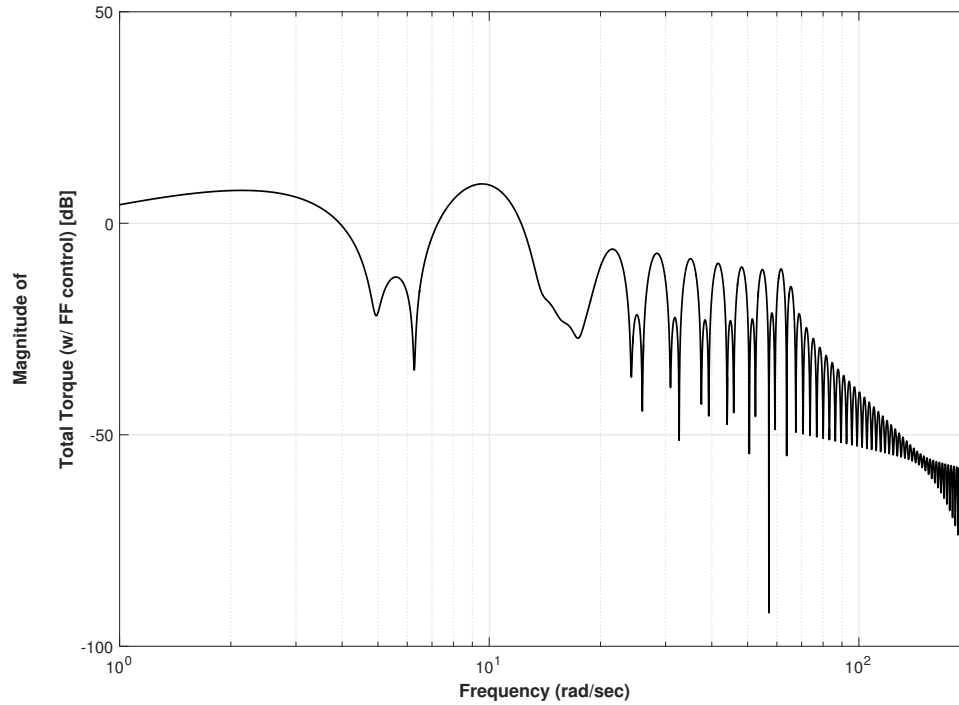


Figure 4.37. Example FFT of the total controller output for a ramped sinusoid profile with $\kappa = 3$, a PD controller of $K_c = 20$ and $z_{pd} = -30$, and a -5% error in the natural frequencies.

Notice that the frequency spectrum for the feedforward controller does look very similar to the frequency spectrum of the input profile, although there are some differences due to the frequency response of the feedforward controller.

Figure 4.39 shows the same system, but this time using a ramped sinusoid profile with $\kappa = 3$ instead. Note that there are some differences in the frequency spectrum of the input profile and in the shape of the acceleration signal. This can be most easily observed by looking at the acceleration of the first mass.

This also still has a decent level of residual vibration, so κ is increased to 15. This results in the response shown in Figure 4.40.

Figure 4.40 shows several differences with Figure 4.39. First of all, the frequency spectrum of the input profile has much deeper attenuation windows. This is expected, as this profile is designed so that it very heavily penalizes the energy in the natural

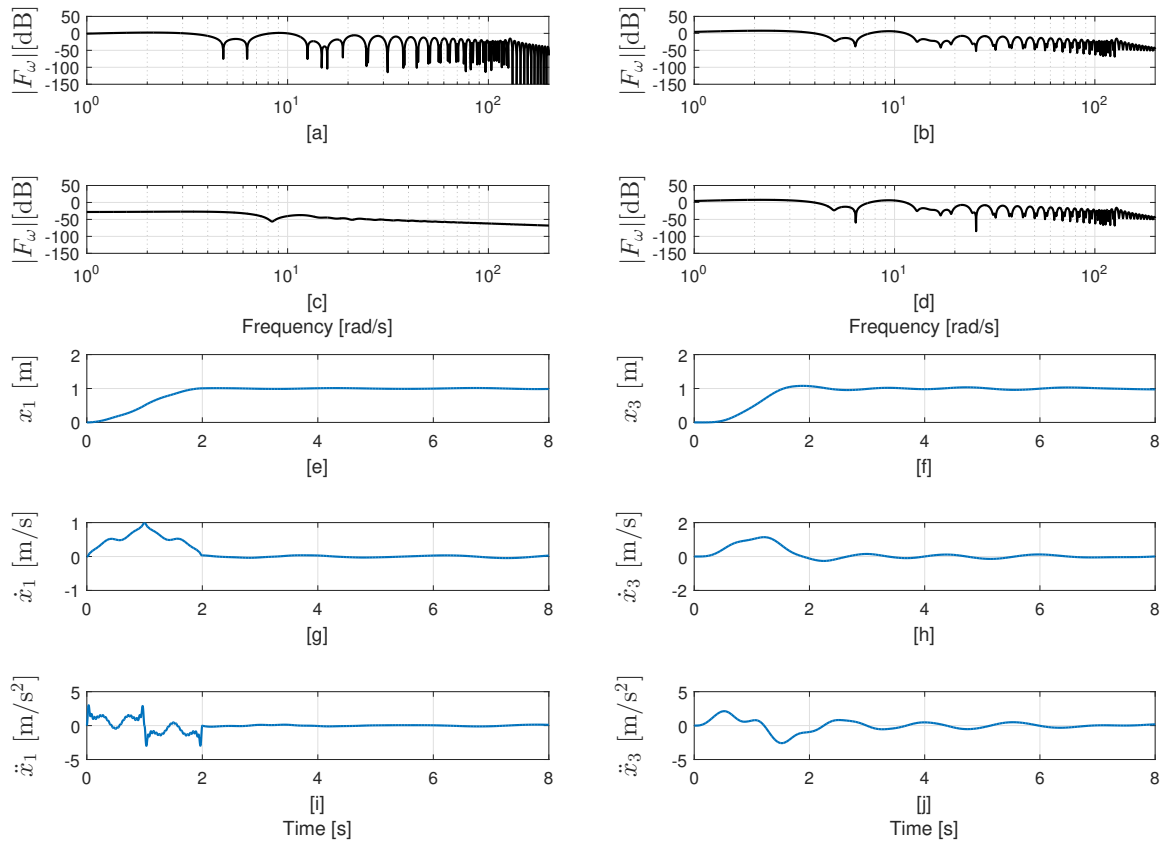


Figure 4.38. Simulated response of the three-mass system using the feedforward configuration for a PD controller with $K_c = 20$, $z_{pd} = -30$, -5% error, and a versine profile with $\kappa = 3$. [a] through [d] are the magnitude spectra of the input profile, the feedforward controller, the feedback controller, and the total controller output, respectively. [e] and [f] are the positions of mass 1 and mass 3, [g] and [h] are the velocities of mass 1 and mass 3, and [i] and [j] are the accelerations of mass 1 and mass 3.

frequencies. The cost for this is that it requires much higher accelerations for the first mass. However, the overall level of residual vibration has greatly diminished.

This type of analysis will be continued throughout this section. Observe that the performance of the system is measured in several different ways. These will be calculated algorithmically so that many cases can be compared against each other. First, the average is taken of the energy levels of the total controller output around the natural frequencies. This utilizes the FFT as discussed in section 4.6.1. This should provide a direct measure of the level of residual vibration that will result from motion,

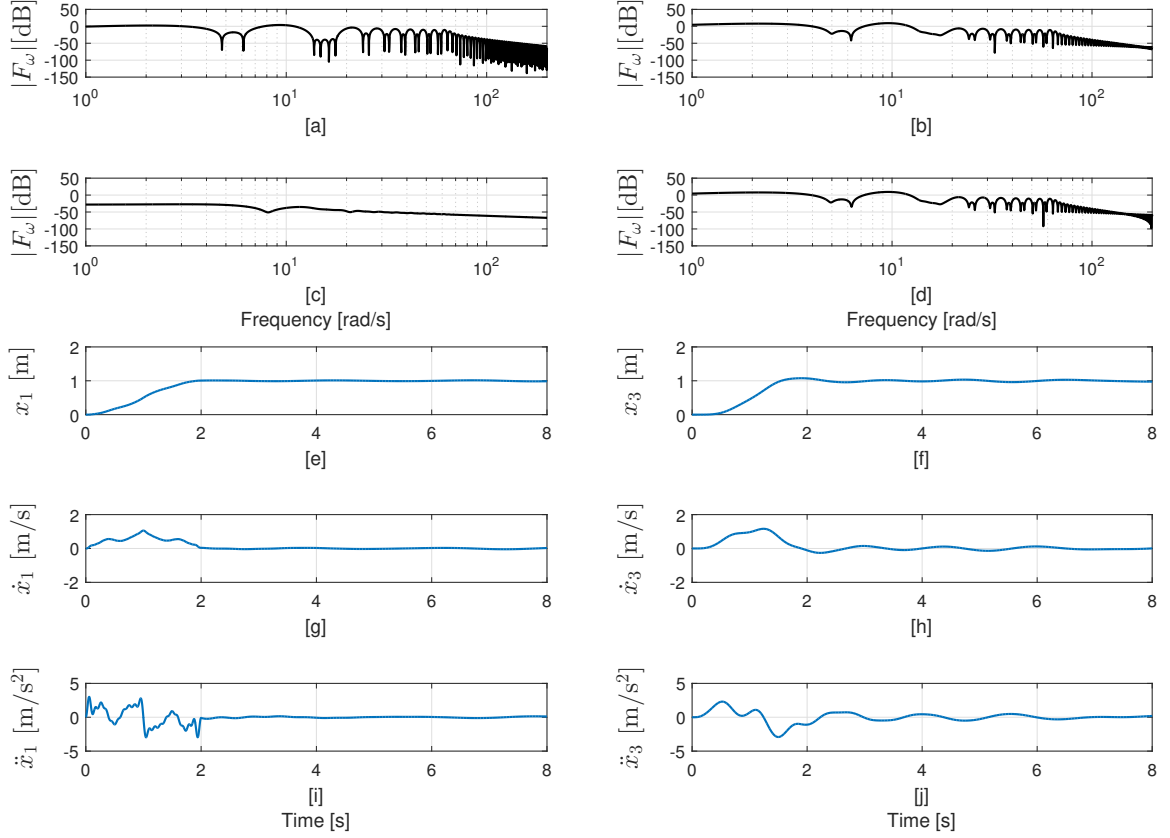


Figure 4.39. Simulated response of the three-mass system using the feedforward configuration for a PD controller with $K_c = 20$, $z_{pd} = -30$, -5% error, and a ramped sinusoid profile with $\kappa = 3$. [a] through [d] are the magnitude spectra of the input profile, the feedforward controller, the feedback controller, and the total controller output, respectively. [e] and [f] are the positions of mass 1 and mass 3, [g] and [h] are the velocities of mass 1 and mass 3, and [i] and [j] are the accelerations of mass 1 and mass 3.

and so it is compared with the values of the performance metrics that were presented in section 4.5. Most of the performance metrics are measured using the motion of the third mass, which is where the residual vibration needs to be minimized. However, the peak acceleration of the first mass after the move is also included in these plots to show the vibration performance on the motor side of the system as well.

Figures 4.41 and 4.42 show the performance of the system when using an ideal feedforward controller and $\kappa = 3$. Note that these results are plotted as a function

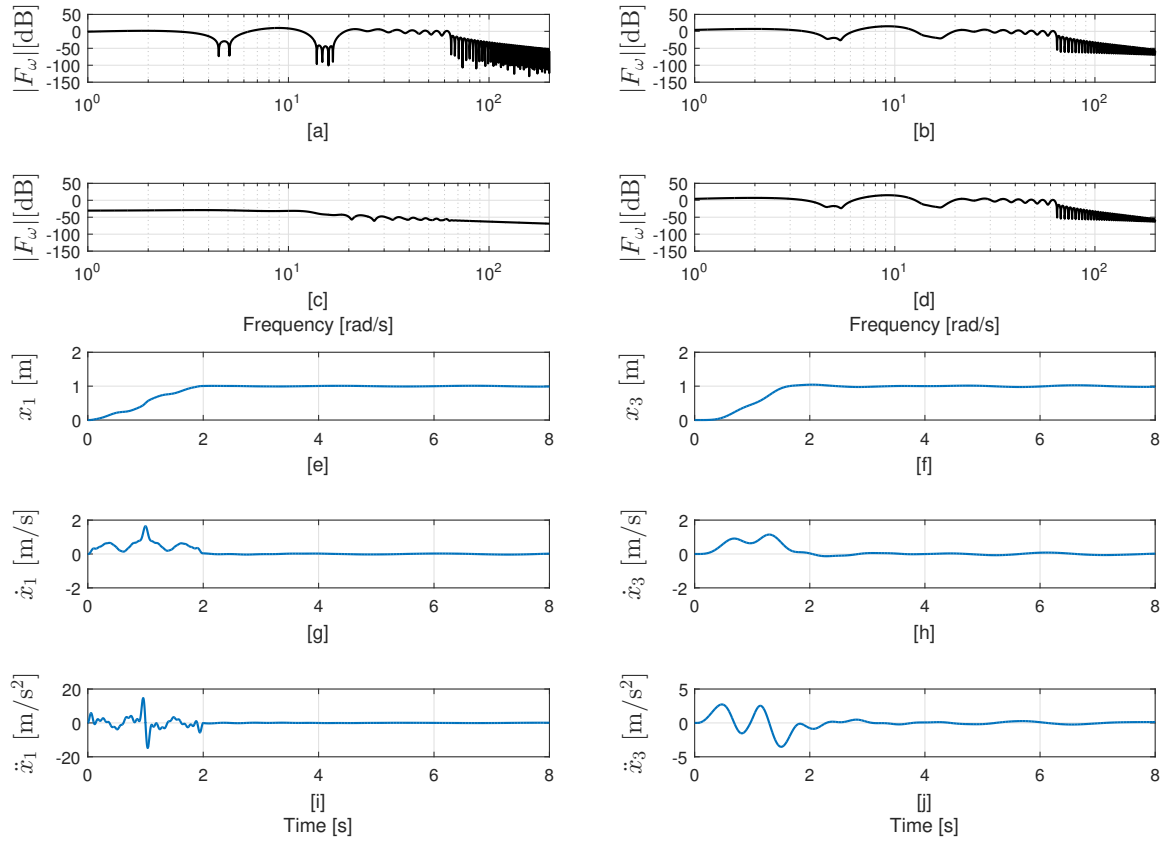


Figure 4.40. Simulated response of the three-mass system using the feedforward configuration for a PD controller with $K_c = 20$, $z_{pd} = -30$, -5% error, and a ramped sinusoid profile with $\kappa = 15$. [a] through [d] are the magnitude spectra of the input profile, the feedforward controller, the feedback controller, and the total controller output, respectively. [e] and [f] are the positions of mass 1 and mass 3, [g] and [h] are the velocities of mass 1 and mass 3, and [i] and [j] are the accelerations of mass 1 and mass 3.

of the location of the controller zero, z_{pd} , and the different data sets correspond to different values of the control gain K_c .

Note how the feedback has very little effect on any of the variables measured in Figures 4.41 and 4.42. This is because the feedforward controller is a perfect inverse of the system plant and thus is taking care of everything needed to track the reference signal. In essence, the feedback controller is not required.

This is an interesting, but already well-known, result. In practice, this will never be the case, as it is impossible to obtain a perfect model of the system. This is why

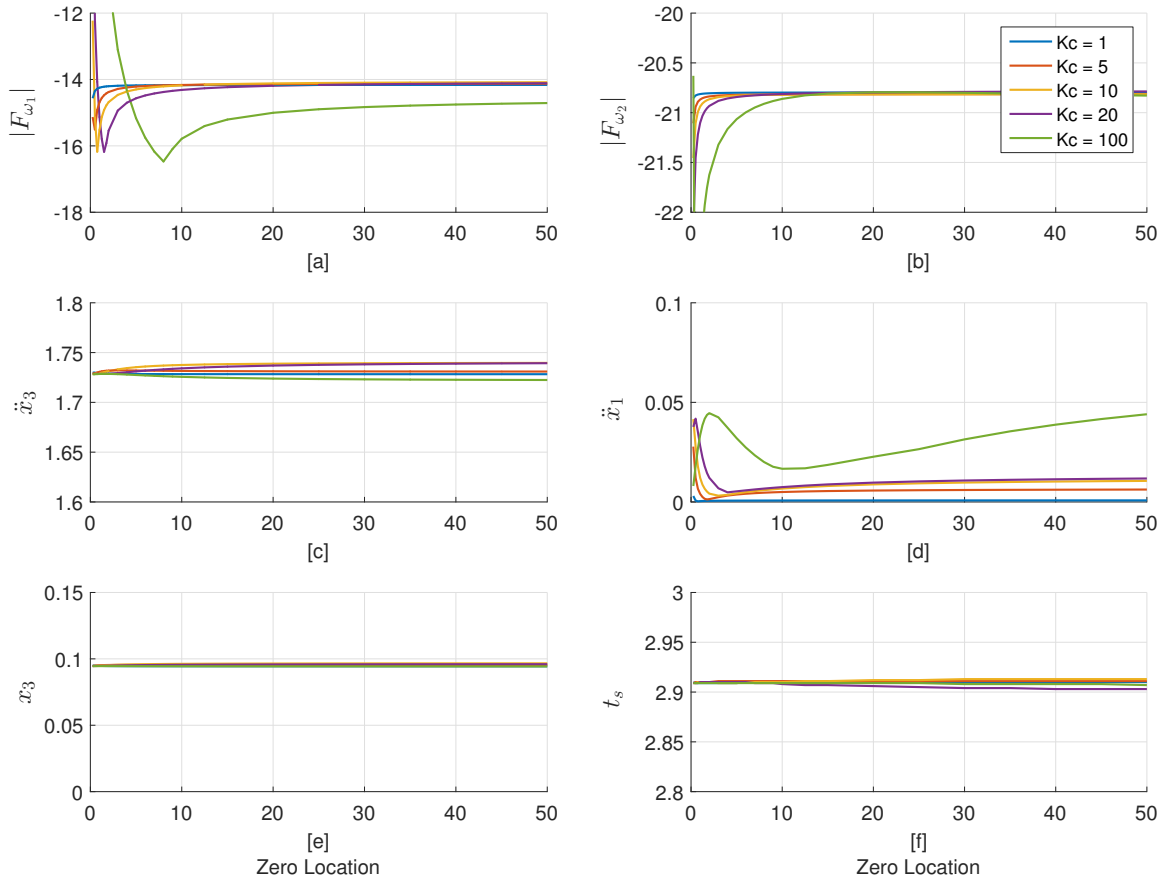


Figure 4.41. Response of the three-mass system for a ramped sinusoid profile with $\kappa = 3$ using feedforward controller and no error in the natural frequencies. [a] and [b] show the average magnitude of the first and second modes, respectively. [c] shows the peak-to-peak acceleration of mass 3, while [d] shows the peak-to-peak acceleration of mass 1. [e] and [f] show the peak deflection and the settling time of mass 3.

it is important to study the system when the feedforward controller is not a perfect inverse of the system. Figures 4.43 and 4.44 show the response when there is a -5% error in the natural frequencies, while Figures 4.45 and 4.46 show the response when there is a $+5\%$ error in the natural frequencies.

By comparing the ramped sinusoid results of Figure 4.43 with Figure 4.45, the system performs worse when the actual natural frequency is less than the nominal natural frequency. This is because of the results found in Figure 4.23, which shows that the feedforward controller will not perform as well when the actual natural frequency is less than the nominal. This result is also seen with the versine profile, as

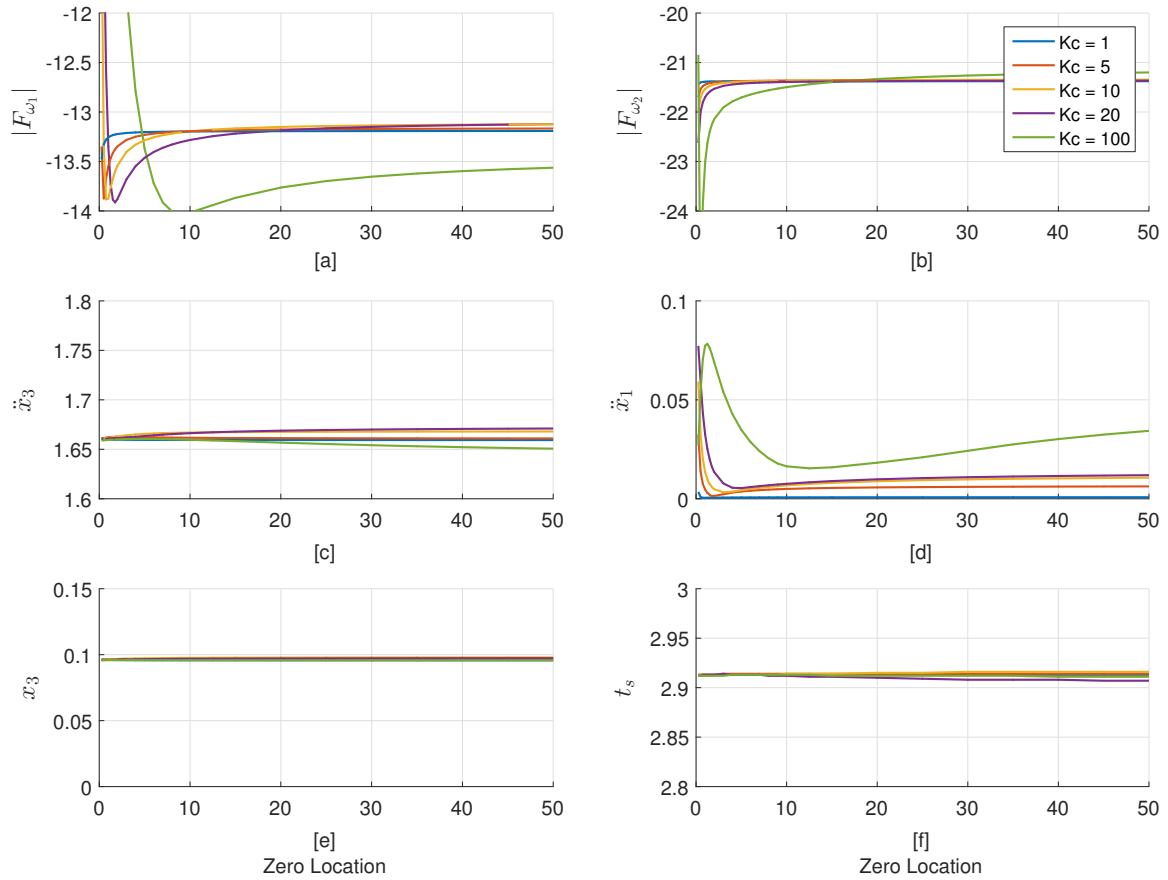


Figure 4.42. Response of the three-mass system for a versine profile with $\kappa = 3$ using feedforward controller and no error in natural frequencies. [a] and [b] show the average magnitude of the first and second modes, respectively. [c] shows the peak-to-peak acceleration of mass 3, while [d] shows the peak-to-peak acceleration of mass 1. [e] and [f] show the peak deflection and the settling time of mass 3.

can be observed when comparing Figure 4.44 with Figure 4.46. Overall the performance of the system is more sensitive to variations in the natural frequencies that are lower than the nominal natural frequency. Because of this it will always perform worse for these cases compared to when there is positive error in the natural frequencies. This also results in different trends in the performance due to variations in K_c . For the case of -5% error, it is clear that increasing K_c too high is detrimental to performance, and the best results appear with lower control gains. This is not apparent in the case of $+5\%$ error, where it appears that increasing K_c improves both the peak-to-peak acceleration and the settling time of the third mass. However, note

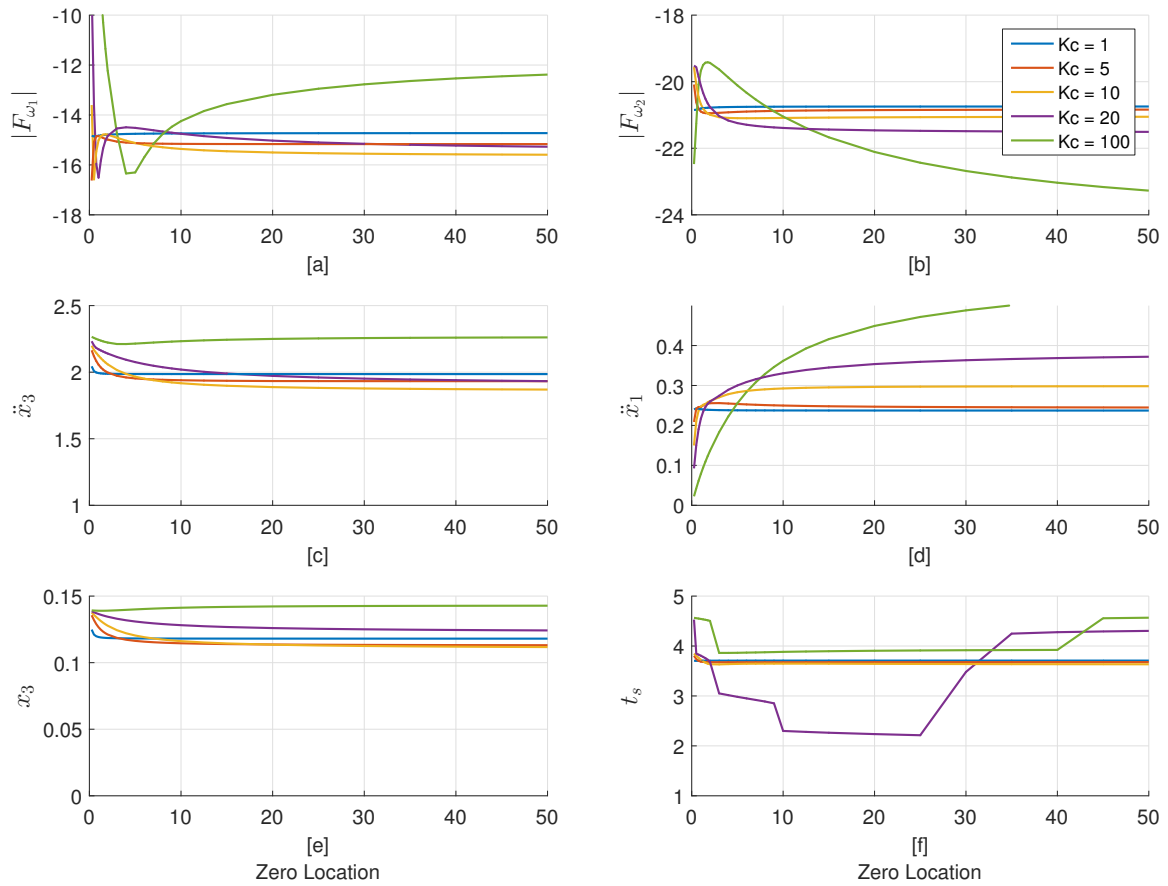


Figure 4.43. Response of the three-mass system for a ramped sinusoid profile with $\kappa = 3$ using feedforward controller and -5% error in the natural frequencies. [a] and [b] show the average magnitude of the first and second modes, respectively. [c] shows the peak-to-peak acceleration of mass 3, while [d] shows the peak-to-peak acceleration of mass 1. [e] and [f] show the peak deflection and the settling time of mass 3.

that the feedforward controller is performing much better in this instance. This is an important distinction, as the overall magnitude of the feedback component is much smaller when there is $+5\%$ error. This means that the feedback will need to be much worse in order to degrade performance.

Observe that the magnitude of the peak acceleration and the peak deflection of the third mass are directly correlated to the spectral energy of the two modes. However, the settling time does not seem to always follow the same trend. This is obvious in Figures 4.41 through 4.46. However, this is easily explained through the analysis performed in section 4.4. There, a discussion was completed on how the closed-loop

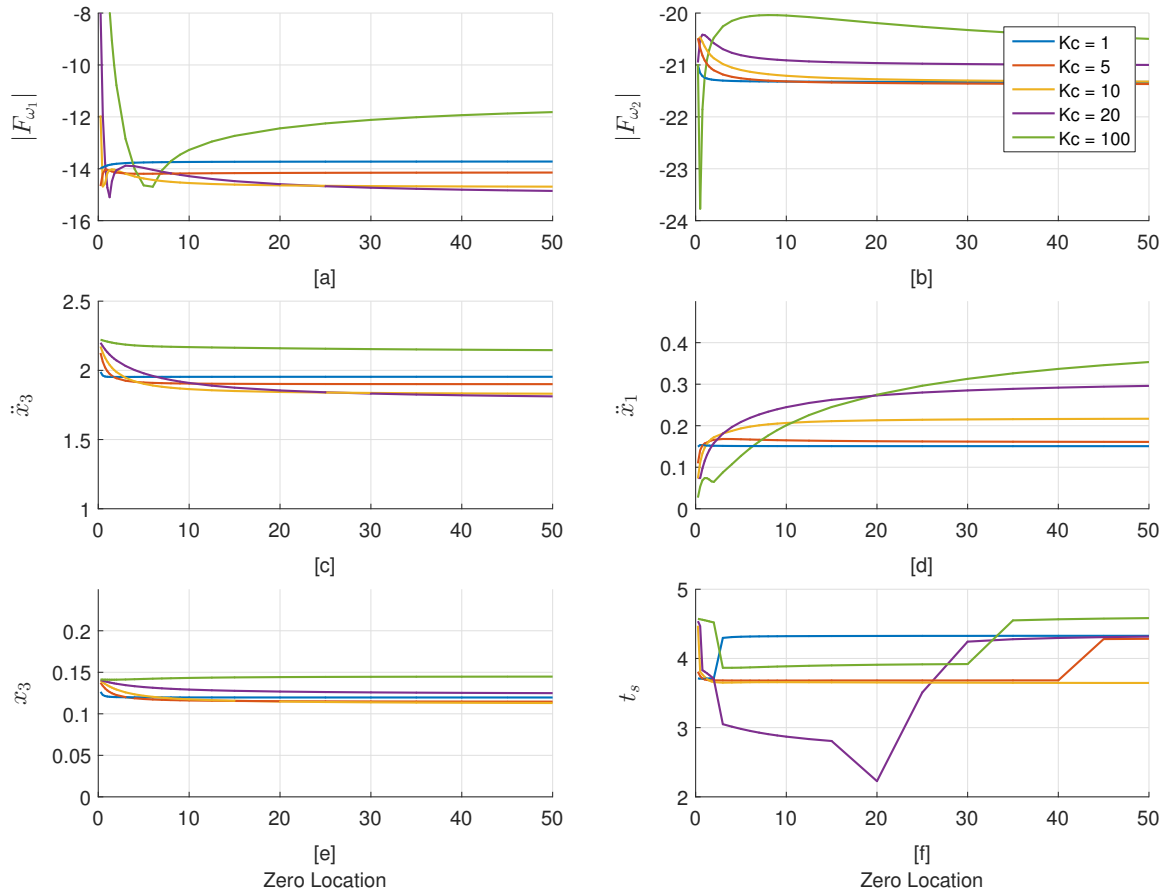


Figure 4.44. Response of the three-mass system for a versine profile with $\kappa = 3$ using feedforward controller and -5% error in the natural frequencies. [a] and [b] show the average magnitude of the first and second modes, respectively. [c] shows the peak-to-peak acceleration of mass 3, while [d] shows the peak-to-peak acceleration of mass 1. [e] and [f] show the peak deflection and the settling time of mass 3.

damping ratio changes as a function of both the controller zero and the control gain. Because of this, the closed-loop system may damp out the residual vibrations faster or slower depending on the location of that zero and the magnitude of the gain.

Also, the frequency response plots of the closed-loop controlled system are directly correlated to these results. For example, Figure 4.16 showed that an increase in K_c will increase the level of energy in the frequency spectra. This is seen in the output of the controller, as measured by an FFT, and is also seen in the actual levels of residual vibration in this system.

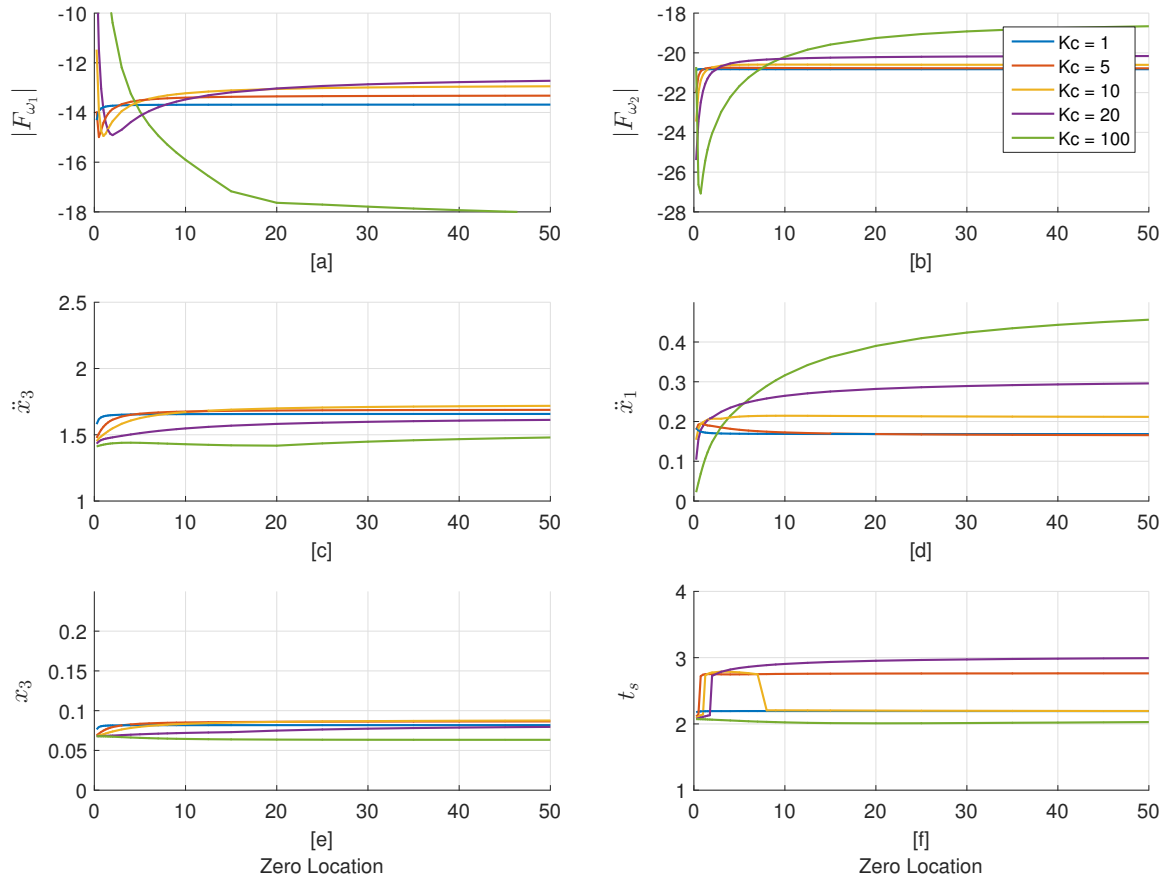


Figure 4.45. Response of the three-mass system for a ramped sinusoid profile with $\kappa = 3$ using feedforward controller and $+5\%$ error in the natural frequencies. [a] and [b] show the average magnitude of the first and second modes, respectively. [c] shows the peak-to-peak acceleration of mass 3, while [d] shows the peak-to-peak acceleration of mass 1. [e] and [f] show the peak deflection and the settling time of mass 3.

Another observation that can be made is that the ramped sinusoid is in general performing better than the versine. This is not surprising, as the main benefit of using the versine comes from its ability to deal with time-varying systems. Also, the versine has been left with a $\pm 5\%$ attenuation window, which means the errors that have been built into the natural frequencies are right at the edge of the frequencies attenuated by the versine. On the other hand, the ramped sinusoid, with its $\pm 10\%$ window, is better able to deal with the error in natural frequencies that has been incorporated. In other words, the ramped sinusoid is more robust than the versine in this instance, since it attenuates a larger window of frequencies.

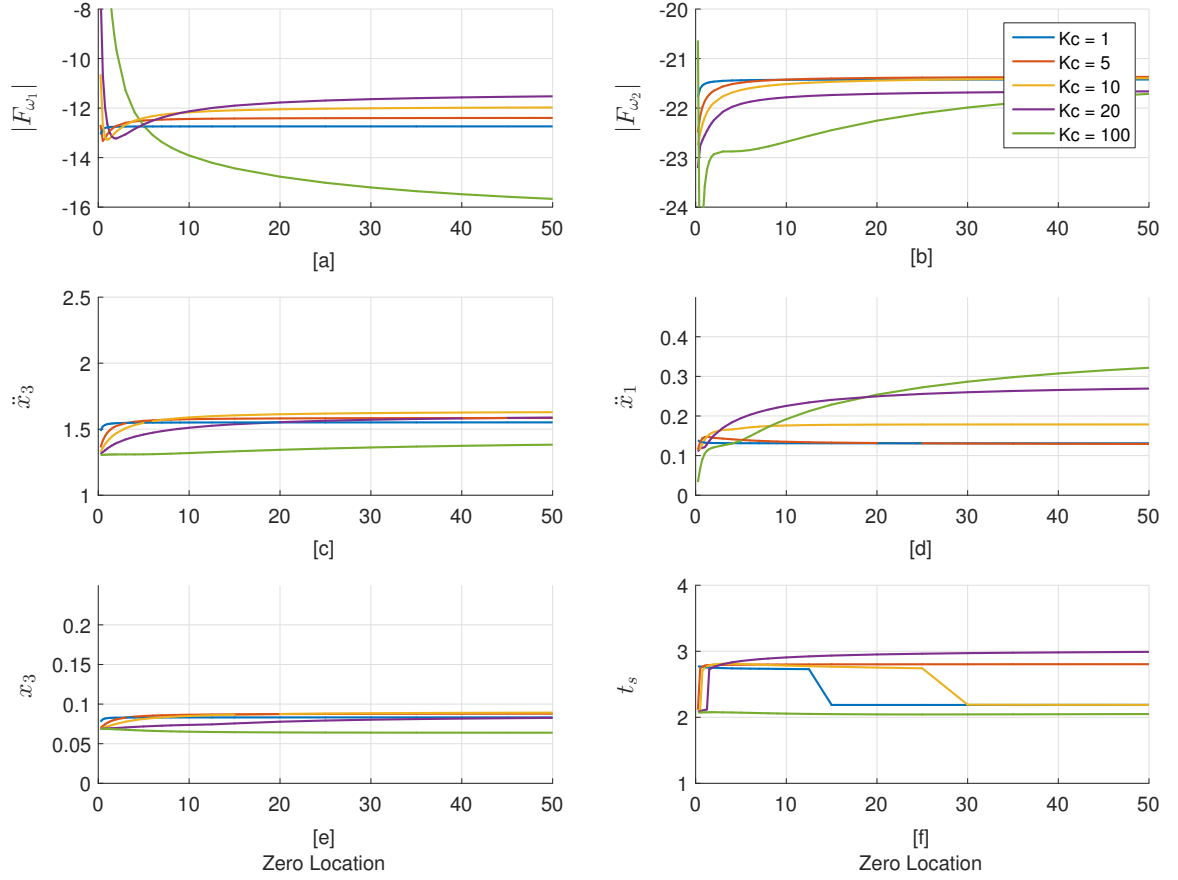


Figure 4.46. Response of the three-mass system for a versine profile with $\kappa = 3$ using feedforward controller and +5% error in the natural frequencies. [a] and [b] show the average magnitude of the first and second modes, respectively. [c] shows the peak-to-peak acceleration of mass 3, while [d] shows the peak-to-peak acceleration of mass 1. [e] and [f] show the peak deflection and the settling time of mass 3.

The magnitudes of the performance metrics for this system decrease for all controllers as κ is increased. This can be seen in Figures 4.47 and 4.48, where κ is increased to 9 and 15, respectively. This trend is the same for both the ramped sinusoid and the versine, including the +5%, -5%, and ideal cases. Since the trend is the same for all these cases, only a subset is shown here. The remaining results can be found in Appendix A.

These results may be compared to the similar results produced using the computed torque controller. Figures 4.49 through 4.52 show these results for $\kappa = 3$. Observe that the level of residual vibration is still directly correlated with the energy of the

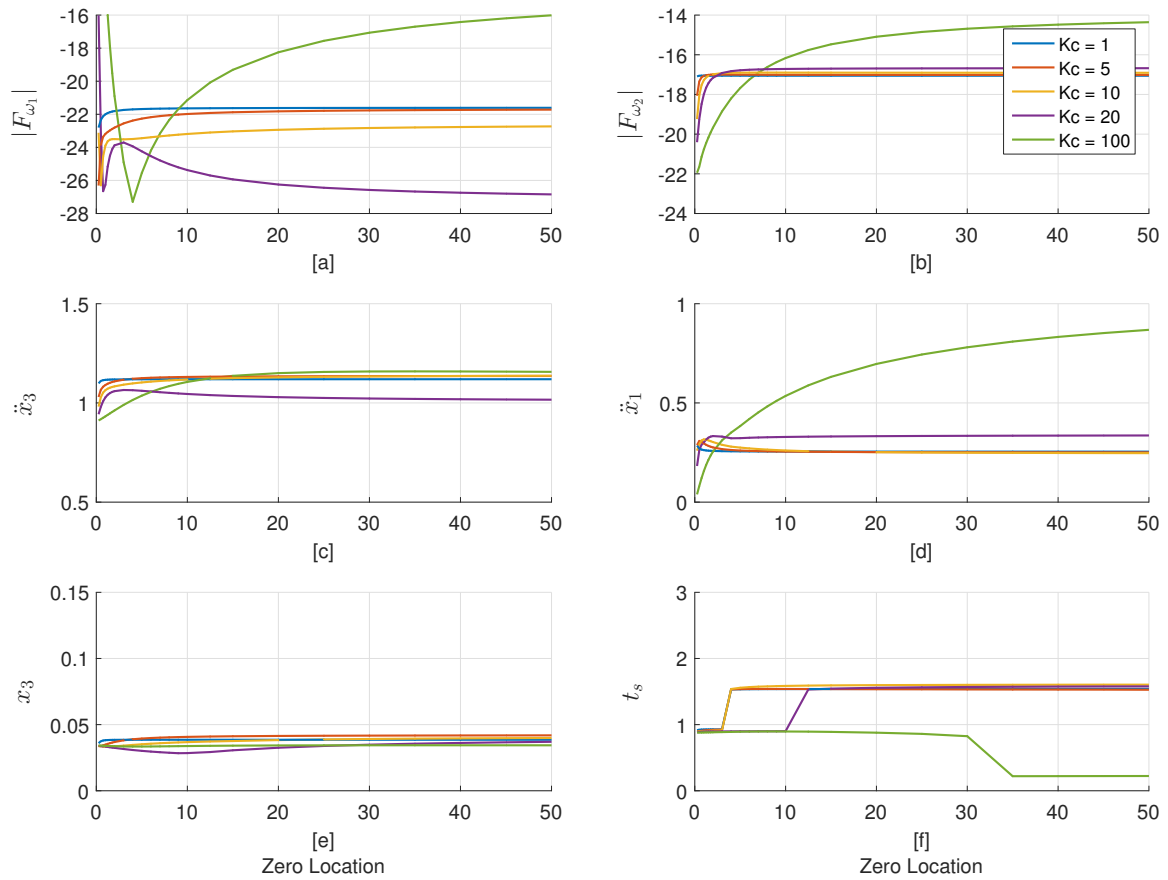


Figure 4.47. Response of the three-mass system for a ramped sinusoid profile with $\kappa = 9$ using feedforward controller and +5% error in the natural frequencies. [a] and [b] show the average magnitude of the first and second modes, respectively. [c] shows the peak-to-peak acceleration of mass 3, while [d] shows the peak-to-peak acceleration of mass 1. [e] and [f] show the peak deflection and the settling time of mass 3.

frequency spectra at the two modes. However, the variations here for different types of feedback controllers are much larger than previously seen.

Comparing Figures 4.49 and 4.50 for the ramped sinusoid, or by comparing Figures 4.51 and 4.52 for the versine, shows that, in general, the cases where there is +5% error perform better. This is identical to the trends already seen in the feedforward case. However, this is not nearly as clean a result as was present when the feedforward element was only added to the feedback. Here, the feedforward is incorporated into the closed-loop system and thus there are significant changes to the closed-loop dynamics.

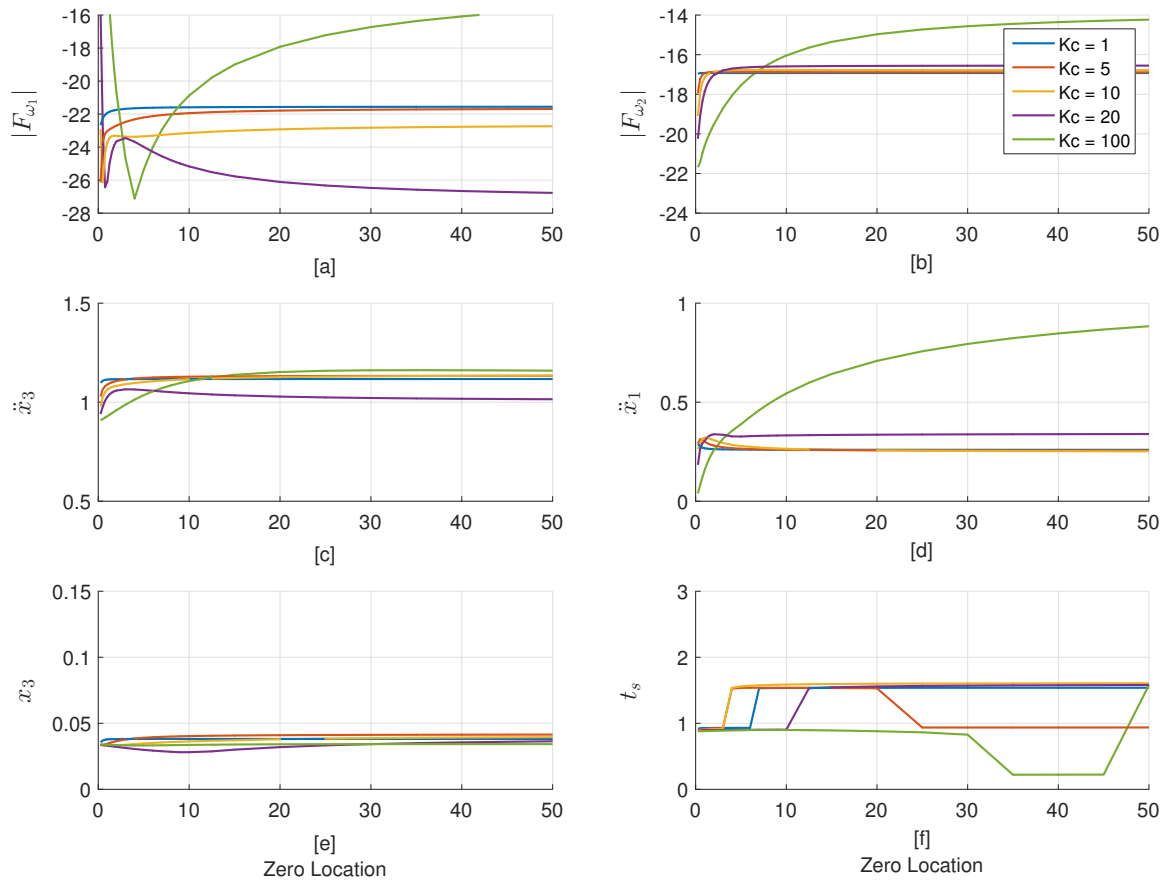


Figure 4.48. Response of the three-mass system for a ramped sinusoid profile with $\kappa = 15$ using feedforward controller and +5% error in the natural frequencies. [a] and [b] show the average magnitude of the first and second modes, respectively. [c] shows the peak-to-peak acceleration of mass 3, while [d] shows the peak-to-peak acceleration of mass 1. [e] and [f] show the peak deflection and the settling time of mass 3.

In these simulation results, these differences result in greater variations in the output for the different feedback controllers that are examined.

Each of these instances may be compared with its counterpart from utilizing the feedforward element outside the closed-loop. For example, Figures 4.45 and 4.50 may be compared. Note also that as κ is increased, the computed-torque-controlled systems also improve. This may be seen in Figure 4.53.

These results show that the overall trends remain the same between the feedforward and computed torque configurations, as the zero location and control gains are varied. However, the computed torque case is much more sensitive to these changes.

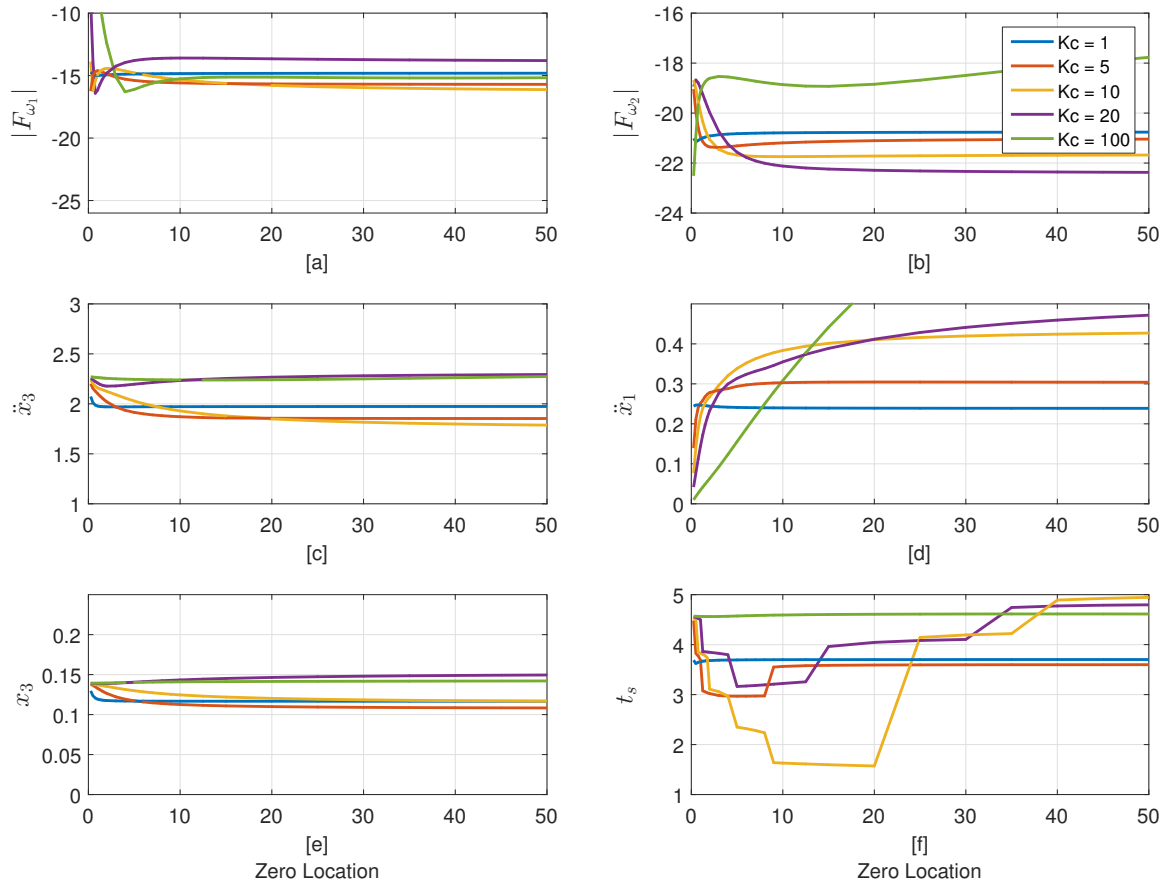


Figure 4.49. Response of the three-mass system for a ramped sinusoid profile with $\kappa = 3$ using computed torque controller and -5% error in the natural frequencies. [a] and [b] show the average magnitude of the first and second modes, respectively. [c] shows the peak-to-peak acceleration of mass 3, while [d] shows the peak-to-peak acceleration of mass 1. [e] and [f] show the peak deflection and the settling time of mass 3.

These similarities between the two closed-loop systems are useful, as they seem to imply that the analysis of the closed-loop that has been completed in this chapter may in fact carry over to other types of controller architectures. Note that the remaining cases where PD is utilized with the computed torque closed-loop system may be found in Appendix A.

One other observation that can be made about the computed torque configuration is that in many cases it starts to perform very poorly if the controller zero z_{pd} is placed too far into the LHP, which was not seen in the feedforward case. This may be due

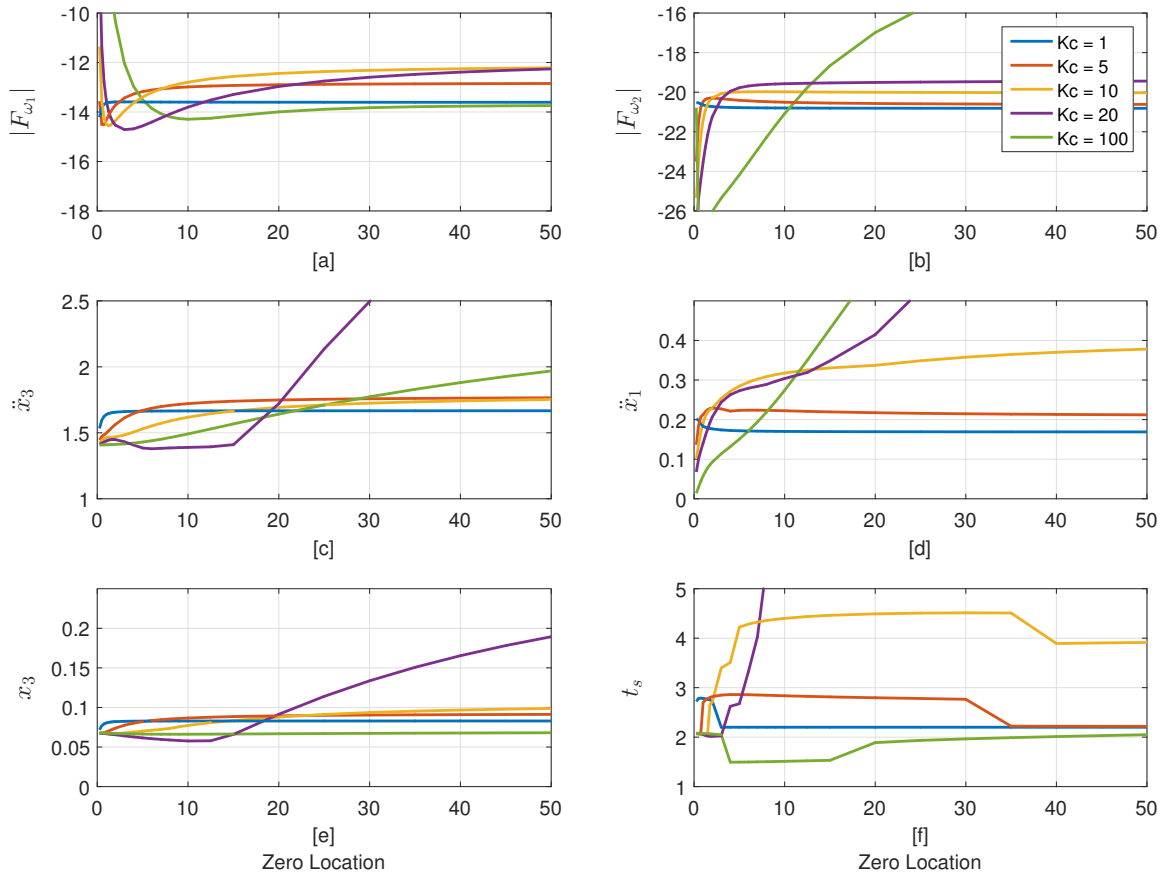


Figure 4.50. Response of the three-mass system for a ramped sinusoid profile with $\kappa = 3$ using computed torque controller and +5% error in the natural frequencies. [a] and [b] show the average magnitude of the first and second modes, respectively. [c] shows the peak-to-peak acceleration of mass 3, while [d] shows the peak-to-peak acceleration of mass 1. [e] and [f] show the peak deflection and the settling time of mass 3.

to the amplification of the higher frequencies that is present in the PD controller. To study this in greater detail, the Lead-Lag compensator is implemented.

First, the feedforward closed-loop system is studied. Figures 4.54 and 4.55 show the performance of a Lead-Lag compensator where $\omega_{center} = 10 \frac{\text{rad}}{\text{s}}$, $\omega_{width} = 1 \frac{\text{rad}}{\text{s}}$, and the control gain and ratio a are varied. Notice that for instances with either low gains or very high gains the Lead-Lag compensator does not perform well. However, for gains in between the two extremes the Lead-Lag system is quite consistent.

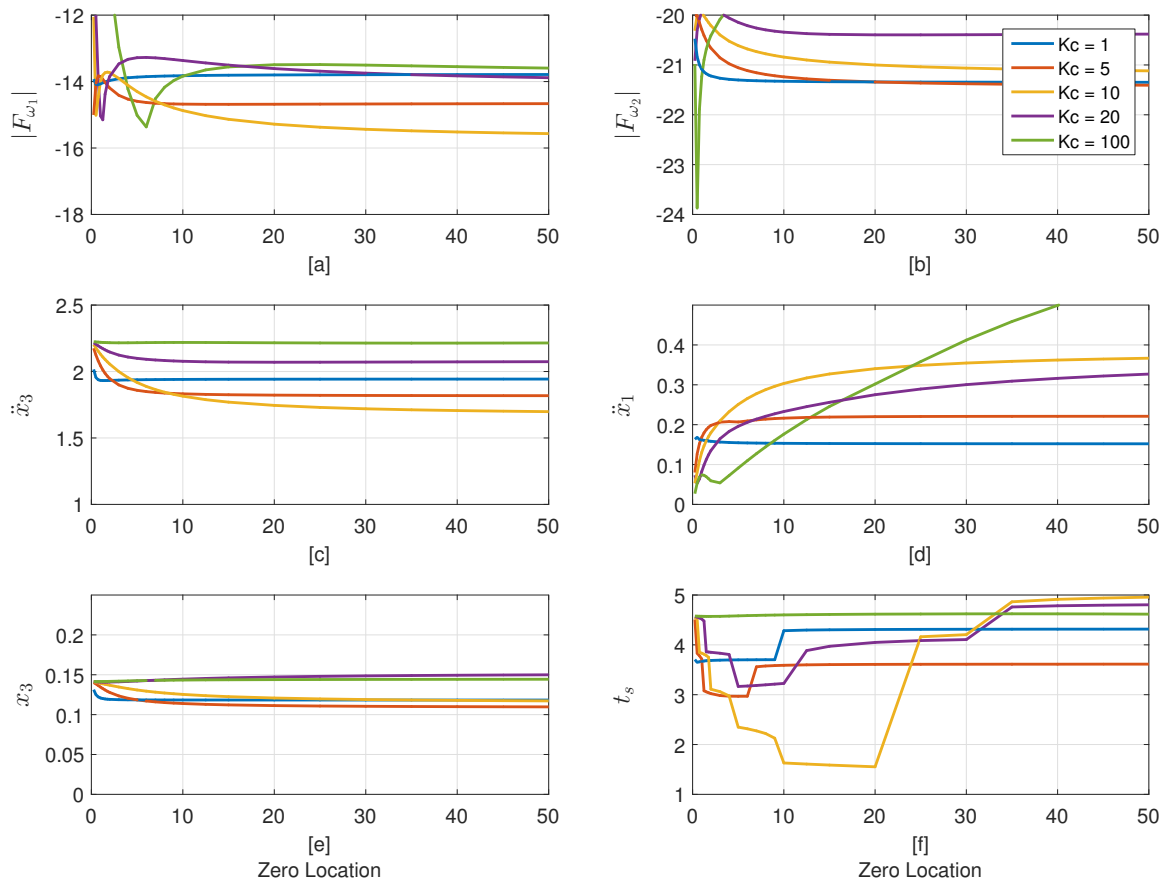


Figure 4.51. Response of the three-mass system for a versine profile with $\kappa = 3$ using computed torque controller and -5% error in the natural frequencies. [a] and [b] show the average magnitude of the first and second modes, respectively. [c] shows the peak-to-peak acceleration of mass 3, while [d] shows the peak-to-peak acceleration of mass 1. [e] and [f] show the peak deflection and the settling time of mass 3.

There is not much variation in performance in this middle range of control gains for variations in K_c or a .

The controllers of Figures 4.54 and 4.55 are attempting to create a window large enough to cover both of the system modes. However, this leads to a wide range of frequencies having lower magnitudes. An alternate strategy would be to attempt to be more precise in this goal, which is done by using a smaller attenuation window. Figures 4.56 and 4.57 show one such instance, where the Lead-Lag compensator is designed to diminish the energy at only the first mode. Observe that while the overall responses are similar for these systems, utilizing a smaller window in the Lead-Lag

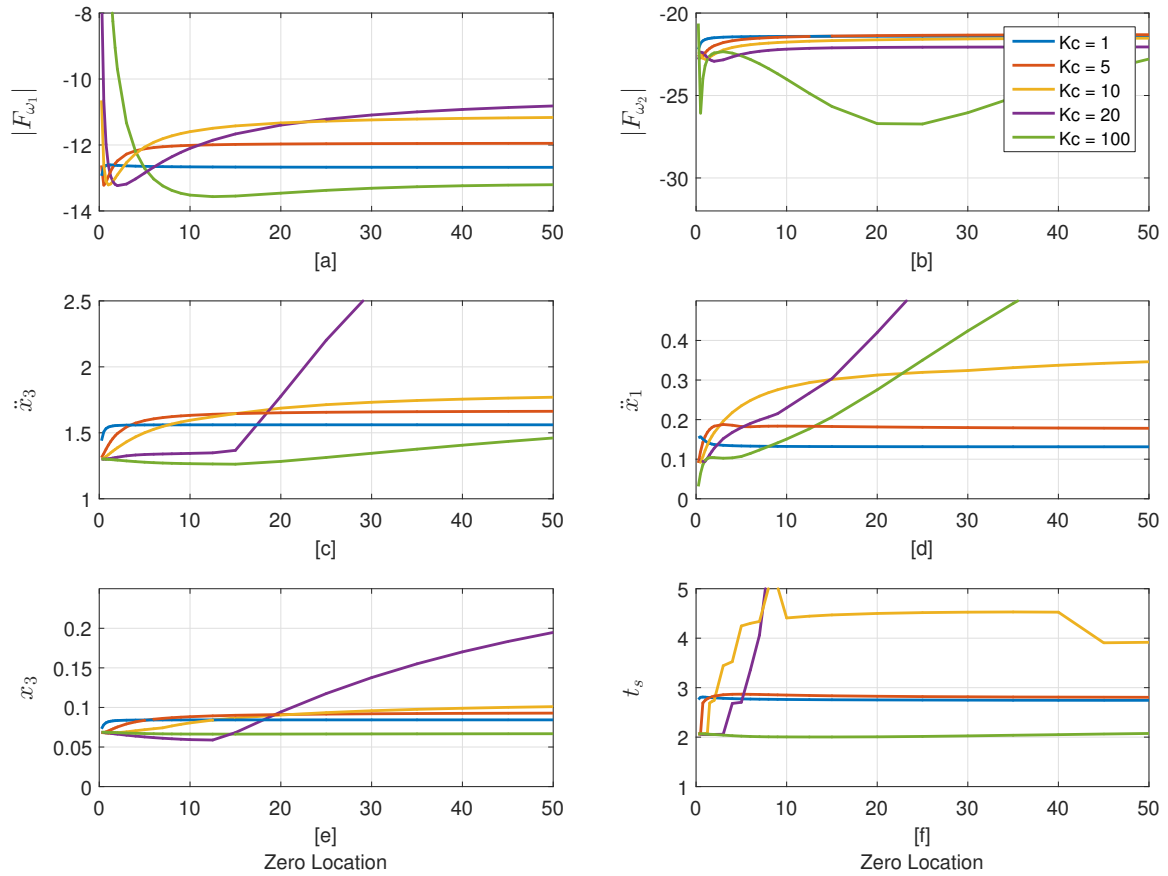


Figure 4.52. Response of the three-mass system for a versine profile with $\kappa = 3$ using computed torque controller and +5% error in the natural frequencies. [a] and [b] show the average magnitude of the first and second modes, respectively. [c] shows the peak-to-peak acceleration of mass 3, while [d] shows the peak-to-peak acceleration of mass 1. [e] and [f] show the peak deflection and the settling time of mass 3.

controller performs better for a much larger range of control gains. This is partly because it is not trying to do everything all at once, which is generally not ideal. This result was actually predicted by the frequency domain analysis of section 4.4.1, where Figure 4.19 shows that the closed-loop systems that have $\omega_{center} = 10 \frac{\text{rad}}{\text{s}}$ tend to inject slightly more energy into the controller signal, but overall the response was fairly consistent.

Another interesting result that can be seen here is that the Lead-Lag controllers are worse than the PD controllers for cases with -5% error, but better when there is $+5\%$ error. Note that the Lead-Lag compensator is utilizing much higher control gains

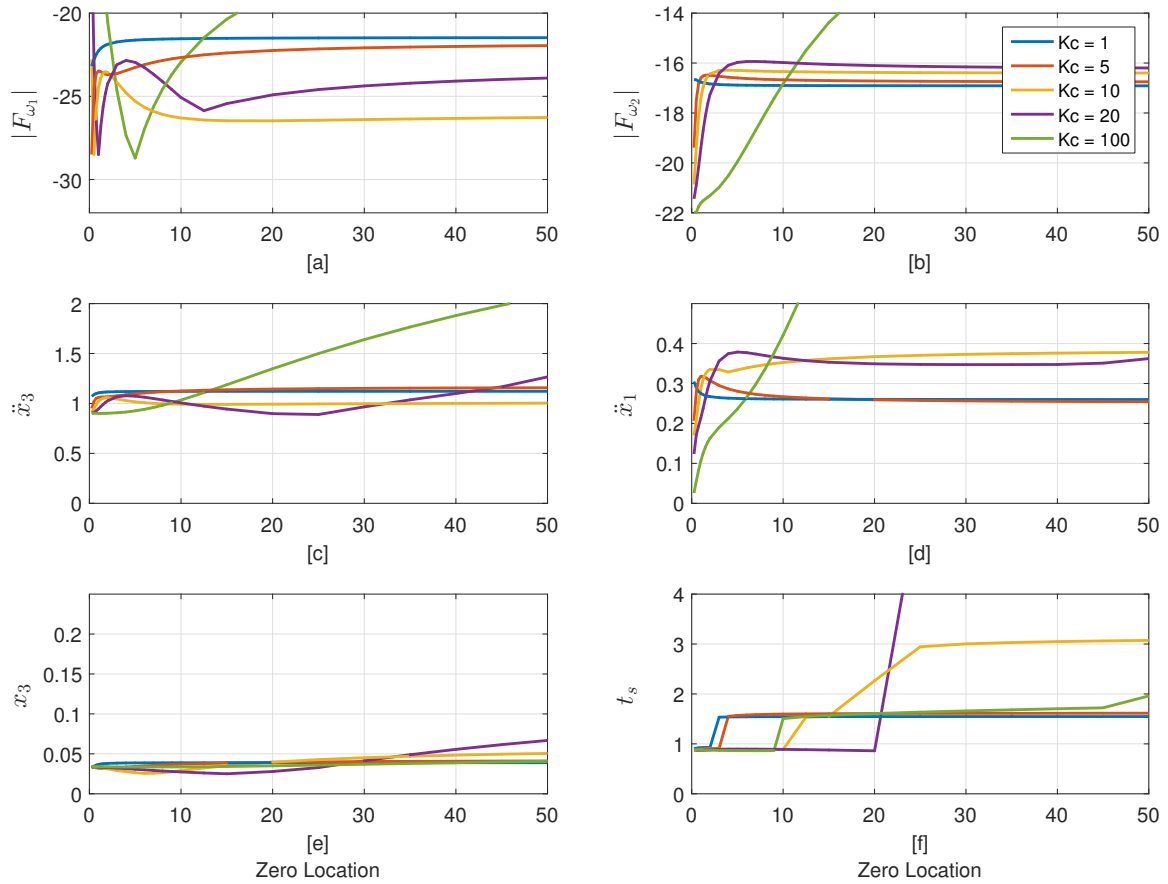


Figure 4.53. Response of the three-mass system for a ramped sinusoid profile with $\kappa = 15$ using computed torque controller and $+5\%$ error in the natural frequencies. [a] and [b] show the average magnitude of the first and second modes, respectively. [c] shows the peak-to-peak acceleration of mass 3, while [d] shows the peak-to-peak acceleration of mass 1. [e] and [f] show the peak deflection and the settling time of mass 3.

than the PD controller, partly because it needs to ensure that the system remains stable. However, this may end up injecting more energy back into the modes of the system, as can be seen in the Bode plots of section 4.4.1. While an attempt has been made to minimize the energy at the natural modes, this does not help much if the entire magnitude plot needs to be shifted upwards.

The computed torque controller can also be examined using Lead-Lag compensators instead of PD controllers. The results are shown in Figures 4.58 and 4.59. Observe that these results are much cleaner than the corresponding figures that uti-

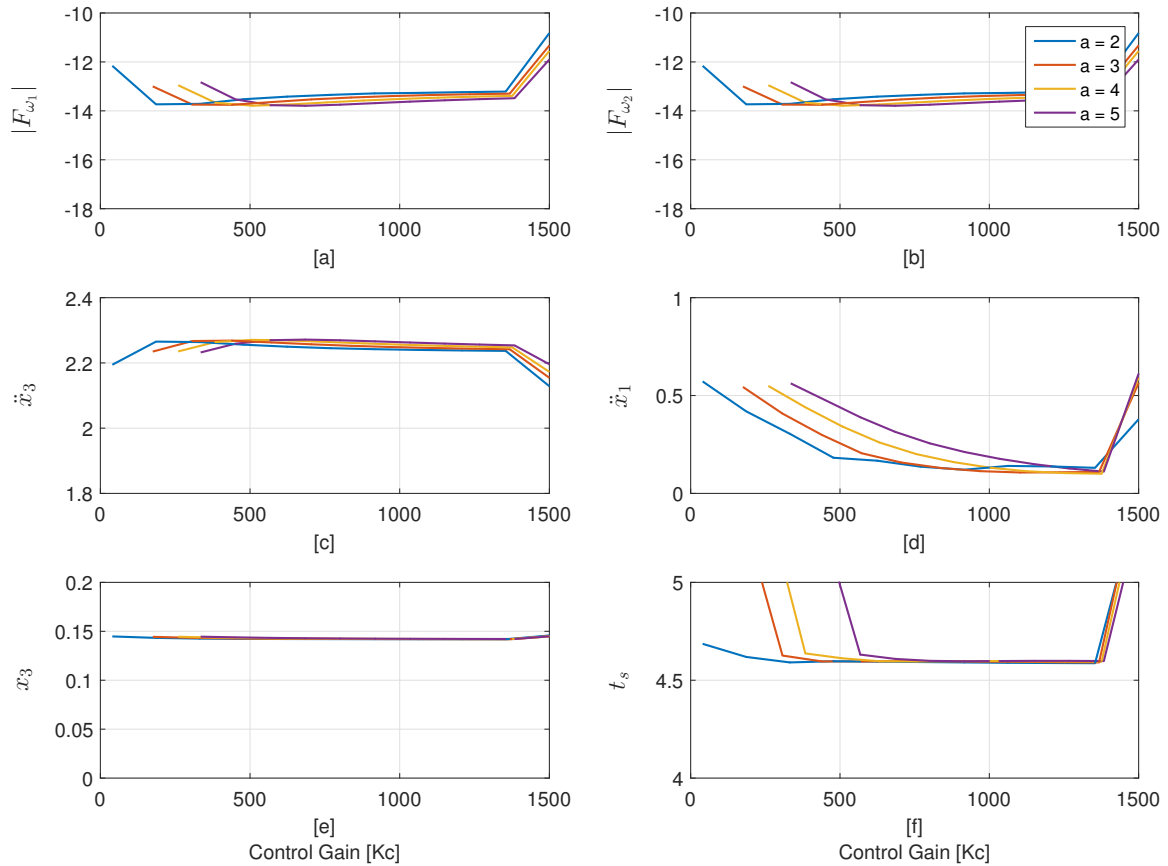


Figure 4.54. Response of the three-mass system for a versine profile with $\kappa = 3$ when using feedforward control with a Lead-Lag compensator with $\omega_{center} = 10 \frac{rad}{s}$, $\omega_{width} = 1 \frac{rad}{s}$ and a -5% error in the natural frequencies. [a] and [b] show the average magnitude of the first and second modes, respectively. [c] shows the peak-to-peak acceleration of mass 3, while [d] shows the peak-to-peak acceleration of mass 1. [e] and [f] show the peak deflection and the settling time of mass 3.

lize PD control in the Computed Torque arrangement. Even with the feedforward controller added to the closed loop, these results still show consistent performance for a wide range of control gains and values of the pole-zero ratio a .

Note that once a controller is set to a given setting, the system will achieve better performance as κ is increased, regardless of the controller that is applied. This means that once a controller has been designed, the input of the system can still be manipulated to improve performance. This is not a new result, as it is the

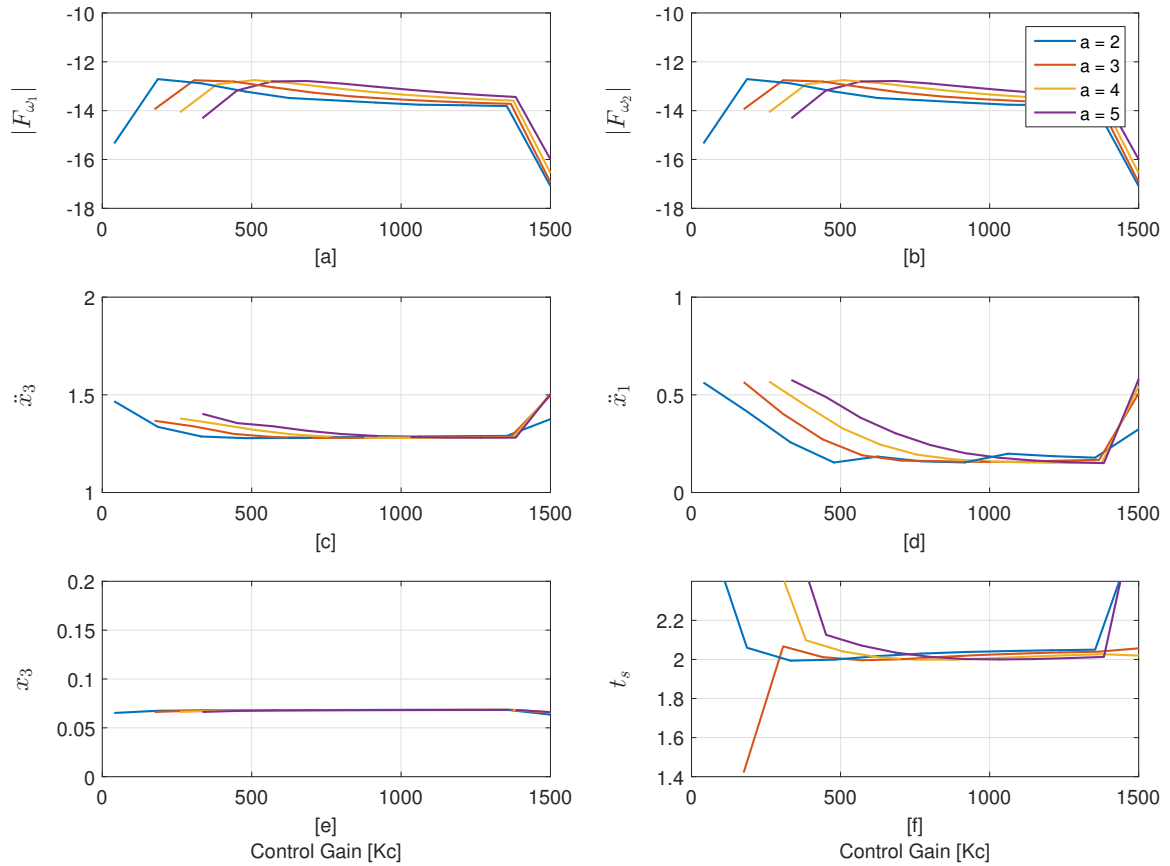


Figure 4.55. Response of the three-mass system for a versine profile with $\kappa = 3$ when using feedforward control with a Lead-Lag compensator with $\omega_{center} = 10 \frac{rad}{s}$, $\omega_{width} = 1 \frac{rad}{s}$ and a +5% error in the natural frequencies. [a] and [b] show the average magnitude of the first and second modes, respectively. [c] shows the peak-to-peak acceleration of mass 3, while [d] shows the peak-to-peak acceleration of mass 1. [e] and [f] show the peak deflection and the settling time of mass 3.

entire basis for the field of command shaping. However, these simulations do provide validation that this in fact does hold true.

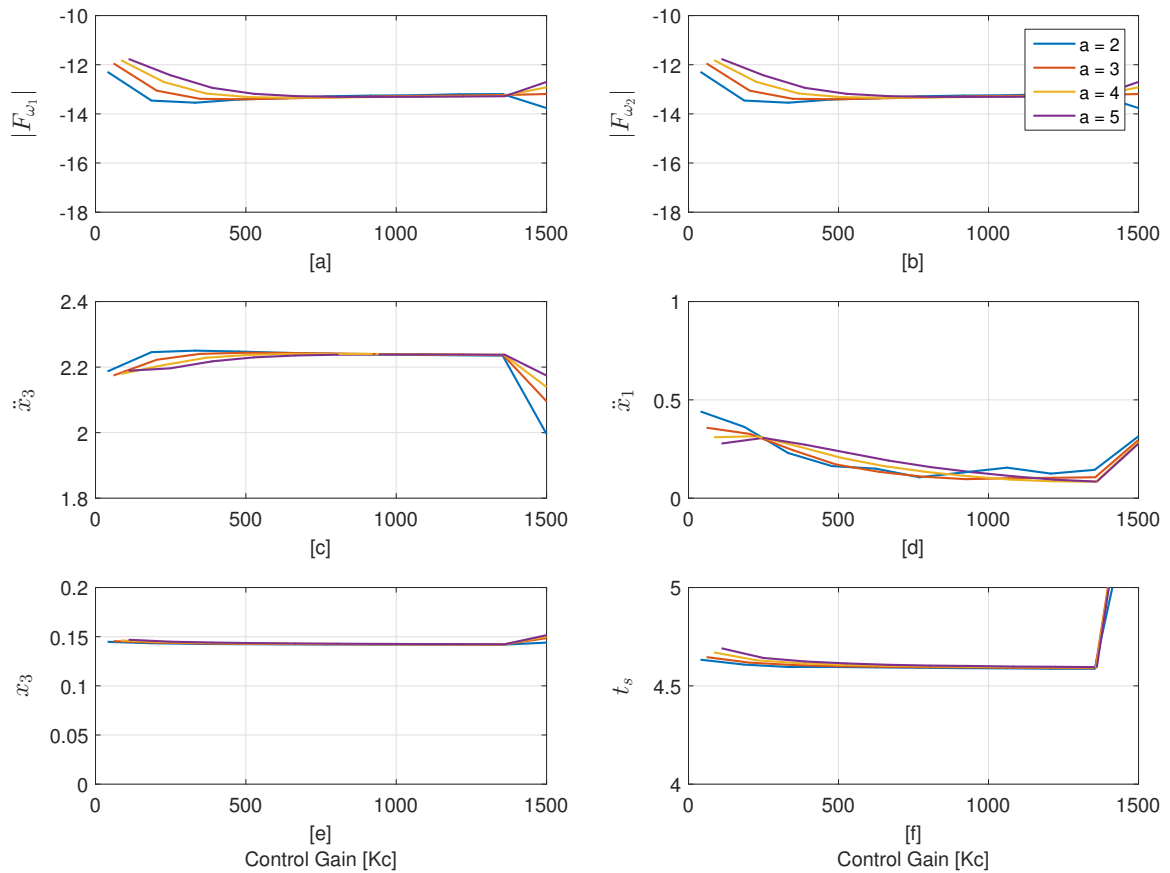


Figure 4.56. Response of the three-mass system for a versine profile with $\kappa = 3$ when using feedforward control with a Lead-Lag compensator with $\omega_{center} = 5 \frac{rad}{s}$, $\omega_{width} = 1 \frac{rad}{s}$ and a -5% error in the natural frequencies. [a] and [b] show the average magnitude of the first and second modes, respectively. [c] shows the peak-to-peak acceleration of mass 3, while [d] shows the peak-to-peak acceleration of mass 1. [e] and [f] show the peak deflection and the settling time of mass 3.

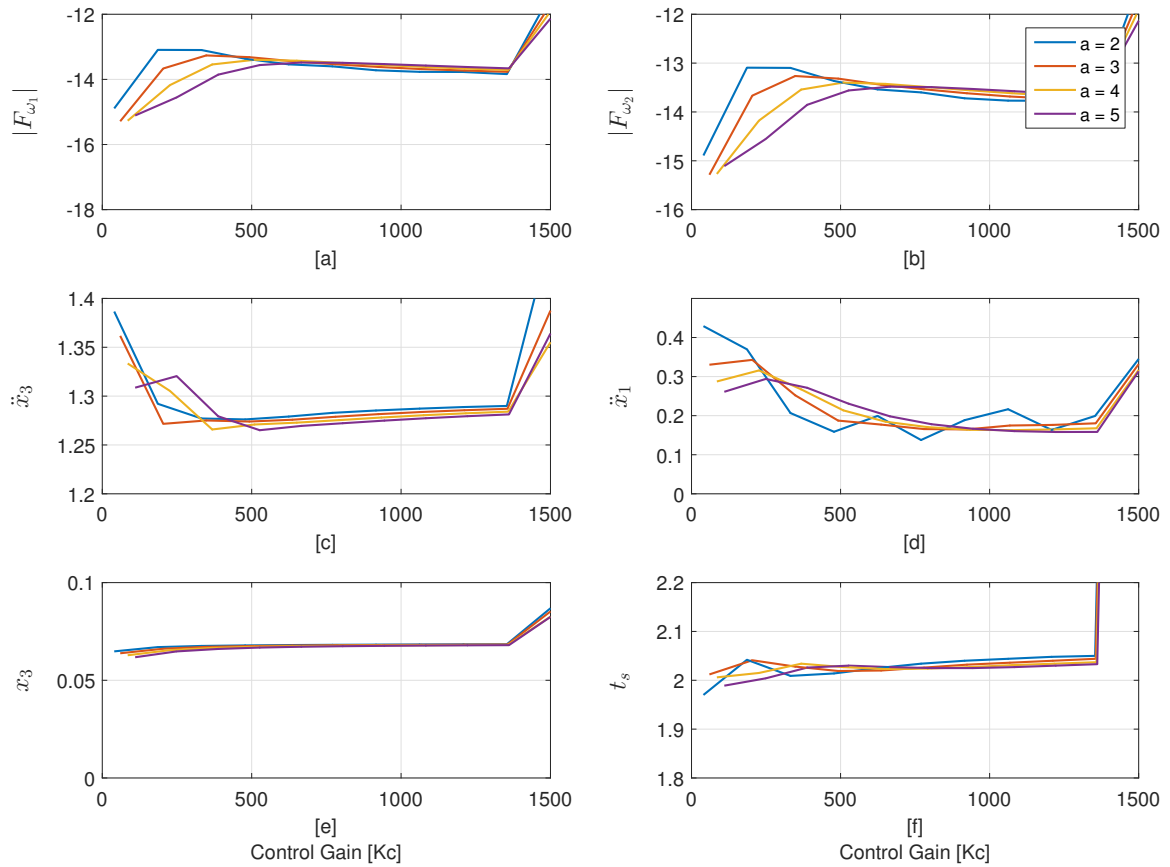


Figure 4.57. Response of the three-mass system for a versine profile with $\kappa = 3$ when using feedforward control with a Lead-Lag compensator with $\omega_{center} = 5 \frac{rad}{s}$, $\omega_{width} = 1 \frac{rad}{s}$ and a +5% error in the natural frequencies. [a] and [b] show the average magnitude of the first and second modes, respectively. [c] shows the peak-to-peak acceleration of mass 3, while [d] shows the peak-to-peak acceleration of mass 1. [e] and [f] show the peak deflection and the settling time of mass 3.

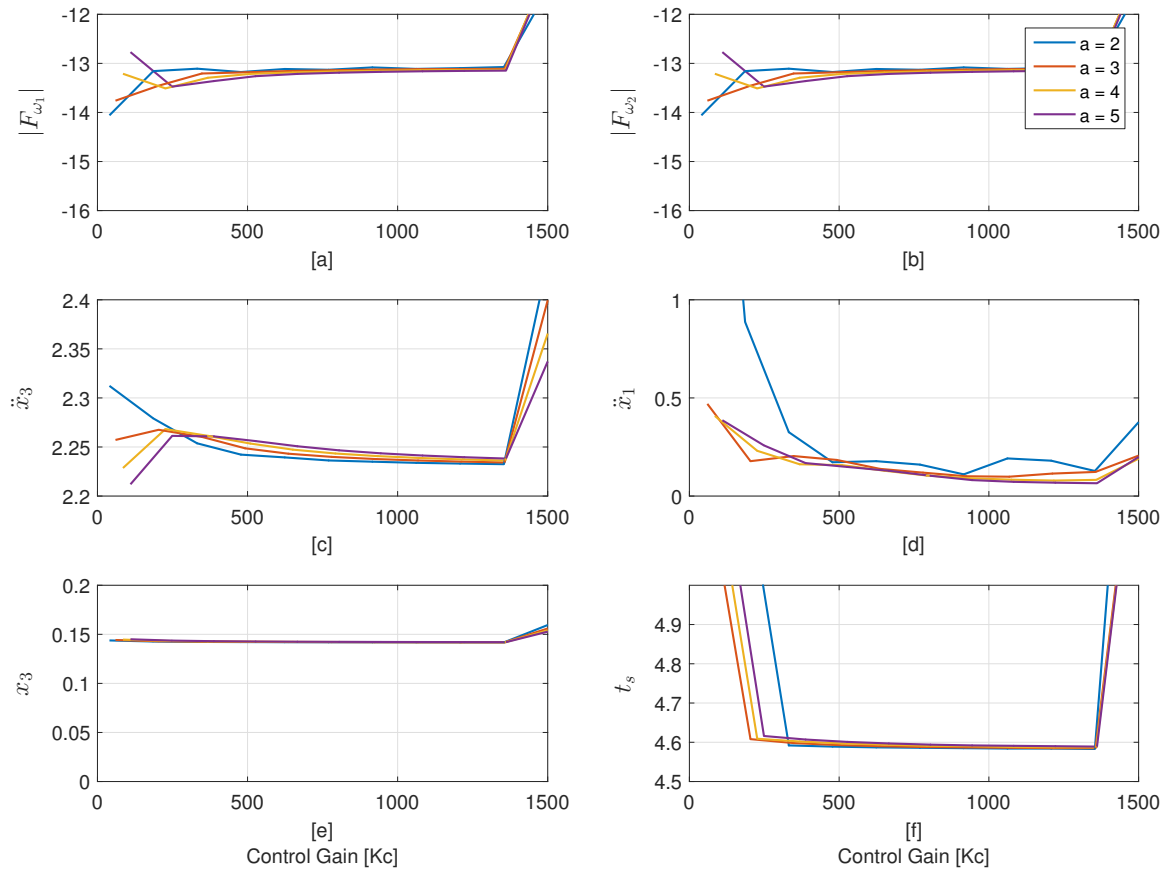


Figure 4.58. Response of the three-mass system for a versine profile with $\kappa = 3$ when using computed torque control with a Lead-Lag compensator with $\omega_{center} = 5 \frac{rad}{s}$, $\omega_{width} = 1 \frac{rad}{s}$ and a -5% error in the natural frequencies. [a] and [b] show the average magnitude of the first and second modes, respectively. [c] shows the peak-to-peak acceleration of mass 3, while [d] shows the peak-to-peak acceleration of mass 1. [e] and [f] show the peak deflection and the settling time of mass 3.

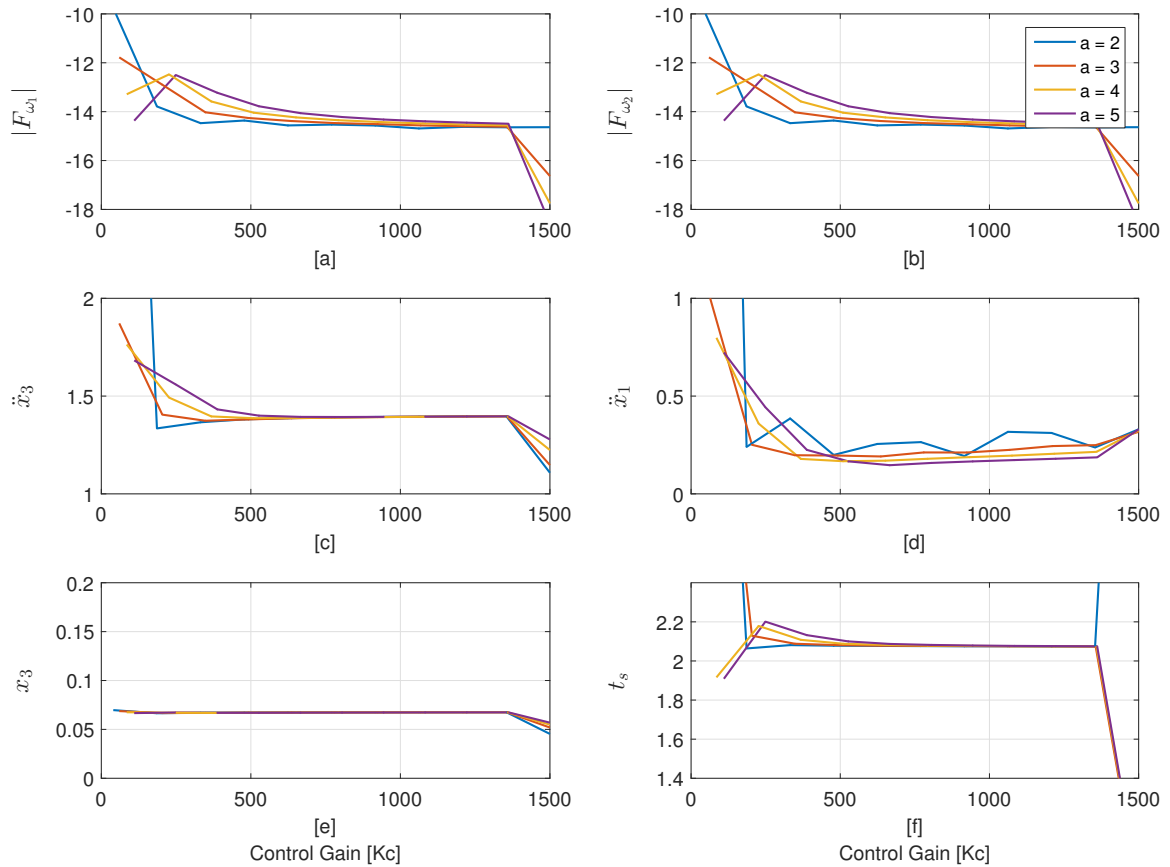


Figure 4.59. Response of the three-mass system for a versine profile with $\kappa = 3$ when using computed torque control with a Lead-Lag compensator with $\omega_{center} = 5 \frac{rad}{s}$, $\omega_{width} = 1 \frac{rad}{s}$ and a -5% error in the natural frequencies. [a] and [b] show the average magnitude of the first and second modes, respectively. [c] shows the peak-to-peak acceleration of mass 3, while [d] shows the peak-to-peak acceleration of mass 1. [e] and [f] show the peak deflection and the settling time of mass 3.

CHAPTER 5. APPLICATION TO THE FLEXIBLE-JOINT ROBOT

Using the results found from the three-mass system, the performance of the two-link flexible-joint robot can now be examined. This chapter will perform this study in order to analyze the feedback controllers of the robot that was modeled in chapter 3. Section 5.1 will provide a description of the experimental hardware and the interfaces between the robot and the computer that are used to control and measure this system. Section 5.2 will then describe how to implement either PD or Lead-Lag control digitally and sections 5.3 and 5.4 will provide the results of the simulations and experiments that test the performance of different controllers of the two-link flexible-joint robot when applying different input profiles.

5.1 Robot Hardware

The two-link flexible-joint robot is driven by two permanent-magnet (PM) direct-current (DC) motors. The motor for the first link has a maximum torque of 2.47 Nm, which occurs at a current of 21.2 A. The second link uses an Inland T-3108-A motor with a maximum torque of 1.35 Nm, which the motor achieves around a current of 2 A. The torque constants are $0.118 \frac{\text{Nm}}{\text{A}}$ and $0.61 \frac{\text{Nm}}{\text{A}}$, respectively. Both motors are driven by Advanced Motion Control brushless pulse-width-modulated (PWM) servo amplifiers, which convert the input voltage signals into current signals. These motor currents are measured using current transducers and are used to calculate the torque provided by each motor. This uses the relationship between the current and the torque, as it is known that they are directly proportional to each other. This can be written as

$$T_m = K_m i, \quad [\text{Nm}] \quad (5.1)$$

where T_m is the torque of the motor, K_m is the torque constant, and i is the current.

Whenever current passes through a circuit, the resistance present will generate heat. This physical phenomenon is known as Joule heating. If the current becomes too large, the windings of a motor could become damaged due to the excessive amount of heat generated. Because of this, protections are typically built in to the circuit design in order to protect the motors from overheating. For the robot, the circuit that contains the motors has been outfitted with Littlefuse 372-Series time-lag fuses, which will burn out if the current becomes too large. This will occur before the motor windings are damaged and thus will prevent damage to the motors themselves.

Four encoders, each having a resolution of $4000 \frac{\text{counts}}{\text{revolution}}$, are used to measure the positions of the links and the motors. Finite differences are applied to obtain the corresponding velocity signals. Signal conditioning is performed using fourth-order Butterworth filters, as calculating the velocities using finite differences is a numerical problem that is known to be ill-conditioned and can be fairly noisy. This filtering will help to smooth out these signals, and will ensure that issues such as aliasing do not occur.

The acceleration of the links is found in the corresponding link reference frame using capacitive accelerometers that are placed at the end of each link. Measuring the acceleration of the links directly is preferable to deriving the acceleration after implementing second-order finite differences on the encoder output, due to the numerical issues that arise.

A National Instruments PCI-7831R Field-Programmable Gate Array (FPGA) is used to deliver high-speed processing of the signals as well as control of the system. The PCI-7831R has multiple digital and analog Input/Output (I/O) ports that measure the sensors of the robot and provide the command outputs to the motors. This is programmed using LabVIEW on a host computer that has an Ethernet connection with the FPGA. The FPGA is then connected to the motors and sensors using two SCB-68 shielded connector blocks from National Instruments.

All experiments contained in this work will use motion profiles that start at $\theta_{1,i} = \theta_{2,i} = 0$ rad and end at $\theta_{1,f} = \theta_{2,f} = 1.2$ rad. This corresponds to the motors moving

from $\theta_{3,i} = \theta_{4,i} = 0$ rad to $\theta_{3,f} = \theta_{4,f} = 6$ rad since the gear ratio of the chain drives is 5. A move time of 2 seconds is predetermined for all point-to-point motion contained in this work, and a sampling rate of 2 kHz is utilized.

5.2 Digital Implementation of Feedback Control

The flexible-joint robot applies the computed torque approach in order to control the motors of the system. This applies closed-loop feedback on the motors to reliably provide fast point-to-point motion. However, in order to implement either PD control or Lead-Lag control on the robot, the discrete forms of these control laws are needed.

In the case of PD control, this is easy to derive and is very well known. For the case of the robot, the velocity signals have already been calculated using backward differences, so those signals can be applied. This digital controller may be given as

$$u[k] = K_p e[k] + K_v \dot{e}[k], \quad (5.2)$$

where $u[k]$ is the control output, $e[k]$ is the error in the motor angle, and $\dot{e}[k]$ is the error in the motor velocity, all calculated at the current instant in time. Note that the backwards difference equations will also require the previous position measurement, and can be given as

$$\dot{e}[k] = \frac{e[k] - e[k-1]}{T_s}, \quad (5.3)$$

where T_s is the sampling rate. This is also known as the backwards Euler approximation.

Finding the discrete equivalent of the Lead-Lag controller is a more complicated task. Note that there are two methods to designing digital controllers. One approach is to start by developing the control law in the discrete domain, which is known as the direct approach. The other method is to design a continuous controller and then transform it by finding an equivalent discrete controller. This process is known as

emulation. Since it is desirable to be able to use the same controller design as was studied in chapter 4, the second method will be applied here.

The first step required in order to emulate a continuous Lead-Lag compensator is to transform it from the continuous s-domain into the discrete z-domain. There are several mappings that will accomplish this, with one of the most common known as Tustin's method. Tustin's method is a little more complicated than some of the other transformations, but it does have the nice property that it preserves the region of stability. That is, the stable region of the s-domain, the LHP, is mapped directly to the stable region of the z-domain, which is the unit circle.

Tustin's method is applied using the mapping

$$s = \left(\frac{2}{T_s} \frac{z-1}{z+1} \right), \quad (5.4)$$

which is also known as the Bilinear Transformation. Plugging Equation (5.4) into Equation (4.71) results in

$$C_{Lead-Lag}(z) = K_c \left(\frac{\left(\frac{1}{\omega_{z,lead}} \right) \left(\frac{2}{T_s} \frac{z-1}{z+1} \right) + 1}{\left(\frac{1}{\omega_{p,lead}} \right) \left(\frac{2}{T_s} \frac{z-1}{z+1} \right) + 1} \right) \left(\frac{\left(\frac{1}{\omega_{z,lag}} \right) \left(\frac{2}{T_s} \frac{z-1}{z+1} \right) + 1}{\left(\frac{1}{\omega_{p,lag}} \right) \left(\frac{2}{T_s} \frac{z-1}{z+1} \right) + 1} \right), \quad (5.5)$$

which can be simplified by multiplying both sides by $\frac{(T_s(z+1))^2}{(T_s(z+1))^2}$. This results in

$$C_{Lead-Lag}(z) = K_c \left(\frac{T_s(z+1) + \left(\frac{2}{\omega_{z,lead}} \right) (z-1)}{T_s(z+1) + \left(\frac{2}{\omega_{p,lead}} \right) (z-1)} \right) \left(\frac{T_s(z+1) + \left(\frac{2}{\omega_{z,lag}} \right) (z-1)}{T_s(z+1) + \left(\frac{2}{\omega_{p,lag}} \right) (z-1)} \right). \quad (5.6)$$

To simplify this even further, the following terms may be defined:

$$r_1 = T_s + \left(\frac{2}{\omega_{z,lead}} \right), \quad (5.7)$$

$$r_2 = T_s - \left(\frac{2}{\omega_{z,lead}} \right), \quad (5.8)$$

$$r_3 = T_s + \left(\frac{2}{\omega_{z,lag}} \right), \quad (5.9)$$

$$r_4 = T_s - \left(\frac{2}{\omega_{z,lag}}\right), \quad (5.10)$$

$$s_1 = T_s + \left(\frac{2}{\omega_{p,lead}}\right), \quad (5.11)$$

$$s_2 = T_s - \left(\frac{2}{\omega_{p,lead}}\right), \quad (5.12)$$

$$s_3 = T_s + \left(\frac{2}{\omega_{p,lag}}\right), \quad (5.13)$$

$$s_4 = T_s - \left(\frac{2}{\omega_{p,lag}}\right), \quad (5.14)$$

which allows the Lead-Lag compensator to be given as

$$C_{Lead-Lag}(z) = \frac{U(z)}{E(z)} = K_c \left(\frac{r_1 z + r_2}{s_1 z + s_2} \right) \left(\frac{r_3 z + r_4}{s_3 z + s_4} \right), \quad (5.15)$$

$$C_{Lead-Lag}(z) = \frac{U(z)}{E(z)} = K_c \left(\frac{r_1 r_4 z^2 + (r_2 r_3 + r_1 r_4) z^1 + r_2 r_4}{s_1 s_4 z^2 + (s_2 s_3 + s_1 s_4) z^1 + s_2 s_4} \right), \quad (5.16)$$

which is the discrete transfer function of the Lead-Lag compensator. Observe that the coefficients that are defined in Equations (5.7) through (5.14) are determined by the zeros and the poles of the continuous controller, as well as the sampling rate. Multiplying the numerator and denominator of Equation (5.16) by z^{-2} results in an alternate form of the controller, which is written as

$$C_{Lead-Lag}(z) = \frac{U(z)}{E(z)} = K_c \left(\frac{r_1 r_4 + (r_2 r_3 + r_1 r_4) z^{-1} + r_2 r_4 z^{-2}}{s_1 s_4 + (s_2 s_3 + s_1 s_4) z^{-1} + s_2 s_4 z^{-2}} \right). \quad (5.17)$$

The definition of the Z-Transform is

$$X(z) = \mathcal{Z}\{x[k]\} = \sum_{k=0}^{\infty} x[k] z^{-k}, \quad (5.18)$$

when defined for $k = 0, 1, 2, \dots, \infty$. This shows that the discrete signal is an infinite series of discrete data points. This can be represented in the time domain using the Kronecker delta function:

$$\delta(k) = \begin{cases} 1 & \text{if } k = 0 \\ 0 & \text{if } k \neq 0, \end{cases} \quad (5.19)$$

which can be shifted to any sampling instant. This results in a modified delta function, given as

$$\delta(n - k) = \begin{cases} 1 & \text{if } n = k \\ 0 & \text{if } n \neq k. \end{cases} \quad (5.20)$$

The Z-Transform of the Kronecker delta is 1. Likewise, when it is shifted in time to another sampling instant, its Z-Transform is z^{-k} , where it has been moved k time steps. This result can be applied here to transform Equation (5.17) back into the time domain. This derivation is performed as follows:

$$\begin{aligned} U(z)(s_1 s_4 + (s_2 s_3 + s_1 s_4)z^{-1} + s_2 s_4 z^{-2}) = \\ E(z)K_c(r_1 r_4 + (r_2 r_3 + r_1 r_4)z^{-1} + r_2 r_4 z^{-2}), \end{aligned} \quad (5.21)$$

$$\begin{aligned} s_1 s_4 u[k] + (s_2 s_3 + s_1 s_4)u[k - 1] + s_2 s_4 u[k - 2] = \\ K_c r_1 r_4 e[k] + K_c(r_2 r_3 + r_1 r_4)e[k - 1] + K_c r_2 r_4 e[k - 2], \end{aligned} \quad (5.22)$$

where solving for the current controller output gives

$$\begin{aligned} u[k] = -\left(\frac{(s_2 s_3 + s_1 s_4)}{s_1 s_4}\right)u[k - 1] - \left(\frac{s_2 s_4}{s_1 s_4}\right)u[k - 2] \\ + K_c \left(\frac{r_1 r_4}{s_1 s_4}\right)e[k] + K_c \left(\frac{(r_2 r_3 + r_1 r_4)}{s_1 s_4}\right)e[k - 1] + K_c \left(\frac{r_2 r_4}{s_1 s_4}\right)e[k - 2], \end{aligned} \quad (5.23)$$

where $u[k - 1]$ and $u[k - 2]$ are the last two controller outputs and $e[k]$, $e[k - 1]$, and $e[k - 2]$ are the current and past errors in the motor angles. Observe that Equation (5.23) is a difference equation that can be directly applied in a digital system, as it only depends on discrete samples of the signal and controller output up to the current

time. The only requirement here is that storing the past controller outputs and the past errors is required. This is because the control law needs to be able to read not only the current sample, but the previous two samples as well.

Note that, in order to ensure stability for a discrete controller, the sampling rate must be sufficiently fast. As noted previously, a 2 kHz sampling rate has been specified for this controller. This is fast enough to ensure that the closed-loop system for the robot remains stable. Also, note that sampling this quickly will not be an issue for the FPGA, as it has a processing speed measured in MHz. The analog output channels also have an update time of 1 μ s, which is much faster than required.

5.3 Simulation Results for the Flexible-Joint Robot

A simulation model has been created in Simulink for the two-link flexible-joint robot. This program applies the full Lagrangian model of the dynamics, as presented in section 3.4, although one change is made. Coulomb friction terms appear both in the simulation model, and also in the model-based portion of the computed torque controller when utilizing the Lagrangian. However, the values of these friction terms are notoriously hard to estimate in practice. Also, the $\text{sign}(\cdot)$ function that appears in the model-based portion of the controller can lead to chattering of the output. Because of these issues, the Coulomb friction is ignored in the robot simulation for both the robot model and the computed torque controller.

This simulation will use a sampling rate of 2 kHz, which matches the rate that is used on the robot itself. Quantization effects are added in order to simulate the digital nature of the controller. This includes quantizing the position feedback of the encoders to $4000 \frac{\text{counts}}{\text{revolution}}$ and including the Digital-to-Analog conversions of the controller output signals. The velocities of the link and motor angles are found by taking backward finite differences of the position feedback, as measured by the four encoders. These velocity measurements are then filtered using fourth-order Butterworth filters

with a cut-off frequency of 60 Hz. The physical limitations of the system are also included, including the saturation of the motor current.

Several cases are shown of the different types of feedback controllers, along with the different input profiles. This will include a combination of simulation and experimental results, which allows the cases to be analyzed first in simulation and then applied to the robot itself. This is done mainly to show how the performance of the robot varies with different controllers, and to show the Lead-Lag compensator successfully applied to the robot itself.

The controllers that are applied to the robot are labeled as follows. The Original PD controller uses the control gains that were utilized in the previous work done on the flexible-joint robot. These control gains are $K_{p,1} = 6400$, $K_{v,1} = 160$, $K_{p,2} = 400$, and $K_{v,2} = 40$. A second PD controller is tried where the control gains for the second link are kept the same, but the controller for the first link is changed. Here the overall gain of the controller is halved and the zero is moved to $z_{pd} = -20$. This corresponds to new control gains of $K_{p,1} = 3200$ and $K_{v,1} = 160$. The intent here is to see if the amount of energy added to natural modes by the feedback controller can be minimized by using the analysis from chapter 4, which showed that excessively high control gains may add energy to the natural modes. This new PD controller is labeled the Alternative PD controller. The simulated responses for these two controllers are shown in Figures 5.1 through 5.2. Note that these trials use a versine input with $\kappa = 6$.

For all simulation results the figures are presented as follows: The first row corresponds to the angular positions of the two links, θ_1 and θ_2 , while the second row shows the angular positions of the two motors, θ_3 and θ_4 . The third row gives the angular accelerations of the two links, $\ddot{\theta}_1$ and $\ddot{\theta}_2$, while the last row gives the torque signals sent to the motors, T_1 and T_2 .

A Lead-Lag Compensator is also implemented on the robot using the discrete control law that was derived in section 5.2. It is important to be careful when designing this controller, as it is crucial that added implementation issues, such as saturation of

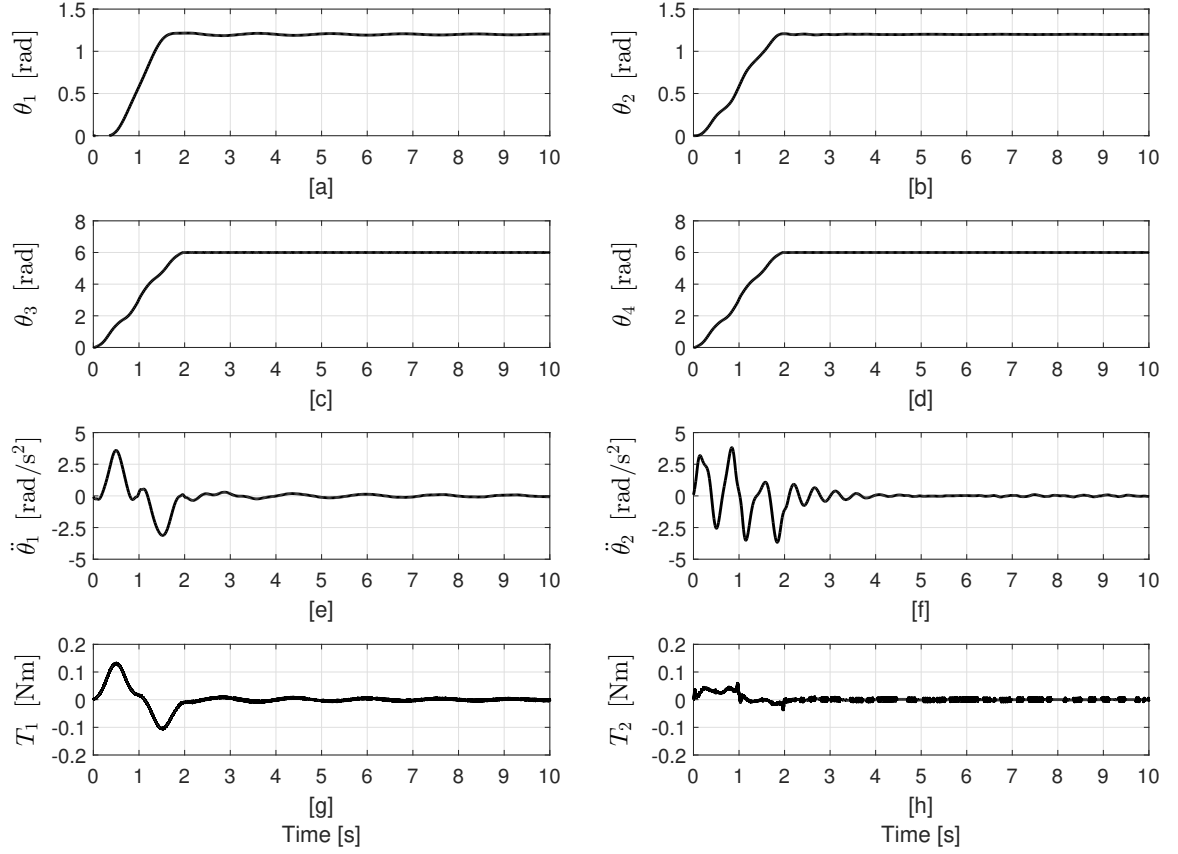


Figure 5.1. Simulated response of Original PD controller with $K_{p,1} = 6400$, $K_{v,1} = 160$, $K_{p,2} = 400$, and $K_{v,2} = 40$ when applying a versine input with $\kappa = 6$. [a] and [b] are the angular positions of links 1 and 2, while [c] and [d] are the angular positions of the shoulder and elbow motors, respectively. [e] and [f] show the angular accelerations of links 1 and 2, while [g] and [h] are the torques of the shoulder and elbow motors.

the output, are avoided. Because of this the decision was made to be conservative in its design, so the Lead-Lag compensator is constructed so that it aims to attenuate the first mode only. Specifically, the control parameters are $K_{c,1} = 3200$, $K_{c,2} = 400$, $\omega_{center,1} = \omega_{center,2} = 3.75 \frac{\text{rad}}{\text{s}}$, $\omega_{width,1} = \omega_{width,2} = 0.5 \frac{\text{rad}}{\text{s}}$, and $a_1 = a_2 = 4$. Observe that the control gains $K_{c,1}$ and $K_{c,2}$ are identical to the new PD controller that has been designed. This is intended, as it allows the Lead-Lag compensator to be compared to a similar PD controller.

The response when applying this Lead-Lag controller is shown in Figure 5.3. Observe that this controller does a better job at attenuating the first mode, but at the

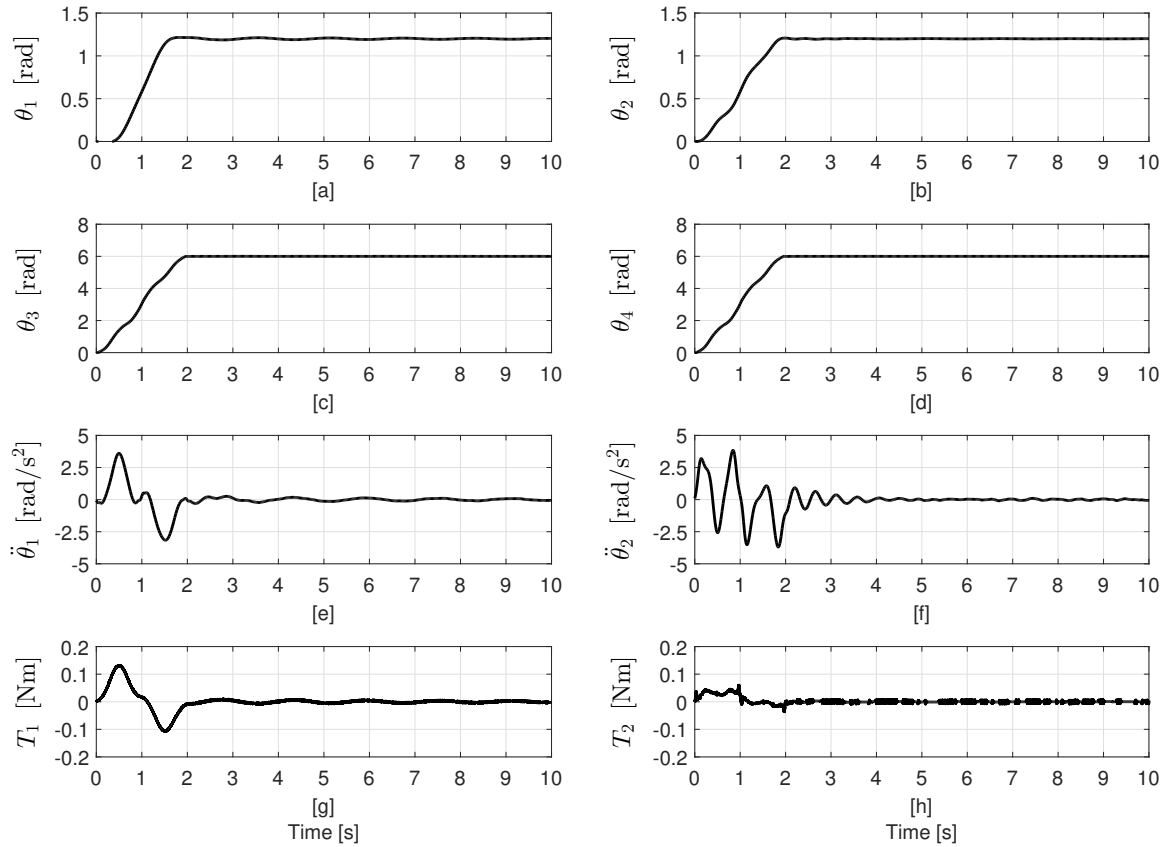


Figure 5.2. Simulated response of Alternative PD controller with $K_{p,1} = 3200$, $K_{v,1} = 160$, $K_{p,2} = 400$, and $K_{v,2} = 40$ when applying a versine input with $\kappa = 6$. [a] and [b] are the angular positions of links 1 and 2, while [c] and [d] are the angular positions of the shoulder and elbow motors, respectively. [e] and [f] show the angular accelerations of links 1 and 2, while [g] and [h] are the torques of the shoulder and elbow motors.

cost of being able to diminish the energy in the second mode. This is partly due to the Lead-Lag compensator not attenuating the second mode, but also occurs due to the very low closed-loop damping that is achieved by this type of controller. This may be seen in the root locus plots that were studied in chapter 4, where the dominant closed-loop damping ratios for the Lead-Lag compensator were generally lower than they were for PD controllers. In fact, the dominant closed-loop damping ratios for the stable Lead-Lag controllers were always below 0.1, while the PD controller may reach up to around 0.3. Note that the actual value of the closed-loop damping depends on the controller parameters themselves. This is why the residual vibration seen in

Figure 5.3 takes much longer to diminish, even though this case does have fairly low peak-to-peak residual acceleration.

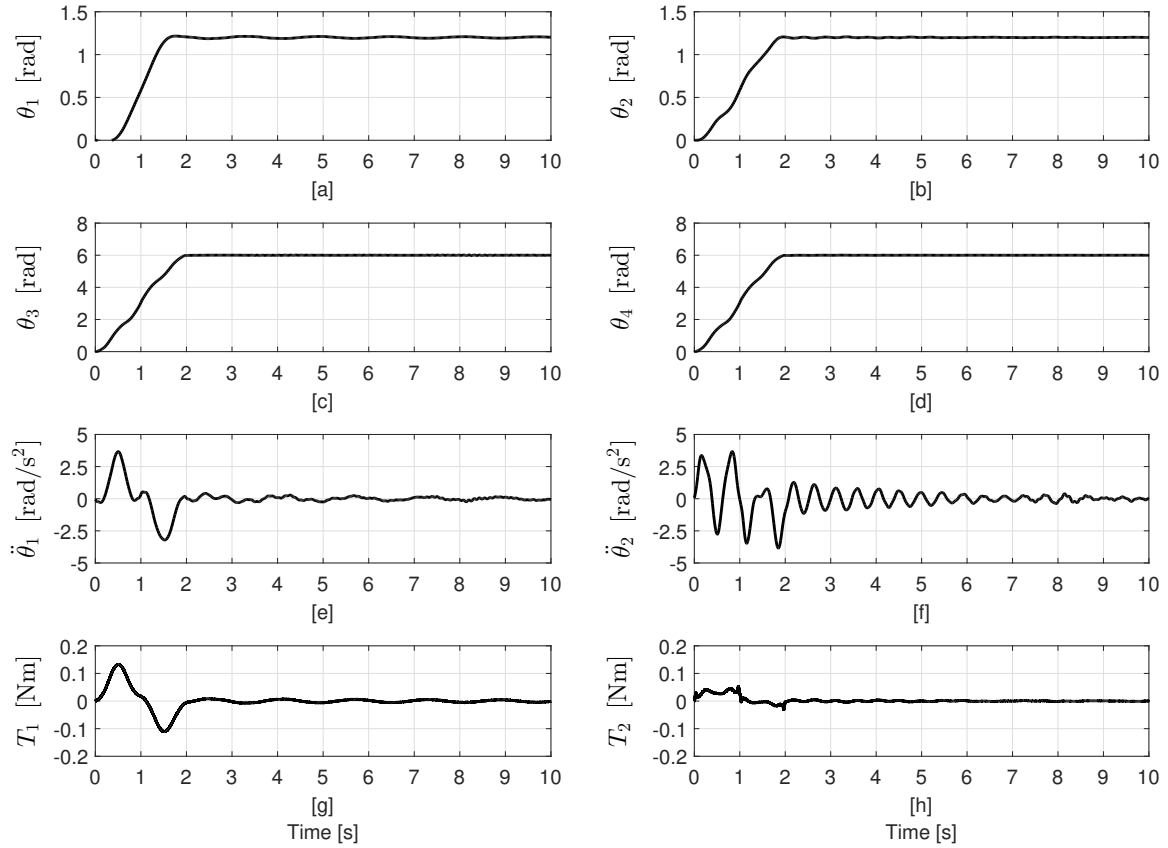


Figure 5.3. Simulated response of Lead-Lag controller when applying a versine input with $\kappa = 6$. [a] and [b] are the angular positions of links 1 and 2, while [c] and [d] are the angular positions of the shoulder and elbow motors, respectively. [e] and [f] show the angular accelerations of links 1 and 2, while [g] and [h] are the torques of the shoulder and elbow motors.

Tables 5.1 and 5.2 show the simulation results for the robot. Notice that, as κ is increased for 6 to 9, the peak residual acceleration and the settling time will both typically decrease. This matches the results seen on the three-mass system and in prior work. The new PD controller does seem to achieve better performance when inspecting the peak-to-peak acceleration, but not when examining the settling time. In fact, the only case in simulation where the Alternative PD controller outperforms the original in terms of settling time is the versine with $\kappa = 6$. This is most likely due

Table 5.1. Simulated results on the residual vibration performance of the two-link flexible-joint robot for the versine profile.

Controller	κ	$a_{xy}[\frac{\text{m}}{\text{s}^2}]$	$t_s[\text{s}]$
Original PD	6	0.3269	1.7670
Alternative PD	6	0.3124	1.4460
Lead-Lag	6	0.2985	3.4850
Hybrid	6	0.2479	1.4025
Original PD	9	0.2759	0.7800
Alternative PD	9	0.2614	1.4000
Lead-Lag	9	0.2333	2.1360
Hybrid	9	0.2017	1.3770

Table 5.2. Simulated results on the residual vibration performance of the two-link flexible-joint robot for the ramped sinusoid profile.

Controller	κ	$a_{xy}[\frac{\text{m}}{\text{s}^2}]$	$t_s[\text{s}]$
Original PD	6	0.3081	3.1935
Alternative PD	6	0.3198	4.6485
Lead-Lag	6	0.4373	7.3540
Hybrid	6	0.3820	6.5055
Original PD	9	0.2312	1.4455
Alternative PD	9	0.2450	2.1190
Lead-Lag	9	0.3671	6.4785
Hybrid	9	0.3481	3.6375

to changes in the closed-loop damping. Remember that on the three-mass system it was noticed that changes to the PD control gain may have a large effect on the closed-loop damping.

The Lead-Lag controller has interesting results, as it does very well with the versine, yet very poorly with the ramped sinusoid. In fact, when using the versine, the Lead-Lag compensator outperforms both PD controllers in terms of peak-to-peak acceleration, but the settling time is much longer. This is unsurprising, as the root locus plots shown for the three-mass system typically had a lower closed-loop damping ratio for the modes of the system when the controller gains were finite.

Note that in all the simulation cases, the controllers do worse in terms of settling time when applying the ramped sinusoid, and this is only magnified when utilizing the Lead-Lag controller.

When observing these results, a question naturally arises. That is, how to successfully minimize both the peak acceleration and the settling time. This is difficult, especially as it appears that different controllers may do better in diminishing one metric at the expense of the other. An attempt was made to accomplish this by creating a controller that utilizes a hybrid scheme. Here the Lead-Lag compensator is used during motion, as it achieves the lowest level of peak-to-peak acceleration for several different profiles. Then, once the motion has ended, the controller is switched to the Alternative PD controller. This way, the closed-loop damping is increased and the residual vibration may settle out faster. This is referred to as the Hybrid controller, as it utilizes both Lead-Lag and PD control. A simulation of the response for this controller when using a versine with $\kappa = 6$ is shown in Figure 5.4.

Observe that the hybrid controller achieves the best performance out of all the cases studied. This is unsurprising as it is successfully applying several of the lessons learned through this work. First, the Lead-Lag controller is attempting to obtain reliable motion without injecting energy into the first mode of the system. This will lower the peak-to-peak amplitude of the residual vibration that results from motion. Then the PD controller will be used to increase the closed-loop damping after the end of motion, which will help the residual vibration settle out faster.

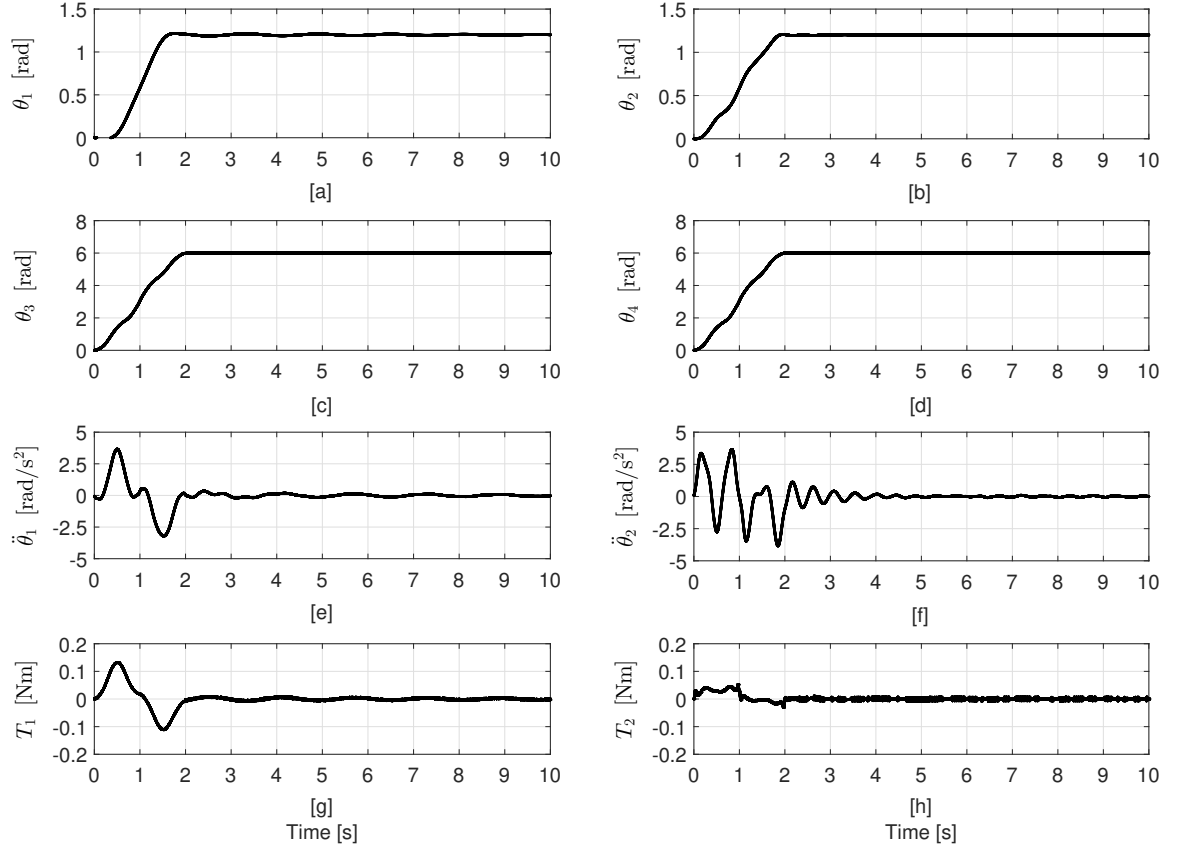


Figure 5.4. Simulated response of Hybrid controller when applying a versine input with $\kappa = 6$. [a] and [b] are the angular positions of links 1 and 2, while [c] and [d] are the angular positions of the shoulder and elbow motors, respectively. [e] and [f] show the angular accelerations of links 1 and 2, while [g] and [h] are the torques of the shoulder and elbow motors.

5.4 Experimental Results for the Flexible-Joint Robot

All the controllers tested in simulation are also applied to the two-link flexible-joint robot in order to collect experimental data. The trials that utilized a versine profile with $\kappa = 6$ are shown in Figures 5.5 through 5.8 and the experimental results are shown in Tables 5.3 and 5.4.

All experimental figures are presented as follows: From left to right, the top row shows the desired input acceleration of the motors, and the magnitude spectrum of the input profile during motion. The second row shows the angular positions of the

two links, θ_1 and θ_2 , while the third row shows the angular positions of the two motors, θ_3 and θ_4 . The fourth row shows the actual angular accelerations of the two links, $\ddot{\theta}_1$ and $\ddot{\theta}_2$, while the last row shows the torque signals, T_1 and T_2 , for each motor, respectively.

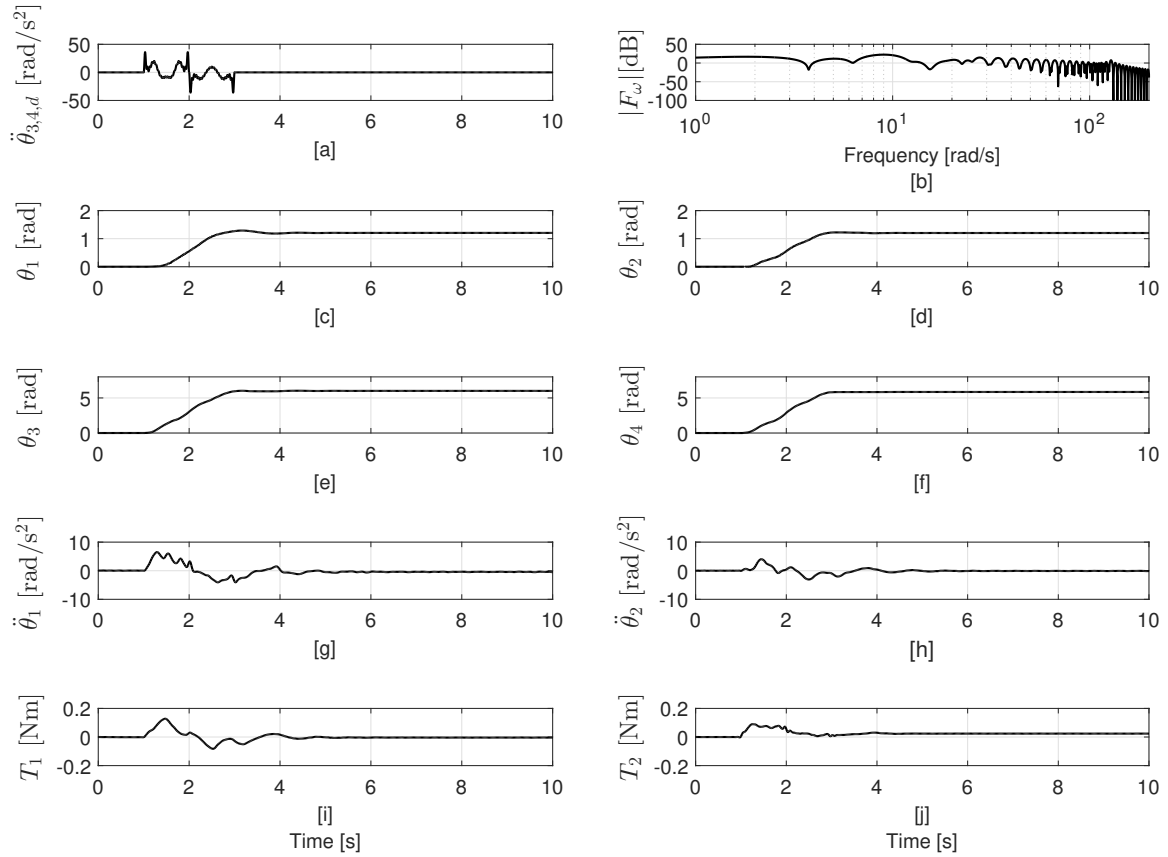


Figure 5.5. Experimental response of Original PD controller with $K_{p,1} = 6400$, $K_{v,1} = 160$, $K_{p,2} = 400$, and $K_{v,2} = 40$ when applying a versine input with $\kappa = 6$. [a] is the desired motor acceleration profile for both motors, and [b] is the magnitude spectrum of the desired acceleration profile for the motors. [c] and [d] are the angular positions of links 1 and 2, while [e] and [f] are the angular positions of the shoulder and elbow motors, respectively. [g] and [h] show the angular accelerations of links 1 and 2, while [i] and [j] are the torques of the shoulder and elbow motors.

Tables 5.3 and 5.4 present the experimental results for the same cases as shown in Tables 5.1 and 5.2, respectively. Observe that the simulated and experimental results match up fairly well for the PD controlled cases. However, the instances that utilized Lead-Lag control did not perform as well in experiment as they did in simulation. Note

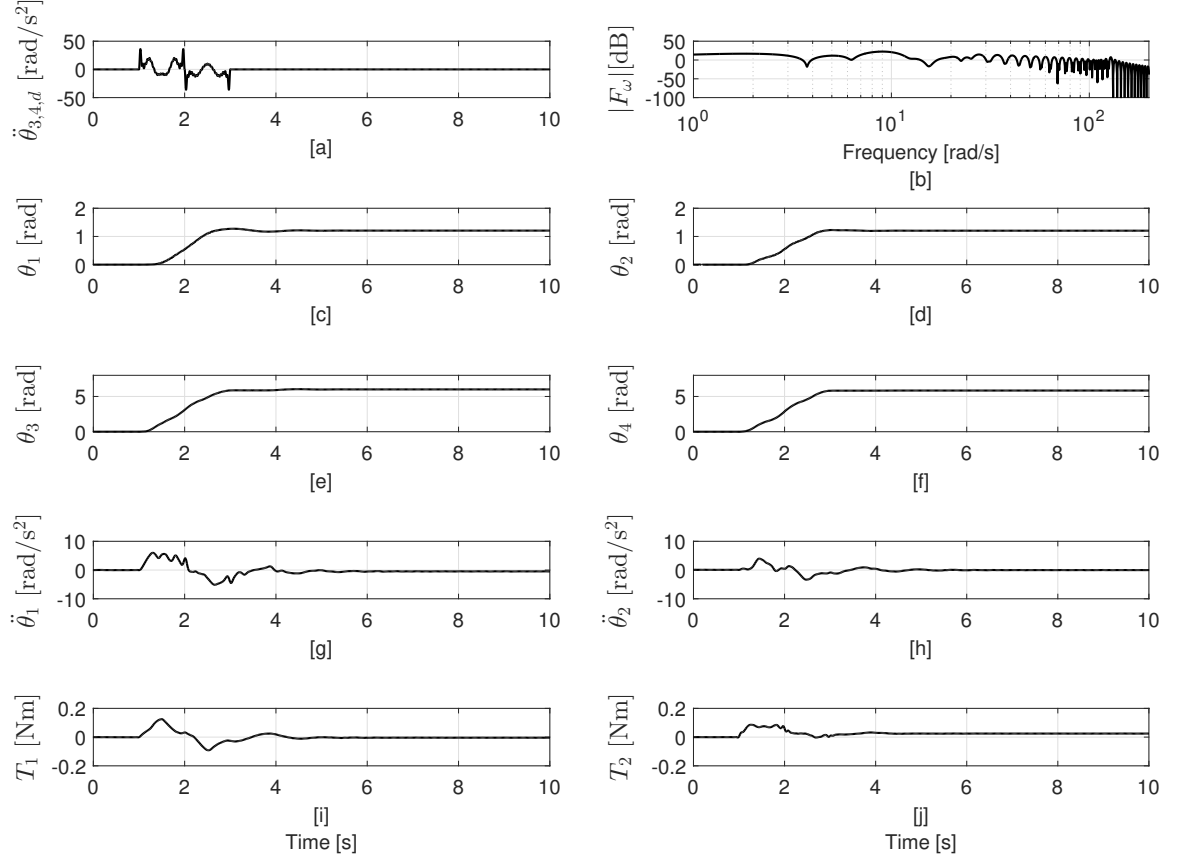


Figure 5.6. Experimental response of Alternative PD controller with $K_{p,1} = 3200, K_{v,1} = 160, K_{p,2} = 400$, and $K_{v,2} = 40$ when applying a versine input with $\kappa = 6$. [a] is the desired motor acceleration profile for both motors, and [b] is the magnitude spectrum of the desired acceleration profile for the motors. [c] and [d] are the angular positions of links 1 and 2, while [e] and [f] are the angular positions of the shoulder and elbow motors, respectively. [g] and [h] show the angular accelerations of links 1 and 2, while [i] and [j] are the torques of the shoulder and elbow motors.

that the simulation is an idealized model, so these discrepancies could be due to some of the simplifications that have been made to the simulation, such as neglecting the Coulomb friction, or to parameter variations between the simulation and experiment.

Observe that there are several similarities and discrepancies between these results and the simulated cases of section 5.3. First, the peak-to-peak accelerations are generally worse in the experiments than they are in the simulations. However, both PD controllers show good correlation between the simulated and experimental results.

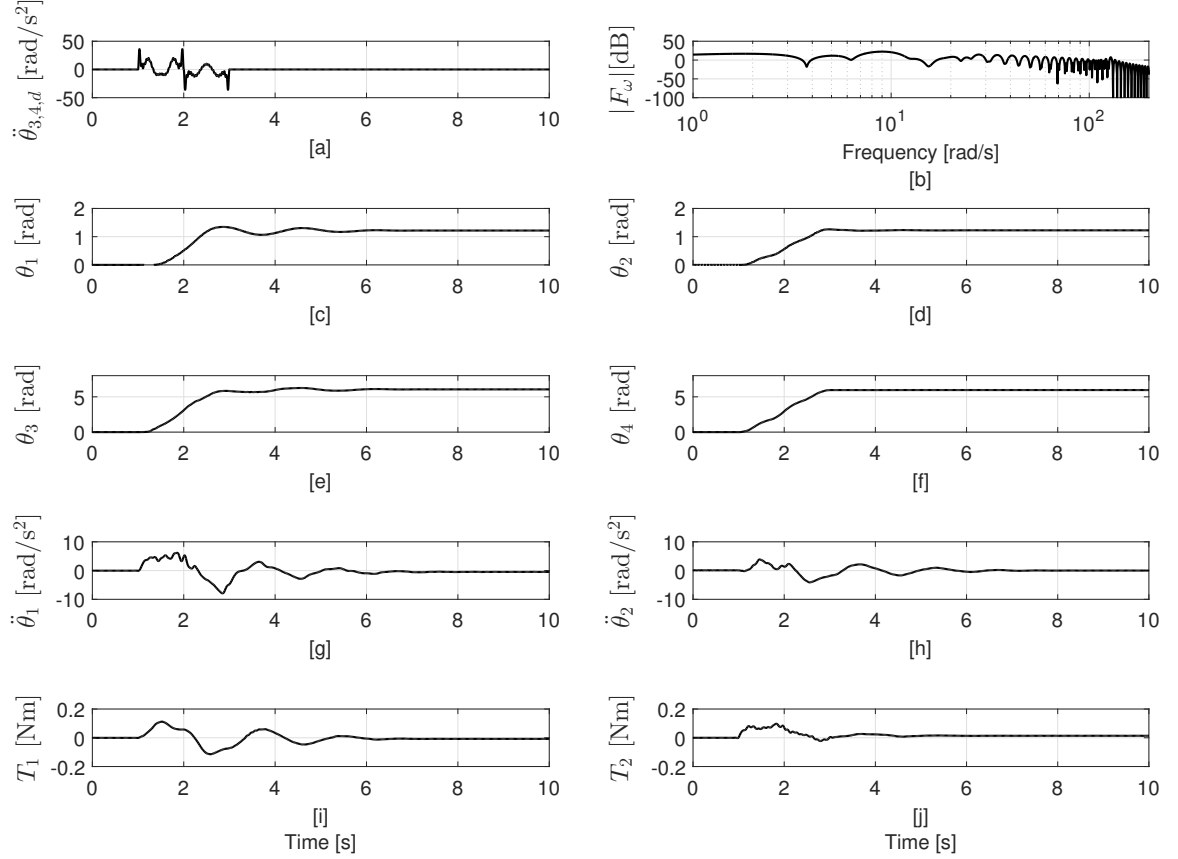


Figure 5.7. Experimental response of Lead-Lag controller with $K_{c,1} = 3200$, $K_{c,2} = 400$, $\omega_{center,1} = \omega_{center,2} = 3.75 \frac{\text{rad}}{\text{s}}$, $\omega_{width,1} = \omega_{width,2} = 0.5 \frac{\text{rad}}{\text{s}}$, and $a_1 = a_2 = 4$ when applying a versine input with $\kappa = 6$. [a] is the desired motor acceleration profile for both motors, and [b] is the magnitude spectrum of the desired acceleration profile for the motors. [c] and [d] are the angular positions of links 1 and 2, while [e] and [f] are the angular positions of the shoulder and elbow motors, respectively. [g] and [h] show the angular accelerations of links 1 and 2, while [i] and [j] are the torques of the shoulder and elbow motors.

That is, in general when a controller does better in simulation, it also does better on the robot itself.

One disagreement that is observed in these data sets concerns the ramped sinusoid. The ramped sinusoid profile always had worse settling times than the versine in simulation, but this trend is not seen in the experiments. In fact, the variation in performance between the versine and the ramped sinusoid is much smaller when these profiles are implemented on the flexible-joint robot itself.

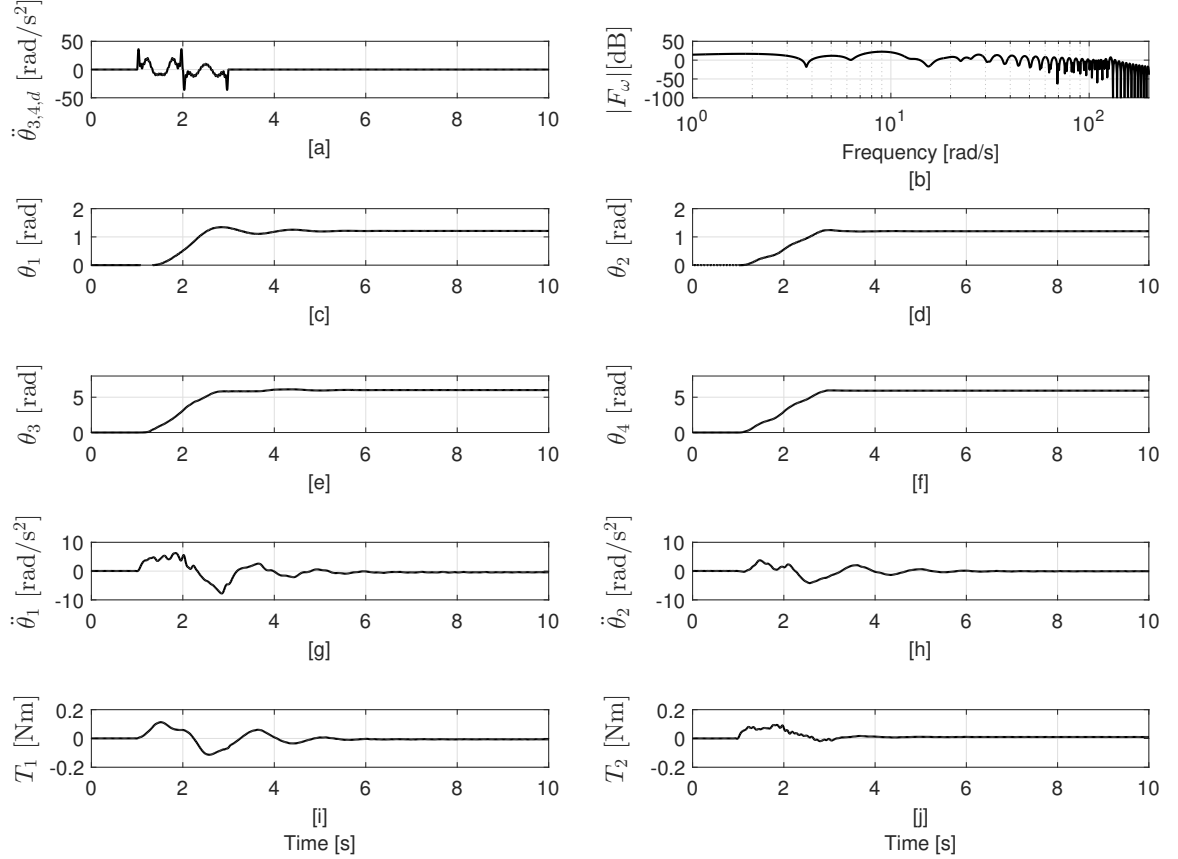


Figure 5.8. Experimental response of Hybrid controller when applying a versine input with $\kappa = 6$. [a] is the desired motor acceleration profile for both motors, and [b] is the magnitude spectrum of the desired acceleration profile for the motors. [c] and [d] are the angular positions of links 1 and 2, while [e] and [f] are the angular positions of the shoulder and elbow motors, respectively. [g] and [h] show the angular accelerations of links 1 and 2, while [i] and [j] are the torques of the shoulder and elbow motors.

Another major difference between simulations and experiments is the performance of the Lead-Lag controller, which also affects the performance of the Hybrid controller. The experimental result for the Lead-Lag controller is much worse when implemented on the robot than it is in simulation. This implies that the differences between the idealized simulation model and the robot itself are significant enough to severely impact the performance of the Lead-Lag controller. However, notice that the Hybrid controller still improves on the performance of the Lead-Lag controller, both in terms of peak-to-peak acceleration and settling time.

Table 5.3. Experimental results on the residual vibration performance of the two-link flexible-joint robot for the versine profile.

Controller	κ	$a_{xy}[\frac{\text{m}}{\text{s}^2}]$	$t_s[\text{s}]$
Original PD	6	0.4718	1.5055
Alternative PD	6	0.3186	1.5850
Lead-Lag	6	0.5868	3.2825
Hybrid	6	0.5163	2.6145
Original PD	9	0.4581	1.4875
Alternative PD	9	0.2800	1.5945
Lead-Lag	9	0.5779	3.3595
Hybrid	9	0.5132	2.2035

Table 5.4. Experimental results on the residual vibration performance of the two-link flexible-joint robot for the ramped sinusoid profile.

Controller	κ	$a_{xy}[\frac{\text{m}}{\text{s}^2}]$	$t_s[\text{s}]$
Original PD	6	0.4702	2.1780
Alternative PD	6	0.3571	1.6285
Lead-Lag	6	0.6041	3.9830
Hybrid	6	0.5867	2.7785
Original PD	9	0.3243	1.4065
Alternative PD	9	0.2706	1.4825
Lead-Lag	9	0.5943	3.3020
Hybrid	9	0.5028	2.6550

The responses for all the remaining experimental cases may be found in Appendix B.

CHAPTER 6. CONCLUSIONS AND RECOMMENDATIONS

The influence of the feedback loop on the level of residual vibration has been examined on two separate systems, a linear three-mass system and a nonlinear robotic manipulator. The linear three-mass system is studied first in order to better understand the behavior of the feedback loop. This is completed by applying techniques and theory that is well-known and grounded in the field of linear systems theory. The guidelines found from this investigation are presented in section 6.1.

These results are then applied to a nonlinear system: the two-link flexible-joint robot. The limited data set obtained using simulations and experiments on the robot does show correlation with the analysis produced using the three-mass system. This provides validation of the work completed and helps to show that the behavior observed on the three-mass system may, in some instances, also extend to nonlinear systems.

This helps to tie together all the different pieces for the problem of minimizing residual vibration while implementing fast point-to-point motion. By combining these results with prior work that has been completed in the field of command shaping, very low levels of residual vibration are achieved.

6.1 General Procedure for Designing a Controller to Minimize Residual Vibration

For the general problem of appropriately designing a controller so as to minimize residual vibration in a system, the following procedure may be applied:

1. First and foremost, stability of the closed-loop system must be ensured.

2. Better modeling of the system plant will, in general, improve the performance of the feedforward controller. This will in turn reduce the variations in performance seen from applying different settings to the feedback controller.

2.1. The caveat to this result is when the feedforward controller injects less energy into the nominal natural frequency when it is higher or lower than the actual natural frequency. For example, the frequency response of the feedforward controller applied for the three-mass system has a frequency response that is asymmetric around the natural frequencies. In this instance, the controller injects less energy into the natural frequencies when it underestimates the values of those frequencies. Here the variation in the feedback controller will become more important, but the closed-loop system may actually perform better at reducing the residual vibration of the end effector.

3. In order to limit the amplitude of the peak-to-peak acceleration after motion, the feedback must lower the amount of energy that it injects into the natural frequencies of the system. This is done by analyzing the frequency response of the closed-loop system that relates the input signal to the controller output. The frequency response itself will depend on the controller type, the overall configuration of the block diagram for the system, and the controller parameters themselves.

3.1. This result assumes satisfactory tracking of the input signal. Note that when the feedback gains are too low, the input reference may not be adequately followed.

3.2. The input signals and the feedforward controller also tie into this result. Performance of the system is also improved by decreasing energy at the natural frequencies in either the input signal or the contribution of the feedforward controller. This is accomplished for the input signal by shaping the input command, as done by command shaping.

- 3.3. Note that a lower peak-to-peak acceleration does not imply a lower settling time. In fact, often the settling time will lengthen when lowering the peak-to-peak residual acceleration. This is a function of the closed-loop damping.
4. In order to lower the settling time, the closed-loop damping of the system must be increased. Observe that, after motion has ended, the closed-loop damping is what will determine how fast the system eliminates the vibration that is present in the system
 - 4.1. However, a controller with the highest closed-loop damping may not necessarily lead to the lowest peak-to-peak acceleration. This is especially true when using a command-shaped input, as the command shaping procedure is designed for an undamped system
5. There is potential to greatly improve performance by applying the best controller for limiting the magnitude of the peak residual acceleration during motion, and then switching to a controller with a larger closed-loop damping ratio after motion in order to reduce settling time.

6.2 Unique Contributions

This work contains several new results. Prior studies on the two-link flexible-joint robot have focused on the input side of the problem of minimizing residual vibration. Thus, the primary contribution contained herein is a complete analysis of the feedback loop, and how the design of the feedback controller affects performance. In order to examine this problem, the three-mass model was developed, and a simulation of this system was constructed. This model and simulation provide a new testbed for studying how well different inputs and controllers reduce vibration. Note that this system may also be applied in the future in order to study other elements of the overall problem of minimizing residual vibration. This is a very useful result,

as the three-mass system is designed to mimic the more complex problem of the two-link flexible-joint robot, but is linear and can thus be studied in a much more straightforward manner using linear techniques and tools.

Further, new results include the full kinematic analysis and the derivation of the Newton-Euler equations for the two-link robot. While this is not applied to the robot in this work, the framework has been developed so that it may be applied in future work so that more analysis may be completed on the feedforward portion of the computed torque controller.

The MATLAB code that simulates the robot behavior has also been modified so as to allow different feedback controllers to be easily examined on the robot itself. The framework for applying Lead-Lag compensators on the robot has been added, as this functionality was not previously incorporated. While the LabVIEW program that controls the flexible-joint robot did already contain the ability to quickly adjust the control gains for the PD controllers of the two links, it did not have the capability to use Lead-Lag control. Thus the robot controller was modified to allow Lead-Lag compensation for the two links. These additions also include the ability to switch between different controllers within a single experiment.

6.3 Future Work

There are several areas of research that need to be examined in the future. First of all, the three-mass system is a useful testbed for studying this type of problem. However, more details are needed on how the results obtained from the three-mass system correlate to the two-link flexible-joint robot. In other words, more investigation into the performance of feedback control on the two-link robot needs to be completed. These results could then be compared to those presented by the three-mass system.

One area that needs to be studied in much greater detail is how, or even if, switching controller types can be used in general to improve performance. There are difficulties, which were not considered here, that arise when performing these

switches. Thus, an examination needs to be completed of how to perform these changes smoothly and robustly.

In this work, only PD and Lead-Lag controllers are studied. Further research could examine different types of control laws and study their performance. For example, how would the system perform when utilizing two lead-lag compensators in series, with each designed to concentrate on attenuating energy at a single, but different, natural frequency. Also, note that the intent of this work is mainly to provide guidelines on how to design feedback control so as to minimize residual vibration. However, further study could be completed in order to find a procedure that develops the optimal feedback controller for minimizing residual vibration. This could perhaps be accomplished by utilizing frequency-domain techniques. Also, a frequency-shaped cost functional could potentially be derived. This would then be used in an optimization routine that would find the optimal feedback controller that minimizes the contribution of the feedback at the natural frequencies. This could then be combined with the command shaping procedure so that both the input profile and the feedback controller are derived at the same time.

Furthermore, only a certain type of command-shaped profile is applied herein. There are several different approaches that may be taken when constructing the command-shaped profile, and validation of these results when utilizing other kinds of inputs would be beneficial. Another good area for further validation would be in the implementation of these concepts on a more complicated system than the two-link flexible-joint robot. Since industrial robotic systems operate in three-dimensional space, testing this research on a three-dimensional robot would be valuable. This work could then be extended so as to study a system with n modes of vibration. While the command shaping procedure is built to handle as many natural frequencies as needed, it weights all of the modes equally. Thus, further study on the influence of each individual mode on the level of residual vibration would be useful, and could potentially lead to more efficient profiles.

Further studies on the effects of the modeling used by the feedforward controller are needed. The computed-torque controller may utilize either the Lagrangian model or the Newton-Euler equations, and an examination of the performance of both in comparison to each other would be useful. This would also help to show if the modeling assumptions used to simplify the Lagrangian model are valid in the case of the two-link robot, and how much they affect the performance of the system.

LIST OF REFERENCES

LIST OF REFERENCES

- [1] K. S. Fu, R. C. Gonzalez, and C. S. G. Lee. *Robotics: Control, Sensing, Vision, and Intelligence*. McGraw-Hill, 1987.
- [2] M. W. Spong, S. Hutchinson, and M. Vidyasagar. *Robot Modeling and Control*. John Wiley & Sons, 2006.
- [3] J. J. Craig. *Introduction to Robotics: Mechanics and Control*. Prentice Hall, 3rd edition, 2004.
- [4] M. C. Good, L. M. Sweet, and K. L. Strobel. Dynamic Models for Control System Design of Integrated Robot and Drive Systems. *Journal of Dynamic Systems, Measurement, and Control*, 107(1):53, 1985.
- [5] P. Tomei. A Simple PD Controller for Robots with Elastic Joints. *IEEE Transactions on Automatic Control*, 36(10):1208–1213, 1991.
- [6] J. Slotine and W. Li. *Applied Nonlinear Control*. Pearson, 1991.
- [7] A. De Luca. Dynamic control of robots with joint elasticity. In *Robotics and Automation, International Conference on (ICRA)*, pages 152–158, 1988.
- [8] M. W. Spong. Modeling and Control of Elastic Joint Robots. *Journal of Dynamic Systems, Measurement, and Control*, 109(4):310, 1987.
- [9] M. C. Readman and P. R. Belanger. Analysis and control of a flexible joint robot. In *Proceedings 1991 IEEE International Conference on Robotics and Automation*, pages 2551–2559, 1991.
- [10] M. W. Spong, K. Khorasani, and P. V. Kokotovic. An Integral Manifold Approach to the Feedback Control of Flexible Joint Robots. *IEEE Journal on Robotics and Automation*, 3(4):291–300, 1987.
- [11] H. Sira-Ramirez and M. W. Spong. Variable structure control of flexible joint manipulators. *Int. Robot. Autom*, 1988.
- [12] A. De Luca and G. Ulivi. Iterative Learning Control of Robots with Elastic Joints. In *Proceedings 1992 IEEE International Conference on Robotics and Automation*, pages 1920–1926, 1992.
- [13] D. Wang. A simple iterative learning controller for manipulators with flexible joints. *Automatica*, 31(9):1341–1344, 1995.
- [14] J. van de Wijdeven and O. Bosgra. Residual vibration suppression using Hankel iterative learning control. In *2006 American Control Conference*, pages 1–16, 2006.

- [15] J. van de Wijdeven and O. Bosgra. Residual vibration suppression using Hankel iterative learning control. *International Journal of Robust and Nonlinear Control*, 18(10):1034–1051, 2008.
- [16] J. van de Wijdeven and O. Bosgra. Hankel iterative learning control for residual vibration suppression with MIMO flexible structure experiments. In *Proceedings of the American Control Conference*, pages 4993–4998, 2007.
- [17] W. Singhose. Command shaping for flexible systems: A review of the first 50 years. *International Journal of Precision Engineering and Manufacturing*, 10(4):153–168, 2009.
- [18] P. H. Meckl. *Control of Vibration in Mechanical Systems Using Shaped Reference Inputs*. PhD thesis, Massachusetts Institute of Technology, 1988.
- [19] S. P. Bhat and D. K. Miu. Precise Point-To-Point Positioning Control of Flexible Structures. *Journal of Dynamic Systems Measurement and Control - Transactions of the ASME*, 112(4):667–674, 1990.
- [20] O. J. M. Smith. Posicast control of damped oscillatory systems. *Proceedings of the IRE*, 45(9):1249–1255, 1957.
- [21] N. C. Singer and W. P. Seering. Preshaping Command Inputs to Reduce System Vibration. *Journal of Dynamic Systems, Measurement, and Control*, 112(1):76–82, 1990.
- [22] J. M. Hyde. *Multiple Mode Vibration Suppression in Controlled Flexible Systems*. SM thesis, Massachusetts Institute of Technology, 1991.
- [23] B. W. Rappole. *Minimizing Residual Vibrations in Flexible Structures*. SM thesis, Massachusetts Institute of Technology, 1992.
- [24] J. Park, P. H. Chang, H. S. Park, and E. Lee. Design of learning input shaping technique for residual vibration suppression in an industrial robot. *IEEE/ASME Transactions on Mechatronics*, 11(1):55–65, 2006.
- [25] W. Singhose and J. Vaughan. Reducing vibration by digital filtering and input shaping. *IEEE Transactions on Control Systems Technology*, 19(6):1410–1420, 2011.
- [26] D. Blackburn, W. Singhose, J. Kitchen, V. Patrangenaru, J. Lawrence, and T. Kamoi. Command Shaping for Nonlinear Crane Dynamics. *Journal of Vibration and Control*, 16(477):1–25, 2010.
- [27] G. G. Parker, K. Groom, J. Hurtado, R. D. Robinett, and F. Leban. Command shaping boom crane control system with nonlinear inputs. In *IEEE Conference on Control Applications - Proceedings*, volume 2, pages 1774–1778, 1999.
- [28] J. Y. Hung. Feedback control with posicast. *IEEE Transactions on Industrial Electronics*, 50(1):94–99, 2003.
- [29] D. M. Aspinwall. Acceleration Profiles for Minimizing Residual Response. *Journal of Dynamic Systems, Measurement and Control*, 102:3–6, 1980.

- [30] P. H. Meckl. *Minimizing Residual Vibration of a Linear System Using Appropriately Shaped Forcing Functions*. SM thesis, Massachusetts Institute of Technology, 1984.
- [31] P. H. Meckl and W. P. Seering. Minimizing Residual Vibration for Point-to-Point Motion. *Journal of Vibration and Acoustics*, 107(4):378–382, 1985.
- [32] P. H. Meckl and W. P. Seering. Experimental Evaluation of Shaped Inputs to Reduce Vibration for a Cartesian Robot. *Journal of Dynamic Systems, Measurement, and Control*, 112(2):159–165, 1990.
- [33] D. De Roover and F. B. Sperling. Point-to-Point Control of a High Accuracy Positioning Mechanism. In *American Control Conference*, pages 1350–1354, 1997.
- [34] R. Lee. *Optimal Parameter Estimation for Long-term Prediction in the Presence of Model Mismatch Applied to a Two-link Flexible Joint Robot*. PhD thesis, Purdue University, 2011.
- [35] V. M. Beazel. *Command Shaping Applied to Nonlinear Systems with Configuration-Dependent Resonance*. PhD thesis, Purdue University, 2004.
- [36] V. M. Beazel and P. H. Meckl. Command Shaping Applied to Nonlinear Systems with Configuration-Dependent Resonance. In *Proceedings of the American Control Conference*, pages 539–544, Portland, OR, 2005.
- [37] A. Agrawal. *Constrained Optimized Command Shaping for Minimizing Residual Vibration in a Flexible Joint Robot*. SM thesis, Purdue University, 2015.
- [38] R. Bellman, I. Glicksberg, and O. Gross. On the "Bang-Bang" Control Problem. *Quarterly of Applied Mathematics*, 14:11–18, 1956.
- [39] J. P. LaSalle. Time Optimal Control Systems. In *Proceedings of the National Academy of Sciences of the United States of America*, volume 45, pages 573–577, 1959.
- [40] H. C. Nho. *Precise Motion Control of Flexible Joint Robot Manipulators With an Intelligent Payload System*. PhD thesis, Purdue University, 2004.
- [41] J. Yegerlehner. *The Application of Artificial Neural Networks to the Control of a Nonlinear System Undergoing Changes in a System Parameter*. SM thesis, Purdue University, 1992.
- [42] R. Kinceler. Manipulator Manual: To Configure from Flexible Joints to Rigid Joints and Vice-Versa. Technical report, Purdue University, 1996.
- [43] R. Cipra. ME 572: Analysis and Design of Robotic Manipulators. Course notes, Purdue University, 2016.
- [44] A. Scheel. Command Shaping Applied to a Two-Link Flexible-Joint Robot. Technical report, Purdue University, 2012.
- [45] W. Chatlatanagulchai, V. M. Beazel, and P. H. Meckl. Command Shaping Applied to Nonlinear Systems with Configuration-Dependent Resonance. In *Proceedings of the 2006 American Control Conference*, Minneapolis, MN, 2006. IEEE.

- [46] G. Buondonno and A. De Luca. A recursive Newton-Euler algorithm for robots with elastic joints and its application to control. In *IEEE International Conference on Intelligent Robots and Systems*, pages 5526–5532, Hamburg, Germany, 2015.
- [47] S. S. Rao. *Mechanical Vibrations*. Prentice Hall, 5th edition, 2010.
- [48] J. W. Cooley and J. W. Tukey. An Algorithm for the Machine Calculation of Complex Fourier Series. *Mathematics of Computation*, 19(90):297–301, 1965.
- [49] M. T. Heideman, D. H. Johnson, and C. S. Burrus. Gauss and the History of the Fast Fourier Transform. *IEEE ASSP Magazine*, pages 14–21, oct 1984.
- [50] C. Van Loan. *Computational Frameworks for the Fast Fourier Transform*. Society for Industrial and Applied Mathematics, Philadelphia, PA, 1992.

APPENDICES

Appendix A. Extra Simulation Results for the Three-Mass System

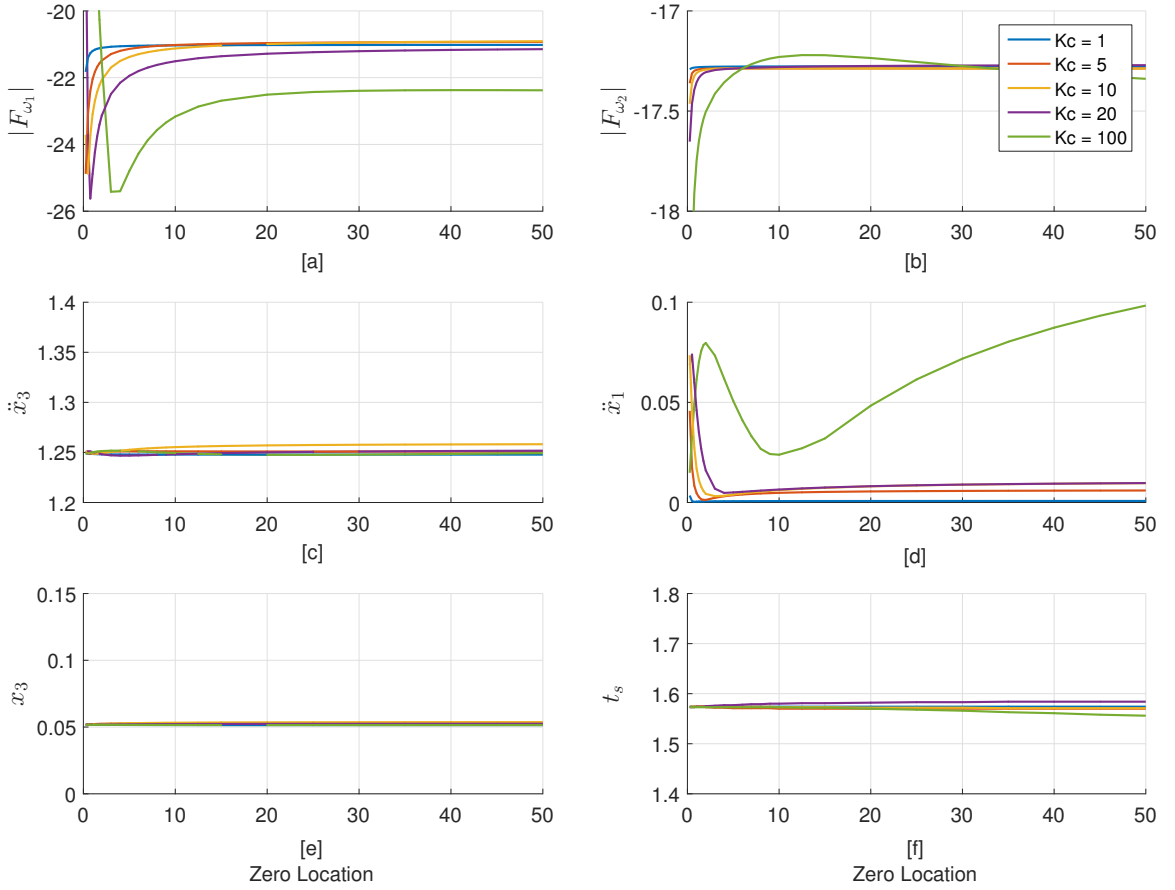


Figure A.1. Response of the three-mass system for a ramped sinusoid profile with $\kappa = 9$ when using feedforward control with a PD controller and no error in the natural frequencies. [a] and [b] show the average magnitude of the first and second modes, respectively. [c] shows the peak-to-peak acceleration of mass 3, while [d] shows the peak-to-peak acceleration of mass 1. [e] and [f] show the peak deflection and the settling time of mass 3.

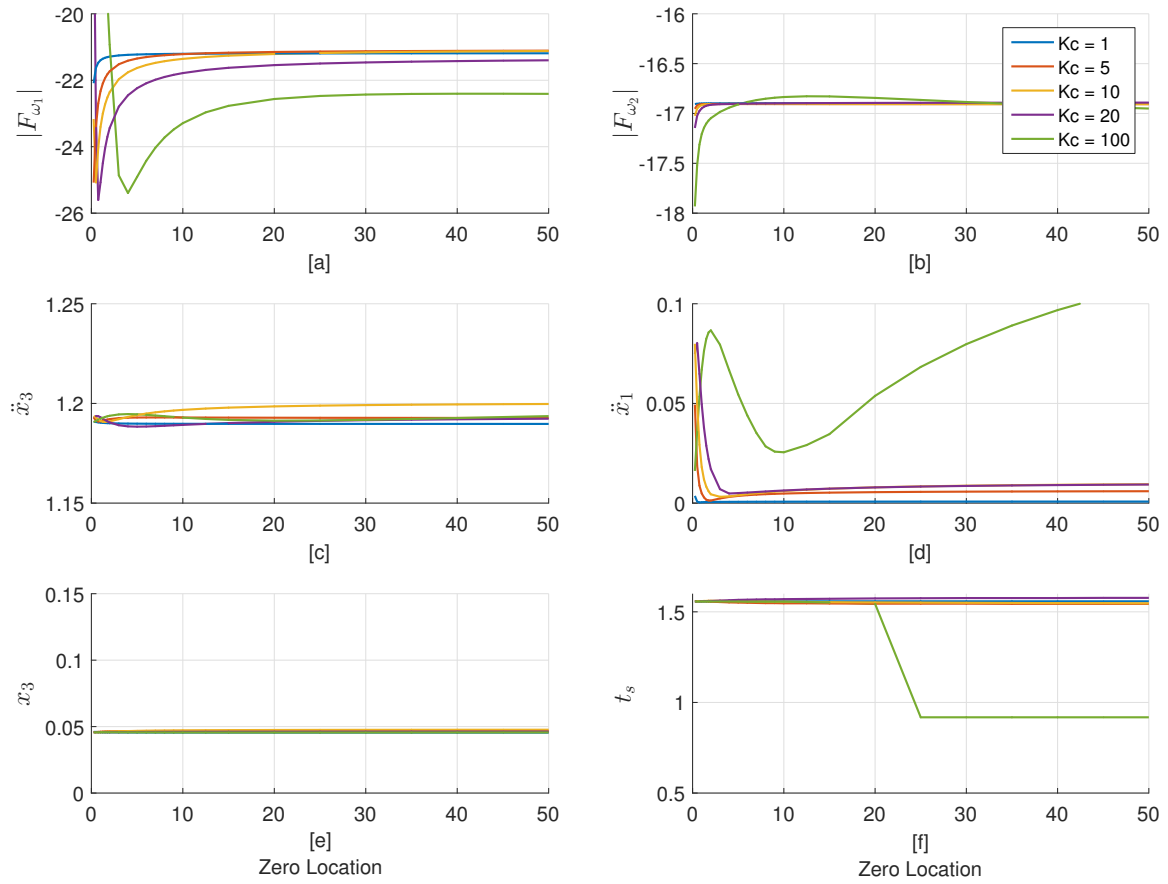


Figure A.2. Response of the three-mass system for a ramped sinusoid profile with $\kappa = 15$ when using feedforward control with a PD controller and no error in the natural frequencies. [a] and [b] show the average magnitude of the first and second modes, respectively. [c] shows the peak-to-peak acceleration of mass 3, while [d] shows the peak-to-peak acceleration of mass 1. [e] and [f] show the peak deflection and the settling time of mass 3.

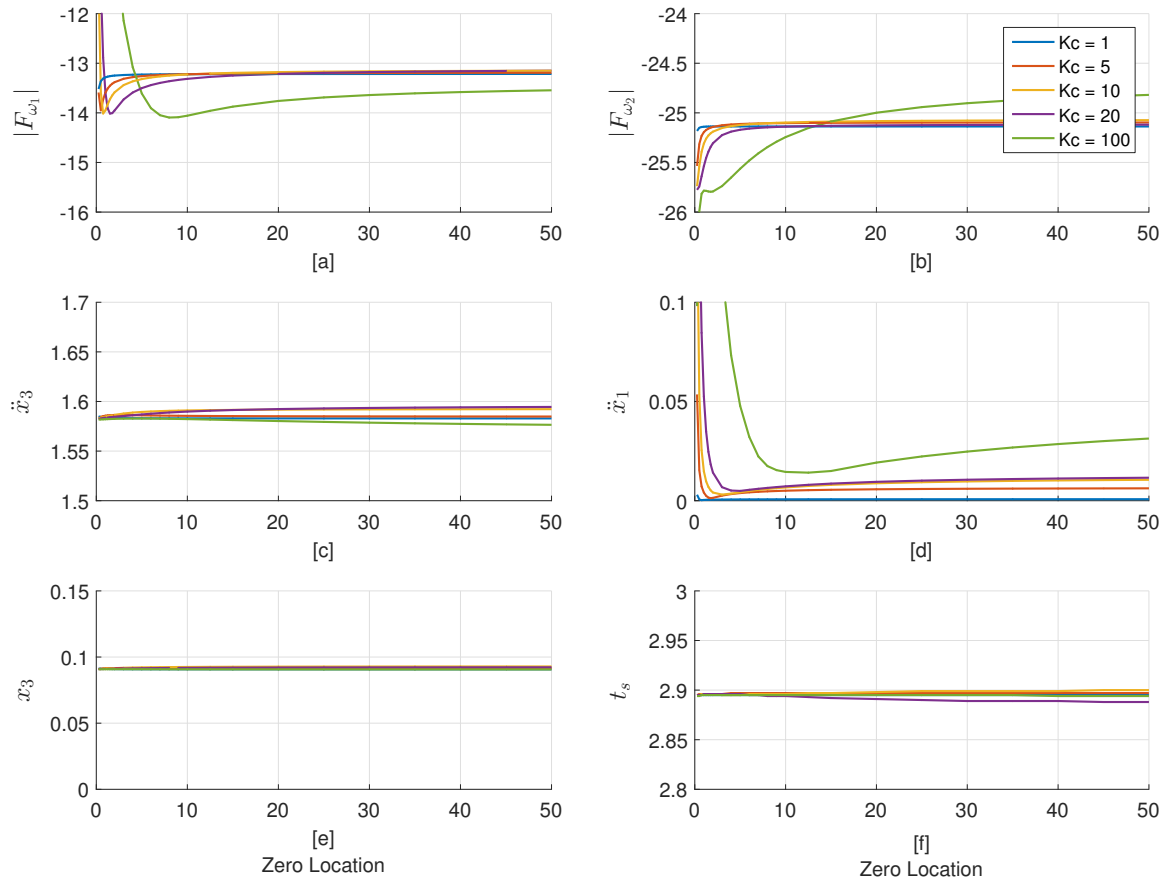


Figure A.3. Response of the three-mass system for a versine profile with $\kappa = 9$ when using feedforward control with a PD controller and no error in the natural frequencies. [a] and [b] show the average magnitude of the first and second modes, respectively. [c] shows the peak-to-peak acceleration of mass 3, while [d] shows the peak-to-peak acceleration of mass 1. [e] and [f] show the peak deflection and the settling time of mass 3.

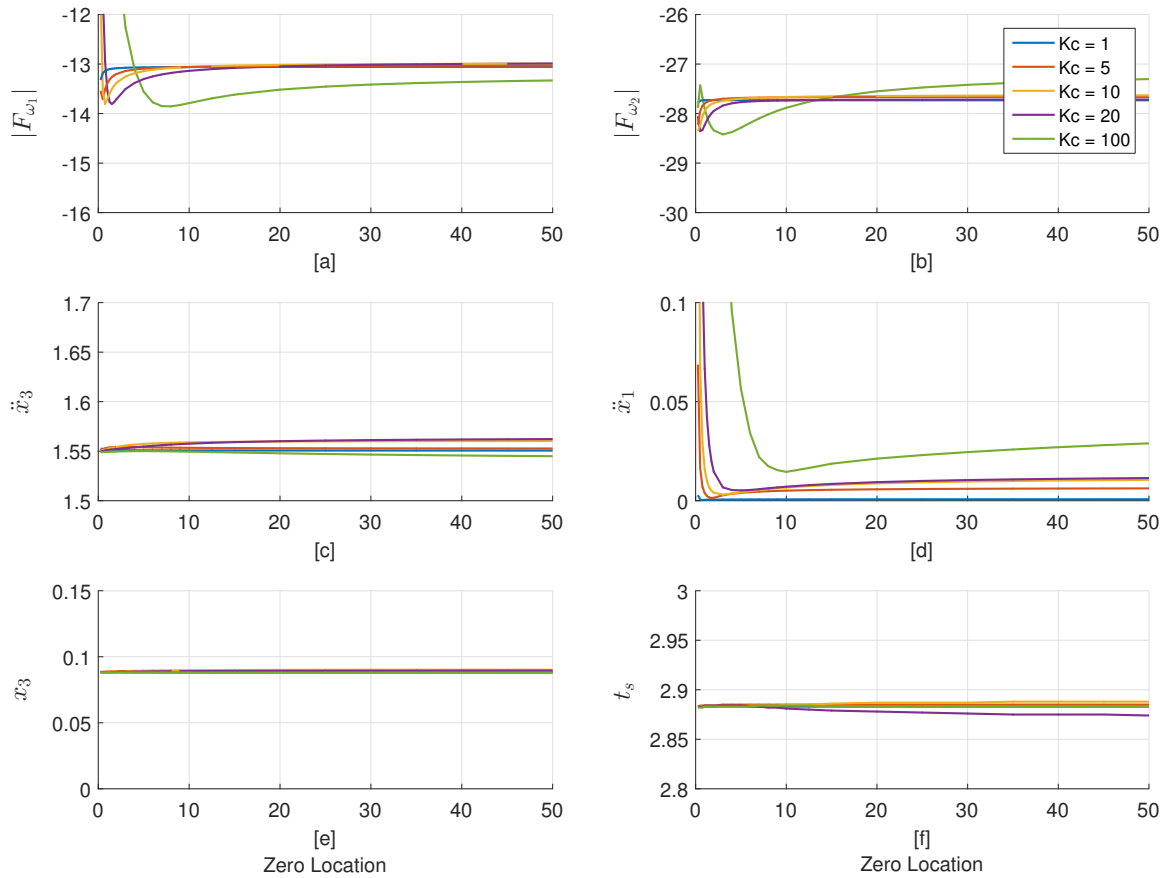


Figure A.4. Response of the three-mass system for a versine profile with $\kappa = 15$ when using feedforward control with a PD controller and no error in the natural frequencies. [a] and [b] show the average magnitude of the first and second modes, respectively. [c] shows the peak-to-peak acceleration of mass 3, while [d] shows the peak-to-peak acceleration of mass 1. [e] and [f] show the peak deflection and the settling time of mass 3.

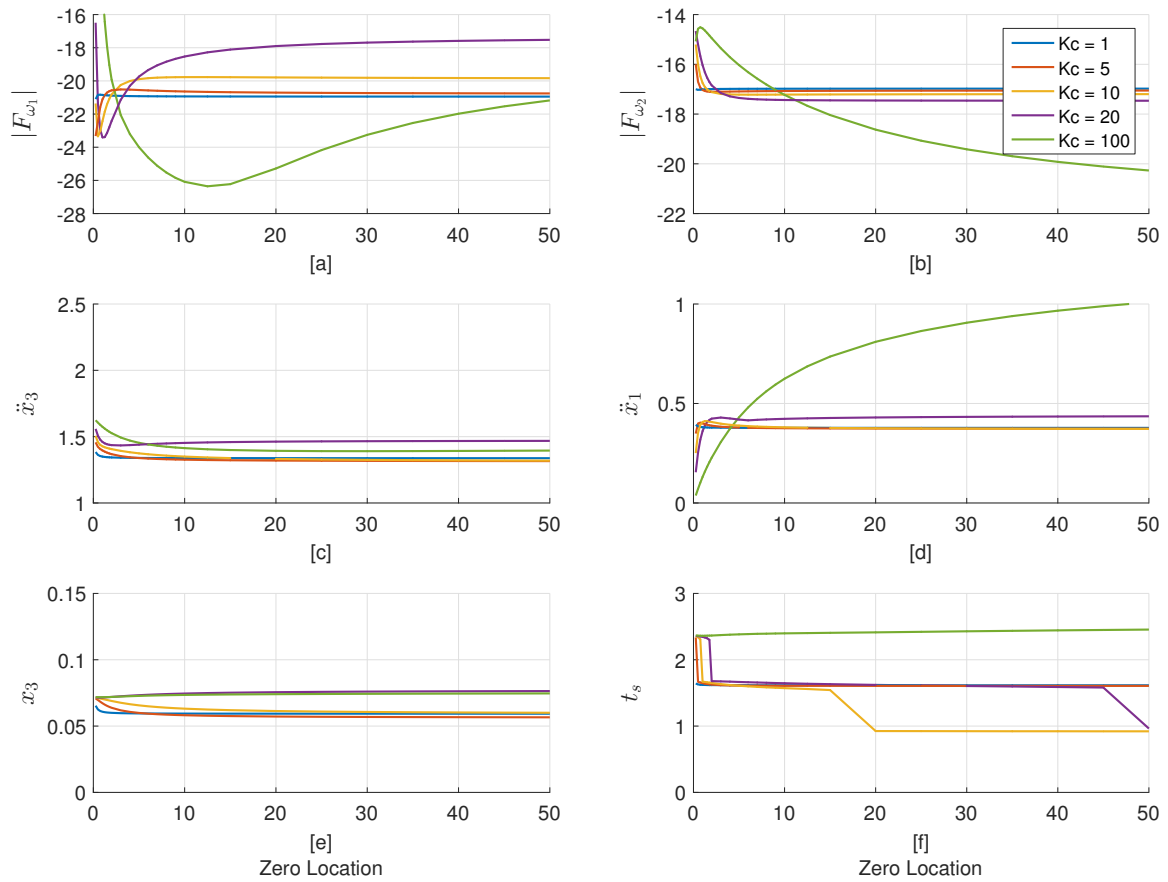


Figure A.5. Response of the three-mass system for a ramped sinusoid profile with $\kappa = 9$ when using feedforward control with a PD controller and -5% error in the natural frequencies. [a] and [b] show the average magnitude of the first and second modes, respectively. [c] shows the peak-to-peak acceleration of mass 3, while [d] shows the peak-to-peak acceleration of mass 1. [e] and [f] show the peak deflection and the settling time of mass 3.

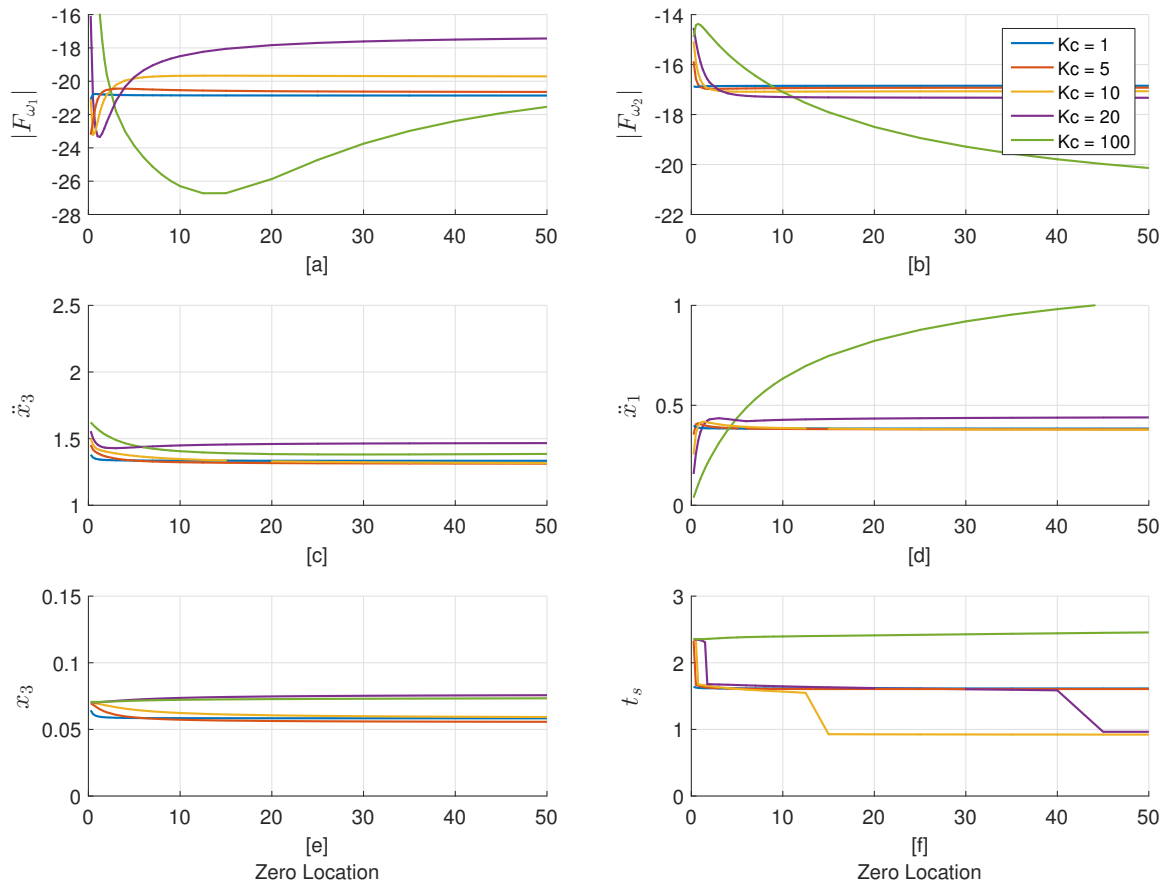


Figure A.6. Response of the three-mass system for a ramped sinusoid profile with $\kappa = 15$ when using feedforward control with a PD controller and -5% error in the natural frequencies. [a] and [b] show the average magnitude of the first and second modes, respectively. [c] shows the peak-to-peak acceleration of mass 3, while [d] shows the peak-to-peak acceleration of mass 1. [e] and [f] show the peak deflection and the settling time of mass 3.

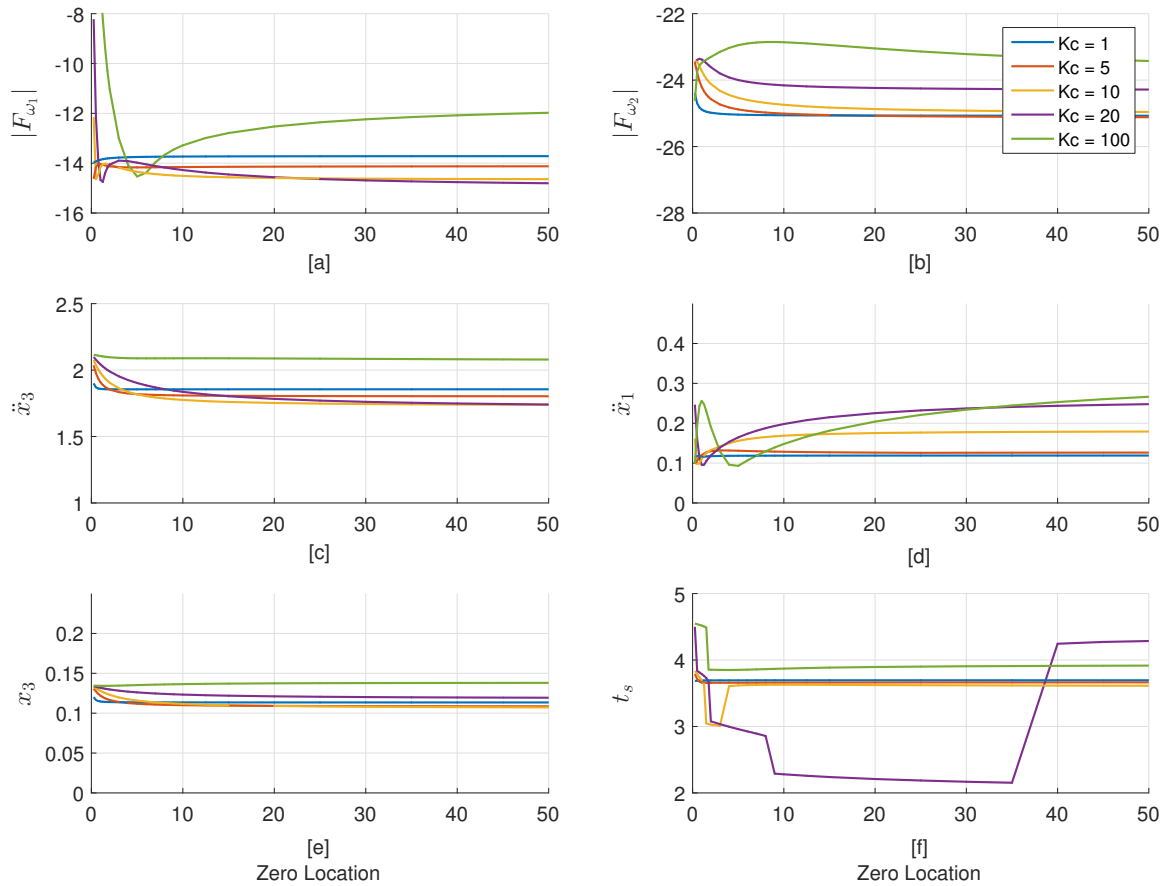


Figure A.7. Response of the three-mass system for a versine profile with $\kappa = 9$ when using feedforward control with a PD controller and -5% error in the natural frequencies. [a] and [b] show the average magnitude of the first and second modes, respectively. [c] shows the peak-to-peak acceleration of mass 3, while [d] shows the peak-to-peak acceleration of mass 1. [e] and [f] show the peak deflection and the settling time of mass 3.

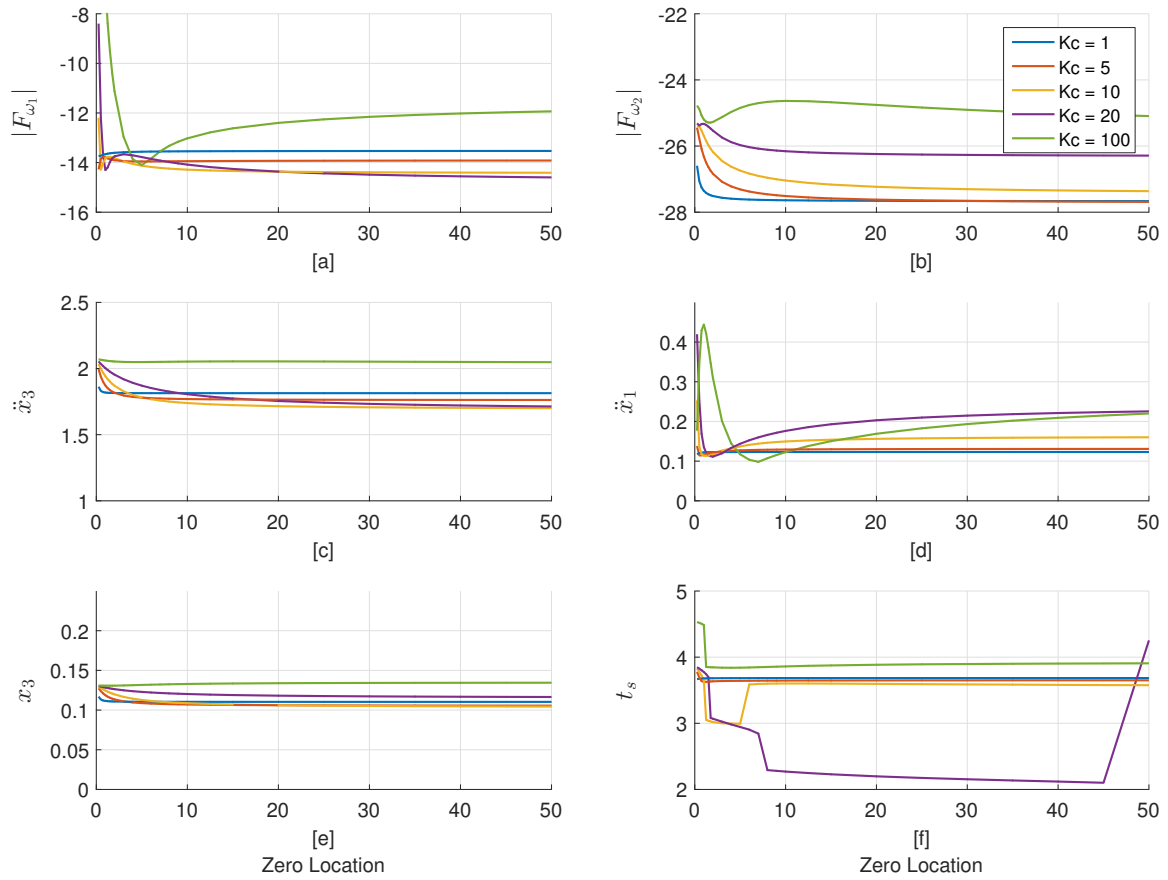


Figure A.8. Response of the three-mass system for a versine profile with $\kappa = 15$ when using feedforward control with a PD controller and -5% error in the natural frequencies. [a] and [b] show the average magnitude of the first and second modes, respectively. [c] shows the peak-to-peak acceleration of mass 3, while [d] shows the peak-to-peak acceleration of mass 1. [e] and [f] show the peak deflection and the settling time of mass 3.

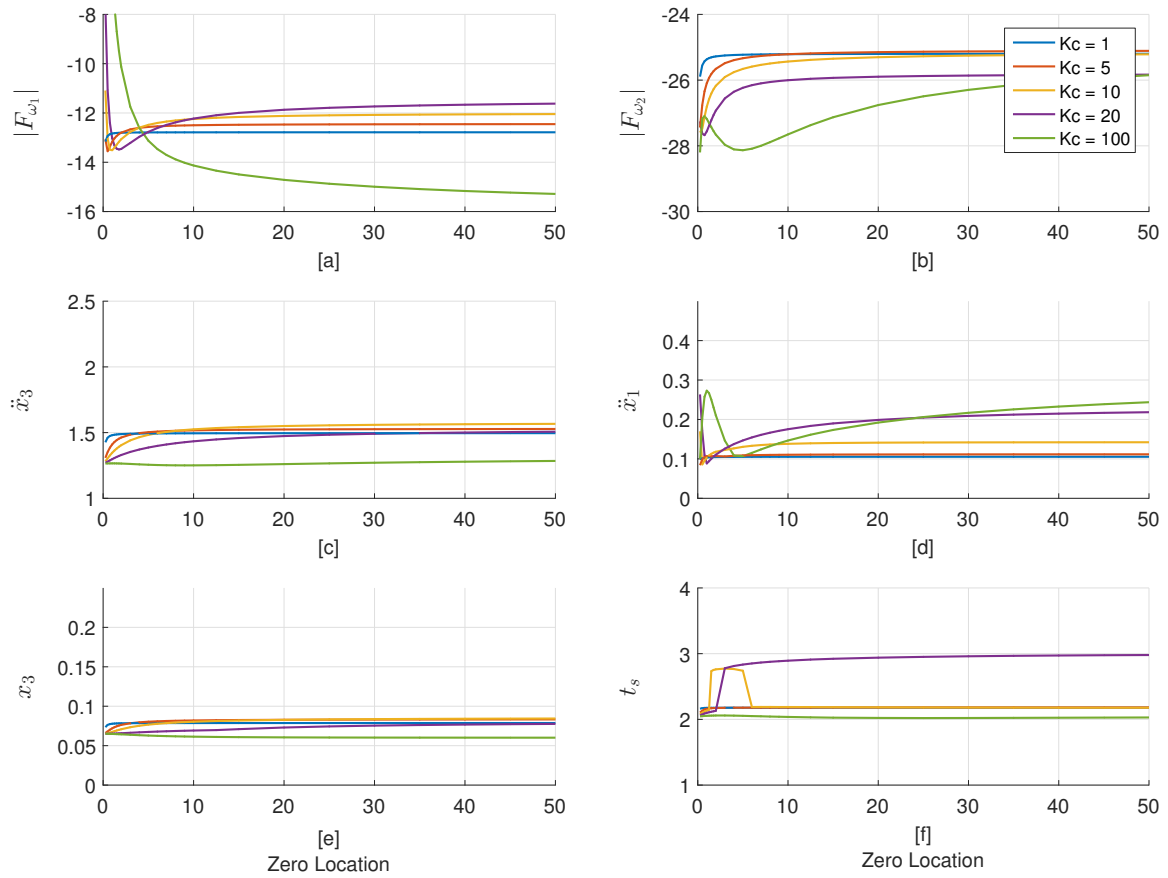


Figure A.9. Response of the three-mass system for a versine profile with $\kappa = 9$ when using feedforward control with a PD controller and +5% error in the natural frequencies. [a] and [b] show the average magnitude of the first and second modes, respectively. [c] shows the peak-to-peak acceleration of mass 3, while [d] shows the peak-to-peak acceleration of mass 1. [e] and [f] show the peak deflection and the settling time of mass 3.

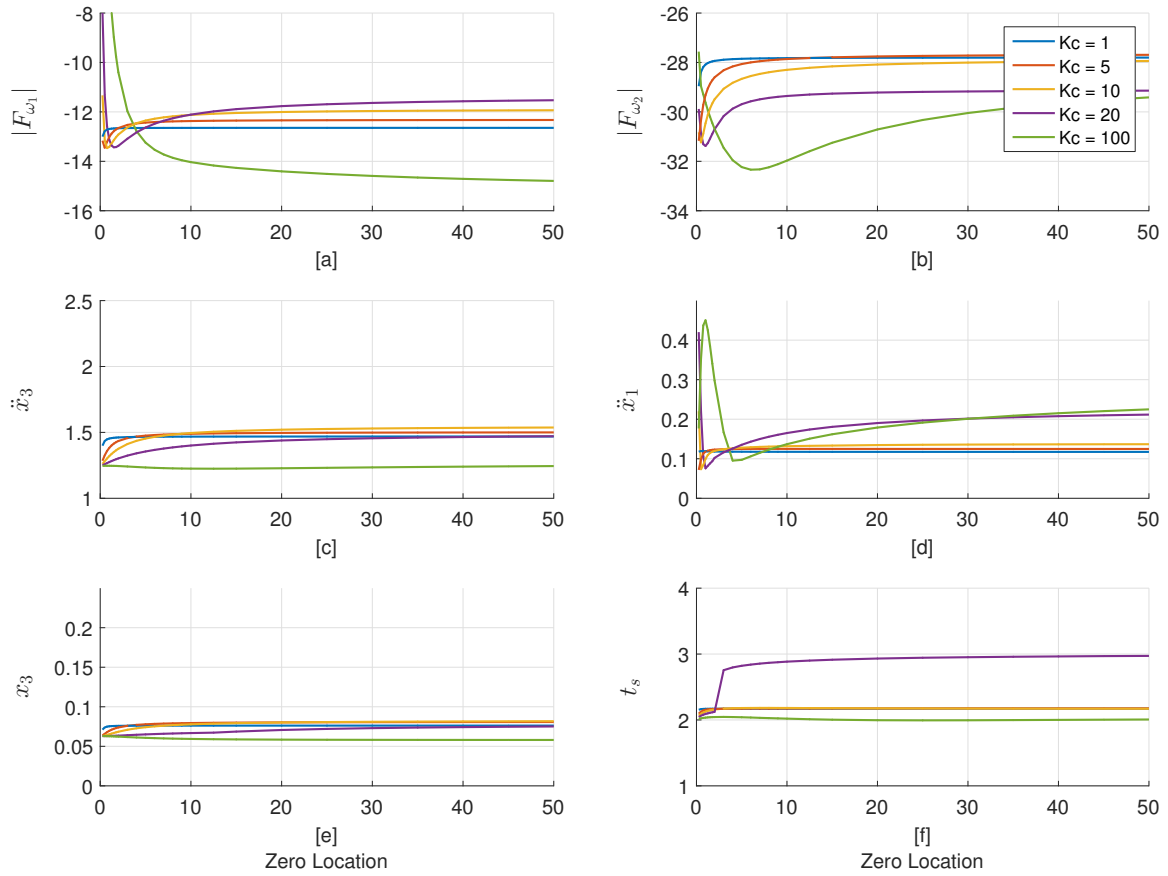


Figure A.10. Response of the three-mass system for a versine profile with $\kappa = 15$ when using feedforward control with a PD controller and +5% error in the natural frequencies. [a] and [b] show the average magnitude of the first and second modes, respectively. [c] shows the peak-to-peak acceleration of mass 3, while [d] shows the peak-to-peak acceleration of mass 1. [e] and [f] show the peak deflection and the settling time of mass 3.

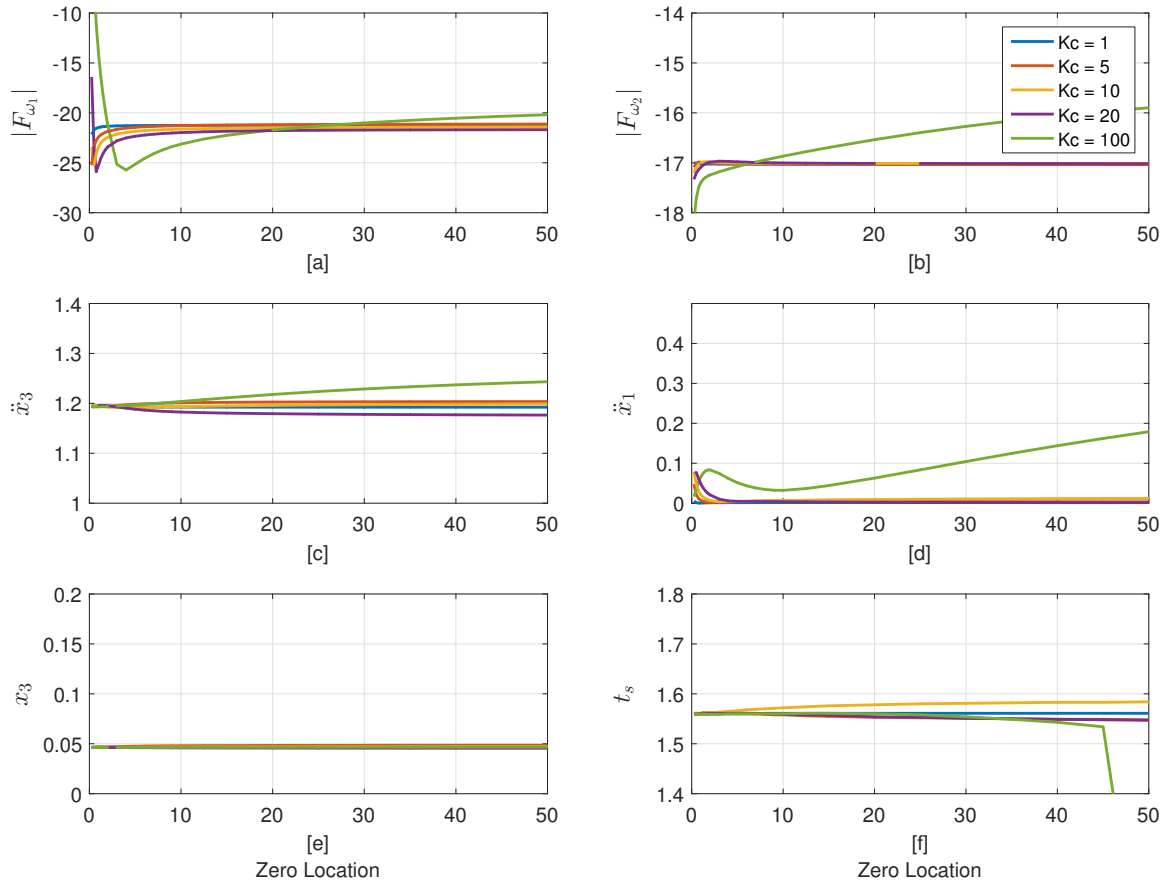


Figure A.11. Response of the three-mass system for a ramped sinusoid profile with $\kappa = 9$ when using computed torque control with a PD controller and no error in the natural frequencies. [a] and [b] show the average magnitude of the first and second modes, respectively. [c] shows the peak-to-peak acceleration of mass 3, while [d] shows the peak-to-peak acceleration of mass 1. [e] and [f] show the peak deflection and the settling time of mass 3.

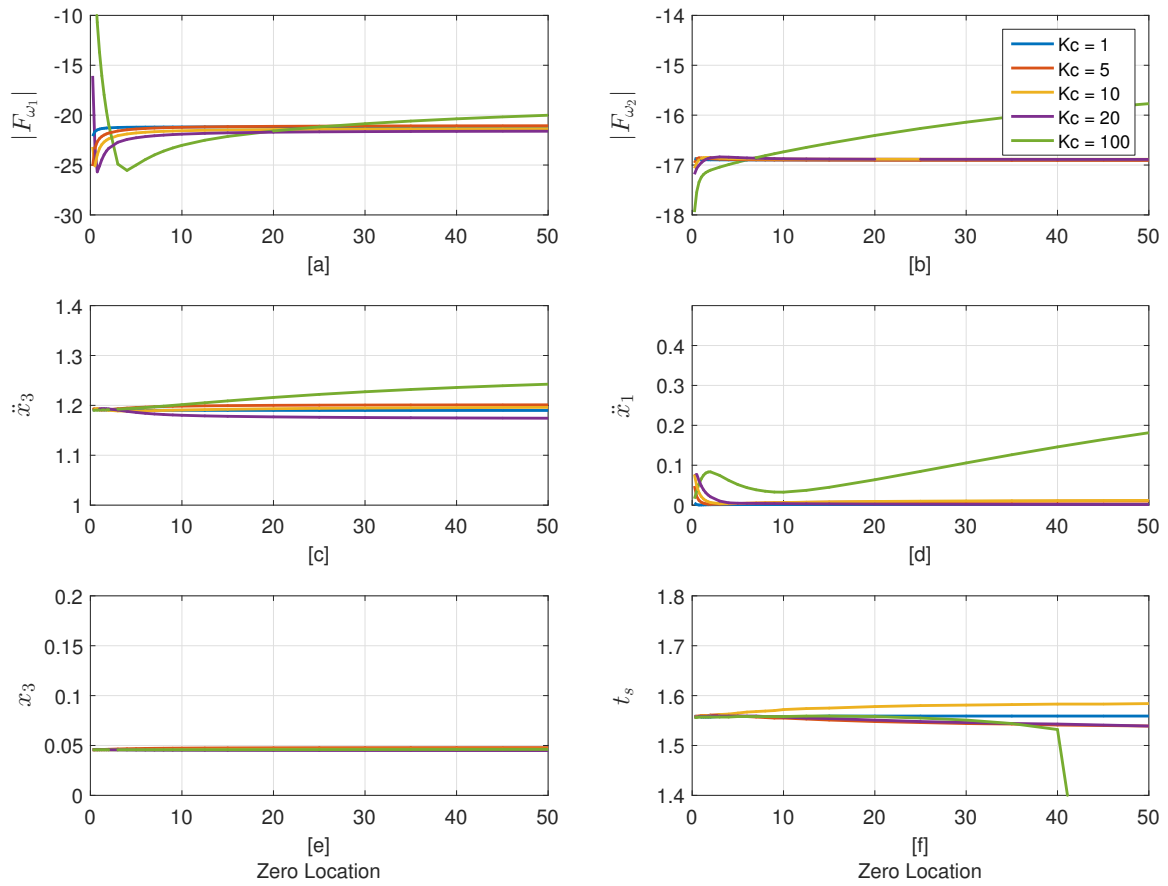


Figure A.12. Response of the three-mass system for a ramped sinusoid profile with $\kappa = 15$ when using computed torque control with a PD controller and no error in the natural frequencies. [a] and [b] show the average magnitude of the first and second modes, respectively. [c] shows the peak-to-peak acceleration of mass 3, while [d] shows the peak-to-peak acceleration of mass 1. [e] and [f] show the peak deflection and the settling time of mass 3.

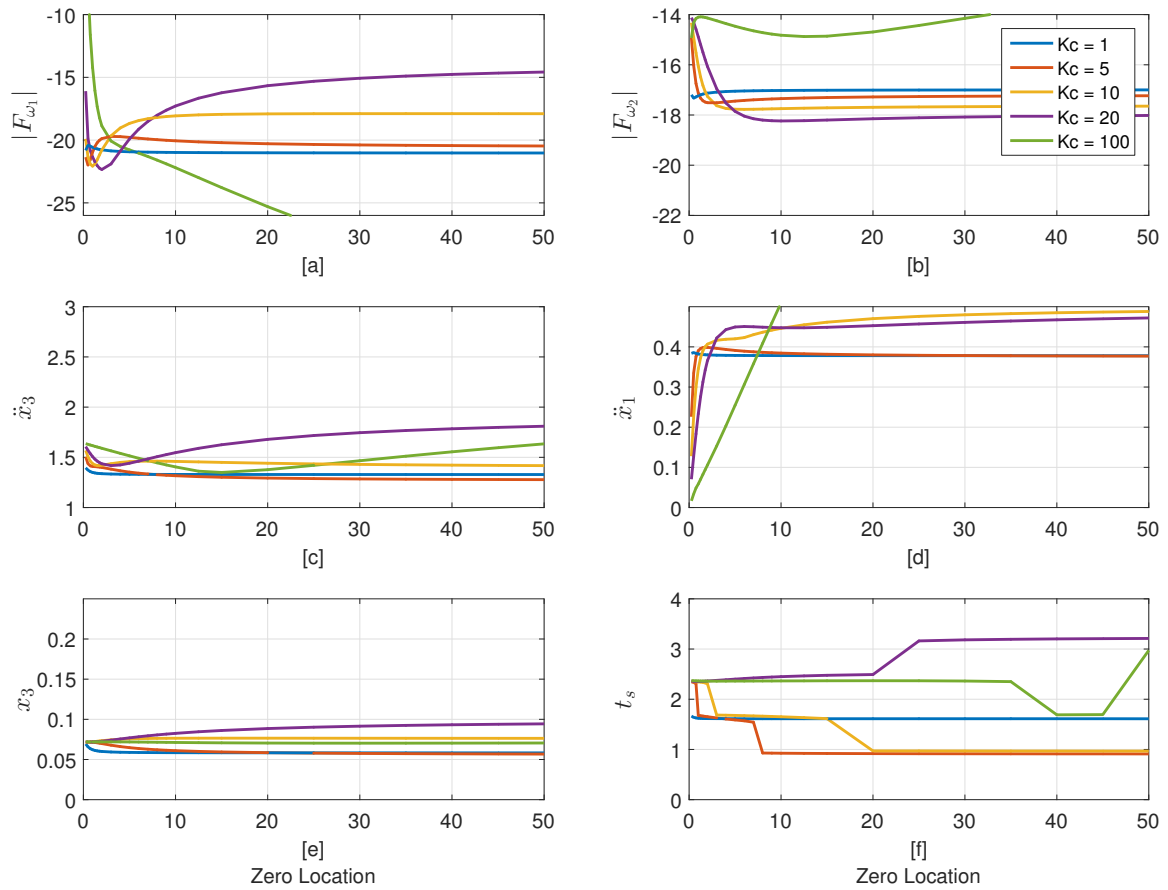


Figure A.13. Response of the three-mass system for a ramped sinusoid profile with $\kappa = 9$ when using computed torque control with a PD controller and -5% error in the natural frequencies. [a] and [b] show the average magnitude of the first and second modes, respectively. [c] shows the peak-to-peak acceleration of mass 3, while [d] shows the peak-to-peak acceleration of mass 1. [e] and [f] show the peak deflection and the settling time of mass 3.

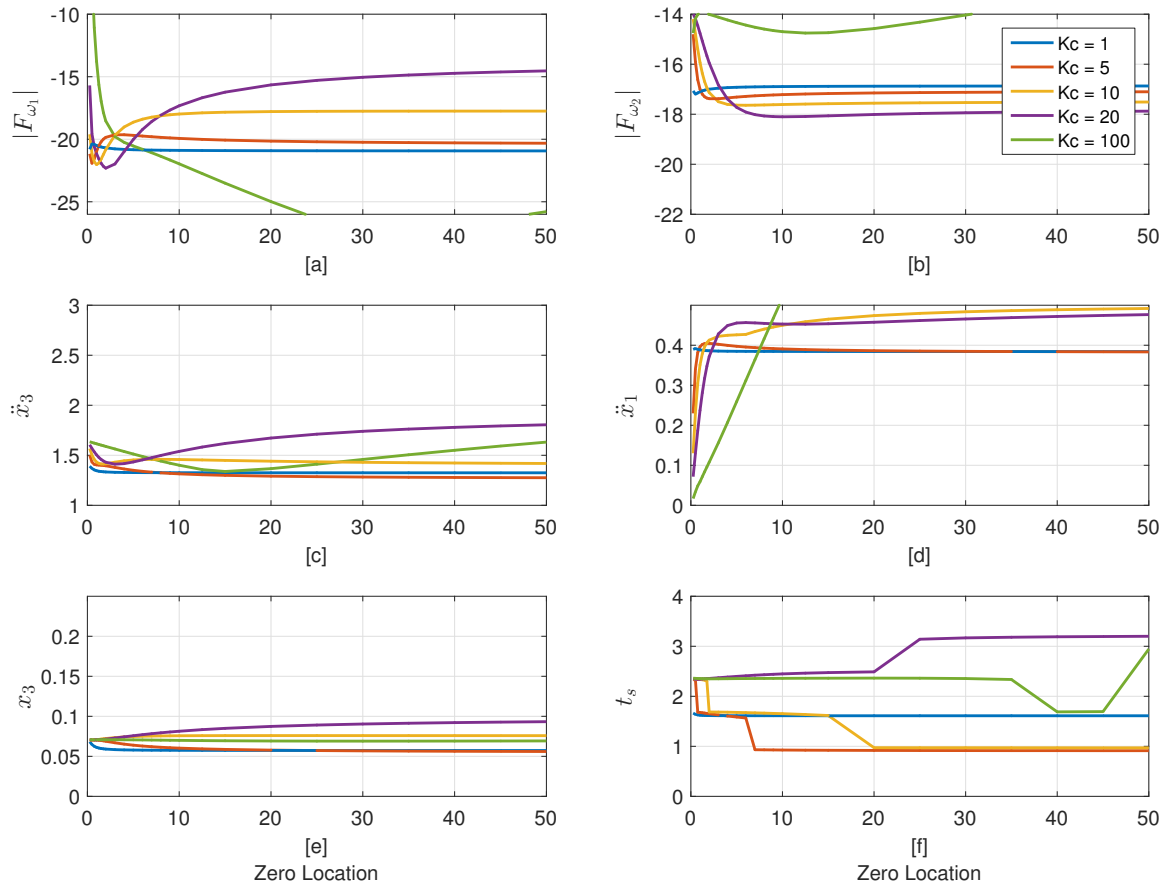


Figure A.14. Response of the three-mass system for a ramped sinusoid profile with $\kappa = 15$ when using computed torque control with a PD controller and -5% error in the natural frequencies. [a] and [b] show the average magnitude of the first and second modes, respectively. [c] shows the peak-to-peak acceleration of mass 3, while [d] shows the peak-to-peak acceleration of mass 1. [e] and [f] show the peak deflection and the settling time of mass 3.

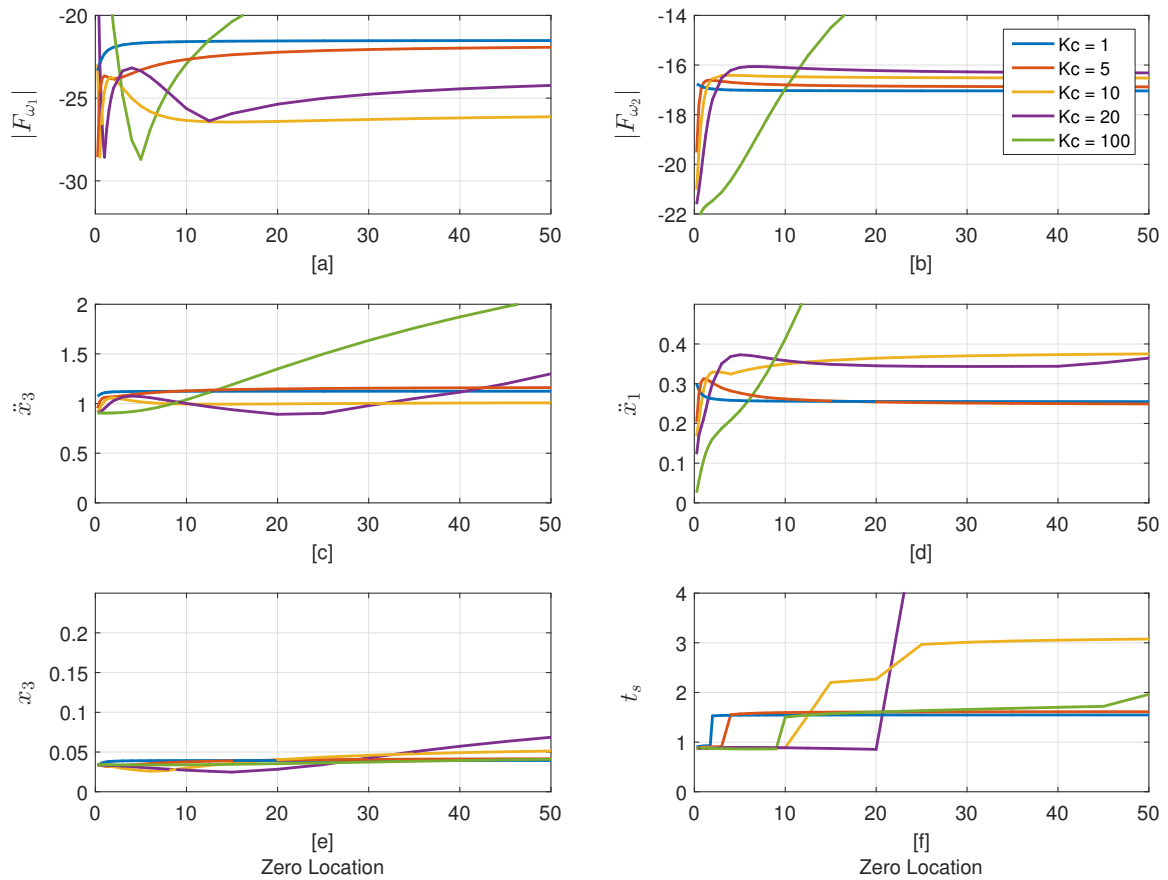


Figure A.15. Response of the three-mass system for a ramped sinusoid profile with $\kappa = 9$ when using computed torque control with a PD controller and +5% error in the natural frequencies. [a] and [b] show the average magnitude of the first and second modes, respectively. [c] shows the peak-to-peak acceleration of mass 3, while [d] shows the peak-to-peak acceleration of mass 1. [e] and [f] show the peak deflection and the settling time of mass 3.

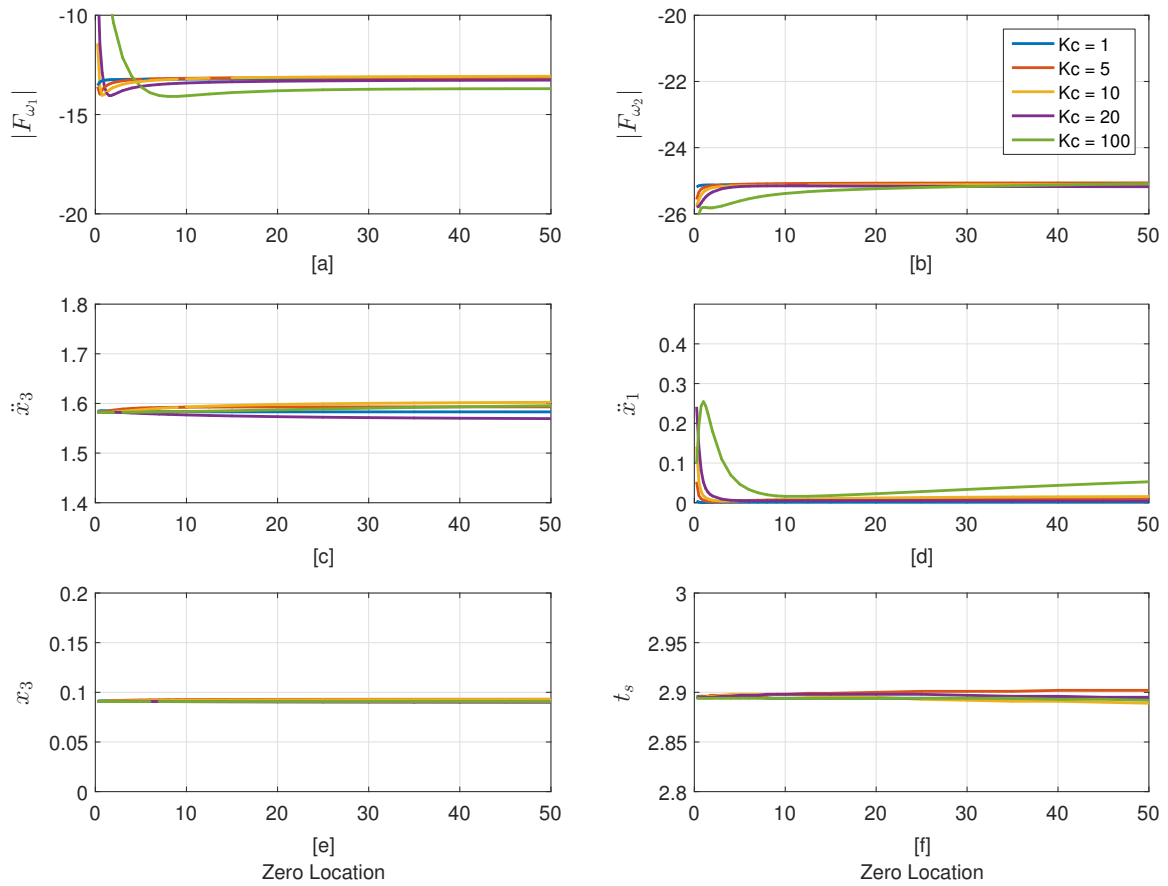


Figure A.16. Response of the three-mass system for a versine profile with $\kappa = 9$ when using computed torque control with a PD controller and no error in the natural frequencies. [a] and [b] show the average magnitude of the first and second modes, respectively. [c] shows the peak-to-peak acceleration of mass 3, while [d] shows the peak-to-peak acceleration of mass 1. [e] and [f] show the peak deflection and the settling time of mass 3.

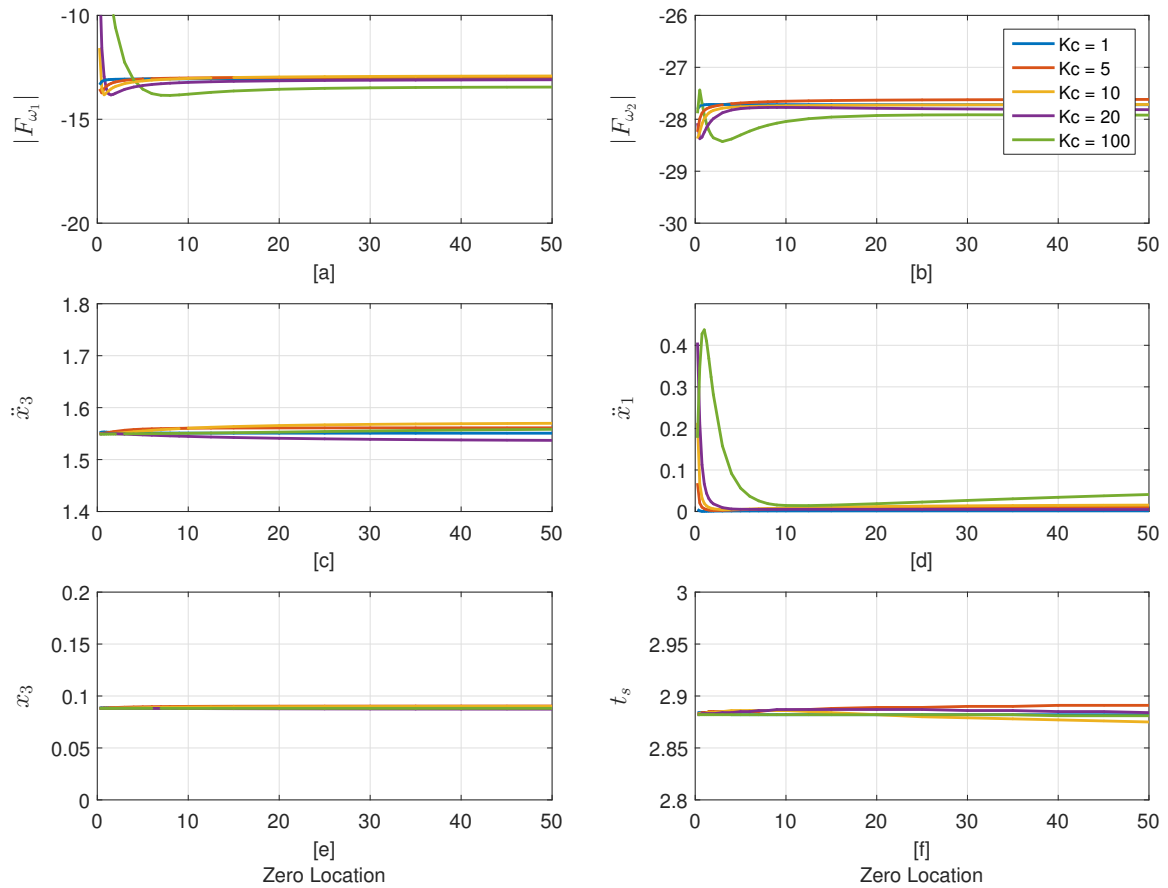


Figure A.17. Response of the three-mass system for a versine profile with $\kappa = 15$ when using computed torque control with a PD controller and no error in the natural frequencies. [a] and [b] show the average magnitude of the first and second modes, respectively. [c] shows the peak-to-peak acceleration of mass 3, while [d] shows the peak-to-peak acceleration of mass 1. [e] and [f] show the peak deflection and the settling time of mass 3.

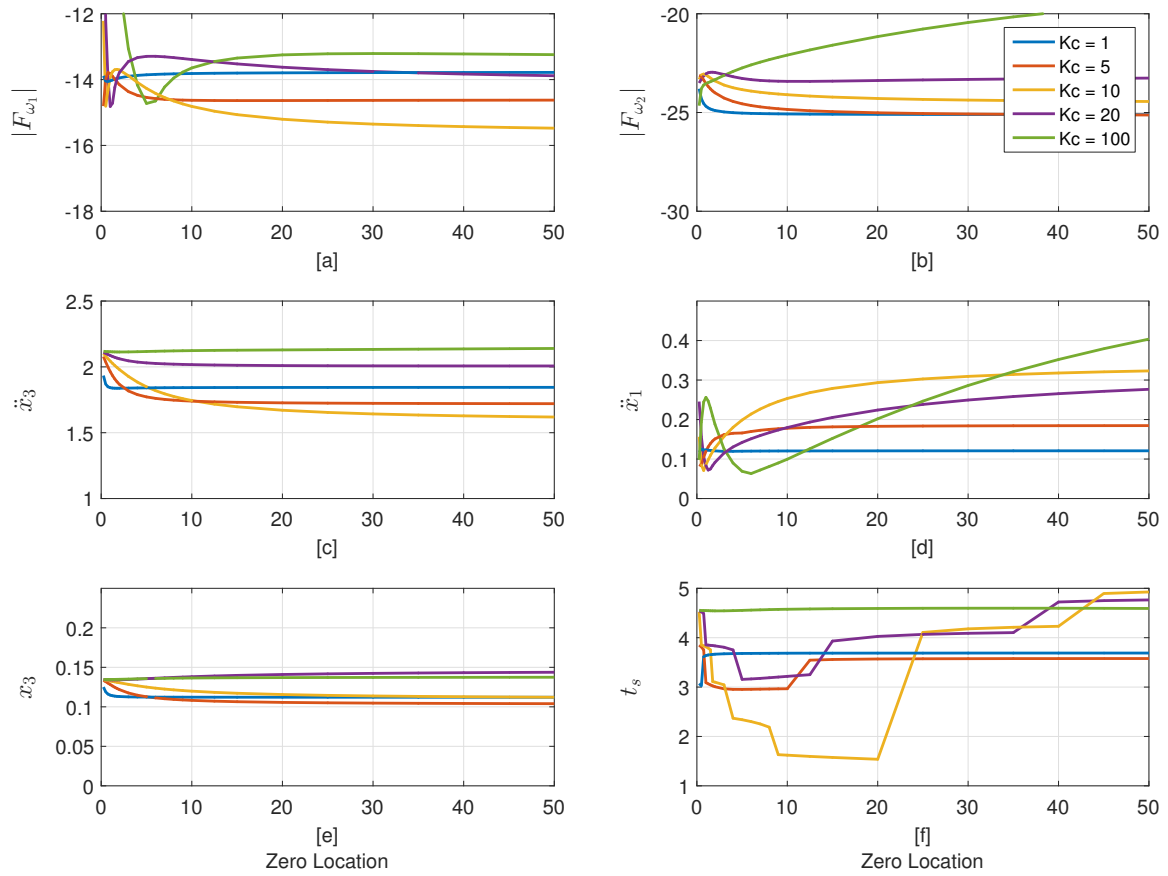


Figure A.18. Response of the three-mass system for a versine profile with $\kappa = 9$ when using computed torque control with a PD controller and -5% error in the natural frequencies. [a] and [b] show the average magnitude of the first and second modes, respectively. [c] shows the peak-to-peak acceleration of mass 3, while [d] shows the peak-to-peak acceleration of mass 1. [e] and [f] show the peak deflection and the settling time of mass 3.

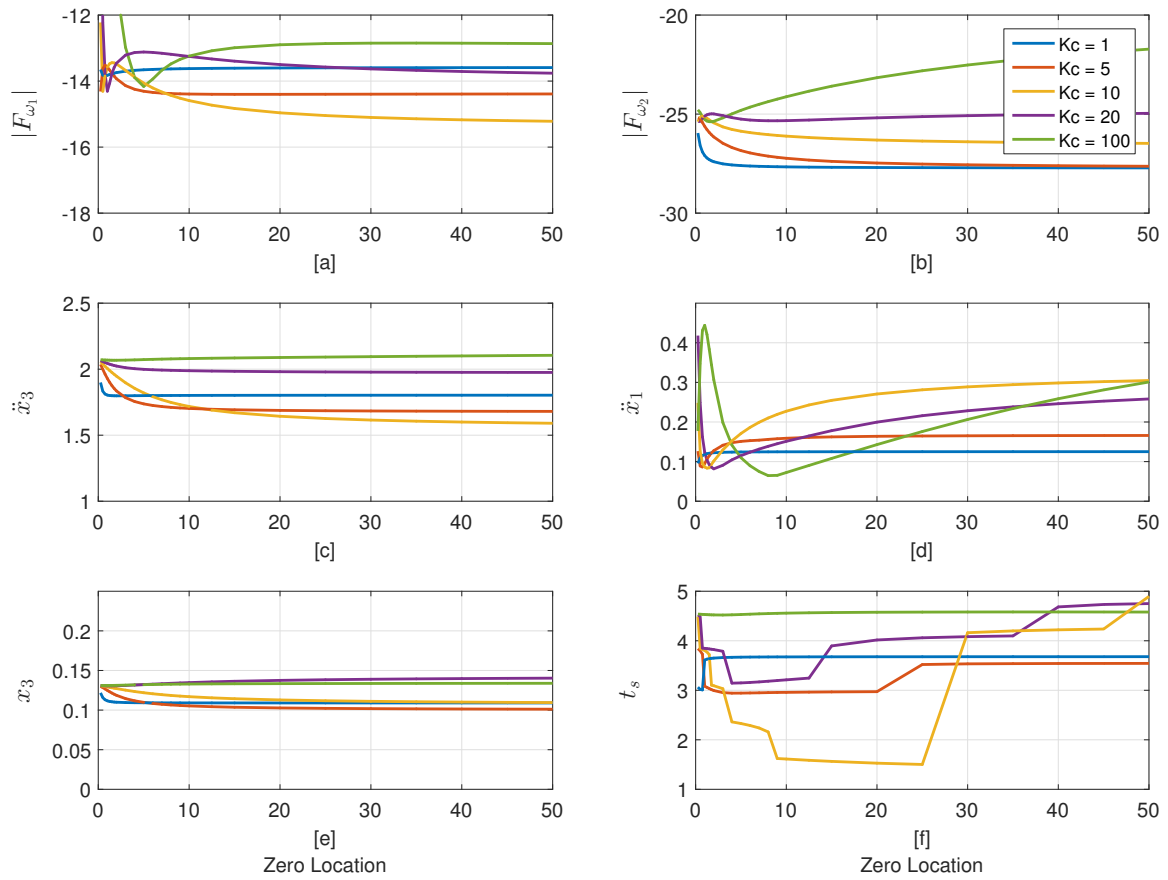


Figure A.19. Response of the three-mass system for a versine profile with $\kappa = 15$ when using computed torque control with a PD controller and -5% error in the natural frequencies. [a] and [b] show the average magnitude of the first and second modes, respectively. [c] shows the peak-to-peak acceleration of mass 3, while [d] shows the peak-to-peak acceleration of mass 1. [e] and [f] show the peak deflection and the settling time of mass 3.

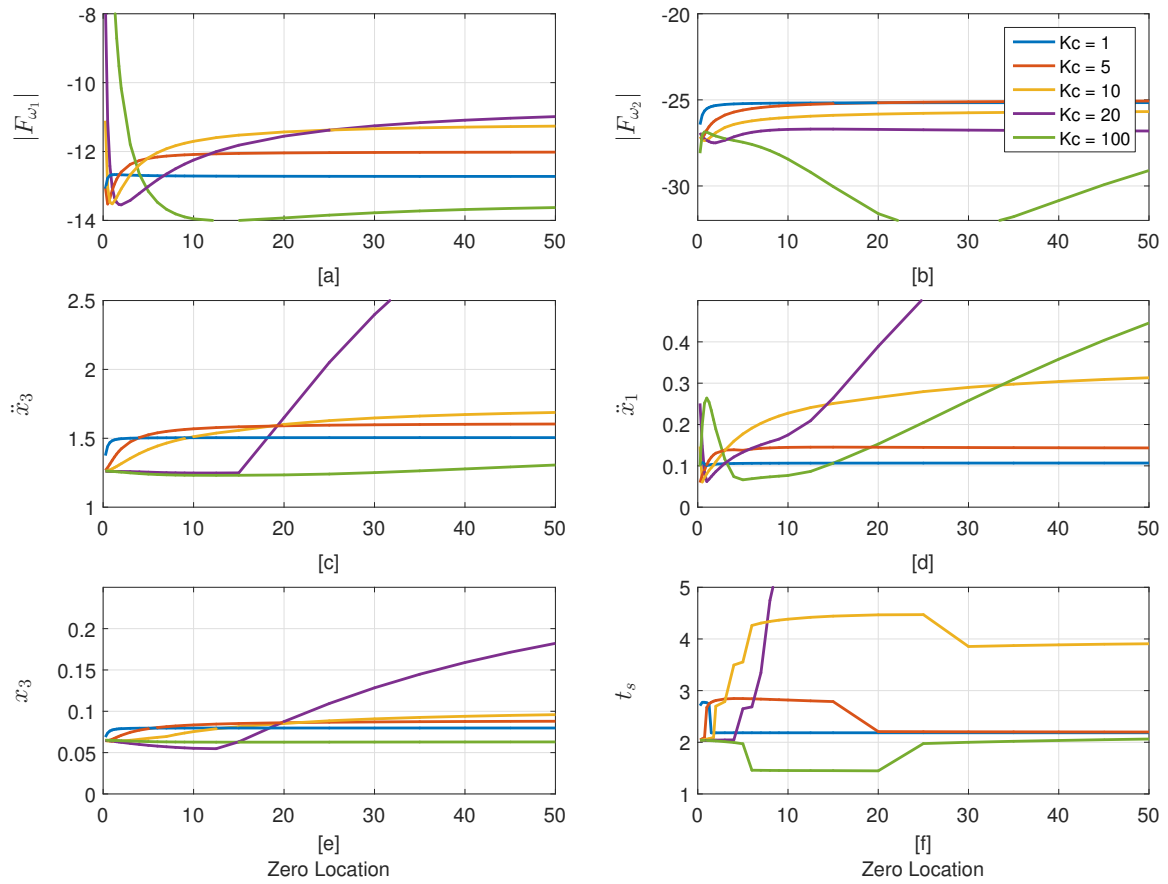


Figure A.20. Response of the three-mass system for a versine profile with $\kappa = 9$ when using computed torque control with a PD controller and +5% error in the natural frequencies. [a] and [b] show the average magnitude of the first and second modes, respectively. [c] shows the peak-to-peak acceleration of mass 3, while [d] shows the peak-to-peak acceleration of mass 1. [e] and [f] show the peak deflection and the settling time of mass 3.

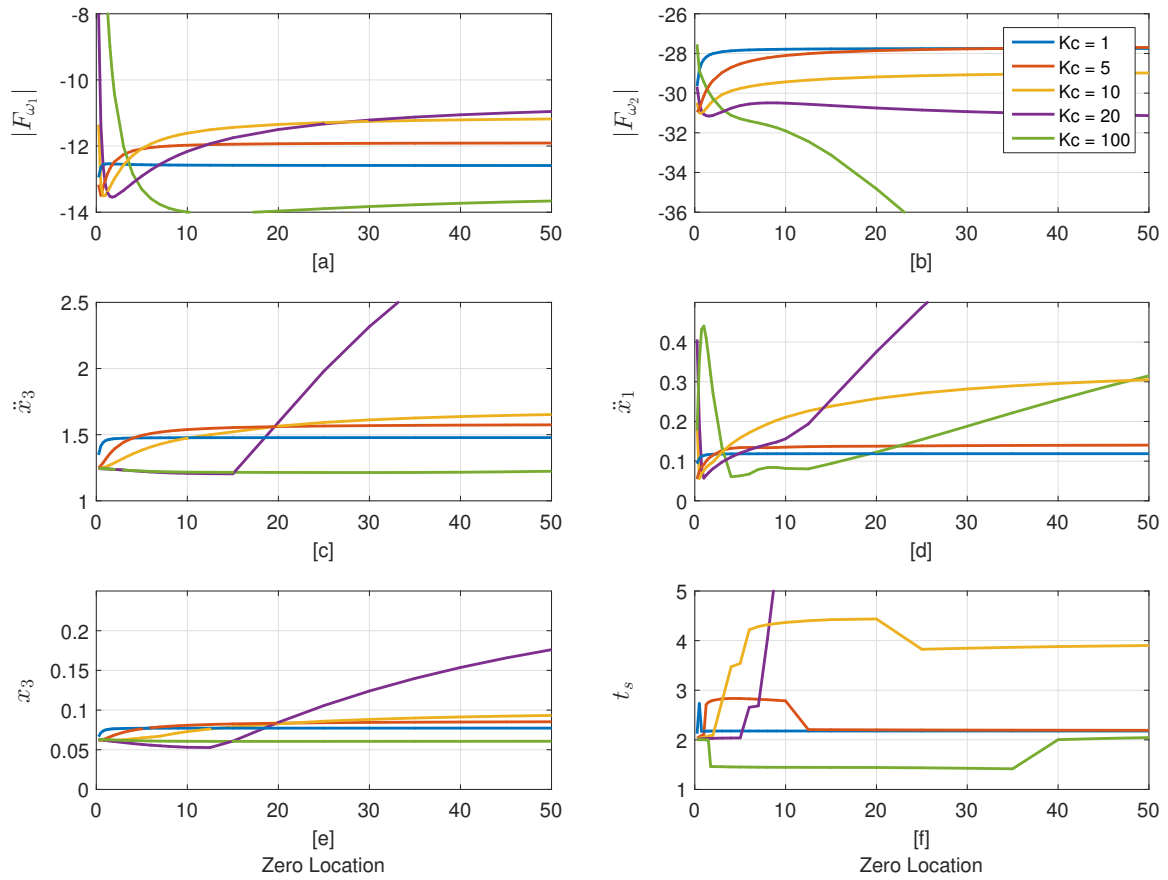


Figure A.21. Response of the three-mass system for a versine profile with $\kappa = 15$ when using computed torque control with a PD controller and +5% error in the natural frequencies. [a] and [b] show the average magnitude of the first and second modes, respectively. [c] shows the peak-to-peak acceleration of mass 3, while [d] shows the peak-to-peak acceleration of mass 1. [e] and [f] show the peak deflection and the settling time of mass 3.

Appendix B. Extra Experimental Results for the Flexible-Joint Robot

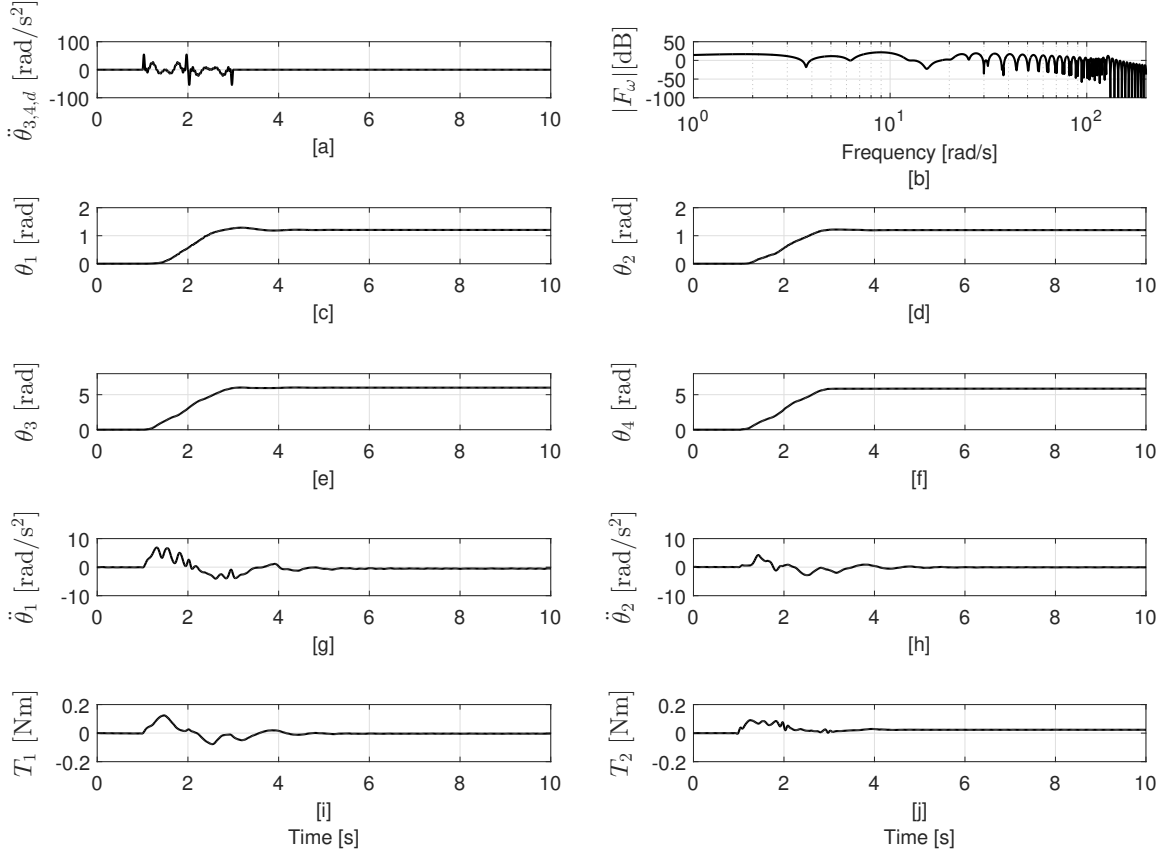


Figure B.1. Experimental response of Original PD controller when applying a versine input with $\kappa = 9$. [a] is the desired motor acceleration profile for both motors, and [b] is the magnitude spectrum of the desired acceleration profile for the motors. [c] and [d] are the angular positions of links 1 and 2, while [e] and [f] are the angular positions of the shoulder and elbow motors, respectively. [g] and [h] show the angular accelerations of links 1 and 2, while [i] and [j] are the torques of the shoulder and elbow motors.

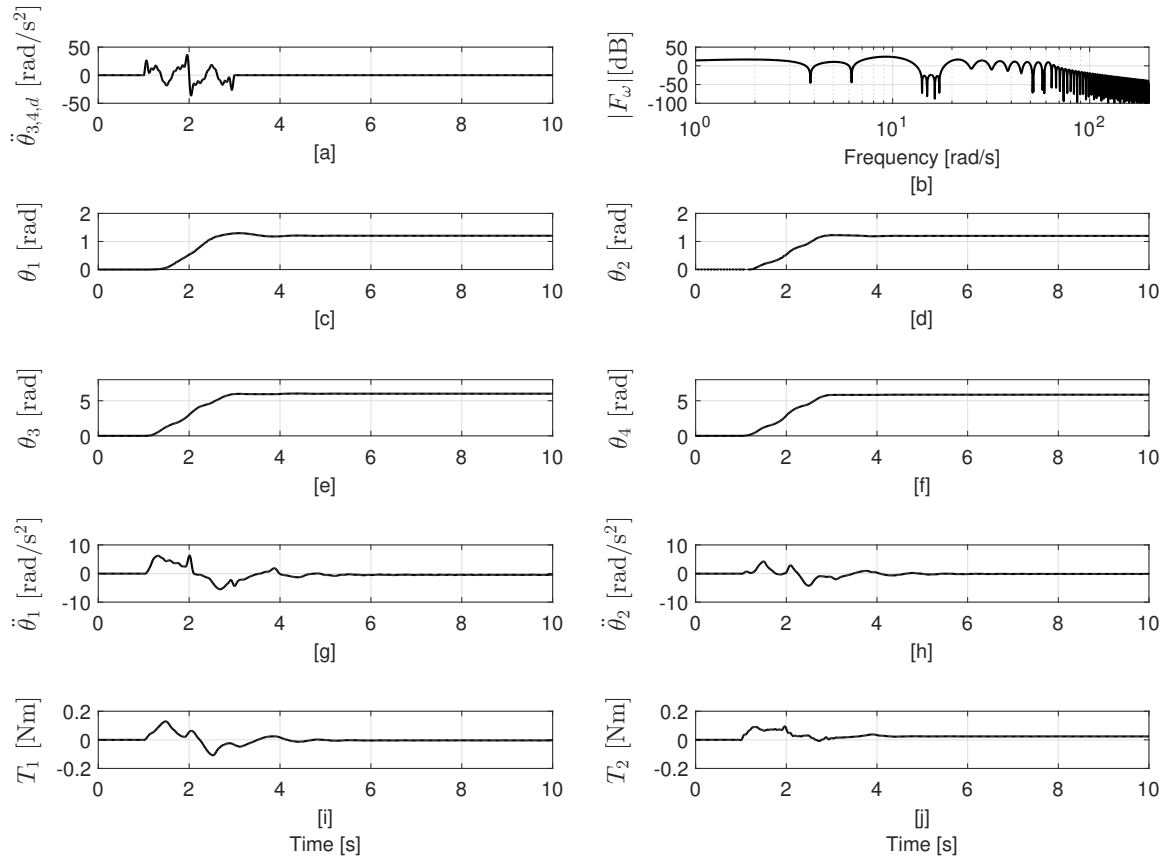


Figure B.2. Experimental response of Original PD controller when applying a ramped sinusoid input with $\kappa = 6$. [a] is the desired motor acceleration profile for both motors, and [b] is the magnitude spectrum of the desired acceleration profile for the motors. [c] and [d] are the angular positions of links 1 and 2, while [e] and [f] are the angular positions of the shoulder and elbow motors, respectively. [g] and [h] show the angular accelerations of links 1 and 2, while [i] and [j] are the torques of the shoulder and elbow motors.

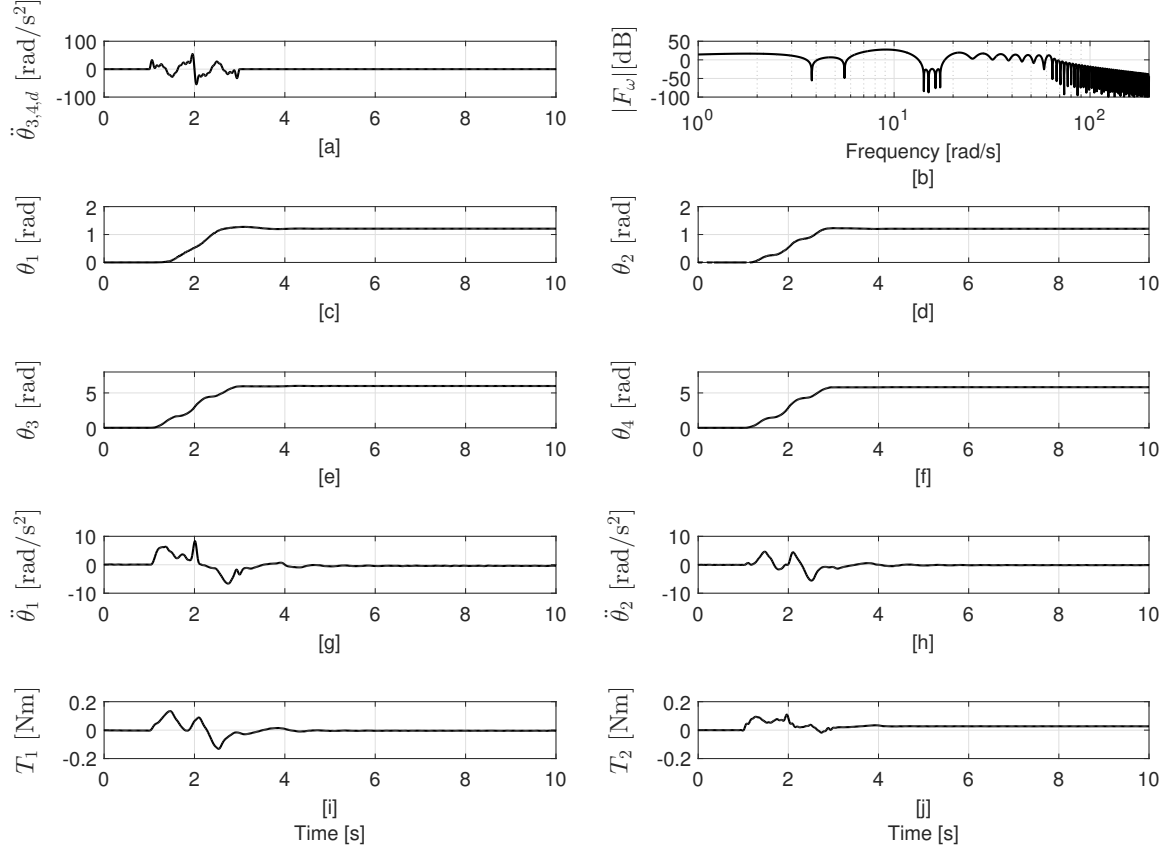


Figure B.3. Experimental response of Original PD controller when applying a ramped sinusoid input with $\kappa = 9$. [a] is the desired motor acceleration profile for both motors, and [b] is the magnitude spectrum af the desired acceleration profile for the motors. [c] and [d] are the angular positions of links 1 and 2, while [e] and [f] are the angular positions of the shoulder and elbow motors, respectively. [g] and [h] show the angular accelerations of links 1 and 2, while [i] and [j] are the torques of the shoulder and elbow motors.

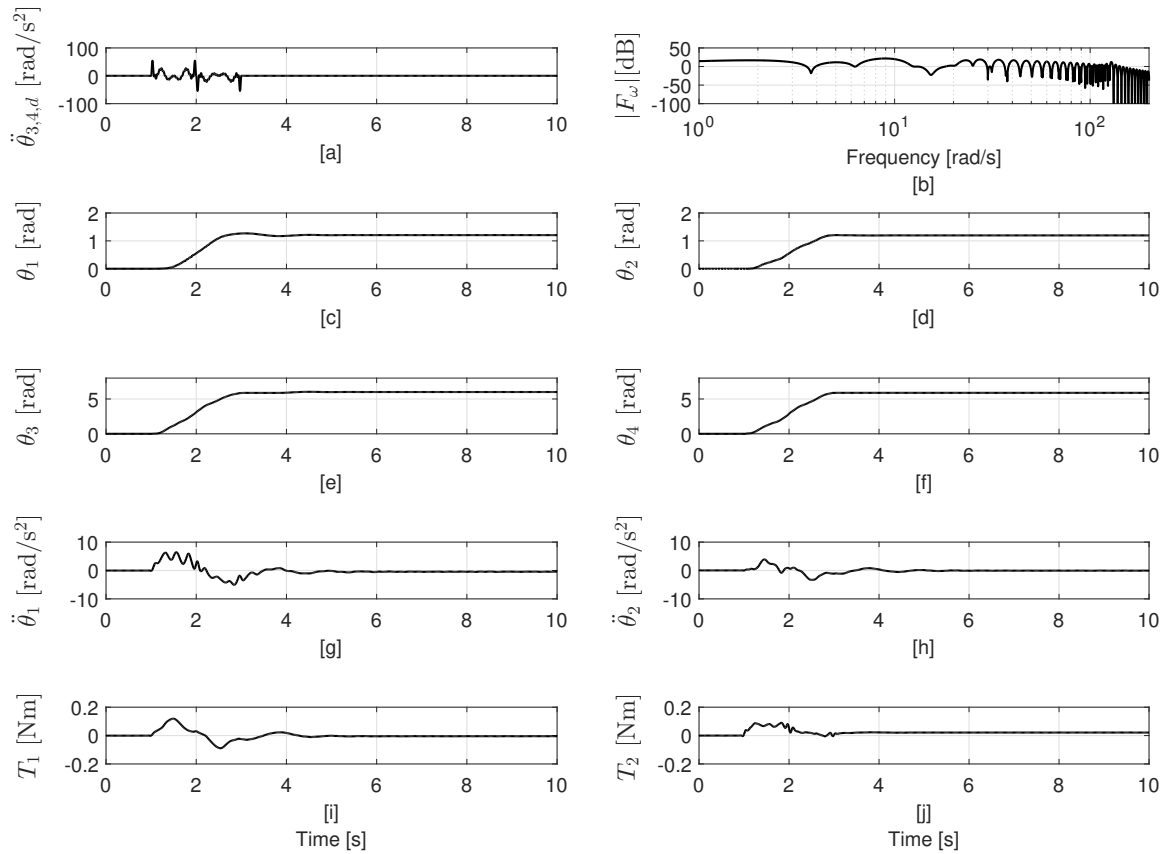


Figure B.4. Experimental response of Alternative PD controller when applying a versine input with $\kappa = 9$. [a] is the desired motor acceleration profile for both motors, and [b] is the magnitude spectrum of the desired acceleration profile for the motors. [c] and [d] are the angular positions of links 1 and 2, while [e] and [f] are the angular positions of the shoulder and elbow motors, respectively. [g] and [h] show the angular accelerations of links 1 and 2, while [i] and [j] are the torques of the shoulder and elbow motors.

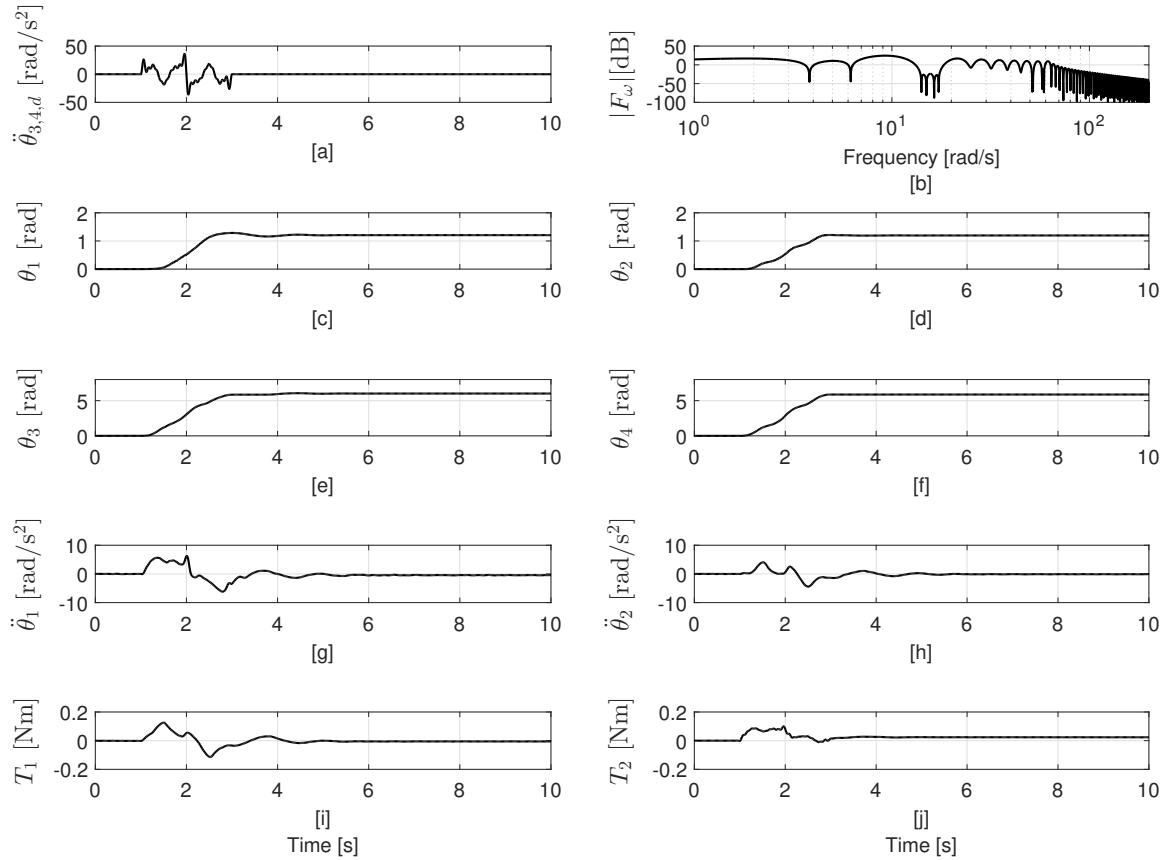


Figure B.5. Experimental response of Alternative PD controller when applying a ramped sinusoid input with $\kappa = 6$. [a] is the desired motor acceleration profile for both motors, and [b] is the magnitude spectrum of the desired acceleration profile for the motors. [c] and [d] are the angular positions of links 1 and 2, while [e] and [f] are the angular positions of the shoulder and elbow motors, respectively. [g] and [h] show the angular accelerations of links 1 and 2, while [i] and [j] are the torques of the shoulder and elbow motors.

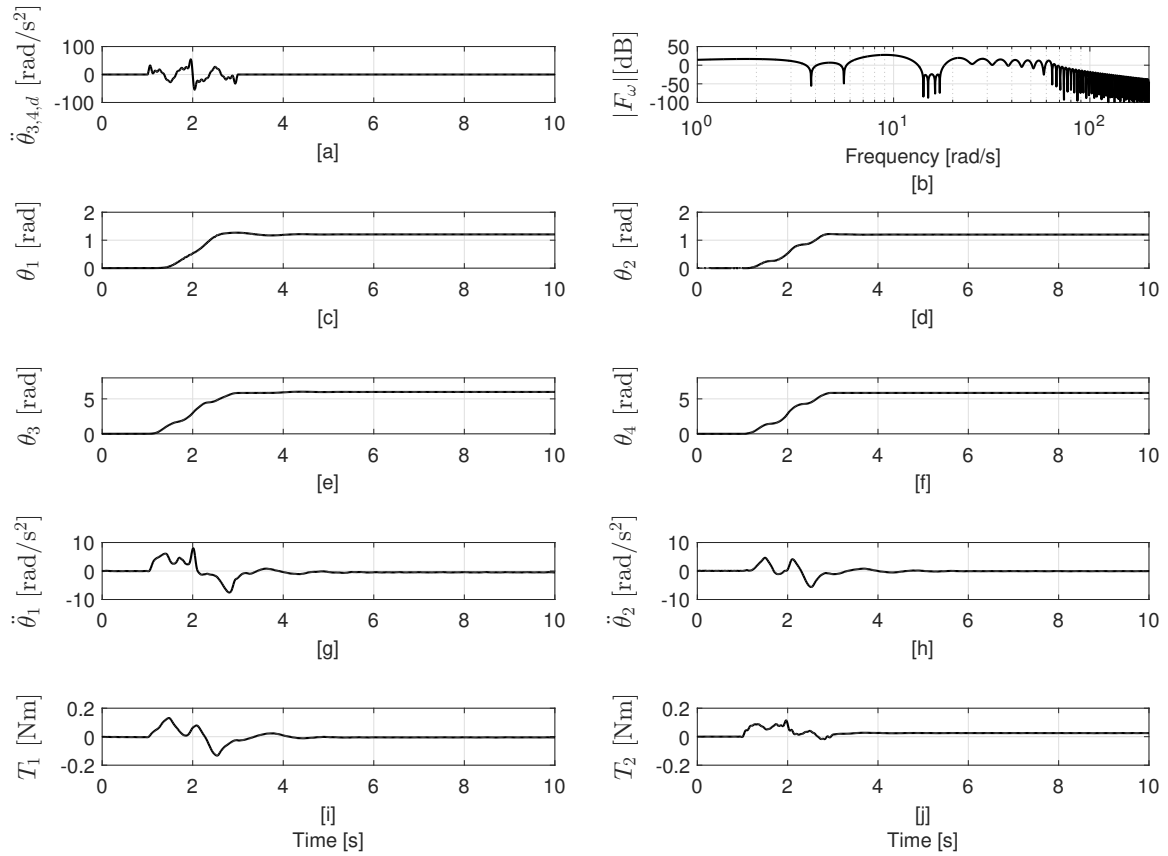


Figure B.6. Experimental response of Alternative PD controller when applying a ramped sinusoid input with $\kappa = 9$. [a] is the desired motor acceleration profile for both motors, and [b] is the magnitude spectrum of the desired acceleration profile for the motors. [c] and [d] are the angular positions of links 1 and 2, while [e] and [f] are the angular positions of the shoulder and elbow motors, respectively. [g] and [h] show the angular accelerations of links 1 and 2, while [i] and [j] are the torques of the shoulder and elbow motors.

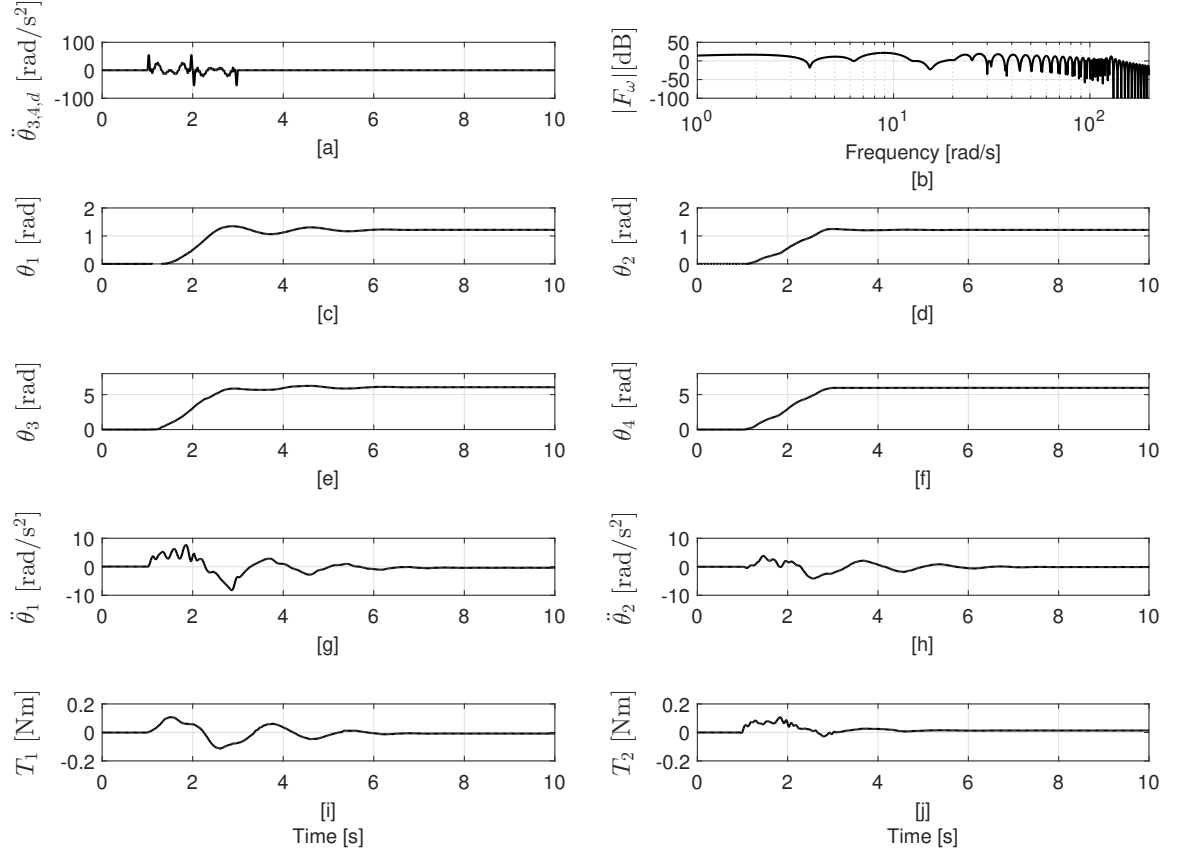


Figure B.7. Experimental response of Lead-Lag controller with $K_{c,1} = 3200$, $K_{c,2} = 400$, $\omega_{center,1} = \omega_{center,2} = 3.75 \frac{\text{rad}}{\text{s}}$, $\omega_{width,1} = \omega_{width,2} = 0.5 \frac{\text{rad}}{\text{s}}$, and $a_1 = a_2 = 4$ when applying a versine input with $\kappa = 9$. [a] is the desired motor acceleration profile for both motors, and [b] is the magnitude spectrum of the desired acceleration profile for the motors. [c] and [d] are the angular positions of links 1 and 2, while [e] and [f] are the angular positions of the shoulder and elbow motors, respectively. [g] and [h] show the angular accelerations of links 1 and 2, while [i] and [j] are the torques of the shoulder and elbow motors.

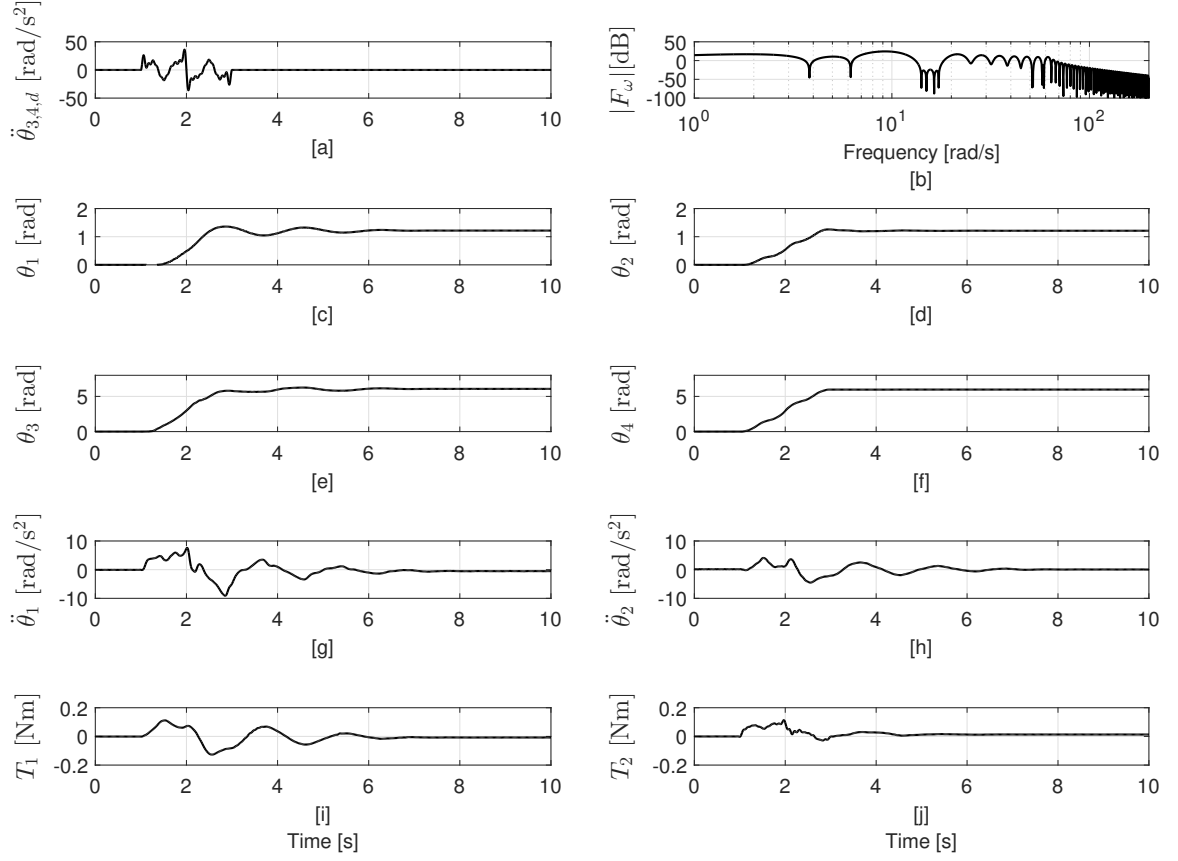


Figure B.8. Experimental response of Lead-Lag controller with $K_{c,1} = 3200$, $K_{c,2} = 400$, $\omega_{center,1} = \omega_{center,2} = 3.75 \frac{\text{rad}}{\text{s}}$, $\omega_{width,1} = \omega_{width,2} = 0.5 \frac{\text{rad}}{\text{s}}$, and $a_1 = a_2 = 4$ when applying a ramped sinusoid input with $\kappa = 6$. [a] is the desired motor acceleration profile for both motors, and [b] is the magnitude spectrum of the desired acceleration profile for the motors. [c] and [d] are the angular positions of links 1 and 2, while [e] and [f] are the angular positions of the shoulder and elbow motors, respectively. [g] and [h] show the angular accelerations of links 1 and 2, while [i] and [j] are the torques of the shoulder and elbow motors.

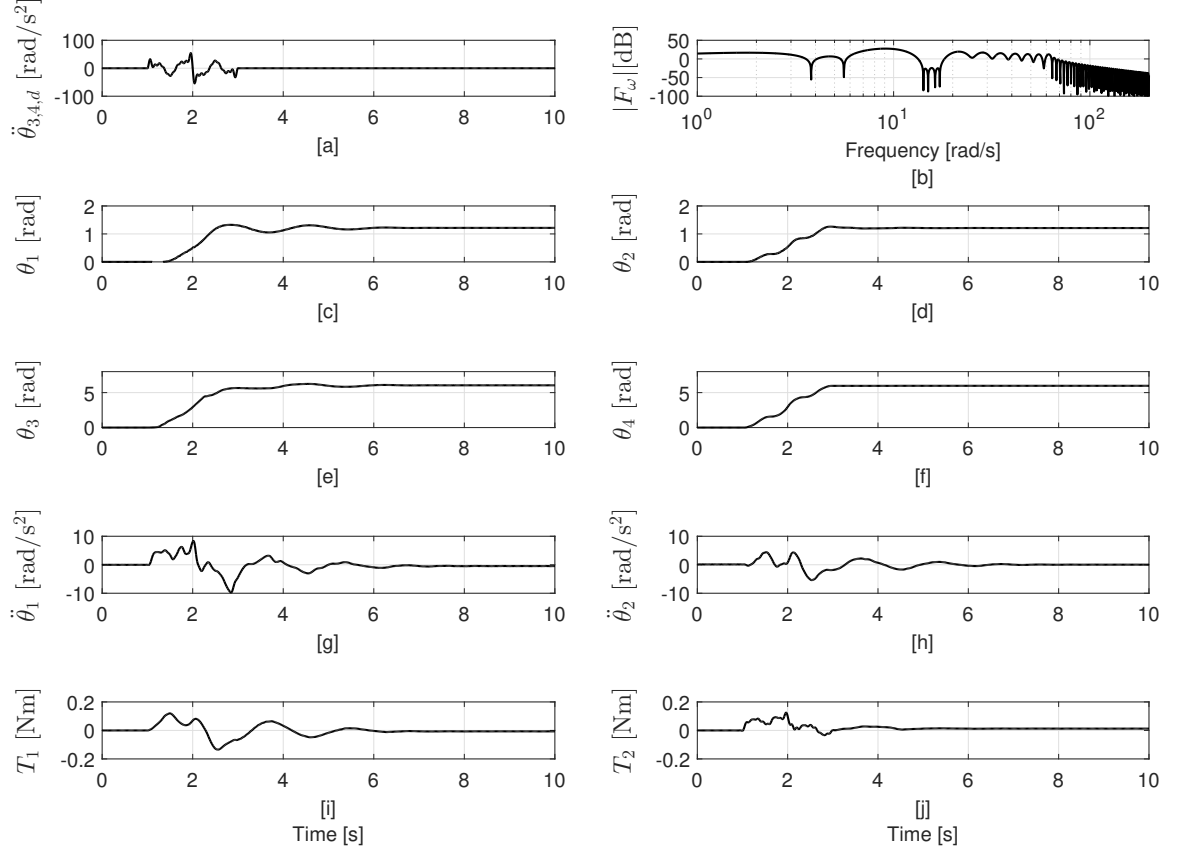


Figure B.9. Experimental response of Lead-Lag controller with $K_{c,1} = 3200$, $K_{c,2} = 400$, $\omega_{center,1} = \omega_{center,2} = 3.75 \frac{\text{rad}}{\text{s}}$, $\omega_{width,1} = \omega_{width,2} = 0.5 \frac{\text{rad}}{\text{s}}$, and $a_1 = a_2 = 4$ when applying a ramped sinusoid input with $\kappa = 9$. [a] is the desired motor acceleration profile for both motors, and [b] is the magnitude spectrum of the desired acceleration profile for the motors. [c] and [d] are the angular positions of links 1 and 2, while [e] and [f] are the angular positions of the shoulder and elbow motors, respectively. [g] and [h] show the angular accelerations of links 1 and 2, while [i] and [j] are the torques of the shoulder and elbow motors.

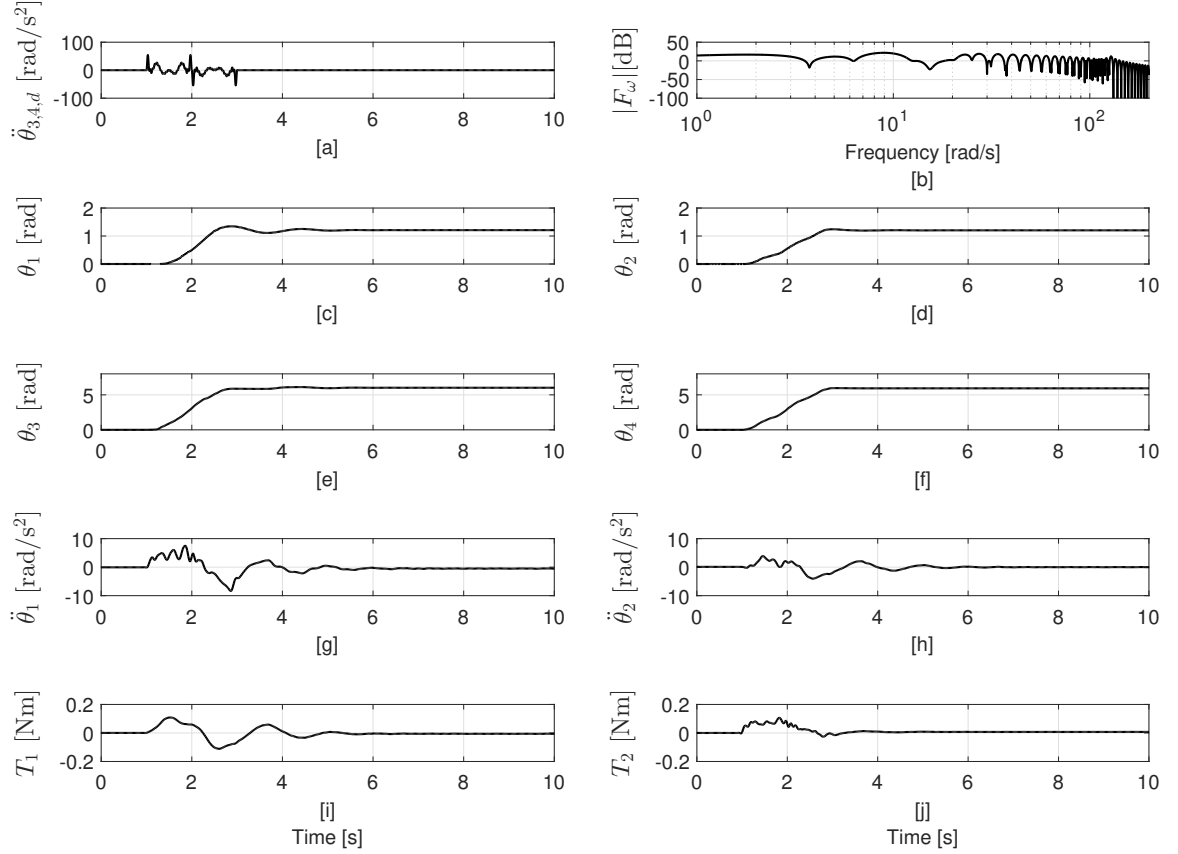


Figure B.10. Experimental response of Hybrid controller when applying a versine input with $\kappa = 9$. [a] is the desired motor acceleration profile for both motors, and [b] is the magnitude spectrum of the desired acceleration profile for the motors. [c] and [d] are the angular positions of links 1 and 2, while [e] and [f] are the angular positions of the shoulder and elbow motors, respectively. [g] and [h] show the angular accelerations of links 1 and 2, while [i] and [j] are the torques of the shoulder and elbow motors.

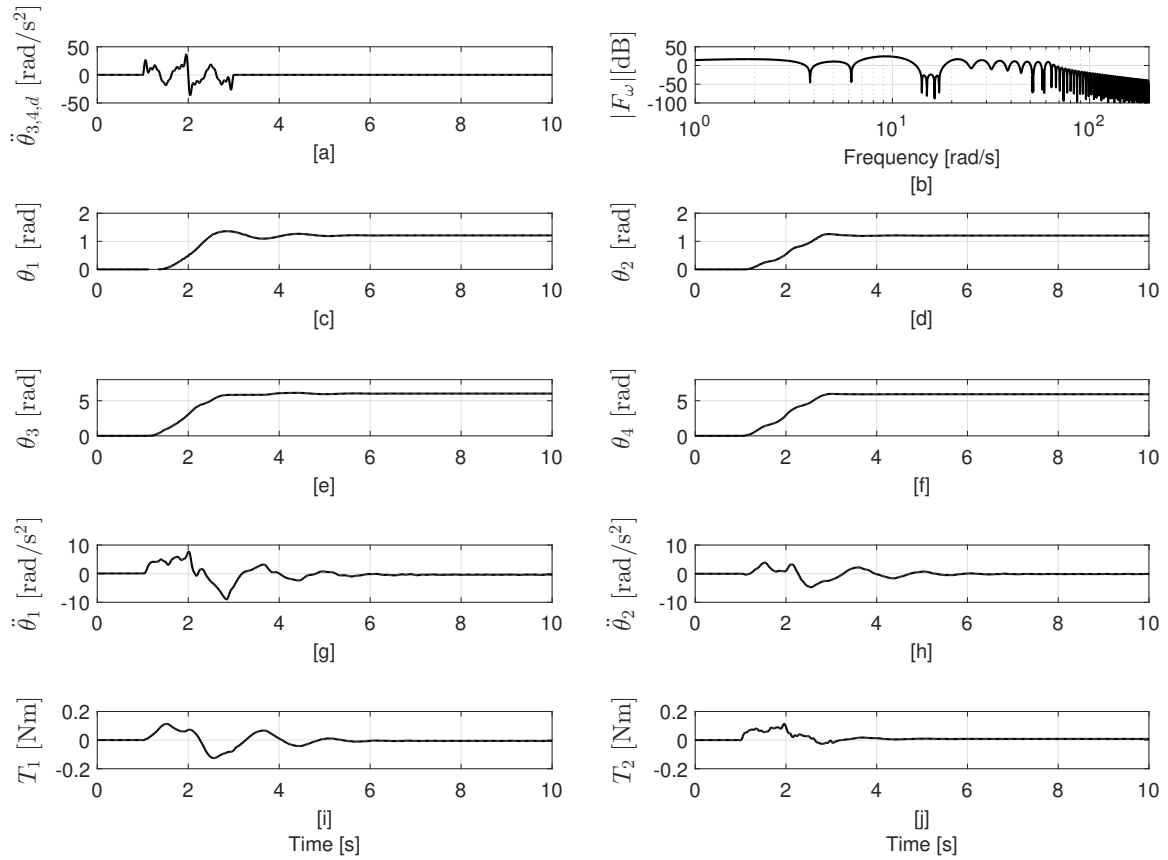


Figure B.11. Experimental response of Hybrid controller when applying a ramped sinusoid input with $\kappa = 6$. [a] is the desired motor acceleration profile for both motors, and [b] is the magnitude spectrum of the desired acceleration profile for the motors. [c] and [d] are the angular positions of links 1 and 2, while [e] and [f] are the angular positions of the shoulder and elbow motors, respectively. [g] and [h] show the angular accelerations of links 1 and 2, while [i] and [j] are the torques of the shoulder and elbow motors.

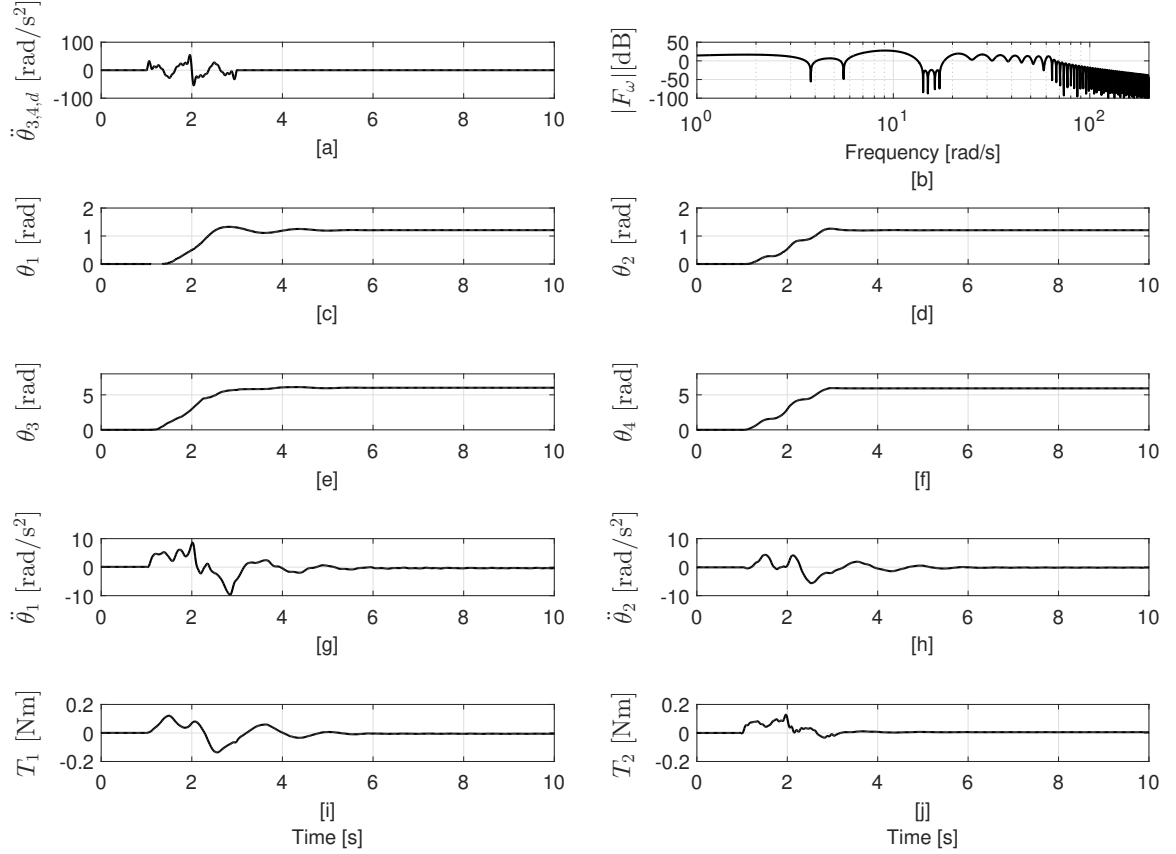


Figure B.12. Experimental response of Hybrid controller when applying a ramped sinusoid input with $\kappa = 9$. [a] is the desired motor acceleration profile for both motors, and [b] is the magnitude spectrum of the desired acceleration profile for the motors. [c] and [d] are the angular positions of links 1 and 2, while [e] and [f] are the angular positions of the shoulder and elbow motors, respectively. [g] and [h] show the angular accelerations of links 1 and 2, while [i] and [j] are the torques of the shoulder and elbow motors.